Depositional Environment, Reservoir Properties, and EOR Potential of an Incised-valley-fill Sandstone, Pleasant Prairie Oilfield, Haskell County, Kansas

By

© 2012
Peter J. Senior
B.S., Kansas State University, 2009

Submitted to the graduate degree program in Geology and the Graduate Faculty of the University of Kansas in partial fulfillment of the requirements for the degree of Master of Science

Advisory Committee:

_____
Anthony W. Walton, Chair

_____
Eugene C. Rankey

_____
Stephen T. Hasiotis

Date defended: 10/02/2012

The Thesis Committee for Peter J. Senior certifies
that this is the approved version of the following thesis:

Depositional Environment, Reservoir Properties, and EOR Potential of an Incised-valley-fill Sandstone, Pleasant Prairie Oilfield, Haskell County, Kansas

Chairperson:

_____

Anthony W. Walton, Chair

Date Approved: 10/02/2012

Abstract

Incised-valley-fill deposits form important hydrocarbon reservoirs and can have internal heterogeneities that affect recovery of hydrocarbon resources. Better understanding of the internal heterogeneity of incised-valley-fill reservoirs will help in more accurate reservoir modeling and more efficient recovery of hydrocarbon resources. Pleasant Prairie oilfield in Haskell County, Kansas, produces oil from an incised-valley-fill reservoir in the Chesterian (Upper Mississippian) Shore Airport Formation. The reservoir is part of a larger paleovalley trend interpreted as a tide-dominated, estuarine depositional system; depositional environments within such systems vary spatially as a result of interactions of tidal and fluvial processes.

Core analysis suggests that the reservoir at Pleasant Prairie oilfield is a stacked series of conglomerate-based, fining-upward siliciclastic successions deposited in the river-dominated part of a tide-influenced estuarine system. Core petrophysical data and well-log correlations suggest that reservoir heterogeneity occurs in the form of vertical and lateral compartmentalization. Reservoir modeling indicates a current field-wide recovery factor of 0.30–0.36 of original oil in place. Comparison of modeled original oil in place to production data suggests inaccuracy of reservoir models at the scale of individual well drainage areas.

Waterflooding of the reservoir has proven successful for >10 years, and remaining oil in place ranges from 7.8–10.1 mmbo according to Petrel™ models, indicating potential for future enhanced oil recovery operations such as CO_2 or chemical flooding. Other incised-valley-fill reservoirs, such as Morrowan (Lower Pennsylvanian) oilfields in Colorado and Kansas, originated in similar depositional settings and display similar reservoir properties; such reservoirs may also have potential for future enhanced oil recovery operations.

Acknowledgements

Table of Contents

Introduction

  a. **Background and Location**

      Depositional environments within incised valleys vary due to the interplay of fluvial, tidal, and marine influences (Dalrymple et al., 1992; Zaitlin et al., 1994). Such depositional complexity commonly is recorded in variations in the geologic character of hydrocarbon reservoirs deposited in different parts of an incised valley. A better understanding of the internal depositional complexities of incised valleys can aid in more efficient exploitation of reservoirs developed within such deposits. Although no two reservoirs are alike, insights into a particular reservoir may be applicable to other reservoirs deposited in similar environments.

      This study examines rocks from the Pleasant Prairie oilfield, which covers parts of four counties in southwestern Kansas and produces oil and gas from several stratigraphic intervals, including the Shore Airport Formation (Abegg, 1994a) in Upper Mississippian Chesterian strata. The Chesterian reservoir is an incised-valley fill sandstone occupying a narrow, north–south oriented channel in Haskell County, Kansas, and produces from wells that form a linear trend stretching over 6 km (Figure 1). The Chesterian reservoir at Pleasant Prairie oilfield is part of a larger trend of oil production from an incised paleovalley that extends over 80 kilometers from north to south (Figure 2). The incised Mississippian paleovalley in southwestern Kansas has been interpreted as a tide-dominated, estuarine depositional system (Montgomery and Morrison, 1999; Cirilo, 2002), and the original extent of the paleovalley is unknown because post-depositional erosion has truncated Chesterian valley-filling strata north of the Pleasant Prairie area (Goebel, 1968).

1
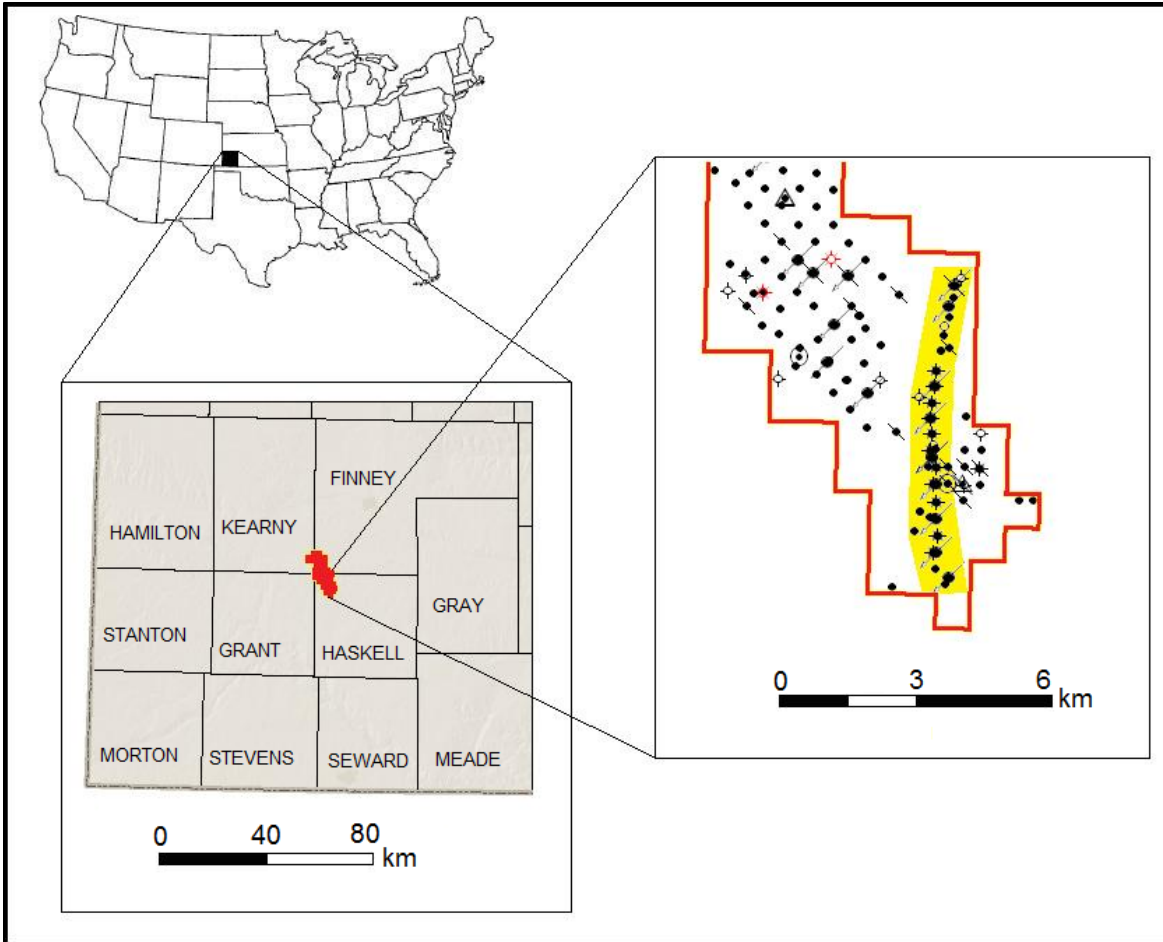
Figure 1: Location of Pleasant Prairie oilfield in southwest Kansas. Inset map at bottom left shows Kansas counties, and Pleasant Prairie oilfield as red polygon. Wells that penetrate Chesterian sandstone are highlighted yellow in inset map of oilfield at right. Note the limited and linear extent of the sandstone reservoir, as indicated by the linear group of wells.
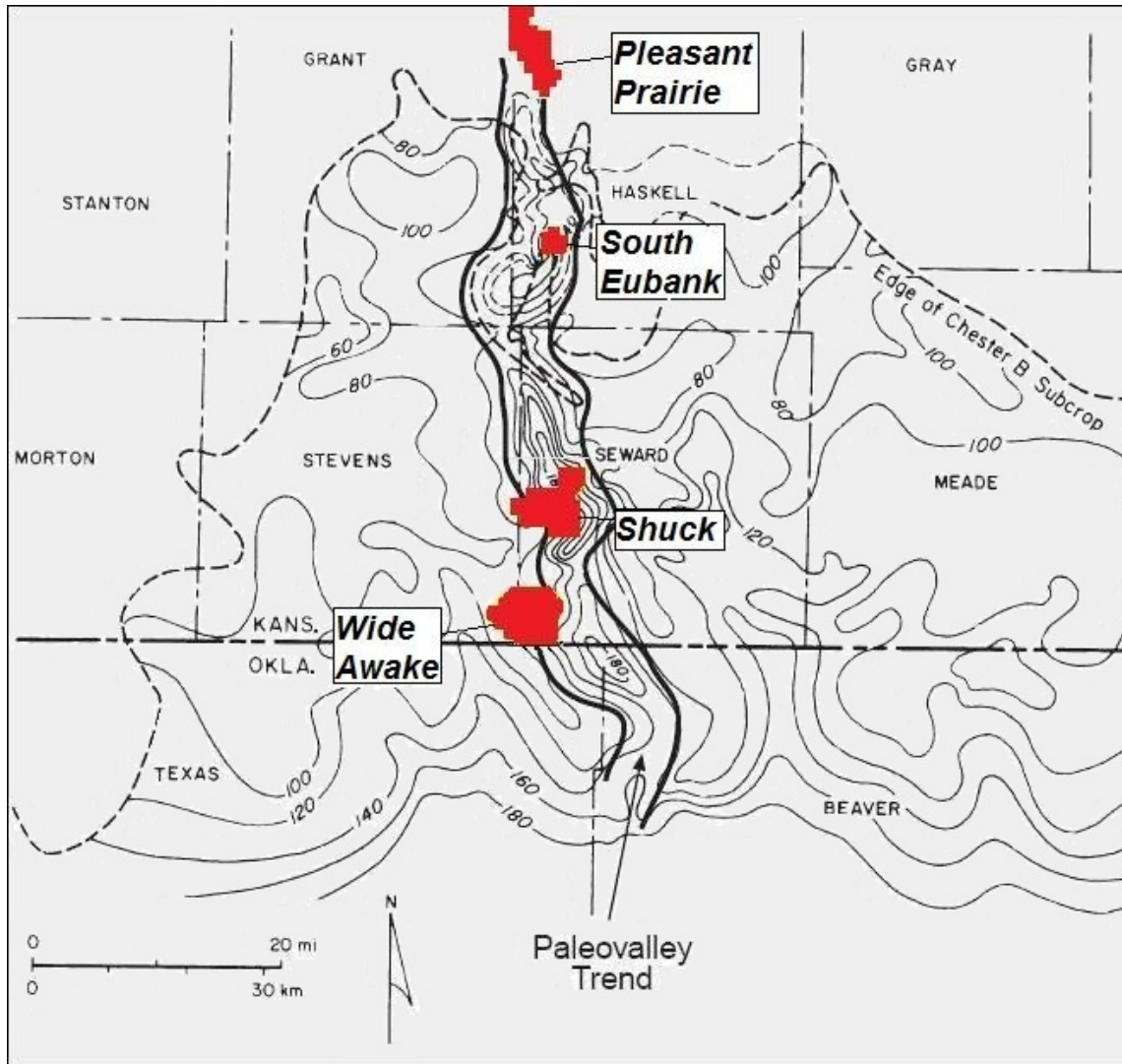
Figure 2: Thickness map of the Upper Mississippian paleovalley trend in southwest Kansas. Modified from Montgomery and Morrison (1999) after Severy (1975), with contours in feet thickness. Oilfields producing from the incised valley are marked by red polygons. Pleasant Prairie oilfield lies updip and in line with this trend.

This study seeks to understand the depositional environments of the Chesterian Shore Airport Formation sandstone reservoir at Pleasant Prairie oilfield in the larger context of the incised paleovalley trend, and to examine the internal petrophysical and stratigraphic architecture of the reservoir using well logs, core data, and three dimensional (3D) reservoir models. Many prolific oil and gas fields of eastern Colorado and western Kansas are found in Lower Pennsylvanian Morrowan sandstones, which were deposited in incised valleys similar to the Mississippian paleovalley trend (Krystinik and Blakeney, 1990; Bowen andWeimer, 2003). Origins in a similar depositional setting implies the possibility of similar reservoir character, therefore insights from this study into the internal character of Pleasant Prairie oilfield may be useful to characterization of some Morrowan reservoirs and have similar implications for reservoir management.

The Chesterian sandstone reservoir at Pleasant Prairie is currently under waterflood, and further enhanced oil recovery (EOR) operations, including CO_2 or surfactant flooding, are being considered. Creation of reservoir models to illustrate predicted spatial distribution of lithofacies and petrophysical properties provides insight into the internal distribution of reservoir fluids, and comparisons of modeled oil in place to cumulative production data can provide insight into remaining reserves and their distribution. Such insights gained through reservoir modeling may prove useful in locating underdeveloped parts of the field or assessing whether enough reserves remain for operators to justify pursuit of further EOR operations.

b. Stratigraphy

The Chesterian is the uppermost stage of the Mississippian Subsystem of the Carboniferous System (Goebel, 1968; Sawin et al., 2009). In southwestern Kansas, the

Chesterian includes the Shore Airport Formation and Ste. Genevieve Limestone (Figure, 3; Abegg, 1994a; Maples, 1994). Strata deposited as part of the incised paleovalley trend are contained in the Shore Airport Formation. A locally extensive unconformity in southwestern Kansas separates Shore Airport Formation strata from underlying Ste. Genevieve and St. Louis limestone strata, and a more regionally extensive unconformity separates Chesterian strata from overlying Pennsylvanian strata (Merriam, 1963; Goebel, 1968). The unconformity separating Mississippian and Pennsylvanian strata is a major feature in the subsurface of Kansas and surrounding states, and corresponds to a chronological boundary in global stratigraphy. Chesterian sandstones in the paleovalley trend generally are incised into and overlie the Ste. Genevieve strata, but in the Pleasant Prairie oilfield, well completion forms filed with the Kansas Corporation Commission and publicly available on the website of the Kansas Geological Survey (KGS; www.kgs.ku.edu) indicate that Chesterian strata are incised through the Ste. Genevieve Limestone and directly overlie St. Louis strata.

System	Subsystem	Series	Stage	Formation or Group
Carboniferous	Pennsylvanian	Lower Pennsylvanian	Atokan	Gray Group
			Morrowan	Kearny Formation
	Mississippian	Upper Mississippian	Chesterian	Shore Airport Fm.
				Ste. Genevieve Limestone
			Meramecian	St. Louis Limestone
				Salem Limestone
				Warsaw Limestone
			Osagian	Burlington-Keokuk Limestone

Figure 3: Generalized Mississippian–Lower Pennsylvanian stratigraphy of study area, compiled from Kansas Geological Survey website (KGS, http://www.kgs.ku.edu), Abegg (1994), and Maples (1994). Shaded yellow interval indicates the stratigraphic position of the incised-valley fill that is the subject of this study.

c. Tectonic and Depositional History

The Hugoton Embayment of the Anadarko Basin covers much of southwestern Kansas, including the area of Pleasant Prairie oilfield and the incised Mississippian paleovalley. The Anadarko Basin, a major structural feature of the region (Figure 4), is the deepest basin in the interior of the North American craton, with up to 12,000 m (40,000 ft) of accumulated sediments (Johnson, 1989). The incised Mississippian paleovalley predates the Anadarko Basin, however, which did not exist as currently defined until early Pennsylvanian time (Johnson, 1989; Perry, 1989).

Tectonic development of the Anadarko Basin area has been interpreted by Johnson (1989) and Perry (1989) to include four phases. The first included emplacement of intrusive and extrusive igneous rocks in Precambrian to Early Cambrian time; these igneous rocks form the basement of the area. The second phase, from Cambrian through Mississippian time, consisted of rifting followed by shallow marine sedimentation in a broad epicontinental sea; the area at this time is referred to as the Oklahoma Basin, ancestral to the Anadarko Basin. Cambrian rifting created the Southern Oklahoma Aulacogen in the area of present-day southwestern Oklahoma. Post-rift cooling and subsidence, coupled by a long-term global rise in sea level, resulted in marine inundation in the epicontinental sea in which as much as 4600 m (15,000 ft) of sediment accumulated. The third phase is marked by the onset of orogenic activity in Late Mississippian (Perry, 1989) or Pennsylvanian (Johnson, 1989) time, and lasted until the end of Pennsylvanian time. This orogeny included folding, faulting, downwarp, and uplift. As a result, the broad epicontinental sea of the Oklahoma Basin area developed into a series of well-defined uplifts and basins, including the Anadarko Basin. In association with this tectonic activity, a marked unconformity developed between older Mississippian and younger Pennsylvanian strata in much

of the area. The fourth phase covers Permian through Holocene time, and is characterized by infill of the basin area with sediment, mostly during Permian time. Late Cretaceous to Early Paleogene uplift associated with the Laramide orogeny to the west marked the final withdrawal of seas from the area.

The emergence of the Central Kansas uplift as a positive structural feature by Pennsylvanian time (Merriam, 1963) is the major tectonic event relating to the present-day subsurface distribution of Mississippian rocks in the Oklahoma–Anadarko Basin area. As a result of the orogenic activity through Late Mississippian–Early Pennsylvanian time, Mississippian strata were uplifted and tilted so that they dipped in a general southerly direction, towards the deepening depocenter of the Anadarko Basin. The uplift and tilting exposed much of the Mississippian strata and allowed weathering and erosion to remove large quantities of rock, including portions of the incised paleovalley north of Pleasant Prairie oilfield.

Throughout much of Mississippian time in present-day southwestern Kansas, warm, shallow marine conditions prevailed; the area was near the equator during Mississippian time (Figure 5). Deposition of sediments was limited mostly to carbonates; however, late in Mississippian time, a notable increase of siliciclastic deposition occurred (Goebel and Stewart, 1979). The presence of appreciable amounts of siliciclastic sediments characterizes the Chesterian Stage after deposition of the Ste. Genevieve Limestone, and differentiates these strata from those of previous Mississippian stages (Goebel, 1968; Goebel and Stewart, 1979). The incised paleovalley that is the focus of this study developed as a result of subaerial exposure and erosion of Ste. Genevieve and older strata during regression (Severy, 1975; Cirilo, 2002). The location of the paleovalley may have been influenced by block faulting in subjacent strata

(Shonfelt, 1988). The paleovalley trends north–south and extends from Haskell County, Kansas, in the north through Seward and Stevens Counties, Kansas, and into Oklahoma.

Late Mississippian time in the area was characterized by overall shoreline regression, punctuated by minor transgressions (Goebel, 1968; Shonfelt, 1988). Transgressive–regressive cycles associated with incised-valley fills can be associated with eustasy (Van Wagoner et al., 1990), and such an association has been proposed for Chesterian incised-valley fills in the Illinois Basin, to the east of the Oklahoma–Anadarko Basin area (Smith and Read, 2000). Smith and Read (2000) propose that the Chesterian incised paleovalleys in the Illinois Basin represent evidence of increases in amplitude of sea-level fluctuation driven by marked increases of continental ice volume associated with the onset of major late Paleozoic glaciation. Similarly, coastal onlap curves suggest an increase in the amplitude of sea level fluctuations during Chesterian time (Ross and Ross, 1985; Rygel et al., 2008). Such fluctuations suggest that multiple glacioeustatically driven transgressive–regressive cycles may have influenced filling of the Chesterian incised paleovalley in southwestern Kansas.
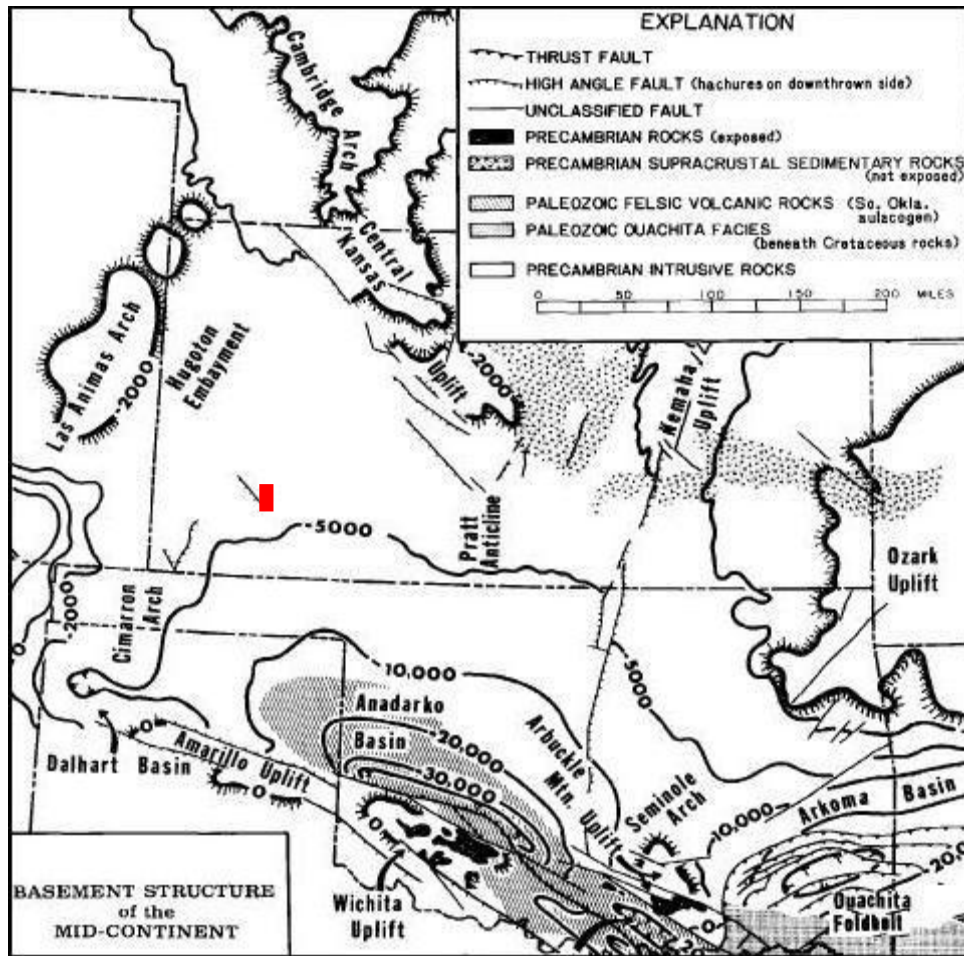
Figure 4: Major structural features of the mid-continent region. Modified from Rascoe and Adler (1983). Red polygon indicates study area, showing the location of Pleasant Prairie oilfield on the relatively low-relief shelf of the Hugoton Embayment of the Anadarko Basin.
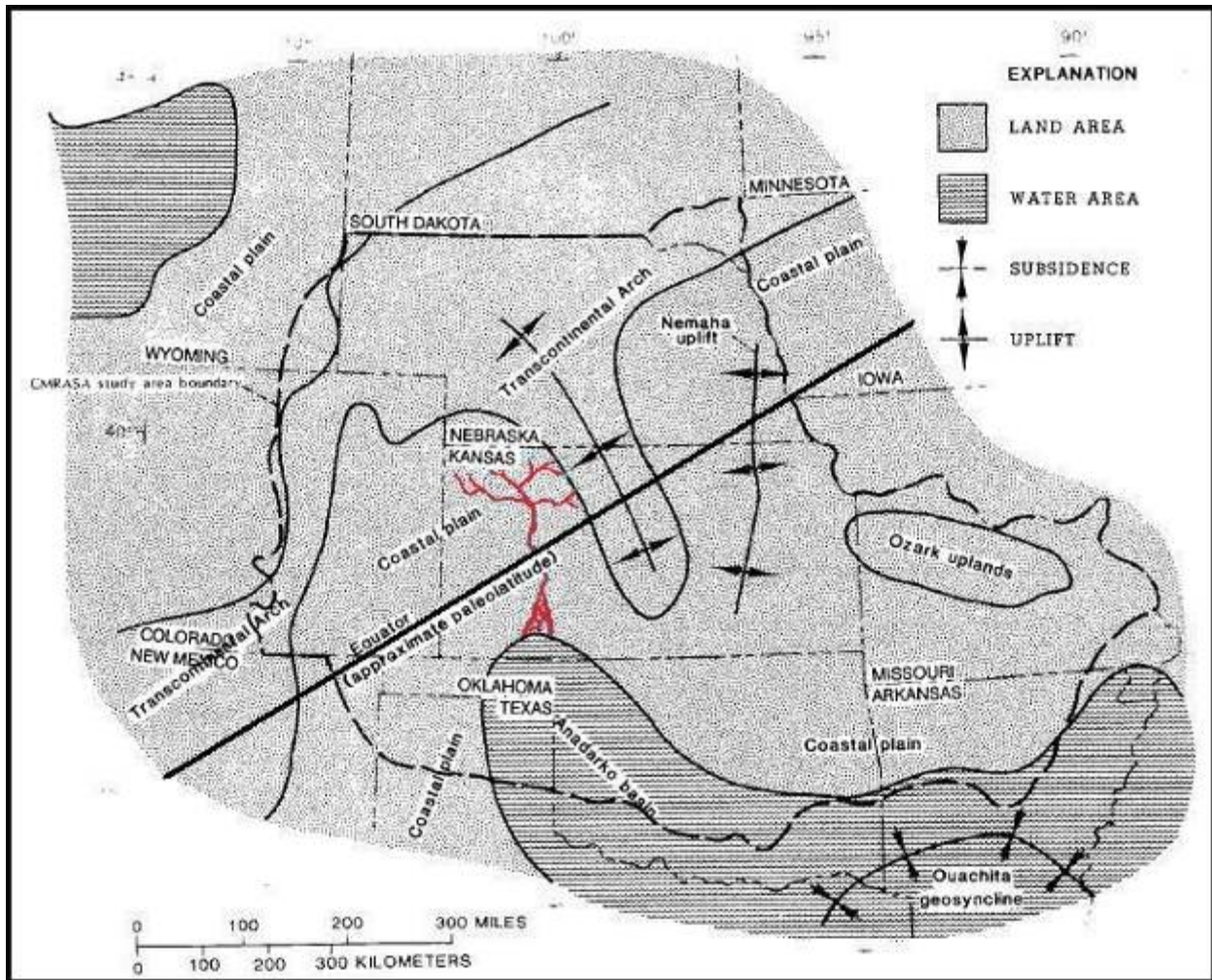
Figure 5: Late Mississippian paleogeographic map of mid-continent region, with hypothetical drainage system (red). This map shows a conceptual picture of the actual size of the drainage system that is now partially preserved as an incised paleovalley in southwest Kansas which contains several hydrocarbon reservoirs. Modified from Jorgensen (1989).

d. Previous Work

Production of oil from the Chesterian sandstones dates back to at least 1958 (Fugitt and Wilkinson, 1959), but the combination of more deep wells in the Hugoton Embayment and the advent of 3D seismic study in more recent decades has allowed more thorough exploration and exploitation of the sandstones. The Chesterian sandstone is the subject of few published studies because of its relatively recent development as a target for the petroleum industry. Montgomery and Morrison (1999) highlighted successful redevelopment activity of the Chesterian sandstone reservoir at South Eubank oilfield in Haskell County, Kansas, using seismic and core data. Sorensen et al. (1999) described tar mats, layers of solid bituminous material, in the Hitch subunit of the Shuck oilfield in Seward County, Kansas. In addition to published studies, relevant unpublished M.S. theses have described and interpreted these strata. For example, Severy (1975) concentrated on regional stratigraphy of the Chesterian in the Hugoton Embayment area (Figure 2). Shonfelt (1988) presented a detailed study of heterogeneities in the Kinney–Lower Chester oilfield (now called Wide Awake oilfield) in Seward and Stevens Counties, Kansas. Finally, Cirilo (2002) concentrated on the deposition and diagenesis of the Chesterian sandstone in the Shuck oilfield in Seward County, Kansas.

Montgomery and Morrison (1999) outlined a core and 3D seismic survey study that mapped the details of the incised paleovalley in the South Eubank oilfield area in southern Haskell County, Kansas. Accurate delineation of the paleovalley and characterization of the Chesterian sandstone within it led to drilling of thirty new oil-producing wells in the field, adding 2.5 million barrels of reserves and more than tripling the daily oil production rate. In their study, Montgomery and Morrison (1999) interpreted the Chesterian sandstone to represent tide-influenced estuarine deposits, and identified four types of deposits which they described in

12

the context of depositional environment: intertidal flat, storm deposit, tidal-flat–estuarine channel, and sand wave–tidal bar. The intertidal flat deposits are sandstone characterized by very high clay content—up to 17%—and abundant shale laminations and occasional thin coal seams. Sedimentary structures include flaser and wavy bedding, convolute bedding, and fluid-escape structures. The storm deposits are clayey siltstone layers with highly disrupted and convoluted bedding. The tidal-flat–estuarine channel deposits are a series of 1.5–3 m (5–10 ft) thick fining-upward successions going from pebbly lag deposits with shale and carbonate clasts to flaser and wavy and convolute-bedded siltstone and shale. The sand wave–tidal bar deposits display a coarsening-upward trend and have very low clay content; these deposits change upward from rippled and wavy bedded to planar and low-angle cross-bedded.

Sorenson et al. (1999) describe a low permeability tar mat, or dead oil zone, in the Hitch subunit of the Shuck oilfield. Dead oil zones are important to consider for this study, because their presence at Pleasant Prairie oilfield could affect enhanced oil recovery operations; according to Sorenson et al. (1999), CO_2 flooding can potentially mobilize the bituminous material in dead oil zones or lead to further precipitation, negatively impacting reservoir performance. Failure to recognize the presence of a tar mat can also lead to erroneously high original oil in place calculations because the tar mat represents a zone of solid material that will not flow (unless, for example, the solid material is remobilized by CO_2 flooding), rather than pore space filled with reservoir fluids. Standard laboratory procedures for preparing core samples for measurements of porosity and permeability can dissolve and wash out any solid bituminous material, thereby potentially resulting in inaccurately high values for those variables and introducing error into reservoir volumetrics. Sorenson et al. (1999) identified the tar mat in the Shuck oilfield through visual examination of cores. The tar mat was recognizable in core due

13

to its dark gray color as opposed to the brown oil-stained color of the rest of the reservoir, and consisted of a 9 m (30 ft) thick layer of pore-filling solid bituminous material. Study of cores indicated that the tar mat is laterally extensive and compartmentalizes the reservoir vertically. Nonetheless, neutron and density porosity logs failed to show reduced values in the tar mat zone because the solid bituminous material does not differ markedly in hydrogen concentration or density from liquid-phase oil in the reservoir. Thus, the size of the tar mat and the impact on the reservoir went unnoticed until elucidated by Sorenson et al. (1999).

Severy (1975) is the earliest available study focusing on the Chesterian Stage in southwestern Kansas. The study focused defining the subsurface distribution of Chesterian rocks and subdividing them into mappable, recognizable units based on well-log and core data, and presented hypotheses regarding depositional environments. Severy (1975) divides the Chesterian into five zones, in ascending stratigraphic order noted as A through E, with the petroliferous sandstone occurring in Zone A. At the time of that publication (i.e., Severy, 1975), no conceptual models for the origin of the Chesterian Zone A sandstone had been proposed. Five cores were examined in the study, all from Seward and Stevens Counties, Kansas. Of the five, the core closest to Pleasant Prairie oilfield was from over 40 km to the south; Pleasant Prairie is in Township 27 south, while the nearest core in Severy's (1975) study is in Township 32 south. Sedimentary structures in the Chesterian sandstone noted by Severy (1975) include planar crossbeds, horizontal bedding, and small-scale ripple marks. These three structures, along with a lack of trough crossbeds, led Severy (1975) to interpret the depositional environment of the Chesterian sandstone as a braided fluvial system, an interpretation he regarded as a working hypothesis based on limited data available at the time. Severy (1975) considered an alternative hypothesis of a channelized tidal flat depositional environment, based on the presence of abraded

marine fossil fragments in the sandstone. A lack of trace fossils or mudcracks, however, weakened this hypothesis in his eyes in comparison to the braided fluvial interpretation.

Shonfelt (1988) focused the Kinney–Lower Chester field (now called Wide Awake field) in Stevens and Seward Counties, Kansas. The thesis explored the relation of geologic characteristics, such as lithofacies, depositional history, porosity, and permeability to reservoir quality characteristics, such as fluid storage capacity, flow capacity, and relative recovery efficiency. Shonfelt (1988) examined six cores from the field and described four sandstone lithofacies: quartz sandstone, mixed quartz–carbonate sandstone, banded sandstone, and flaser-bedded sandstone. Possible bidirectional cross-stratification was identified in each lithofacies. The mixed quartz–carbonate lithofacies includes peloids and abundant fossil fragments of bryozoans, brachiopods, and echinoderms, and the banded sandstone lithofacies consists of alternating lithologies of quartzose sandstone and arenaceous limestone. The abundance of possible bidirectional cross-stratification and carbonate material, along with reactivation surfaces and common flaser and lenticular bedding lead Shonfelt (1988) to interpret the depositional environment as a channel inlet in an estuarine–peritidal strandline complex.

Cirilo (2002) focused on depositional and diagenetic history of Chesterian Zone A sediments, concentrating the study in the Shuck oilfield area, but the study also provided insight and information on the broader context of the Chesterian deposits within the incised paleovalley system. Core study subdivided the Chesterian into local deposit types in the Shuck oilfield, described and interpreted in the context of depositional environment, including mixed-bedding tidal flat, subaqueous tidal sand bar, tidal-creek sandstone, and vegetated tidal-flat marsh or swamp mudstone. A suite of features revealed in the study indicates tidal influence. Crinoid debris and shell fragments are present in all deposit types except the vegetated tidal-flat marsh or

swamp mudstone deposits. The mixed bedding tidal-flat deposits, which directly overlie the basal Chesterian unconformity, consists of interlaminated mud and sand, and are characterized by possible bidirectional cross-stratification, wavy, lenticular, and flaser bedding, and soft-sediment deformation structures. The subaqueous tidal sand-bar deposits contain glauconite, mud laminae, and reactivation surfaces; these deposits are characterized by horizontal to steeply dipping cross-bedding, with a lack of trough cross-bedding. The lack of trough cross-bedding was interpreted as evidence against a strictly fluvial origin of the deposits. The tidal-creek sandstone deposits contain carbonate grains and possible bidirectional cross-stratification, and the deposit name derives from the channel morphology revealed by 3D seismic imagery. Cirilo (2002) noted bioturbation in the tidal-creek sandstone—lined, mud- or sand-filled *Ophiomorpha* and *Thalassinoides* burrows up to 3 cm in diameter—and in the vegetated tidal-flat marsh or swamp mudstone deposits—calcite-cemented *Planolites* and *Terebellina* burrows up to 3 cm in diameter. Cirilo interprets the Chesterian strata in the Shuck oilfield area to have been deposited in the central to outer part of a tide-dominated estuary, following the facies models of Dalrymple et al. (1992) and Zaitlin et al. (1994), and probably closer to the estuary mouth than the river-dominated, upper or inner estuary zone.

Methods

To define lithofacies, reservoir architecture, and physical properties of the Chesterian (Upper Mississippian) Shore Airport Formation reservoir at Pleasant Prairie oilfield, this study used analysis of core and well logs, agglomerative hierarchical clustering analysis of lithofacies, analysis of core petrophysical data, prediction of lithofacies in uncored wells through the use of artificial neural networks. These methods were integrated into a reservoir modeling workflow (Figure 6) leading to creation of a 3D cellular model of the reservoir using Schlumberger Petrel™ software.
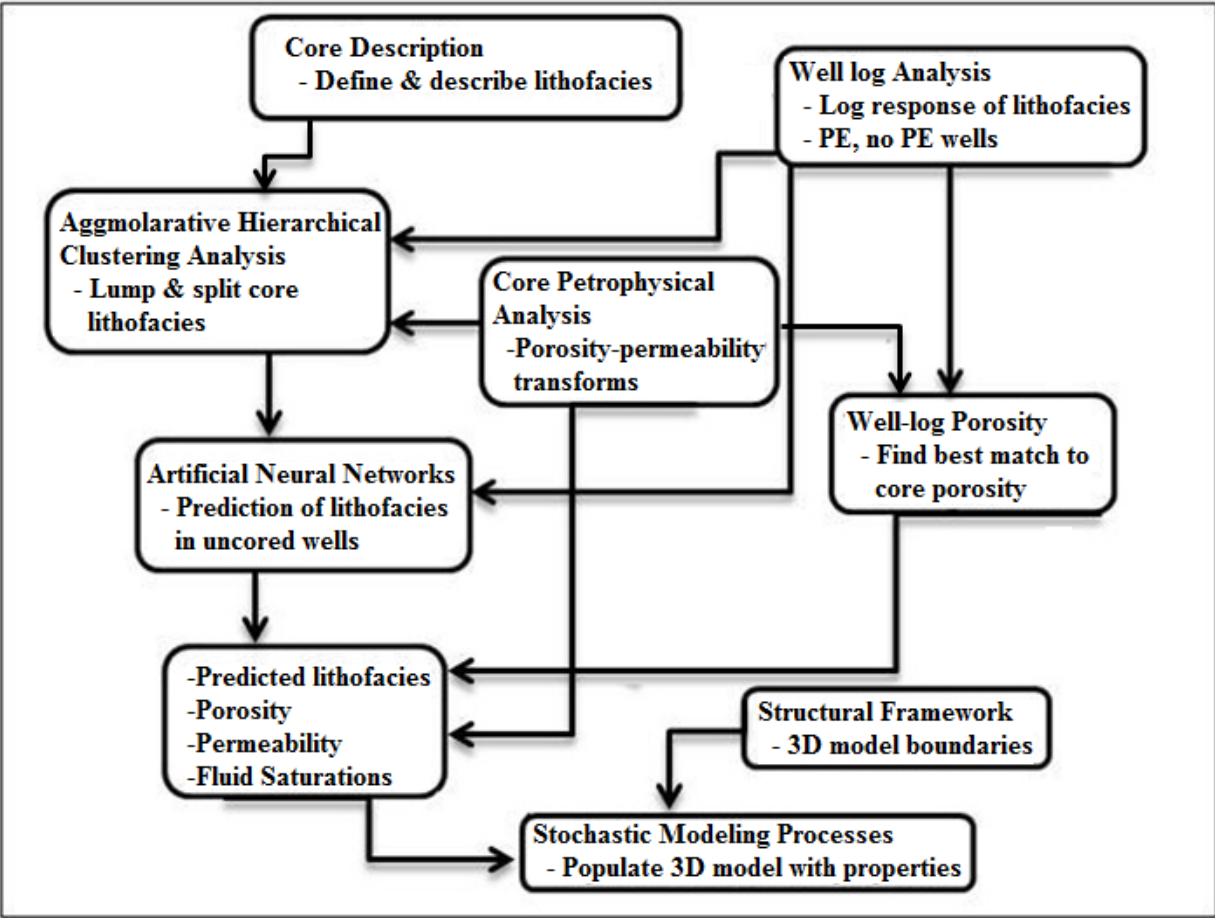
Figure 6: Schematic diagram illustrating the integration of methods used in this study into a reservoir modeling workflow.

a. Core Description

Visual examination of cores aided identification of descriptive lithofacies. Cores were available from two wells in the Pleasant Prairie oilfield: Moody D2 (API# 15-081-21255) and Mary Jones #2 (API# 15-081-21334). Both cores are stored at the Kansas Geological Survey in Lawrence, Kansas. The two cores were examined visually, with the use of both a hand lens and a binocular microscope, and under both wet and dry conditions. Key surfaces in the cores were identified on well logs, to establish a depth correction that could be applied to match each of the core samples and their corresponding petrophysical and grain density measurements to the well logs. Color, lithology, sedimentary structures, fossil content, grain size, sorting, rounding, pore throat size, argillaceous content, and cement mineralogy were described at intervals of 0.15 m (0.5 ft) using a numerical classification scheme (Table1). Sedimentary structures were described according to the terminology of Ingram (1954), where laminae are < 1 cm thick (thin laminae are 0–0.5 cm thick, and thick laminae are 0.5–1.0 cm thick) and beds are >1 cm thick (very thin beds are 1–5 cm thick, and thin beds are 5–10 cm thick). The geometry of laminae and beds is described as planar or tangential, and the geometry of surfaces bounding sets of laminae or beds is described as straight or curved. Colors were described using a Munsell geological rock-color chart (2009 edition, retrieved from Munsell website at

http://www.munsellstore.com/files/CIPA00011%5C599.pdf. Pore throat size and argillaceous content were estimated visually (see Table 1 for categorization). Core descriptions are included in Appendix A, and complete images of both cores are included in Appendix B. Core-analysis reports included helium-measured porosity, permeability to air, and grain density at 0.3 m (1 ft) intervals, and those data provided the basis for petrophysical analysis. Porosity data can be averaged using a simple arithmetic mean calculation, and such calculations were applied to each

19

core-defined lithofacies. Permeability, however, is log-distributed data and so another method

should be used to state the average permeability. The geometric mean of permeability data is

generally considered a good measure of average permeability (Warren et al., 1961), but the

median has also been suggested as a good representation of average permeability (Rollins et al.,

1992), therefore this study includes both the geometric mean and median of core permeability for

each core-defined lithofacies.

Table 1: Numerical classification scheme used to describe lithology, sedimentary structures, fossil content, grain size, sorting, rounding, pore throat size, argillaceous content, and cement mineralogy in Chesterian cores from Pleasant Prairie oilfield. Scheme developed by M. Dubois *in* Dubois et al. (2006), modified for this study by J. Youle, M. Dubois, and P. Senior. For a given 0.15 m (0.5 ft) sample of core, a numerical class was assigned for each parameter—e.g., a given sample could have rock type of 7, pore type of 3, etc.

CODE	Rock Type	Dunham/Folk Classification	Grain Size (diameter)	Bedding (size)
9	Conglomerate	cobble conglomerate	very coarse rudite/cobble conglomerate (>64mm)	Chaotic
8	Dolomite	sucrosic/pebble conglomerate	medium–coarse rudite/pebble conglomerate (4–64mm)	planar, low angle cross-bed
7	Limestone	baffle–boundstone/very coarse sandstone	fine rudite/very coarse sand (1–4mm)	climbing ripples
6	Sandy Limestone	grainstone/coarse sandstone	arenite/coarse sand (500–1000µm)	soft sediment deformation/early diagenetic compaction
5	Limey Sandstone	packstone-grainstone/medium sandstone	arenite/medium sand (250–500µm)	large cross-bed (>4mm), trough
4	Sandstone/Siltstone	packstone/fine sandstone	arenite/fine sand (125–250µm)	small cross-bed (<4mm), ripple
3	Flaser Sandstone-Siltstone/Shale	wackestone-packstone/very fine sandstone	arenite/very fine sand (62–125µm)	Graded
2	Wavy Sandstone-Siltstone/Shale	wackestone/coarse siltstone	coarse lutite/coarse silt (31–62µm)	thick lamination couplets (>4mm)
1	Linsen or Sandy Shale	mudstone-wackestone/very fine-medium siltstone	fine–medium lutite/very fine–medium silt (4–31µm)	thin lamination couplets (<4mm)
0	Shale	mudstone/shale/clay	clay (<4µm)	massive/structureless

Table 1 (continued):

CODE	Argillaceous Content	Principal Pore Size (diameter)	Cement or Pore-Filling Material (density)
9	Fracture-fill 10–50%	cavern vugs (>64mm)	Sulfide (ρ=3.85–5.0)
8	Fracture-fill 5–10%	medium-large vugs (4-64mm)	Siderite (ρ=3.89)
7	Shale >90%	sm vmf (1-4mm)	Phosphate (ρ=3.13–3.21)
6	Shale 75–90%	coarse (500-1000µm)	Anhydrite (ρ=2.35–2.98)
5	Shale 50–75%	medium (250-500µm)	Dolomite (ρ=2.87)
4	Shale 25–50%	fine (125-250µm)	Calcite (ρ=2.71)
3	Shale 10–25%	pinpoint-very fine (62-125µm)	Quartz (ρ=2.65)
2	wispy 5–10%	pinpoint (31-62µm)	Clay (ρ=2.0–2.7)
1	trace 1–5%	microporous (<31µm)	Carbonaceous (ρ=2.0)
0	Clean <1%	Nonporous	Uncemented (ρ=1.0)

b. Well-log Analysis

Chesterian wells in the Pleasant Prairie oilfield generally have both neutron–density and resistivity logs. Correlation and analysis of these well logs provided the basis for analysis of the structural and stratigraphic character of the Chesterian Shore Airport Formation reservoir body. Analysis of well-log data, including creation of well-to-well cross-sections, was performed using PETRA™, a subsurface GIS program by IHS. Manual digitization of raster log images for wells where digital .las logs were not already available was also performed using PETRA™, since creation of a 3D reservoir model requires digital log data.

c. Agglomerative Hierarchical Clustering (AHC) Analysis

To aid in determining appropriate lithofacies divisions for prediction in uncored wells using artificial neural networks, core and log data were analyzed using a form of multivariate statistical analysis called agglomerative hierarchical clustering (AHC) analysis (Everitt et al., 2001). The goal of AHC analysis was to examine multivariate statistical dissimilarity of individual core-defined lithofacies, using the statistical dissimilarity to aid in deciding whether or not to lump or split the lithofacies for artificial neural network prediction in uncored wells. For this study, a quantitative limit of dissimilarity was not used to determine whether or not core-defined lithofacies should be lumped or split. Rather, the goal of using AHC was to analyze visually the general patterns of multivariate statistical dissimilarity of the core-defined lithofacies using dendrograms.

Variables used in AHC in this study included both well-log and core-description data. Well-log data used included gamma-ray, photoelectric effect, bulk density, neutron-porosity and density-porosity logs, and neutron–density porosity average. Core description data used in AHC

included grain size, argillaceous content, pore throat size, cement mineralogy, and porosity and permeability. Each 0.5 ft (0.15 m) interval of core had a suite of numerical values for each of the well-log and core variables. AHC analysis measures the multivariate statistical dissimilarity of each 0.5 ft (0.15 m) sample through use of the Euclidean distance formula:

$$d = \sqrt{\sum_{i=1}^{N} \left| I_i - J_i \right|^2}$$

Where d is distance, I_i and J_i are individual data samples of core or log variables, such as gamma-ray intensity or core porosity, at depth **i**. ACH was done in XLSTAT, an add-in for Microsoft Excel, and dendrograms were created as visual representations of the AHC analysis to characterize multivariate statistical dissimilarity of each depth sample of each lithofacies. AHC starts by making the smallest clusters possible, pairs, then clusters pairs together, continuing until all data have been clustered. AHC is a bottom up method, as opposed to a top down method, which would start by making the largest clusters possible and proceeding to split them into smaller and smaller clusters. Dendrograms are created by drawing connecting lines between each most similar pair of depth samples, then each pair of pairs, continuing until all data are linked into a structure which allows visual examination of clustering patterns (e.g., see Results section on AHC below).

The primary goal of examining the dendrograms in this study was to ascertain whether core-defined sandstone lithofacies formed discrete clusters or tended to be mixed together.

23

Mixing of sandstone lithofacies in dendrograms would indicate that they were similar enough to be lumped together. Secondarily, dendrograms were used to examine any other patterns in the clustering behavior of the core-defined lithofacies. The overall goal was to help define a classification scheme of lithofacies for prediction in all wells using artificial neural networks by noting the general patterns of dissimilarity between lithofacies as expressed in the dendrograms.

d. Petrophysics

Several methods were used to estimate porosity from well logs. The goal of trying several methods was to find the closest correlation to core porosity, as measured by the coefficient of determination, R^2, which indicates the amount of variance in the dependent variable (estimated porosity) that is explained by the independent variable (core porosity). The method that showed the closest correlation was then used to calculate new estimated porosity logs for all wells in the study area. The methods (Table 2) used in this study to generate estimated porosity logs for the cored wells are: single-variable regression analysis of the bulk density logs, because bulk density can be directly related to porosity (Davis, 1954); using the average of neutron- and density-porosity logs, since averaging neutron porosity and density porosity is commonly used to estimate porosity in siliciclastic rocks; multivariate regression analysis of neutron- and density-porosity logs together; linear regression of porosity estimated using the equation:

Equation 1:   Phi = (Rhoma-Rhob)/(Rhoma-Rhof)

Where Rhoma equals apparent matrix density in grams per cubic centimeter (g/cc), Rhob is the value from the bulk density log, and Rhof is the density of pore fluid. To get the closest

correlation to core porosity possible using Equation 1, several variables were used as Rhoma, and the resulting correlations were compared. Variables used as Rhoma were: 2.68 g/cc (density of calcite-cemented sandstone), 2.65 g/cc (density of silica-cemented sandstone), and the actual bulk density of each core sample. Rhof was set at the density of water, 1.00 g/cc.

Table 2: List of methods used to estimate porosity.

Methods:
1. Regression analysis of:
a) RHOB
b) NPHI DPHI
c) NPHI-DPHI Average
2. PHI = (Rhoma-RHOB)/(Rhoma-Rhof)
a) Rhoma = 2.68 g/cc
b) Rhoma = 2.65 g/cc
c) Rhoma = grain density from core report at each 0.15 m (0.5ft) step
(Rhof always = 1.0 g/cc)

In all methods, the resulting estimated porosity values were plotted with core porosity data in scatterplots, and linear regression was performed in Microsoft Excel to obtain the statistical correlation as measured by the coefficient of determination, R^2. The method that provided the highest coefficient of determination, R^2, was selected for use to calculate logs of estimated porosity for all wells in the study area; the estimated porosity values were used in Archie equation calculations of fluid saturation (Archie, 1942) and in 3D modeling of the reservoir. The Archie equation is given as:

$$\text{Equation 2: } S_w = [(a / \Phi^m)*(R_w / R_t)]^{(1/n)}$$

Where S_w is water saturation, Φ is porosity, R_w is formation water resistivity, R_t is observed bulk resistivity, a is a constant, m is the cementation exponent, and n is the saturation exponent.

Values for the Archie equation for cementation exponent (m), saturation exponent (n), water resistivity (R_w), and constant (a), were based on a proprietary petrophysical study on Chesterian sandstone in the nearby Eubank oilfield. Formation resistivity (R_t) for the Archie equation was taken from the deep resistivity logs in each well. Archie equation variables (Table 3) used in this study are similar to published values used in other Chesterian sandstone (e.g., Doveton, 1999), and fluvial Morrowan sandstone (e.g., Hartman and Coalson, 1990). Archie equation calculation of water saturation was performed in PETRA, a subsurface GIS program developed by IHS, Inc.

Table 3: Variables used in Archie equation for calculating water saturation.

Variable:	This study	Doveton (1999) Chesterian	Hartman and Coalson (1990) Morrowan
cementation exponent m	1.8	1.8	1.8
saturation exponent n	1.9	2	2
formation water resistivity R_w (ohm*m)	0.04	0.05	0.04
constant a	1	1	1

Data from core reports were used to construct porosity–permeability cross-plots to use in estimating permeability as a function of well-log porosity in wells without core. The cross-plots were in semi-log format, with log-scaled permeability on the y-axis and normally (linear) scaled porosity on the x-axis. Core data from limestone were not included in the cross-plots because limestone was not included in the 3D model of the reservoir. Cross-plots were created with all the data points together, with sandstone and conglomerate separated, and with all core-defined lithofacies separated. Power trend lines were fit to the different combinations of lithofacies to find the best method for estimating permeability, as measured by the coefficient of determination, R^2, which reflects the amount of variance in the dependent variable (permeability) that is explained by the independent variable (porosity).

As with AHC analysis, porosity–permeability cross-plots were useful in determining a lithofacies classification scheme for prediction with artificial neural networks in uncored wells. Permeability in the 3D geologic model would be estimated as a function of porosity, based on the grouping of lithofacies which gave the highest coefficient of correlation, R^2, between porosity and permeability. Therefore, since permeability is a function of lithofacies, whatever grouping of lithofacies was best on the porosity–permeability cross-plots would also be the same grouping used in artificial neural network prediction of lithofacies.

e. Lithofacies Prediction with Artificial Neural Networks (ANN)

Artificial neural network (ANN) modeling to predict lithofacies in wells without core was performed using Kipling.xla, an add-in for Microsoft Excel (Bohling and Doveton, 2000). An ANN consists of an input layer, hidden layers, and an output layer, with each layer made up of nodes (Figure 7). Each node in the input layer corresponds to a variable to be used in prediction,

the number of nodes in the hidden layer or layers is set by the user and can be adjusted, and the number of output layer nodes corresponds to the number of possible outcomes. An ANN made with Kipling.xla has a single hidden layer, although theoretically an ANN can have multiple such layers. In this study, each input layer node corresponds to a log variable (e.g., gamma-ray intensity) and each output layer node is a numerical value that represents a lithofacies class (e.g., conglomerate=1, sandstone=2, etc.). Outputs are generated in the form of statistical probabilities; for each depth interval with a set of input (log) variables, a statistical probability is generated for each of the possible lithofacies classes, and the ANN assigns the predicted lithofacies at each depth interval to the lithofacies with the highest probability. Prediction of lithofacies using Kipling.xla is an iterative process of training and testing ANN using different values for the number of hidden layer nodes and a damping parameter.

The number of hidden layer nodes is essentially the size of the ANN. The more hidden layer nodes, the larger the ANN and the more likely it is to be able to reproduce or predict with 100% accuracy the training dataset.   The damping parameter is a number that acts as a constraint on randomly generated weights (constants) by which input data are multiplied before being passed through a mathematical function that transforms the inputs into outputs as statistical probabilities. Decreasing the damping parameter allows the ANN to reproduce or predict the training dataset more accurately. As a general rule of thumb, it is desirable to use a low number of hidden layer nodes and a high damping parameter to avoid overtraining, or tuning to the training dataset such that it cannot be used to accurately predict using other data. In training and testing an ANN, several values for both the number of hidden layer nodes and the damping parameter should be tried to find the optimal values for those parameters.
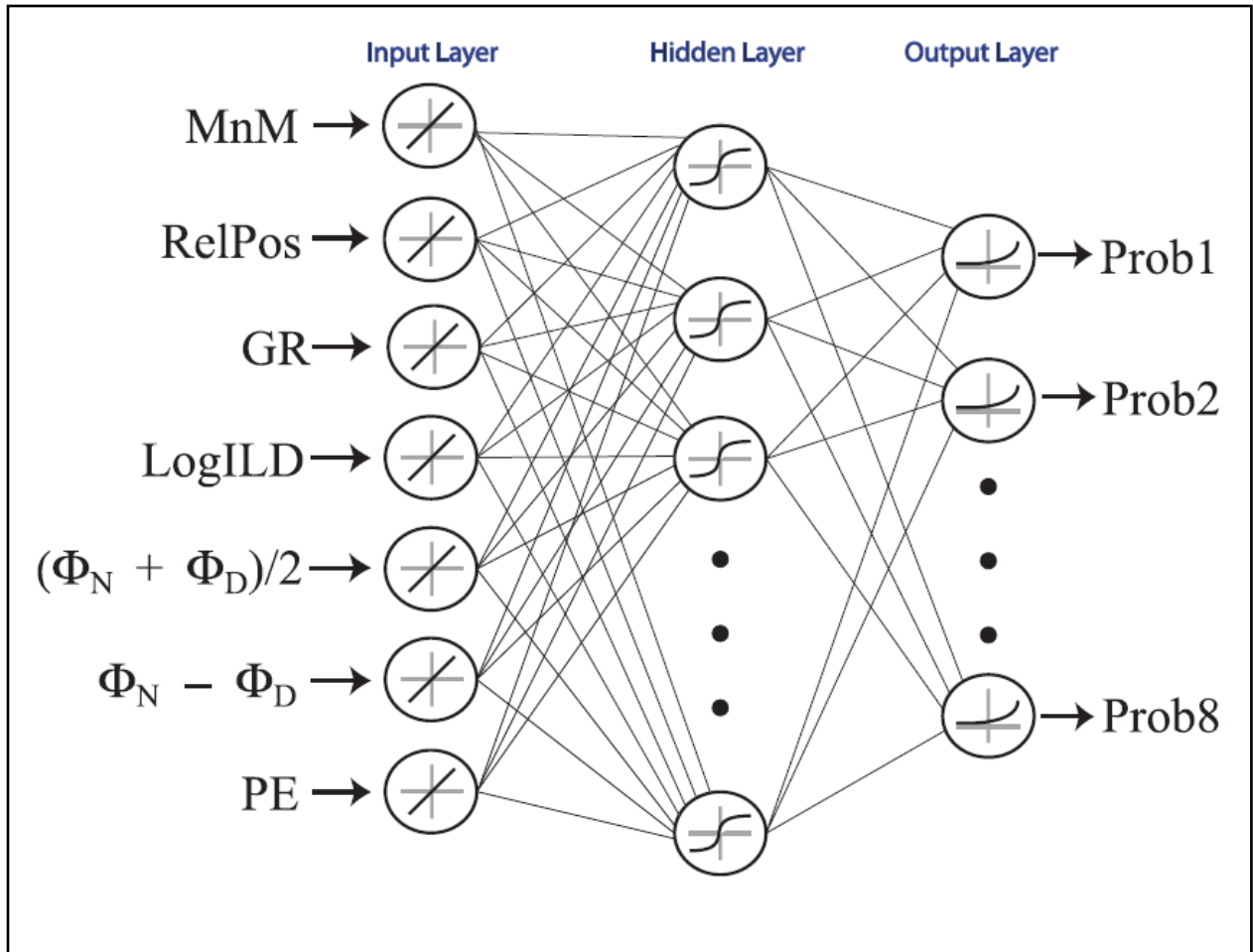
Figure 7: Schematic diagram of the organization of an Artificial Neural Network (ANN). From Dubois et al. (2006). Well-log variables are abbreviated at left (e.g. GR is short for gamma-ray), MnM abbreviates a depositional interpretation—marine or non-marine. The nodes (circles) are connected by lines to show a conceptual vision of the interconnected structure of nodes within an ANN. At the output layer at right, the ANN calculates the probability that each sample, with its depth-specific input variables, has of being any number of specific categorical outcomes. In the case of Dubois et al. (2006) and in this study, the well-log variables are inputs and the ANN calculates the probability of each sample belonging to a certain lithofacies class.

The dataset for training and testing ANNs in this study was the set of log variables and known, core-defined lithofacies from the cored wells. Log variables used to train the network included gamma-ray intensity, neutron–density porosity average, neutron porosity minus density porosity, logarithm of deep induction, and a relative position log. The relative position log assigns a number between zero (deepest) and one (shallowest) for each depth interval and was generated in Microsoft Excel. This group of variables is common to all wells used in the study, and also has been used in ANN prediction of lithofacies in other studies (e.g., Dubois et al., 2006). This study also uses the photoelectric (PE) log and logs of estimated apparent grain density (Rhomaa) as variables. The estimated apparent grain density logs were generated using the equation:

Equation 3:   Rhomaa=(Rhob-Phi)/(Rhob-Rhof)

Where Rhob is the value from the bulk density log, Phi is porosity, and Rhof is the density of pore fluid, set to the density of water, 1.00 g/cc. Two sets of porosity logs were used: Phi as the average of neutron and density porosity, and Phi as the best match to core porosity as outlined in the Petrophysics section above. Whereas the PE log was available only on a subset of wells in the field, generating the estimated apparent grain-density logs allowed an additional variable to be used in all wells.

Four cases were defined using different combinations of the well-log variables (Table 4). For each case, four values for number of hidden layer nodes and four values for damping parameter were used (Table 5) to create a total of sixteen ANNs for each case. The default values in Kipling.xla for number of hidden layer nodes and damping parameter were used as a

32

starting point and values above and below the defaults were used. Following the methods of

Dubois et al. (2006), ANNs were trained using half of the core data and tested on the other half;

the core data was split into groups of three depth-consecutive samples and alternating groups

were assigned to the testing or training dataset. In this study, overtraining would be noted when

an ANN could correctly predict lithofacies in the half of the core data used for training, but could

not correctly predict lithofacies in the other half of the core data.

Statistical success of lithofacies prediction for each of the sixteen ANNs created for each

of the four cases was compared in Microsoft Excel, following the methodology of Dubois et al.

(2006) by using three calculations. The first two calculations determined the total percentage of

correct predictions for 1) all data, and 2) reservoir (sandstone) lithofacies. The third calculation

determines the percentage of predictions that were within one numerical lithofacies class (e.g., if

the prediction was 2 and actual was 1 or 3). Comparison among the sixteen ANNs created for

one of the four cases allowed a 'winner' to be selected from among the sixteen based on success

in the three calculations outlined above, and showed the optimal number of hidden layer nodes

and optimal damping parameter for that particular case. After finding 'winners' for each of the

four cases, the results of prediction were compared using the same three calculations, and also in

wells where geologist's reports were available showing the actual observed lithologies of

sandstone, conglomerate, and shale. The case or cases with the most correct predictions were

then used to generate logs of predicted lithofacies for all wells in the study area.

Table 4: Combinations of variables defining four Cases for ANN prediction of lithofacies.

Case #:	Variables:
1	Gamma-ray, neutron-density porosity average, neutron porosity minus density porosity, logarithm of deep induction, relative position
2	Gamma-ray, neutron-density porosity average, neutron porosity minus density porosity, logarithm of deep induction, relative position, photoelectric effect
3	Gamma-ray, neutron-density porosity average, neutron porosity minus density porosity, logarithm of deep induction, relative position, apparent grain density from neutron-density porosity
4	Gamma-ray, neutron-density porosity average, neutron porosity minus density porosity, logarithm of deep induction, relative position, apparent grain density from bulk density regression porosity

Table 5: ANN variables tested for each of four cases in prediction of lithofacies.

# Hidden Layer Nodes	Damping Parameters
10	0.01, 0.1, 1, 10
20	0.01, 0.1, 1, 10
40	0.01, 0.1, 1, 10
80	0.01, 0.1, 1, 10

f. 3D modeling

    A 3D model of the reservoir was created using Petrel™, a Schlumberger subsurface data

analysis and reservoir modeling software program. The 3D reservoir model provided

visualizations of the predicted spatial distribution of lithofacies, porosity, permeability, and fluid

saturations. Visualization of such properties in three-dimensional space provided insight into the

spatial character of the reservoir and implications for future reservoir management, including

potential for further recovery of remaining hydrocarbon resources. The 3D model is composed

of cells measuring 17 m (55 ft) on each side and 0.6 m (2 ft) vertically. Digital well-log data at

0.15 m (0.5 ft) resolution were imported into the software, including the lithofacies predicted

using ANN modeling and logs of estimated porosity. The 0.15 m (0.5 ft) resolution well logs of

porosity and predicted lithofacies were then upscaled to the 0.6 m (2 ft) vertical resolution of the

3D model; porosity was upscaled using a simple arithmetic average and logs of predicted

lithofacies were upscaled by assigning the most abundant lithofacies class that occurred in each

0.6 m (2 ft) vertical interval. From the upscaled cells at individual wells, the entire 3D model

was populated with lithofacies and porosity using stochastic modeling processes. Sequential

indicator simulation (SIS), a method commonly applied to discrete data, was used for populating

the model with predicted lithofacies. Subsequently, sequential Gaussian simulation (SGS),

which is commonly applied on continuous data, was used to populate the lithofacies model with

porosity. The model was populated with permeability using lithofacies-specific mathematical

transforms of porosity based on analysis of core porosity–permeability cross-plots (e.g., see

Results section on petrophysics below). Population of the model with water saturation was

accomplished using a modified version of the Leverett J-Function equation (Leverett, 1941; see

Appendix C for modifications). Structure maps based on a proprietary 3D seismic survey and

formation tops from wells provided constraints for the geometry of the reservoir model.

Multiple fluid-saturation models were constructed using a range of values for irreducible water saturation (Swirr), Formation Volume Factor (FVF), and Free Water Level (FWL). A detailed outline of the construction of the reservoir model and population of the model with properties is provided in Appendix C.

Results

a. Core Lithofacies and Petrophysics

Examination of 49 m (161 ft) of core, 26 m (86 ft) in the Mary Jones #2 core and 23 m
(75 ft) in the Moody D2 core provided the basis for defining seven lithofacies, subdivided on the
basis of lithology, grain size, and sedimentary structures. The Shore Airport Formation
comprises a total of 45.2 m (148.3 ft) of core, 25.1 m (82.5 ft) in the Mary Jones #2 core and
20.1 m (65.8 ft) in the Moody D2 core, with the remainder being St. Louis Limestone.
Variations in fossil content, sorting, rounding, pore throat size, and argillaceous content were not
unique to individual core lithofacies. Lithologies in the two cores include limestone,
conglomerate, sandstone, and heterolithic mudstone–sandstone. Conglomerate is cemented with
calcite, whereas sandstones are generally silica-cemented with some isolated calcite-cemented
patches. The seven lithofacies described from initial core examination are: limestone,
conglomerate, interbedded quartzarenite and heterolithic mudstone–sandstone, cross-bedded
sandstone, laminated sandstone, weakly stratified sandstone, and pebbly sandstone (Table 6).
Variations in sedimentary structures and grain size define the four types of sandstone lithofacies.
Core porosity and permeability data was available from core analysis reports (Table 6).

Both cores are composed of a series of stacked fining-upward successions (Figure 8).
Each succession starts with a conglomerate deposited on an erosive surface scoured into
underlying limestone or sandstone. Conglomerate bodies generally are overlain gradationally by
sandstone.   An exception occurs above the basal conglomerate in the in the Moody D2 core,
which is overlain first by the interbedded quartzarenite and heterolithic mudstone–sandstone,
which then transitions upwards into a weakly stratified sandstone. The fining upward

successions observed in the two cores are not complete in the sense that they do not grade to fine clay-rich deposits.

Lithofacies Name	Description	Interpretation	Typical well log response	Core Porosity (%)		Core Permeability (millidarcies)		
				range	arithmetic average	range	geometric average	median
Limestone	Stylolitic mudstone-wackestone, some packstone to grainstone; chert nodules up to 2–4.5 cm diameter; grains include coated grains, peloids, crinoid, bryozoan, skeletal fragments. Forms walls and floor of incised valley. 3.9 m of core. 1 unit in Mary Jones #2 core; 1 in Moody D2 core	Shallow marine depositional environment, stable, generally aggradational carbonate shelf with some eolian input (Abegg, 1994b; Qi et al., 2007)	Low gamma-ray: 15–30 API units, porosity ≤5%, PE log ~5	N/A	N/A	N/A	N/A	N/A
Conglomerate	Oligomictic paraconglomerate, pebble–cobble clasts of grainstone, lime mudstone, qtz. sandstone, chert. Forms base of fining-upward sequences, scoured into underlying limestone or sandstone. 9.4 m of core. 4 units in Mary Jones #2 core; 4 in Moody D2 core.	Lag deposit in deep part of channel; beginning of deposition after erosive scour into underlying units; few fossils could indicate tidal or marine influence, or could be derived from subjacent limestone; fluvial-dominated depositional environment.	Moderate gamma-ray: 15–40 API units, porosity generally <10%, PE log ~3	1.5–10.6	4.82	0.01–72	0.22	0.15

Table 6: Summary of core-defined lithofacies characteristics.

39

Lithofacies Name	Description	Interpretation	Typical well log response	Core Porosity (%)		Core Permeability (millidarcies)		
				range	arithmetic average	range	geometric average	median
Pebbly Sandstone	Fine-medium grain sublitharenite. Pebbly calcareous mudstone clasts often along cross-bed foresets. Abrupt basal contact with conglomerate or weakly stratified sandstone. 3.2 m of core. 2 units in Moody D2 core, none in Mary Jones #2 core.	Sedimentary structure size up to few cm indicates ripple bedforms; 3D seismic survey suggests deposition in a channel; channel deposition suggests bar-forms; clast-rich intervals could indicate fluctuating flow, but are not rhythmic, suggesting little if any tidal influence; fluvial-dominated depositional environment.	Low gamma-ray: ~15 API units, porosity 7–15%, PE log ~2.5	2.2–13	10.33	0.224–418	83.37	128
Cross-bedded sandstone	Fine-medium grain quartzarenite, large-scale cross-bedding, few 1-2 mm thick mud streaks. Gradational basal contact with conglomerate. 5.8 m of core. 1 unit in Mary Jones #2 core, none in Moody D2 core.	Sedimentary structure size up to few cm indicates ripple bedforms; 3D seismic survey suggests deposition in a channel; channel deposition suggests bar-forms; proximity to conglomerate suggests mid to lower part of bar forms; mud streaks only feature possibly suggestive of tidal influence; fluvial-dominated depositional environment.	Low gamma-ray: 15–20 API units, porosity 6–14%, PE log ~2.5	1.8–15.1	10.47	0.01–316	13.08	14.85

Table 6 (continued): Summary of core-defined lithofacies characteristics.

Lithofacies Name	Description	Interpretation	Typical well log response	Core Porosity (%)		Core Permeability (millidarcies)		
				range	arithmetic average	range	geometric average	median
Laminated Sandstone	Very fine-fine grain quartzarenite; 30-60 cm thick sets of well-developed 0°-10° laminations. Laminae dip in same direction within sets. Gradational to abrupt basal contact with conglomerate, gradational basal contact with weakly stratified sandstone. 14.8 m of core. 2 units in Mary Jones #2 core, 1 unit in MoodyD2 core.	Sedimentary structure size (< 1cm) indicates ripple bedforms; 3D seismic survey suggests deposition in a channel; channel deposition suggests bar-forms; upper position in fining-upward successions indicates upper part of bar forms; no apparent bundling or cyclicity in laminae; fluvial-dominated depositional environment.	Low gamma-ray: 15–20 API units, porosity ~15%, PE log ~2	0.9–17.9	13.22	0.01–535	49.62	111.5
Weakly stratified sandstone	Very fine-fine grain quartzarenite; mostly structureless appearance with some faint laminations or bedding in places; aligned plant debris visible in places. Gradational basal contact with conglomerate or laminated sandstone; abrupt basal contact with heterolithic mudstone-sandstone. 10.1 m of core. 1 unit in Mary Jones #2 core, 2 units in Moody D2 core.	Sedimentary structures up to a few cm indicates origin as ripple bedforms; 3D seismic survey suggests deposition in a channel; channel deposition suggests bar-forms; position in fining-upward successions indicates mid to upper part of bar forms; no apparent cyclicity in sedimentary structures; fluvial-dominated depositional environment.	Low gamma-ray: 15–20 API units, porosity ~15%, PE log ~2	1.6–20.1	11.42	0.03–629	38.72	170

Table 6 (continued): Summary of core-defined lithofacies characteristics.

41

Lithofacies Name	Description	Interpretation	Typical well log response	Core Porosity (%)		Core Permeability (millidarcies)		
				range	arithmetic average	range	geometric average	median
Interbedded quartzarenite and heterolithic mudstone-sandstone	15-60 cm thick layers of shaly heterolithic material interbedded with 10-30 cm thick quartzarenite, flaser to wavy bedding in heterolithic intervals, structureless to weakly stratified in quartzarenite intervals. Gradational basal contact with conglomerate. 1.8 m of core. 1 unit in Moody D2 core, none in Mary Jones #2 core.	Flaser to wavy bedding with high content of fine sediment intervals alternating with clean quartzarenite intervals suggests fluctuating flow; no cyclicity apparent such as bundling; fluvial examples of similar description rare, but known; fluvial-dominated depositional environment	Moderate gamma-ray: 30–60 API units; porosity ≤ 10%; PE log ~2.5	5.5–13.2	9.11	0.334–10	1.23	0.9

Table 6 (continued): Summary of core-defined lithofacies characteristics.
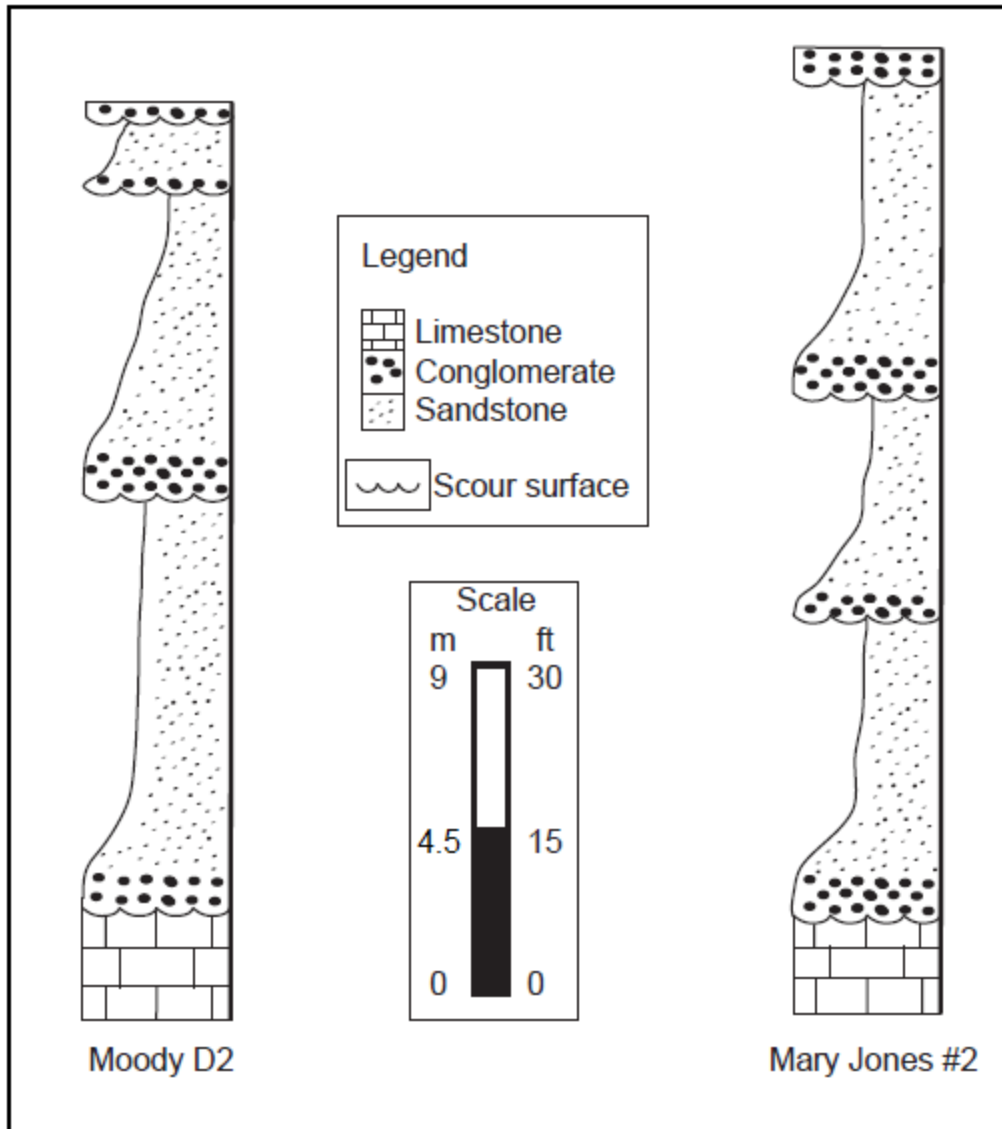
42

Figure 8: Generalized lithology profile showing that Chesterian cores from Pleasant Prairie oilfield comprise a stacked series of conglomerate-based siliciclastic fining-upward successions.

1. Limestone

Description:

Limestone (Figure 9) ranges from mudstone to wackestone–packstone and grainstone and is very light gray to light gray (N8–N7; here and below, Munsell color codes are given in parentheses next to color names in the lithofacies descriptions) and stylolitic. Rounded to elongate or irregular chert nodules are present and range in size from 2 to 4.5 cm in diameter. Grains within the limestone include coated grains, peloids, and crinoid, bryozoan, and skeletal fragments. Nuclei of coated grains are commonly quartz sand grains and less commonly skeletal fragments. Limestone is the basal lithofacies of the study, and is in erosional contact with overlying conglomerate, forming the base of the focus interval. The base of the limestone is not present in either core, or on their well logs, and thus the true thickness and nature of the basal contact of the limestone with underlying strata are unknown. The cores contain a total of 3.9 m (12.7 ft) of limestone—1.1 m (3.5 ft) in the Mary Jones #2 core and 2.8 m (9.2 ft) in the Moody D2 core.

Interpretation:

The St. Louis Limestone underlies the Chesterian Shore Airport Formation in the two cores from Pleasant Prairie oilfield. The limestone represents deposition of carbonate sediment in a shallow sea; the depositional environment of the St. Louis Limestone generally is interpreted as a stable, generally aggradational carbonate shelf, with some aeolian input (Abegg, 1994b; Qi et al., 2007). The seas of the shallow shelf were inhabited by a typical late Paleozoic assemblage of organisms such as crinoids, bryozoans, etc. The presence of quartz grains in the limestone indicates input and reworking of some terrigenous detrital sediment, possibly of aeolian origin

(Abegg, 1994b); the quartz may have ultimately been derived from nearby igneous provinces such as the Central Kansas uplift or Transcontinental arch.

2.   Conglomerate

Description:

Conglomerates (Figure 9) from the two cores are oligomictic paraconglomerates, meaning they are generally matrix-supported with clasts of a limited suite of lithologies. Color ranges from white to very light gray (N9–N8), or oil-stained to yellowish gray to light olive gray (5Y 8/1–5Y 6/1) or moderate to dusky yellowish-brown (10YR 5/4–10YR 2/2). They have a moderately to very well sorted matrix of very fine to medium grained, subrounded to well-rounded quartz sand, and are cemented with calcite. Clasts range in size from coarse sand to cobble size and are subangular to well-rounded. Clast types include grainstone, lime mudstone, quartz sandstone, and chert. A few fossils are evident in conglomerate units. In the Mary Jones #2 core two abraded brachiopod shells and a wood fragment occur in the basal conglomerate, rhizoliths occur in a middle conglomerate unit, and minor amounts of crinoid debris are present in the uppermost conglomerate. The rhizoliths are up to about 1.3 cm (0.5 in) in diameter. Individual rhizoliths were visible either on the cut, flat core surface or on the outer, round core surface. The rhizoliths were discontinuous, not traceable through the core to the other side. In the Moody D2 core, an echinoid fragment and a horn coral fragment occur in the basal conglomerate, and minor amounts of crinoid debris and a bone fragment are included in the successive conglomerate. Black carbonaceous plant debris is present in the basal conglomerate of both cores, and decreases in abundance in successively (stratigraphically) higher conglomerate units. Basal conglomerates are deposited on erosive scour surfaces cut into underlying limestone

strata, and other conglomerates are deposited on erosive scour surfaces cut into weakly stratified, laminated, or pebbly sandstone lithofacies.

Arithmetic average core porosity in conglomerate is 4.82%, with a range of 1.5–10.6%. The geometric average permeability in conglomerate is 0.22 md, with a median of 0.15 md and a range of 0.01–72 md. Four conglomerate beds in each core combine for a thickness of 9.4 m (30.9 ft), or 21% of the total Shore Airport Formation core thickness of 45.2 m (148.3 ft).

Interpretation:

A proprietary, confidential 3D seismic map of the Pleasant Prairie oilfield area (see Methods section on 3D modeling) shows that the incised valley is a narrow (0.4 km or 0.25 mile wide), elongate, straight feature aligned almost exactly north–south. Deposition in such a narrow, elongate incised valley, directly on erosive scour surfaces suggests that these conglomerates originated as in the deeper part of channels, possibly in the thalwegs. The conglomerates form the base of fining upward successions, which transition upward from conglomerate to cleaner sandy intervals. The intervals between conglomeratic units range from 1.4 to 11.6 m (4.5 to 38 ft) with a mean of 6.1 m (20.l ft). Each scour surface is interpreted to represent an erosional event that removed the upper parts of underlying fining upward successions. The clasts found in these conglomerates are the same lithologies as strata underlying the Shore Airport Formation (limestone and chert), and therefore the clasts are interpreted to have been sourced from the underlying strata.

Within incised valleys, various subenvironments may occur (e.g., Van Wagoner et al., 1990; Dalrymple et al., 1992; Zaitlin et al., 1994). The minor fossil content in conglomerate units could indicate tidal influence. Alternatively, the fossils could have been derived from the

limestone strata that underlie and form the walls of the incised valley. Rhizoliths in the Mary

Jones #2 core are discontinuous; as such, they do not appear to have grown in place, but instead

are interpreted to be traces of rhizolith fragments that were eroded and redeposited. The

decreasing abundance of carbonaceous plant debris from lower to higher conglomerate beds,

along with the appearance of crinoid debris in middle and upper conglomerate beds is interpreted

to possibly indicate a shift from a more fluvial setting to a slightly more tide-influenced setting

as the valley filled. The conglomerate units, however, do not display any sedimentary structures

that would indicate tidal influence, such as bidirectional cross-stratification. Pleasant Prairie

oilfield is updip within the larger incised-valley trend relative to other Chesterian deposits

interpreted as tide-dominated estuarine environments (e.g., South Eubank oilfield, Montgomery

and Morrison, 1999). Thus, instead of a tide-dominated setting, the overall paucity of fossil

debris, the presence of terrigenous material including plant debris, redeposited rhizoliths, a wood

fragment, and a bone fragment, the lack of sedimentary structures consistent with a tide-

influenced interpretation, and the updip position within the incised-valley trend are interpreted as

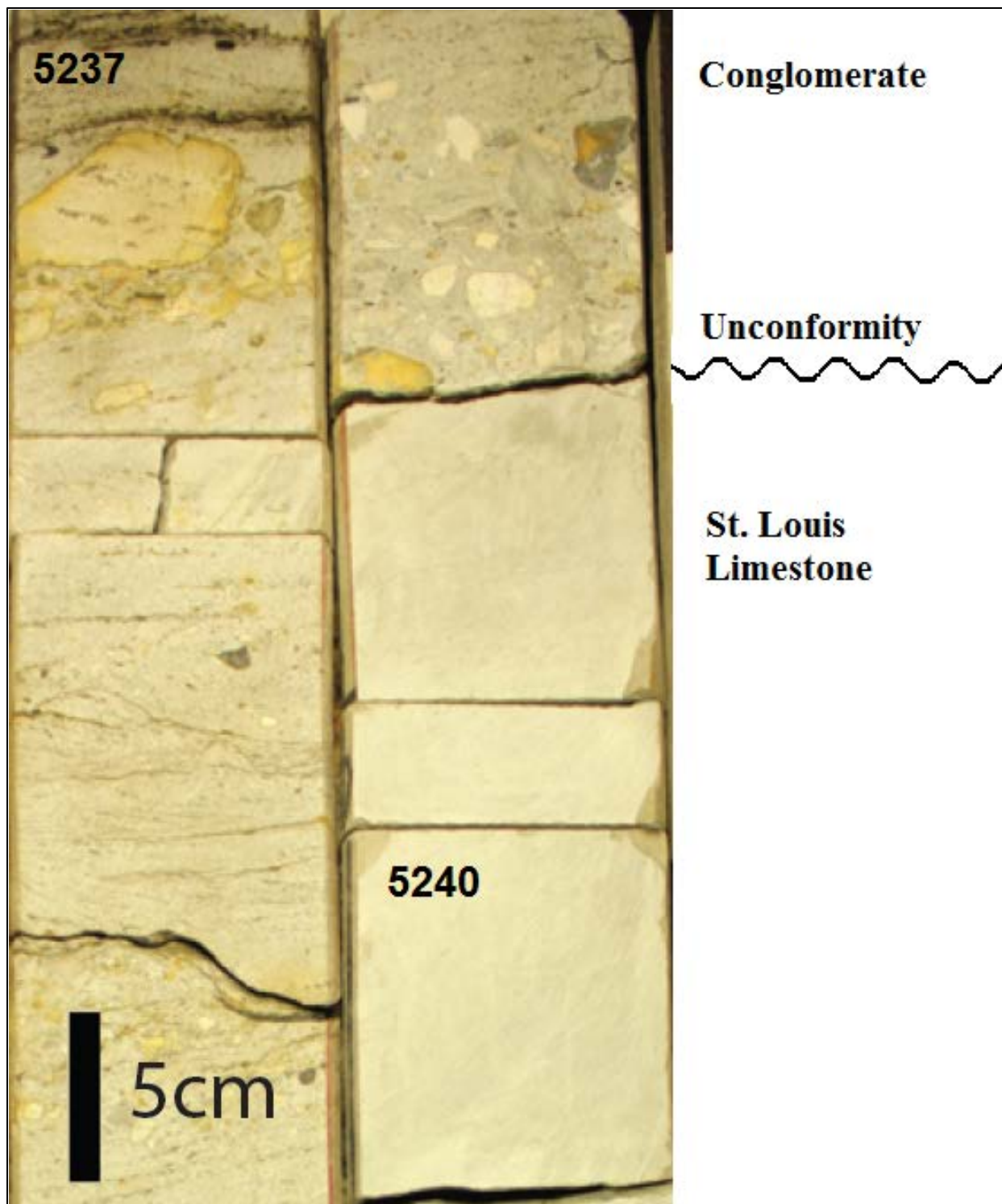evidence of a more river-dominated depositional environment.

Figure 9: Conglomerate lithofacies unconformably overlying limestone lithofacies, Mary Jones #2 core. Depths on core are measured depth in feet

3. Pebbly sandstone

Description:

The pebbly sandstone lithofacies (Figure 10) is classified as a sublitharenite because of the presence and abundance of clasts; it is oil-stained to dusky yellow (5Y 6/4) or pale to dark yellowish brown color (10YR 6/2–10YR 4/2). The sand is fine to medium grained, rounded to well-rounded and well to very well sorted, and contains coarse sand to pebble sized, subangular to well-rounded calcareous mudstone clasts. Abundance of clasts is generally 2–5%, but reaches up to 10–20% in some intervals. The clasts occur in linear streaks and commonly are oriented along 10–20° dipping foresets of very thin cross-beds; sets of cross-beds have planar boundaries and are approximately 10–40 cm (4–16 in) in thickness, and the geometry of the cross-bed foresets is generally planar. One set of cross-beds shows a slight steepening-upward trend, indicating tangential foresets (Figure 10). Tangential foresets are consistent with trough cross-stratification; however, because no curved bounding surfaces were identified on cross-bed sets trough cross-stratification could not be definitively identified in this lithofacies. A few discontinuous, diffuse streaks of black carbonaceous plant material are present, as well as a few mud streaks < 0.5 cm (0.2 in) in thickness. Pebbly sandstone occurs in two units, and only in the Moody D2 core. The two units are separated by an approximately 30 cm (12 in) thick layer of conglomerate, and the uppermost conglomerate unit of the core overlies the upper pebbly sandstone unit. Basal contacts of both pebbly sandstone units are abrupt; the upper pebbly sandstone unit abruptly overlies a conglomerate unit, and the lower pebbly sandstone unit abruptly overlies weakly stratified sandstone.

Arithmetic average core porosity of pebbly sandstone is 10.03%, with a range of 2.2–13%. The geometric average permeability of pebbly sandstone is 83.37 md, with a median of

128 md and a range of 0.224–418 md. Two pebbly sandstone beds in the Moody D2 core

combine for a thickness of 3.2 m (10.5 ft), or 16% of the Moody D2 Shore Airport Formation

core.

Interpretation:

Sedimentary structures up to a few cm in thickness indicate an origin as ripples, bedforms

up to about 4 cm in amplitude and tens of cm in wavelength (Allen, 1985). Incised valleys such

as the one revealed on the proprietary 3D seismic map often contain bar-form deposits

(Dalrymple et al., 1992), and ripples commonly form in the upper part of bar-forms. Therefore,

the pebbly sandstone lithofacies is interpreted as deposits the upper part of bar-forms.

The streaks of pebbly material among cleaner sandy intervals in the pebbly sandstone lithofacies

could indicate fluctuating flow strength (Nio and Yang, 1991), suggestive of tide influence.

Nonetheless, the streaks of pebbly material are not rhythmically repeated and thus are not

illustrative of cyclicity, which would be consistent with an interpretation of tidal influence on

their deposition (Nio and Yang, 1991). This lithofacies is interpreted as part of a bar-form,

deposited in a narrow channel with no apparent tidal influence, updip from tide-influenced

estuarine deposits (e.g., South Eubank oilfield, Montgomery and Morrison, 1999). Thus, the

depositional environment is interpreted to have been the river-dominated part of an estuarine
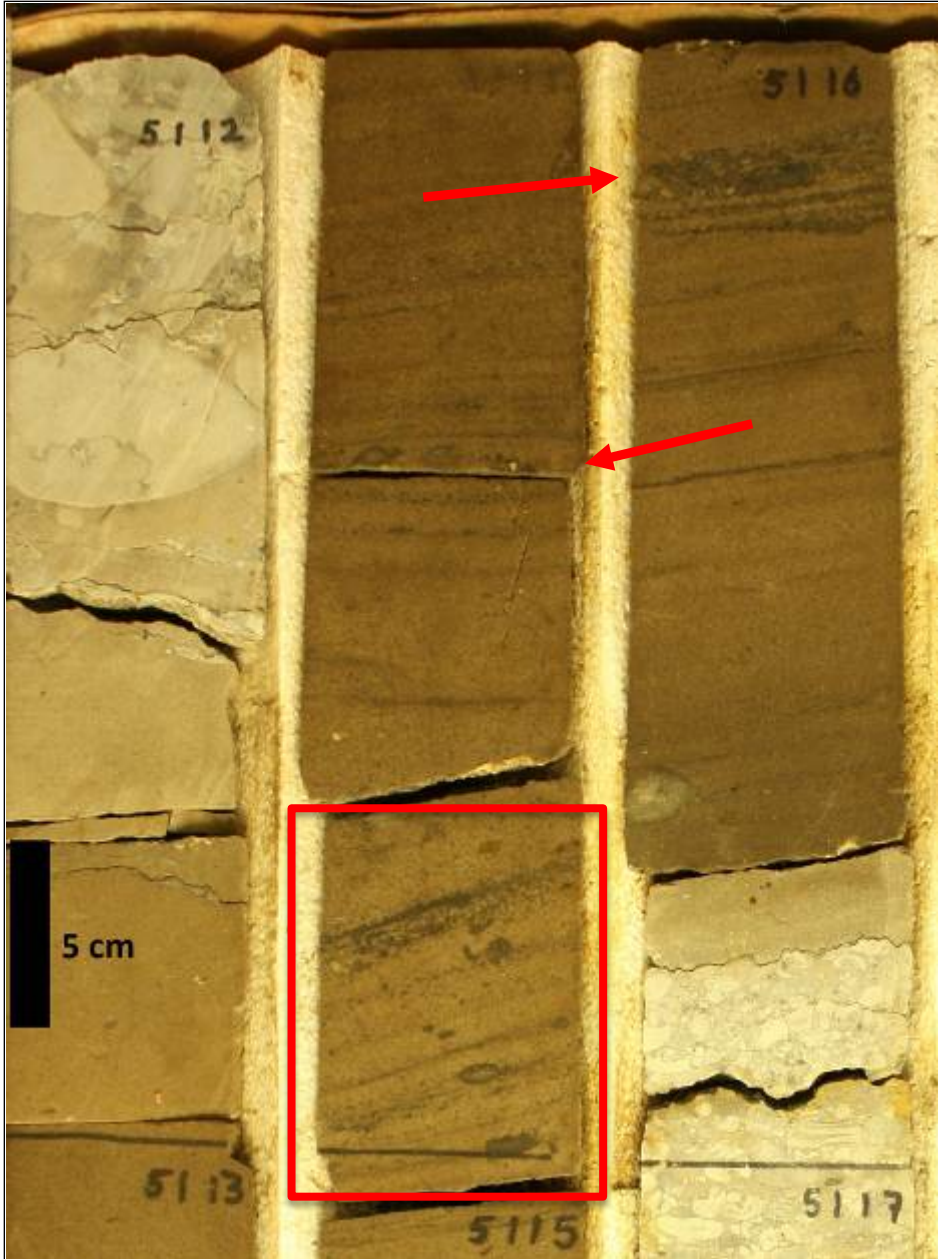
system.

Figure 10: Pebbly sandstone lithofacies in Moody D2 core. Arrows indicate pebbly streaks, and box indicates set of steepening-upward beds. Depths on core are measured depth in feet; conglomerate beds are at upper left and lower right.

4. Cross-bedded sandstone

Description:

The cross-bedded sandstone lithofacies (Figure 11) is quartzarenite, and is found only in the Mary Jones #2 core. This lithofacies is mostly dusky brown (5YR 2/2) in color and heavily oil-stained, with some dark yellowish- to grayish-orange (10 YR 6/6–10YR 7/4) tightly silica-cemented areas, and patchy non-oil stained calcite-cemented areas of white to light gray color (N9–N7). It is fine to medium grained and consists of subangular to well-rounded, well to very well sorted grains. The heavy oil staining obscures sedimentary structures for the most part, but two sets of cross-beds are visible—a 23 cm (9 in) thick set of very thin trough cross-beds in one place, and a 5 cm (2 in) thick set of very thin planar cross-beds 2.6 m (8.5 ft) below the trough cross-bed set. Crests were not observed in the sedimentary structures, and no systematic changes in the dip angles of individual cross-bed foresets were observed (e.g., shallowing or steepening upward). The geometry of bounding surfaces of the cross-bed sets, however, forms the basis for the trough and planar nomenclature of the sets. Bounding surfaces of the trough cross-bed set are curved, and bounding surfaces of the planar cross-bed set are straight. Mud drapes occur in the planar cross-bed set, and in the trough cross-bed set black carbonaceous debris occurs along the surfaces of individual cross-beds. Fourteen 1–2 mm thick mud streaks, each about 1 cm apart occur in an apparently structureless part of this lithofacies below the planar cross-bed set. Compared to other sandstone lithofacies, the cross-bedded sandstone has more prevalent cementation. The cross-bedded sandstone lithofacies is present only in the Mary Jones #2 core, where it has a gradational basal contact with the underlying basal conglomerate.

Arithmetic average core porosity of cross-bedded sandstone is 10.47%, with a range of 1.8–15.1%. The geometric average permeability of cross-bedded sandstone is 13.08 md, with a

median of 14.85 md and a range of 0.01–316 md. The only cross-bedded sandstone bed, in the

Mary Jones#2 core, is 5.8 m (19 ft) thick, or 23% of the Mary Jones #2 Shore Airport Formation

core.

Interpretation:

Cross-beds up to a few cm in thickness indicate ripples, bedforms originally up to about 4

cm in amplitude and several cm in wavelength (Allen, 1985). The cross-bedded sandstone

lithofacies overlies and is in gradational contact with the basal conglomerate in the Mary Jones

#2 core. The proximity to underlying conglomerate makes this lithofacies a lower part of a

fining-upward succession; this observation, along with the interpretation of sedimentary

structures as ripples, indicates deposition in the mid to lower part of a bar-form in the narrow,

elongate incised paleovalley at Pleasant Prairie oilfield.

The mud drapes and mud streaks could be interpreted as suggestive of some tidal

influence (Nio and Yang, 1991), but these are the only apparent evidence consistent with such an

interpretation. In Chesterian sandstones downdip from Pleasant Prairie oilfield other studies

(e.g., Montgomery and Morrison, 1999; Cirilo, 2002) interpreted observations such as possible

bidirectional cross-stratification, reactivation surfaces, peloids, and fossils as evidence of tidal

influence. The Chesterian strata at Pleasant Prairie oilfield are updip from such deposits and lack

the observable features interpreted as tidal indicators in the downdip deposits, and therefore this

lithofacies is interpreted to have been deposited under conditions of very weak (if any) tidal

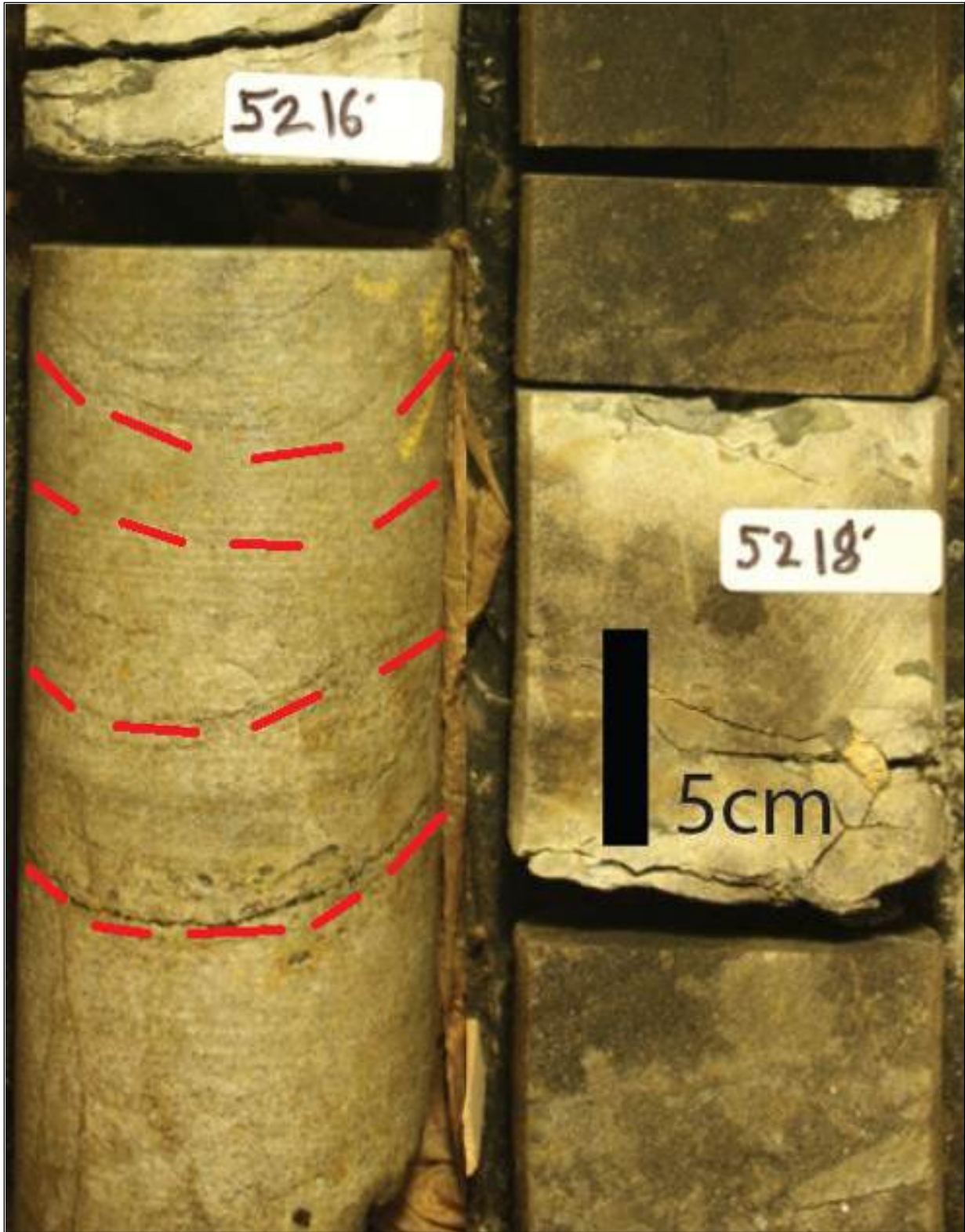influence, in a dominantly fluvial environment.

Figure 11: Cross-bedded sandstone lithofacies in Mary Jones #2 core. Red dashes outline interpreted cross-bedding planes, depths on core are measured depth in feet, light gray areas are tightly calcite-cemented zones.

5. Laminated sandstone

Description:

The laminated sandstone lithofacies (Figure 12) is a quartzarenite, and occurs in both cores. It is oil-stained to colors of pale to dark yellowish brown (10YR 6/2–10YR 4/2), dark yellowish- or grayish-orange (10YR 6/6–10YR 7/4), and dusky brown (5YR 2/2), with a few patchy, calcite cemented, non-oil stained, white to very light gray areas present (N9–N8). Grain size is dominantly very fine to fine, with only a few instances of medium sand observed, and grains are subangular to well-rounded, and well to very well-sorted. This lithofacies is characterized by thin planar laminae that occur in 30 to 60 cm (12 to 24 in) thick sets with straight bounding surfaces; individual laminae appear horizontal or dip at low angles (5–10°). In some places, however, the sand appears structureless due to heavy oil-staining or tight cementation with calcite. Crests were not observed in the sedimentary structures, and no systematic changes in the dip angles of individual laminae foresets were observed (e.g., shallowing or steepening upward). Black carbonaceous plant debris is present in laminated sandstone units in both cores and was noted primarily as discontinuous, diffuse streaks in the apparently structureless sections, but also along foresets of individual laminae. Two units of laminated sandstone were described in the Mary Jones #2 core, both of which have gradational basal contact with underlying conglomerate units. The basal contact of the one laminated sandstone unit in the Moody D2 core is unknown due to approximately 3 m (10 ft) of missing core.

Arithmetic average core porosity of laminated sandstone is 13.22%, with a range of 0.9–17.9%. The geometric average permeability of laminated sandstone is 49.62 md, with a median of 111.5 md and a range of 0.01–535 md. Three laminated sandstone beds, one in the Moody D2

core and two in the Mary Jones #2 core, combine for a thickness of 14.8 m (48.7 ft), or 33% of the combined total Shore Airport Formation core length of 45.2 m (148.3 ft).

Interpretation:

The thickness of the laminae in this lithofacies indicates that they represent ripples, bedforms originally up to about 4 cm in amplitude and several cm in wavelength (Allen, 1985). Incised valleys such as the one revealed on the proprietary 3D seismic map often contain bar-form deposits (Dalrymple et al., 1992), and ripples commonly form in the upper part of bar-forms. The laminated sandstone lithofacies comprises the upper part of conglomerate-based fining upward successions in the Pleasant Prairie cores, and is interpreted to represent upper portions of bar-forms which developed in the incised paleovalley at Pleasant Prairie oilfield.

Sedimentary structures indicative of fluctuations in current direction or intensity characteristic of tidal influence, such as bundling or sand–mud couplets (Nio and Yang, 1991) are lacking in this lithofacies. Also, sedimentary structures interpreted as evidence of tidal influence in Chesterian sandstones downdip from Pleasant Prairie, such as possible bidirectional cross-stratification and reactivation surfaces (e.g., Montgomery and Morrison, 1999; Cirilo, 2002), are lacking in this lithofacies. Instead, this lithofacies displays thick (30 cm or more) sets of homogeneously dipping laminae. Whereas such sedimentary structures could possibly indicate dominance of one tide direction (Allen, 1980), in the absence of other indicators of tidal influence these sets of uniformly dipping laminae are interpreted to represent conditions of unidirectional flow such as would occur in a fluvial environment. Carbonate material such as peloids and fossils, which other studies (e.g., Shonfelt, 1988) have cited as evidence for an interpretation of tidal influence in Chesterian sandstones, are also lacking in this lithofacies. In

sum, therefore, the sedimentary structures and fossil content suggest a river-dominated, rather than tide-dominated, depositional environment.
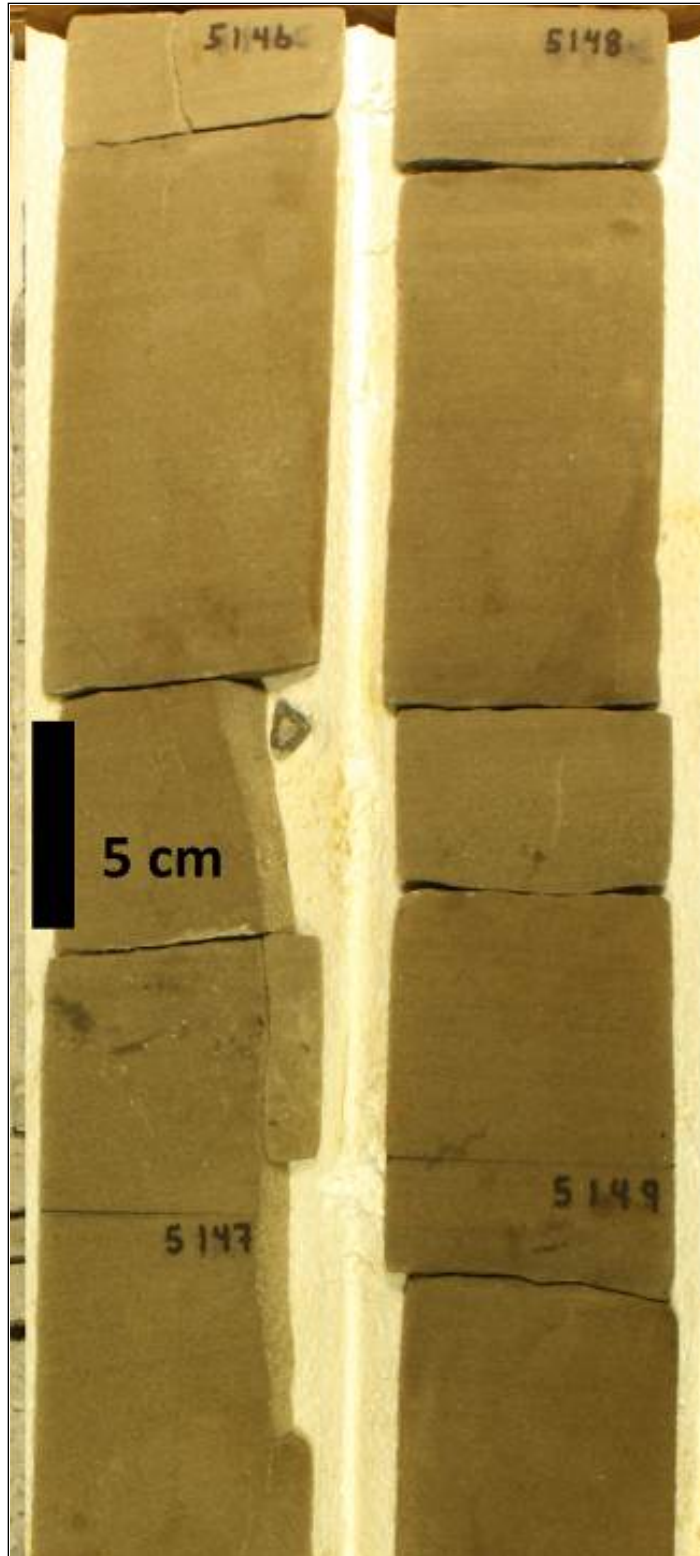
Figure 12: Laminated sandstone lithofacies in Moody D2 core. Depths on core are measured depth in feet. The fine laminated character of this lithofacies is most visible below 5146 and 5148 depth marks.

6.   Weakly stratified sandstone

Description:

The weakly stratified sandstone lithofacies (Figure 13) is a quartzarenite. This lithofacies is generally heavily oil-stained and is pale to dark yellowish brown (10YR 6/2–10YR 4/2), or light olive gray (5Y 6/1), or medium- to dark-gray (N4–N3) to grayish black (N2) in color. It includes a few patchy calcite cemented non-oil stained areas that are white to very light gray (N9–N8). The medium- to dark-gray to grayish black parts of this lithofacies are dead oil zones in which solid bituminous material occludes pore space. Grain size is dominantly very fine to fine, with a few instances of medium size, and the grains are subangular to well-rounded and well to very well-sorted. A few coarse sand- to granule-size clasts of calcareous mudstone are present in places, and in the Mary Jones #2 core, wispy plant fragments with parallel long axes yield a weakly stratified appearance to otherwise homogenous sandstone. Discontinuous, diffuse streaks of black carbonaceous plant material are present in places, as well as a few mud streaks. This lithofacies generally is structureless, but in places faint laminae or very thin beds are evident. Crests were not observed in these faint sedimentary structures, and no systematic changes in the dip angles of individual foresets were observed (e.g., shallowing or steepening upward). In the Mary Jones #2 core, the one unit of weakly stratified sandstone has a gradational basal contact with an underlying unit of laminated sandstone. In the Moody D2 core, two units of weakly stratified sandstone are evident, one with a gradational basal contact with an underlying conglomerate unit and one with an abrupt basal contact with the underlying interbedded quartzarenite and heterolithic mudstone–sandstone lithofacies.

Arithmetic average core porosity of weakly stratified sandstone is 11.42%, with a range of 1.6–20.1%. The geometric average permeability of weakly stratified sandstone is 38.72 md,

with a median of 170 md and a range of 0.03–629 md. Three weakly stratified sandstone beds, two in the Moody D2 core and one in the Mary Jones #2 core, combine for a thickness of 10.1 m (33.2 ft), or 22% of the total combined length of 45.2 m (148.3 ft) of Shore Airport Formation core.

Interpretation:

Whereas most of this lithofacies is apparently structureless, the weak stratification indicates bedforms up to a few cm in amplitude that could be ripples. Ripples are commonly formed on the upper part of bar-forms, such as those that might have developed in the incised paleovalley at Pleasant Prairie oilfield. This lithofacies comprises the mid to upper parts of conglomerate-based fining-upward successions in the Pleasant Prairie cores, and is interpreted to have been deposited in the mid to upper part of bar-forms in the incised paleovalley at Pleasant Prairie oilfield.

The scant coarser material in this lithofacies suggest periods of stronger flow, but no sedimentary structures suggestive of tidal influence, such as bundling or sand–mud couplets (Nio and Yang, 1991) is evident. The lack of tidal evidence in sedimentary structures, and the lack of carbonate material or fossils other authors have associated with an interpretation of tidal influence in downdip Chesterian sandstones (e.g., Shonfelt, 1988), suggests that this lithofacies originated in a river-dominated depositional environment.
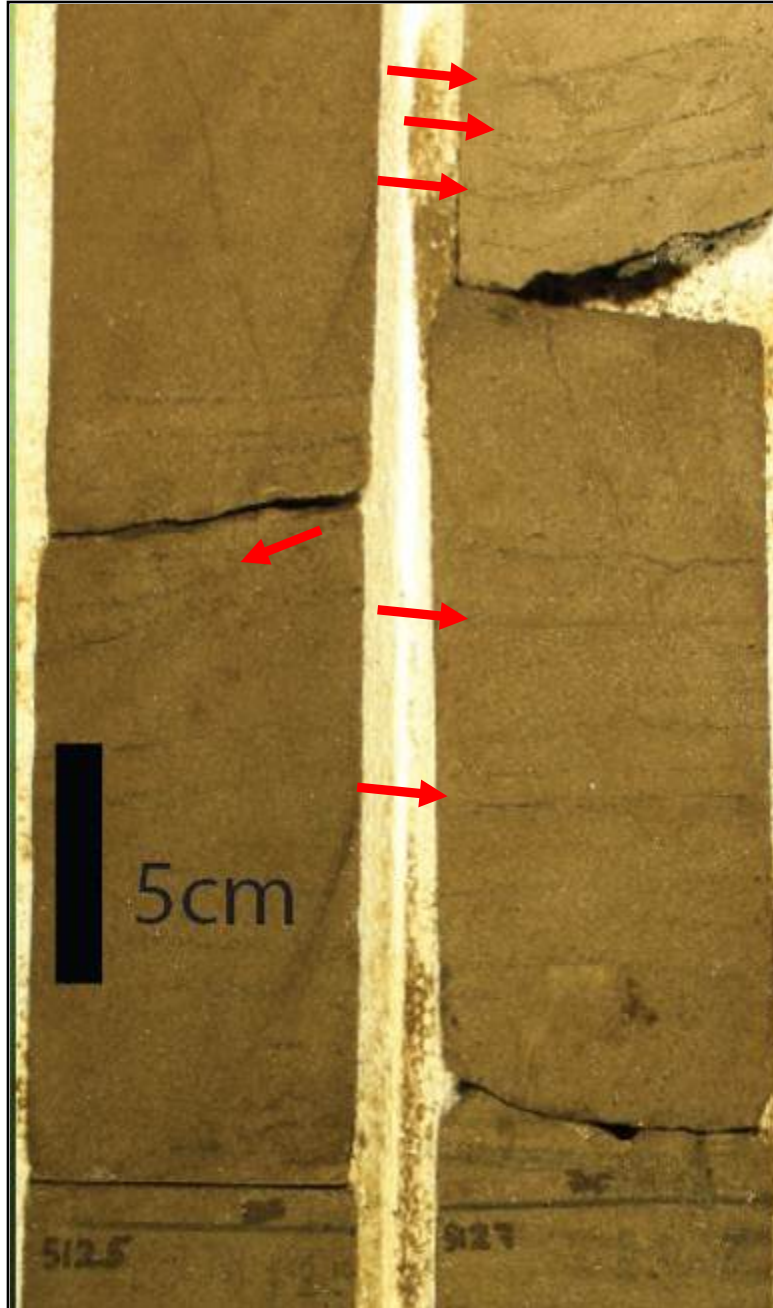
Figure 13: Weakly stratified sandstone lithofacies in Moody D2 core. Depths on core (bottom of photo) are measured depth in feet. Note faint wispy streaks (arrows) that give weakly stratified appearance to otherwise structureless sand.

7. Interbedded quartzarenite and heterolithic mudstone–sandstone

Description:

The interbedded quartzarenite and heterolithic mudstone–sandstone lithofacies (Figure 14) consists of beds of heterolithic mudstone–sandstone 15–60 cm thick interbedded with beds of quartzarenite 10–30 cm thick. The heterolithic mudstone–sandstone layers consist of white to light gray (N9–N7), or oil-stained dusky yellowish brown (10YR 2/2) sand and medium dark gray (N4) silty mud, and are mostly calcite cemented, with some grains held together by clay. The quartzarenite beds are white to light gray (N9–N7) and calcite cemented, or oil-stained dusky yellowish brown (10YR 2/2) and silica cemented. Sand grains in both the quartzarenite and heterolithic mudstone–sandstone beds are very fine to fine grained, subangular to well-rounded, and very well sorted. The heterolithic mudstone–sandstone beds display flaser to wavy bedded ripples with mud drapes, microfaulting, and a few burrows interpreted as *Palaeophycus*—lined, horizontal, and up to 3 mm in diameter (see Discussion section on depositional environment for photograph). The quartzarenite beds are structureless to weakly stratified, with discontinuous, diffuse streaks of black carbonaceous debris and a few small pebbles of carbonaceous shale. The interbedded quartzarenite and heterolithic mudstone–sandstone lithofacies occurs only in the Moody D2 core, where it is in gradational basal contact with the basal conglomerate below and abruptly overlain by weakly stratified sandstone.

Arithmetic average core porosity of interbedded quartzarenite and heterolithic mudstone–sandstone is 9.11%, with a range of 5.5–13.2%. The geometric average permeability of interbedded quartzarenite and heterolithic mudstone–sandstone is 1.23 md, with a median of 0.9 md and a range of 0.334–10 md. The heterolithic bed in the Moody D2 core is 1.8 m (6 ft) thick, or 9% of the Moody D2 Shore Airport Formation core.

Interpretation:

Flaser to wavy bedded sediments are commonly found in tide-influenced environments (Nio and Yang, 1991).The presence of silt- to clay-sized sediment in this lithofacies suggests flow velocities lower than those that deposited the other siliciclastic lithofacies, and the interbedded cleaner sandstone intervals suggest periods of flow stronger than that which deposited the silt- to clay-sized sediments. Thus, this lithofacies appears to have been deposited under conditions of fluctuating flow. Such conditions would be consistent with a tide-influenced depositional environment. Similar heterolithic lithofacies, however, have been described in fluvial deposits, albeit rarely (e.g., Kvale and Vondra, 1993; Bhattacharya, 1997; Miller, 2000). *Palaeophycus* are known to occur in a range of depositional environments from fluvial to estuarine to shoreface, representing a range of salinity conditions from freshwater to brackish to normal marine (Buatois et al., 1999). Further, no cyclicity is evident within the heterolithic mudstone–sandstone intervals which would suggest tidal influence, such as bundling of thick–thin alternating mudstone–sandstone laminae or beds (Nio and Yang, 1991). In sum, this lithofacies could represent tide-influenced estuarine deposits; however, in the present context of association with other lithofacies interpreted as fluvial deposits, and with similar examples documented in fluvial environments (e.g., Bhattacharya, 1997; Miller, 2000), the depositional environment is interpreted as river dominated.
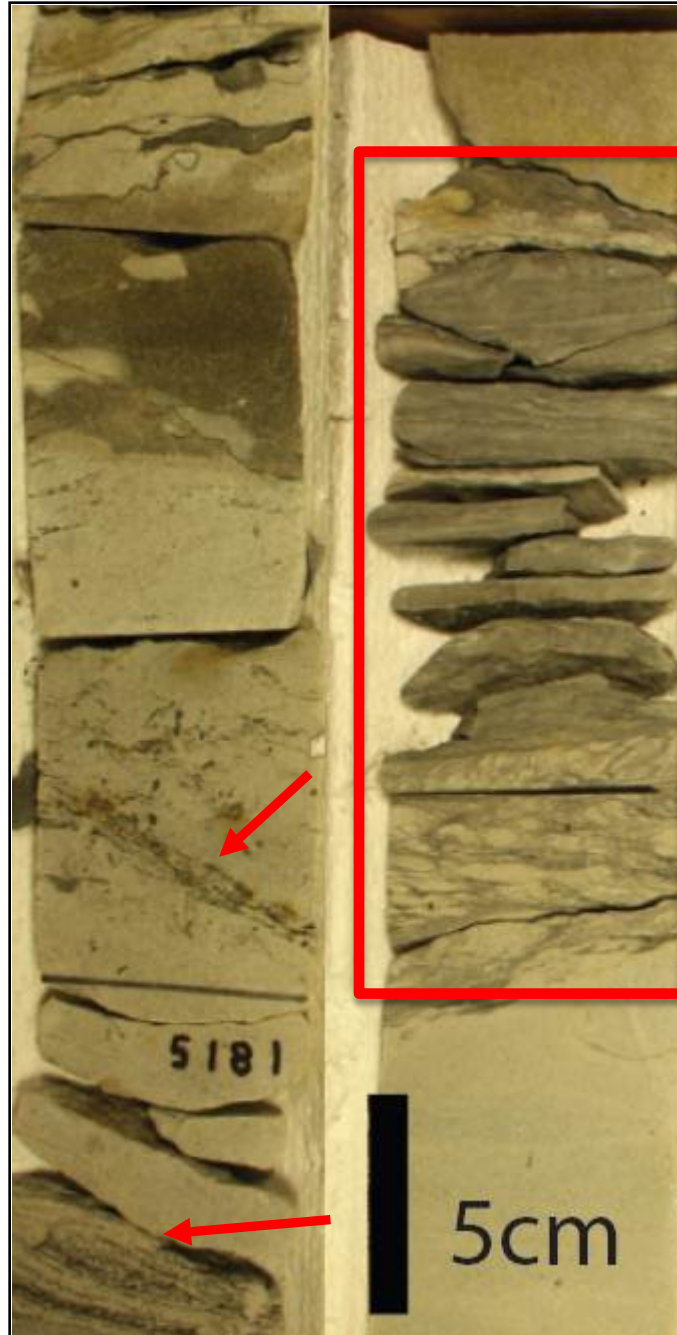
Figure 14: Interbedded quartzarenite and heterolithic mudstone–sandstone lithofacies, Moody D2 core. Depths on core are measured depth in feet. Note shaly interval at right (outlined by box), with clean sandstone above and below, and streaks of black carbonaceous debris (arrows).

b. Well log character and correlations

Well-log based interpretation of lithologies is possible using gamma-ray, photoelectric, and neutron–density porosity logs. Limestone, conglomerate, sandstone, and shale lithologies are all identifiable using an appropriate combination of well-log curves. Limestone, which underlies the Chesterian Shore Airport Formation in all wells, is characterized by low gamma-ray readings, around 15–30 API units, porosity of 5% or less, and photoelectric log value of 5. Since the neutron–density porosity logs in the study area are all scaled to read a limestone matrix, the neutron and density curves generally overlie one another. Conglomerates are characterized by slightly higher gamma-ray readings than either limestone or sandstone, commonly around 15–40 API units, porosity rarely above 10%, and photoelectric log value of about 3. Calcite content in conglomerates due to cementation and the presence of carbonate clasts causes the neutron and density porosity log response to be similar to limestone. Basal conglomerates generally display higher gamma-ray readings than other conglomerates, up to around 50 API units. The interbedded quartzarenite and heterolithic mudstone–sandstone lithofacies has a gamma-ray reading of 30–60 API units; the log response resembles the basal conglomerate which it directly overlies.

Sandstones are characterized by gamma-ray readings around 10–20 API units, photoelectric log value of about 2, high porosities—commonly > 10%—and a characteristic crossover of the neutron and density porosity curves. The crossover of neutron and density porosity curves is an artifact of the scaling of the porosity curves for a limestone matrix. Quartz sandstone has a lower density than limestone (2.65 g/cc compared to 2.71 g/cc), and this lower density causes limestone-scaled density porosity logs to read porosity in sandstone intervals higher than limestone intervals. The neutron porosity log is unaffected by these density

differences, and the commonly resulting crossover of the density porosity curve over the neutron porosity curve is the most useful and easiest way of identifying sandstone in the well logs. The gamma-ray curves in sandstones are generally uniform vertically, changing by only a few API units; this gamma-ray log profile is interpreted as indicating no systematically changing trends in content of fine sediment such as clay, which often contains radioactive elements that would cause increased gamma-ray log response. Individual sandstone lithofacies identified in core cannot be discriminated based on well-log response. Zones of shale are easily identified by gamma-ray readings over 70 API units.

The Moody D2 well provides a typical example of a well log from the Chesterian reservoir at Pleasant Prairie oilfield, and the core-defined lithofacies shown next to the well log (Figure 15) illustrates the typical conglomerate–sandstone stacking pattern which can be interpreted in other well logs in the Chesterian reservoir. Low gamma-ray, low porosity limestone underlies the Shore Airport Formation. Starting at the base of the Shore Airport Formation, conglomerate is overlain by sandstone, then another conglomerate overlain by sandstone, then conglomerate which is abruptly overlain by shaly Pennsylvanian strata. The same pattern of conglomerate–sandstone alternations is apparent in other neutron–density well-logs throughout the study area. Within this framework, four conglomerate beds and four sandstone beds were correlated through the reservoir.

Exceptions to the typical pattern of alternating conglomerate–sandstone stacking pattern occur in three wells in the northern part of the reservoir: the Federal 2, Federal 3, and Kuhn 7-10 wells (API#s 15-081-21332, 15-081-21379, 15-081-21363 respectively). Here, the Shore Airport Formation interval includes a thick shaly zone identified by a high gamma-ray log response (70 API units or greater). The shaly zone vertically separates two sandy zones above

66

and below within the three wells it occurs in, and the top of the shaly zone correlates to the base

of a conglomerate unit (Figure 16). The resistivity log through the dead oil zone identified in the

Moody D2 core showed superimposition of the deep and medium resistivity logs, interpreted as a

reflection of low permeability caused by occlusion of the pore spaces by solid bituminous

material. The dead oil zone could not be identified by any other log signature, and the resistivity

log response could not be correlated to other adjacent wells. Thus, the true extent of the dead oil

zone remains unknown.
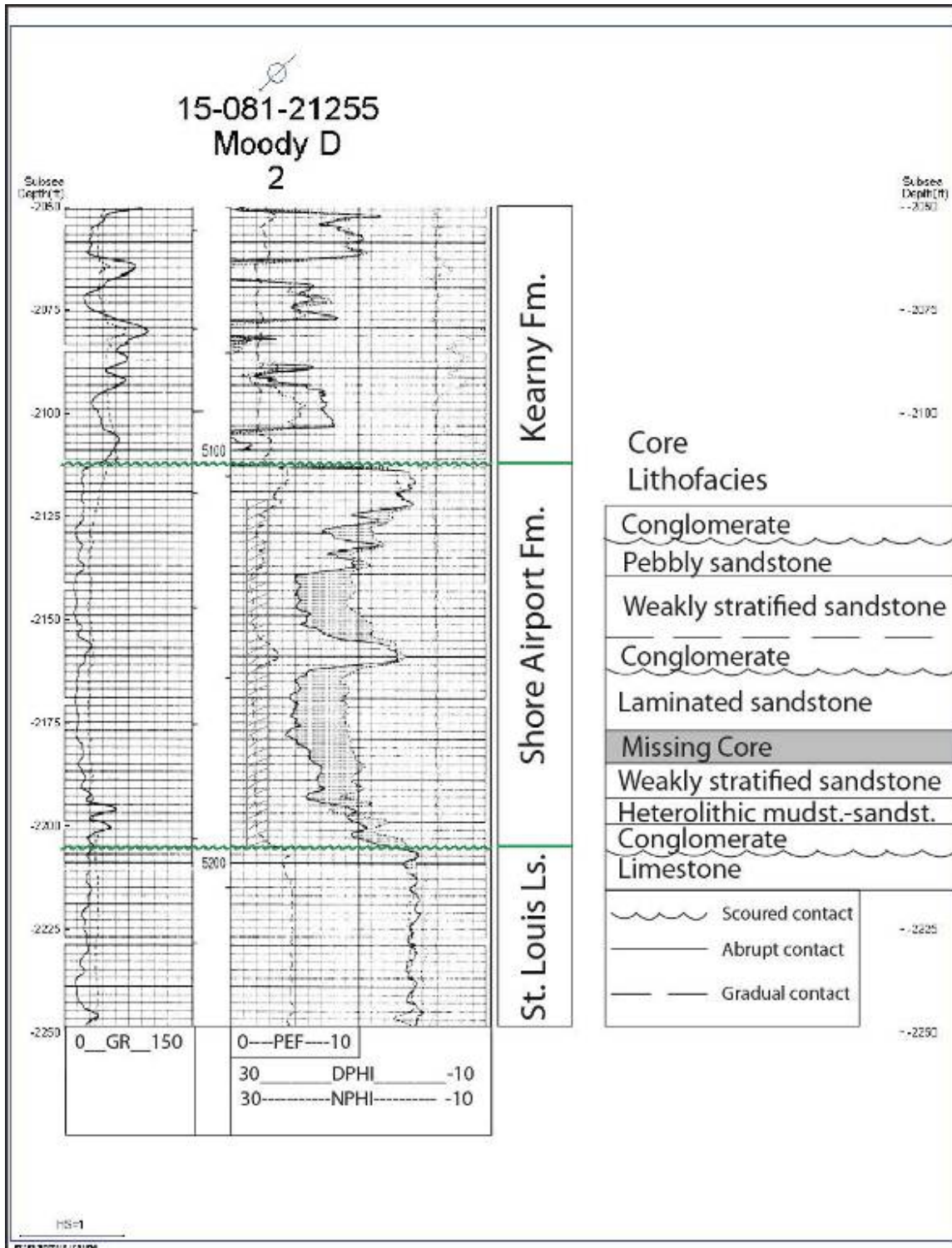
Figure 15: Type log for the Chesterian sandstone reservoir at Pleasant Prairie oilfield (Moody D2). Log shows gamma-ray (GR) in left track, measured depth in middle track, and photoelectric log (PE), and neutron porosity (NPHI) and density porosity (DPHI) in right track. Index map (Figure 15A) shows location of the well.
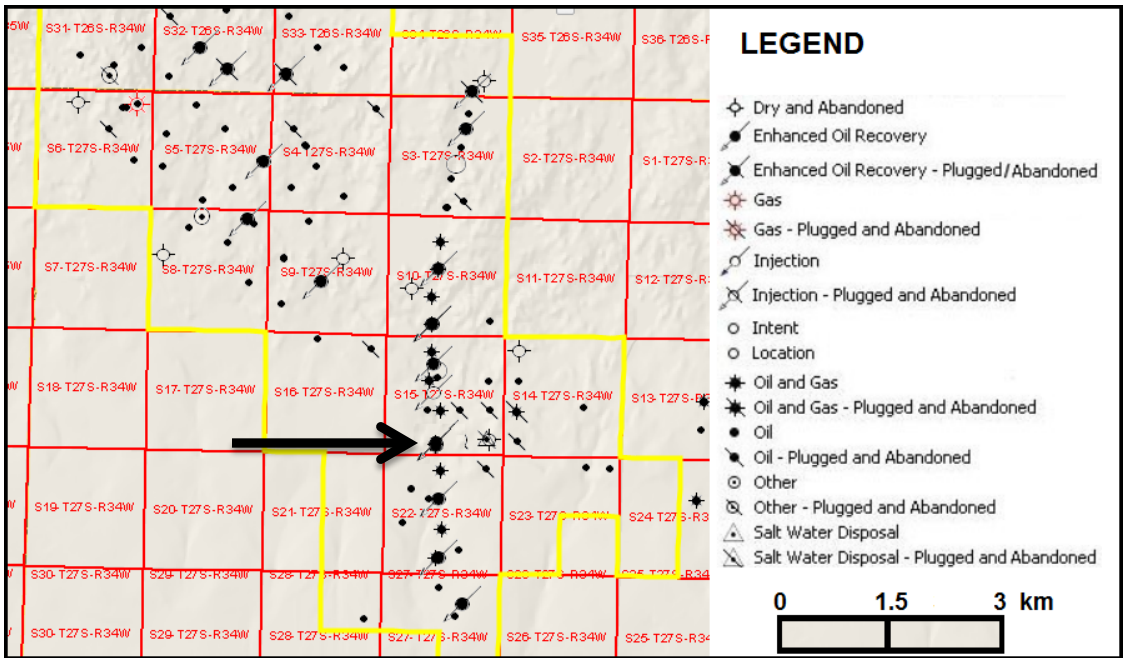
Figure 15A: Index map showing location of Moody D2 well (arrow), used for type log for Chesterian Shore Airport Formation reservoir at Pleasant Prairie oilfield. Scale is approximate, red squares on map are section lines 1.6 km (1 mile) on each side. Modified from KGS website.
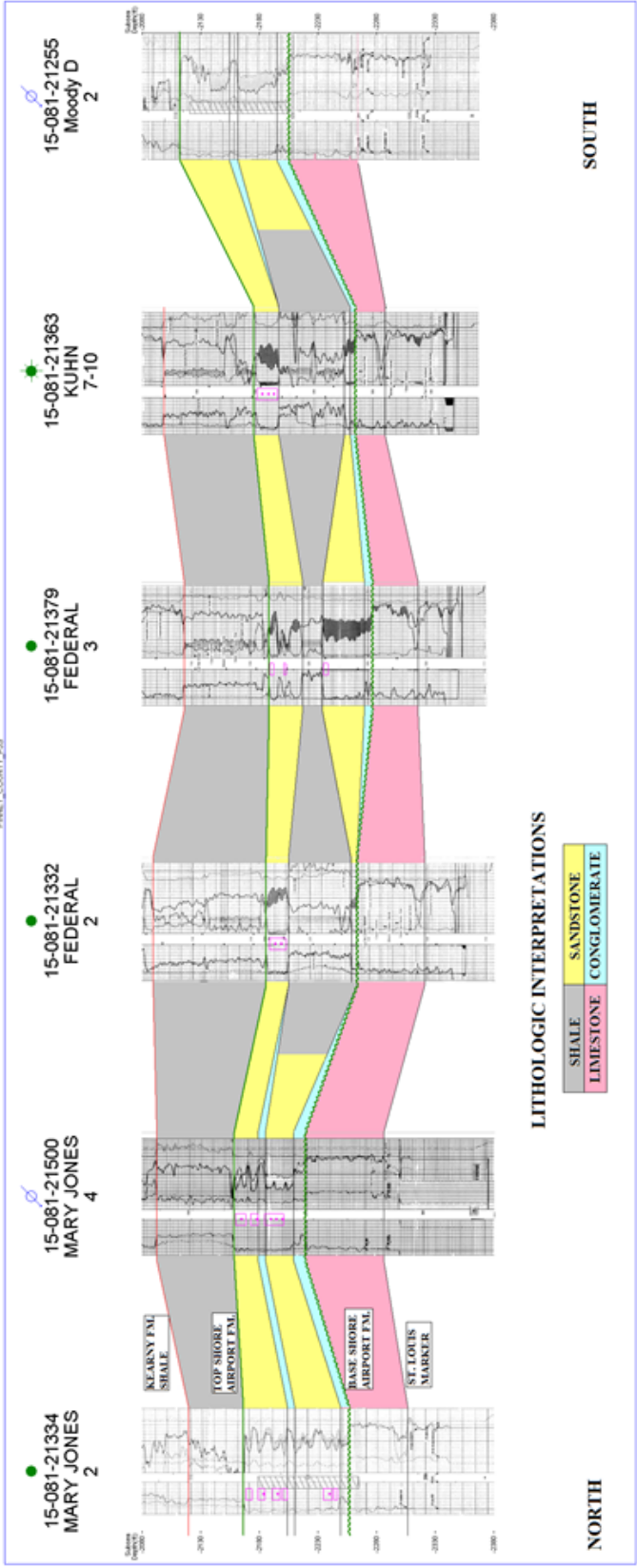
Figure 16: Well-log correlations along length of reservoir, showing typical alternating conglomerate-sandstone stacking pattern (Mary Jones #2, Mary Jones #4, Moody D2) and thick shaly zone identified by high gamma-ray log response (Federal 2, Federal 3, Kuhn 7-10). Note that the top of the shaly zone is correlated to the base of a conglomerate unit. Well logs are gamma-ray on left track, neutron and density porosity on right track, with available perforation data marked by pink boxes in middle of well logs. Well spacing in correlations is shown as even, but true well spacing is indicated on index map below (Figure 16A), showing 1.6 km (1 mile) sections for scale. Datum is set at sea level, showing true structural view of correlations. Stratigraphic relation of shale and sandstone in inter-well space is unknown, thus inter-well space is filled half yellow and half gray.
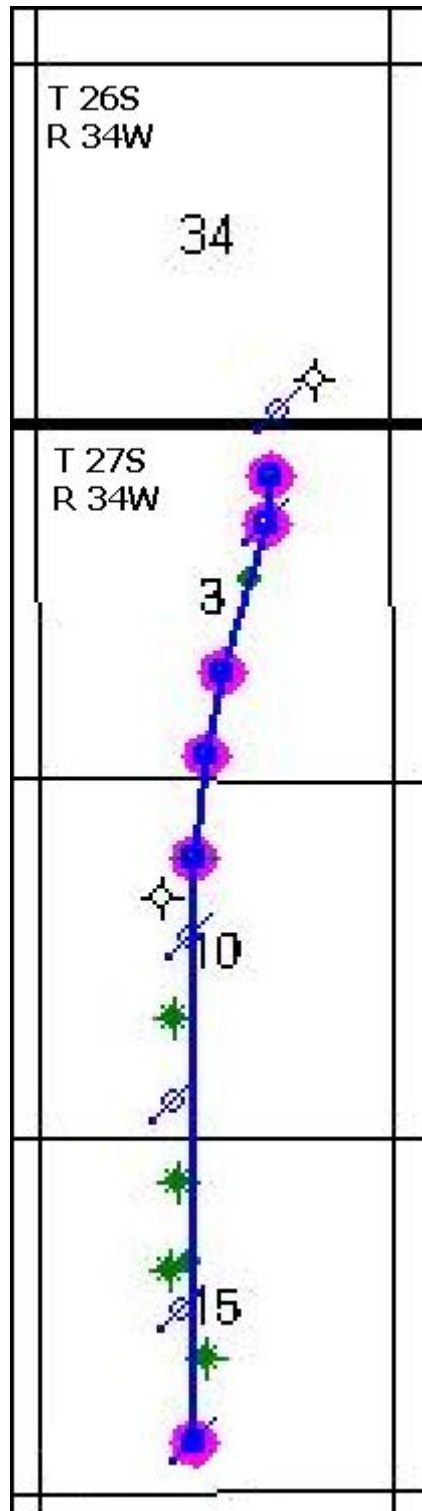
70

Figure 16A: Index map for Figure 16 cross-section. Wells in Figure 16 cross-section are highlighted pink; green wells are oil & gas producers, blue, open circles with diagonal line are water injection wells, and open circles with horizontal and vertical line extensions are dry holes. Each numbered square is a section, measuring 0.6 km (1 mile) on a side.

71

c. **Agglomerative Hierarchical Clustering (AHC) Analysis**

Agglomerative hierarchical clustering (AHC) analysis, performed as a preparatory step to prediction of lithofacies in uncored wells using artificial neural networks, provided insight into patterns of statistical dissimilarity of lithofacies. This step was useful in determining a lithofacies classification scheme that would work in artificial neural network prediction, and hence, in creation of a 3D lithofacies model of the reservoir. Statistical dissimilarity of each sampled interval of the core, as measured by the Euclidean distance formula (see Methods), was computed using both core and log variables, including grain size, argillaceous content, pore throat size, cement mineral, gamma-ray, bulk density, photoelectric factor, neutron and density porosity, average of neutron and density porosity, and neutron porosity minus density porosity. Creation of dendrograms (Figure 17) to illustrate the results of AHC analysis provided a graphical means of examining the general trends in dissimilarity of the core-defined lithofacies.

Sandstone lithofacies generally clustered together in the dendrograms and separately from conglomerates. Conglomerates, though, tended to form separate clusters for basal and non-basal units, with the interbedded quartzarenite and heterolithic mudstone–sandstone lithofacies clustered with basal conglomerates in the dendrograms (Figure 17). The separation of basal and non-basal conglomerates is caused primarily by different well-log responses, but also reflects core porosity and permeability differences; basal conglomerates display generally higher gamma-ray log response and higher porosity and permeability than non-basal conglomerates (Table 6). The core porosity and permeability difference between basal and non-basal conglomerates reflects differences in the amount of calcite cementation; non-basal conglomerates have more calcite cement than basal conglomerates and therefore have lower core porosity and permeability values lower than basal conglomerates. High gamma-ray log readings

are commonly caused by radioactive elements included in fine sediment, and therefore the log character of the conglomerates suggests that the basal conglomerate bed in the Pleasant Prairie oilfield might include fine-grained sediment, or alternatively, Uranium-enriched carbonate cements, whereas younger (higher) conglomerates might not. The interbedded quartzarenite and heterolithic mudstone–sandstone lithofacies in the Moody D2 core directly overlies and grades from the basal conglomerate, and displays well-log response comparable to the Moody D2 basal conglomerate. Core petrophysical values of the interbedded quartzarenite and heterolithic mudstone–sandstone lithofacies are closer to those of basal conglomerates than other lithofacies (Table 6). In sum, the results of AHC analysis suggested that the core-defined lithofacies should be reclassified from the original seven to a smaller group of three: 1) sandstone, 2) basal (shaly) conglomerate plus interbedded quartzarenite and heterolithic mudstone–sandstone, and 3) non-basal (limey) conglomerate.
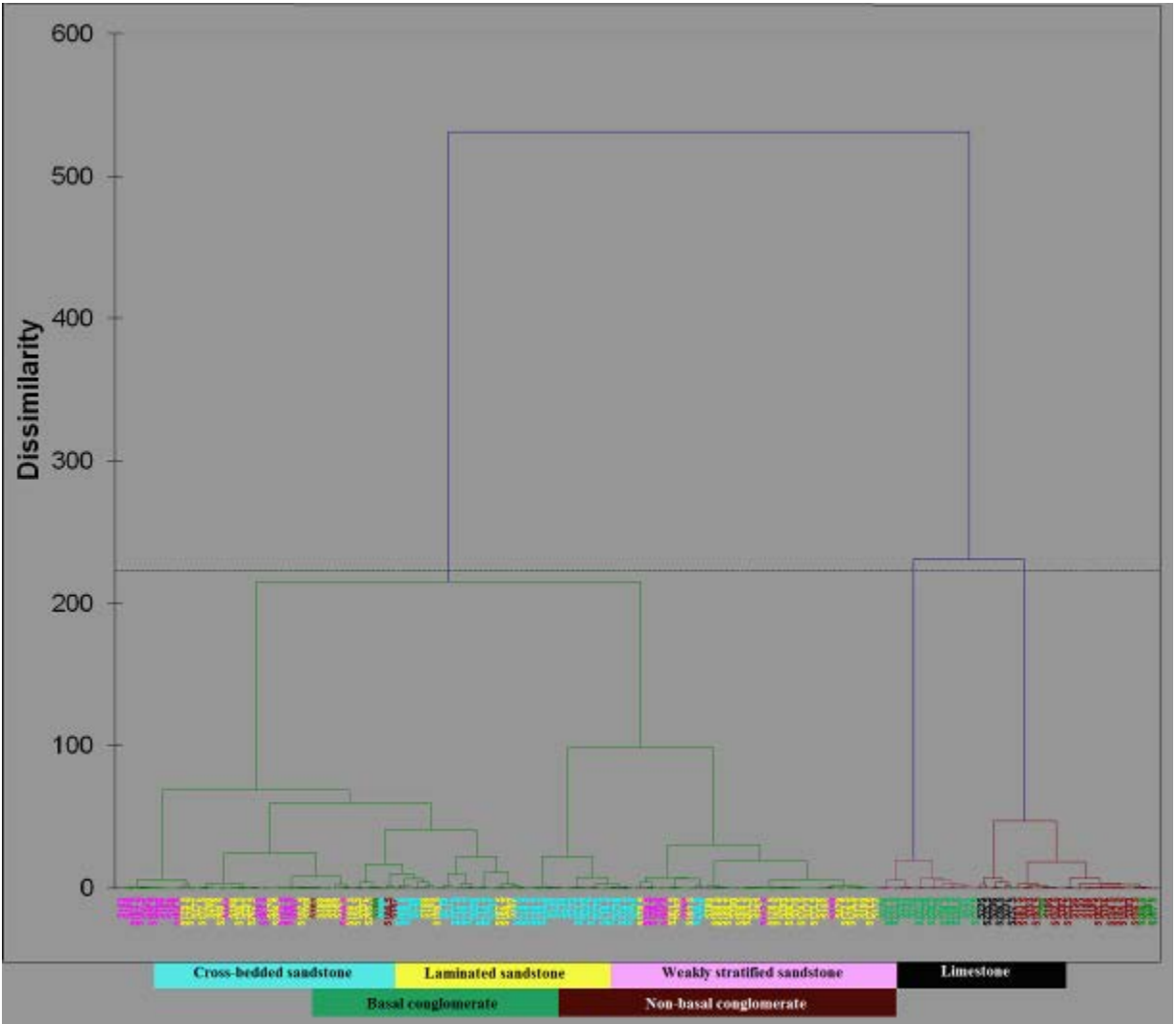
Figure 17: Dendrogram from XLSTAT showing typical clustering behavior of lithofacies, from the Mary Jones #2 core. Lines show connection of clusters based on dissimilarity calculated using Euclidean distance formula. Depths of individual core samples are labeled on x-axis and color coded according to lithofacies. Note how basal and non-basal conglomerates form separate clusters at right, and sandstone lithofacies, particularly laminated and weakly stratified, tend to cluster together at left.

d. Petrophysics

Linear regression analysis between core porosity and estimated porosity obtained from several methods revealed the highest correlation to core porosity, as measured by the coefficient of determination, R^2. Single-variable linear regression analysis was carried out between core porosity and the bulk density log, and between core porosity and the average of neutron and density porosity. Multi-variable linear regression analysis was carried out between core porosity and both the neutron and density porosity logs, and single-variable regression analysis was carried out between core porosity and porosity logs generated using the equation:

Equation 4:   PHI = (Rhoma-Rhob)/(Rhoma-Rhof)

Where Rhoma equals apparent matrix density in grams per cubic centimeter (g/cc), Rhob is the value from the bulk density log, and Rhof is the density of pore fluid. Several variables were used as Rhoma in Equation 4, including 2.68 g/cc (calcite-cemented sandstone), 2.65 g/cc (silica-cemented sandstone), and actual bulk density of each core sample as recorded in the core reports. Rhof was set at the density of water, 1.00 g/cc.

The results of these linear regression analyses revealed that the bulk density log had the highest correlation to core porosity, as measured by the coefficient of determination, R^2. Values of the coefficient of determination, R^2, between core porosity and the several types of estimated porosity ranged from a low of 0.4748 to a high value of 0.6932 (Table 7). The lowest correlation was found between core porosity and porosity estimated using Equation 4, with the actual core-sample bulk density as Rhoma. Regression analysis of the bulk density log, which had the highest correlation, was used to generate new logs of estimated porosity for all wells. The new

logs were generated by using an equation to transform bulk density to porosity. The equation

calculated in Microsoft Excel from the trendline between bulk density and core porosity was:

Equation 5:   Core porosity = -46.775*Rhob + 126.992

Equation 5 was applied to the bulk density logs of all wells in the study area to generate the new

logs of estimated porosity. These new logs of estimated porosity were used in calculations of

fluid saturation, and in the 3D modeling process to populate a model of the reservoir with

porosity values for use in volumetric and fluid saturation calculations.

Table 7: Correlation between core porosity and predicted porosity, measured by coefficient of determination, R^2, for different methods.

Method	Coefficient of determination R^2
1. Regression analysis of:	
a) RHOB	0.6932
b) NPHI DPHI	0.6497
c) NPHI-DPHI Average	0.6199
2. PHI = (Rhoma-RHOB) / (Rhoma-Rhof)	
a) Rhoma = 2.68 g/cc	0.6239
b) Rhoma = 2.65 g/cc	0.6239
c) Rhoma = grain density from core report at each 0.15 m (0.5ft) step	0.4748

Linear regression between core porosity and permeability was performed to obtain an equation or equations to estimate permeability based on porosity. The equation, or equations, would be calculated from the trendline applied on a cross-plot of core porosity and permeability and applied to the 3D geologic model of porosity in order to generate a 3D geologic model of permeability. Each cell in the 3D geologic model would have a porosity value from which an estimated permeability value would be derived through application of the equation or equations. Whether a single equation or more than one would be used would depend on which grouping of core-defined lithofacies resulted in the highest coefficient of determination, R^2, between core porosity and core permeability.

Regression analysis of a cross-plot of core porosity and permeability for all lithofacies excluding limestone suggested coefficient of determination, R^2, value of 0.7993 (Figure 18A). Limestone is not included in the analysis because it will not be included in the 3D reservoir model. Cross-plots of core porosity and permeability show two general groups of data points— one group with porosity < 12% and permeability < 0.02 millidarcies (md), and a higher group with porosity between 7% and 20% and permeability between 5 md and 600 md. The first group represents samples from intervals tightly cemented with calcite or silica, whereas the latter group represents samples with less cementation. Splitting the core porosity and permeability data into reservoir (sandstone) and non-reservoir (conglomerate plus the interbedded quartzarenite and heterolithic mudstone–sandstone) lithofacies groups might result in an improved coefficient of correlation, R^2, and hence, a model of estimated permeability that more accurately reflected the porosity–permeability relationships in the core data. To test that hypothesis, regression analysis was carried out with the reservoir–non-reservoir lithofacies grouping. The results revealed that the coefficient of determination between porosity and permeability for the reservoir group was

78

calculated as 0.8195 and the coefficient of determination for the non-reservoir group was 0.5702

(Figure 18B). The 0.8195 value of the coefficient of determination for the reservoir group is an

improvement over the value of 0.7993 calculated for all data. Therefore, splitting the data into

reservoir and non-reservoir groups and using the separate equations would result in generation of

a more accurate 3D model of estimated permeability in the reservoir lithofacies.

A small cluster of sandstone data points near the upper end of the conglomerate trend line

seems better fitted to the conglomerate trend than the sandstone trend. These sandstone samples

are from the lowermost part of the cross-bedded sandstone lithofacies in the Mary Jones #2 core;

the cross-bedded sandstone at these depths is immediately above the basal conglomerate and,

although oil-stained, is tightly cemented with calcite and silica. The cementation of the cross-

bedded sandstone data explains why they fit better into the non-reservoir group on the porosity–

permeability cross-plots. The geological similarity of these sandstone samples to the non-

reservoir group of samples suggests that moving these sandstone samples to the non-reservoir

group might result in an improved coefficient of correlation, R^2, for the reservoir lithofacies

group, and hence, a more accurate 3D model of estimated permeability. Regression analysis was

therefore performed again with the sandstone samples reassigned. The results of regression

analysis showed improved fit of the trend lines for both groups; R^2 for the reservoir group

improved from 0.8195 to 0.8578, and R^2 for the non-reservoir group improved from 0.5702 to

0.6621 (Figure 18C). Reassigning the sandstone samples to the non-reservoir group therefore

was demonstrated to result in a better correlation of porosity to permeability, and hence, the

equations of the two trendlines could be used to generate a 3D model of estimated permeability

that would reflect the relationship of porosity and permeability shown by the core data more

accurately than such a permeability model made using the equations of trendlines from previous groupings of lithofacies.

One further grouping of lithofacies were tested to see if grouping geologically similar samples would result in improved R2. The non-reservoir group was split into two subgroups: 1) non-basal conglomerate, and 2) basal conglomerate plus the interbedded quartzarenite and heterolithic mudstone–sandstone. Regression analysis of this grouping suggested that the coefficient of correlation, R^2, would be 0.2761for the first subgroup and 0.5893 for the second subgroup, respectively (Figure 18D). The previous regression analysis of all non-reservoir lithofacies together suggested a coefficient of correlation, R^2, of 0.6621. Splitting the non-reservoir lithofacies group into further subgroups, therefore, would not result in trendlines with equations that reflected porosity–permeability relationships more accurately than the previous trendlines based on a single group of non-reservoir data points.

Whereas basal and non-basal conglomerate can be distinguished simply by relative position in all wells in the study area, including those without core, the same cannot be said of individual core-defined sandstone lithofacies. The core sandstone lithofacies cannot be distinguished based on log response or relative position and cannot, therefore, be individually defined in wells without core; thus, while splitting the sandstone lithofacies and performing regression analysis on the individual sandstone lithofacies may result in an improved coefficient of correlation, R^2, the equations for estimating permeability as a function of porosity could not be applied throughout the field. Nevertheless, to test the hypothesis that such splitting of individual core sandstone lithofacies would result in an improved coefficient of correlation, R^2, the regression analysis was carried out for the individual sandstone lithofacies. The results suggested that the coefficient of correlation, R^2, would indeed improve from the previous high

80

value of 0.8578 for three of the lithofacies: the pebbly, laminated, and weakly stratified sandstones (Figure 18E). The results, however, suggest a coefficient of determination, R^2, for the cross-bedded sandstone of only 0.583. Cross-bedded sandstone is part of the reservoir, so obtaining the most accurate function possible to estimate permeability as a function of porosity is important for 3D reservoir modeling. Therefore, even if the individual sandstone lithofacies could be distinguished in wells without core, the coefficient of correlation, R^2, of the cross-bedded sandstone porosity and permeability data suggests that estimated permeability generated using the equation calculated from the trendline for this lithofacies would not be as accurate as estimated permeability for other reservoir lithofacies. The alternative to estimating permeability for individual sandstone lithofacies would be to use the data for all sandstone lithofacies grouped together to generate estimated permeability values. For the present study, the grouping chosen for generating estimated permeability values was the reservoir and non-reservoir groups shown in Figure 18C. The resulting two equations, one from each trendline, were used to generate estimated permeability values as a function of porosity in the reservoir and non-reservoir lithofacies groups, respectively, in the 3D geologic model. A table summarizing the coefficient of correlation, R^2, data for the core porosity–permeability cross-plot regression analysis is included (Table 8).
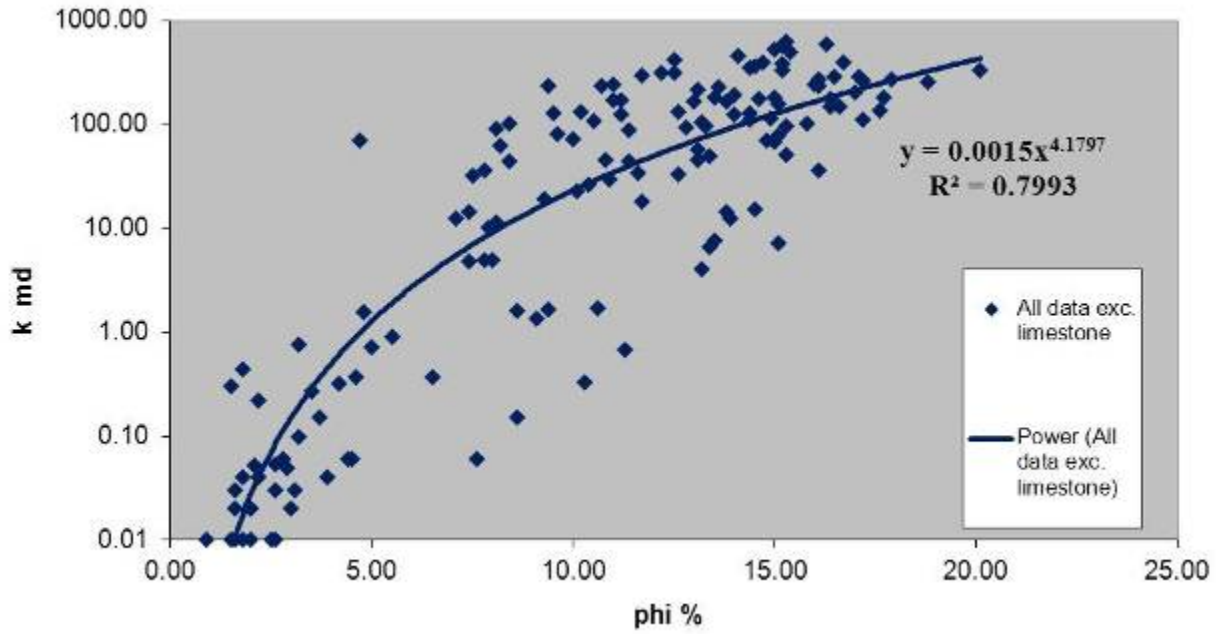
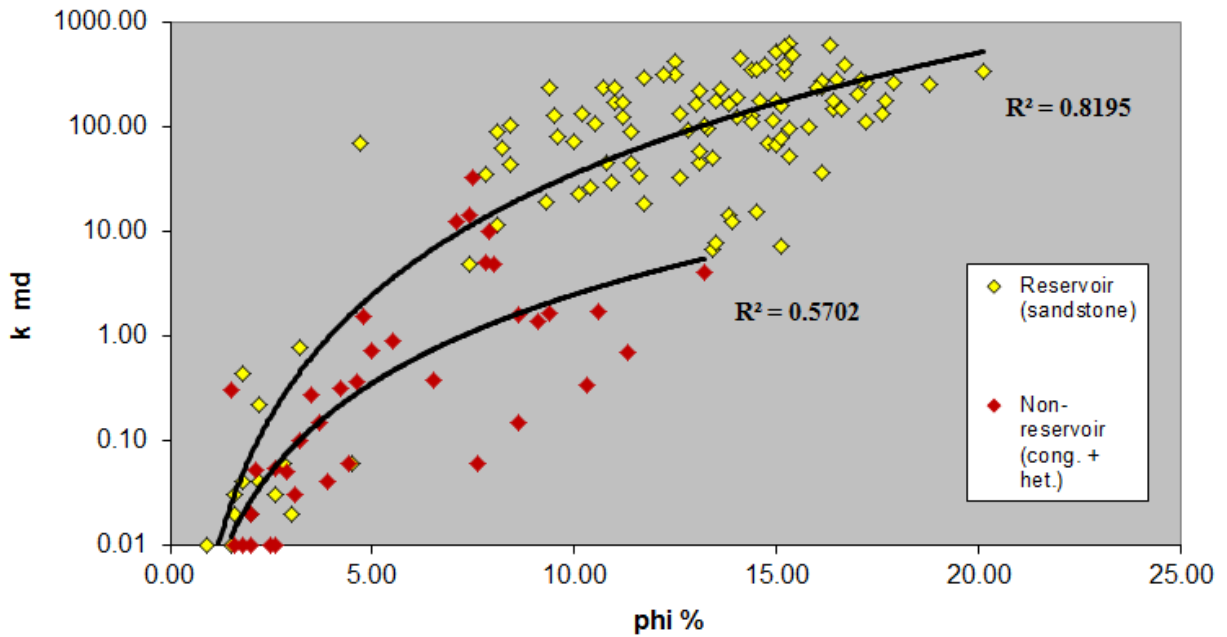Figure 18A: Porosity–permeability cross-plot for all core data except limestone.

Figure 18B: Porosity–permeability cross-plot for sandstone and conglomerate.
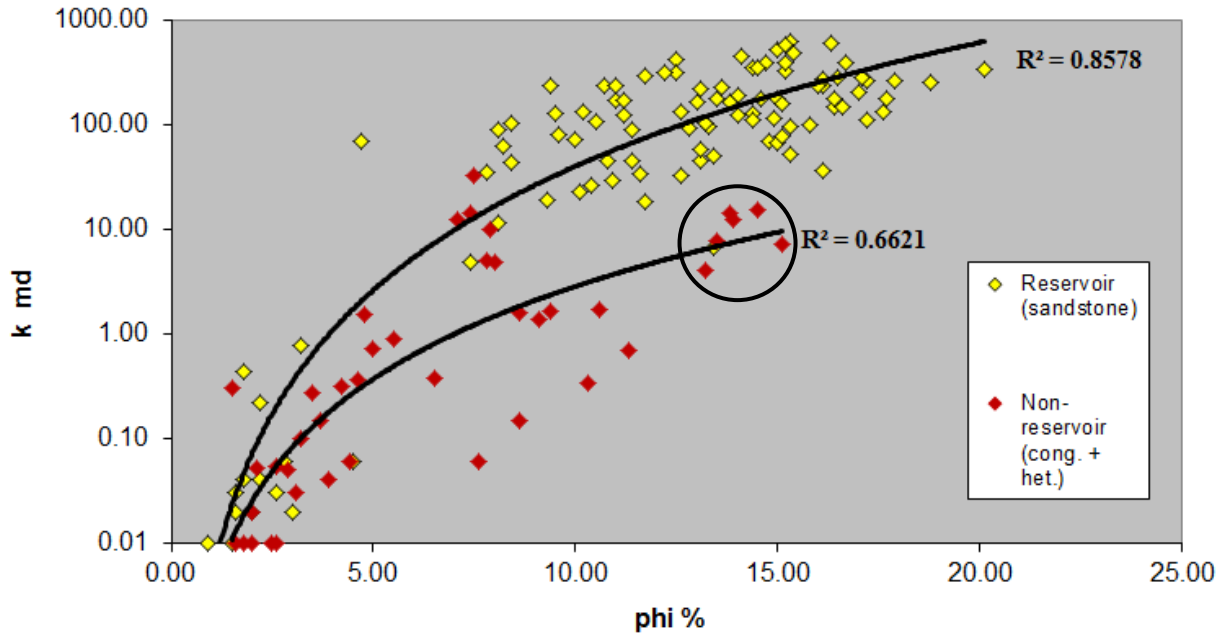These data illustrate that each type of rock includes different trends.

Figure 18C: Porosity–permeability cross-plot showing separate trends for sandstone and conglomerate. In this plot, some samples (circled) were moved from sandstone to conglomerate trendline because they directly overlie and are in gradational contact with a conglomerate bed, and display similar cementation. Moving the samples to the conglomerate group results in improved R^2 for both conglomerate and sandstone groups.
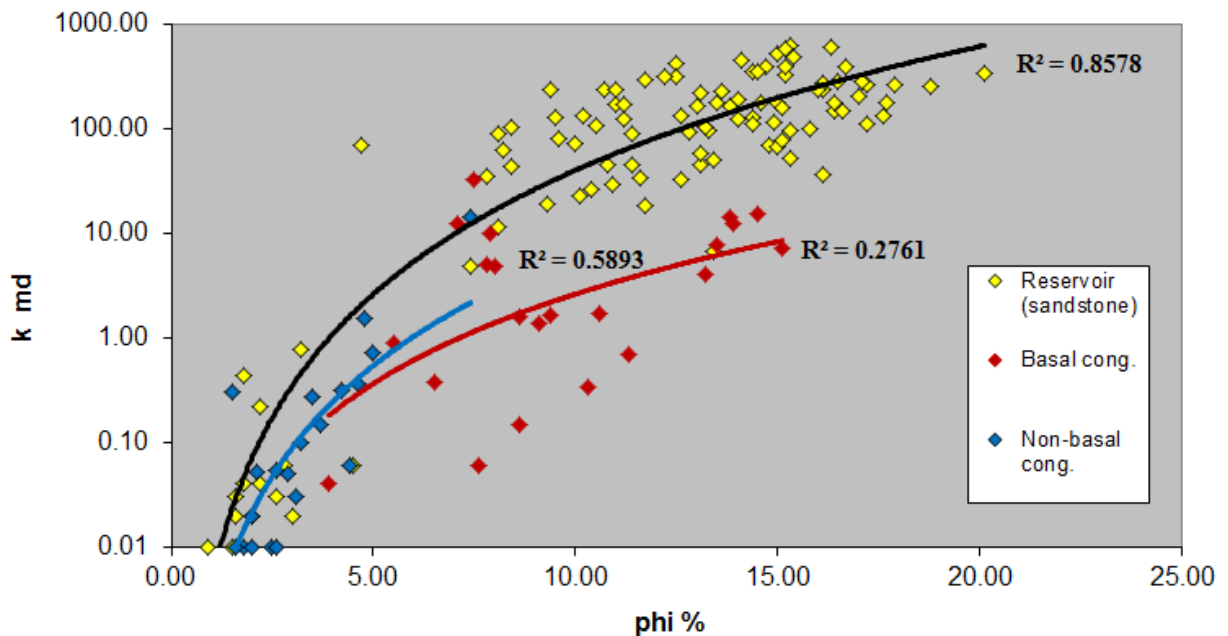
Figure 18D: Porosity–permeability cross-plot, with conglomerate split into basal and non-basal types. These data illustrate decreased R^2 relative to the un-differentiated data.

83
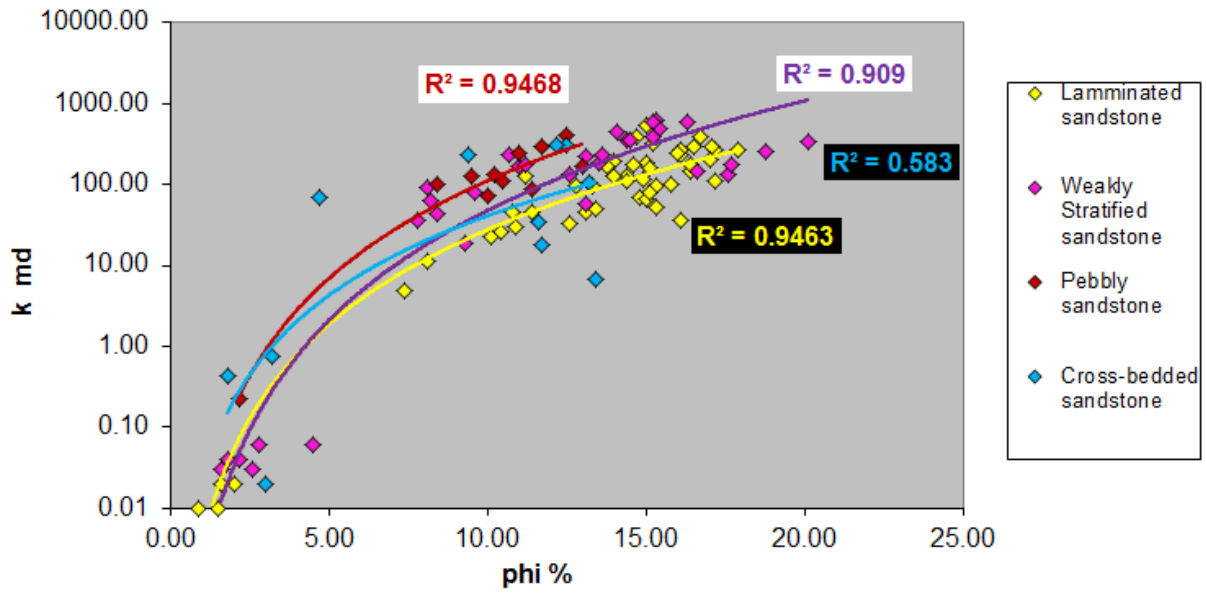
Figure 18E: Porosity–permeability relationships of four sandstone lithofacies. R^2 values for all sandstone lithofacies are enhanced relative to lumped data (Figure 18A), except cross-bedded sandstone.

Table 8: Summary of coefficient of correlation, R^2, for core porosity–permeability trend lines for different combinations of lithofacies.

Lithofacies for trend lines:	Corresponding porosity–permeability cross-plot figure	Coefficient of determination R^2
All lithofacies exc. Limestone	18A	0.7993
All conglomerate	18B	0.5702
All conglomerate w/re-assigned data points from sandstone	18C	0.6621
Non-basal conglomerate	18D	0.5893
Basal conglomerate	not illustrated	0.0888
Basal conglomerate w/re-assigned data points from sandstone	18D	0.2761
All sandstone	18B	0.8195
All sandstone w/o data points re-assigned to conglomerate	18C	0.8578
Laminated sandstone	18E	0.9463
Weakly stratified sandstone	18E	0.909
Pebbly sandstone	18E	0.9468
Cross-bedded sandstone	not illustrated	0.4169
Cross-bedded sandstone w/ data points re-assigned to conglomerate	18E	0.583

e. Lithofacies Prediction with Artificial Neural Networks (ANN)

For the purpose of lithofacies prediction in uncored wells, well-log analysis, porosity–permeability cross-plot analysis, and AHC patterns indicated that the core sandstone lithofacies should be lumped together and that conglomerates should be split into basal and non-basal types, with the heterolithic lithofacies added to basal conglomerate. In addition to the sandstone and conglomerate lithofacies, well-log analysis indicated that a shaly zone is present in the northern part of the field. Thus the four lithofacies to be predicted with artificial neural networks (ANN) and used in creation of a 3D model were: 1) shale, 2) basal (shaly) conglomerate, 3) non-basal (limey) conglomerate, and 4) reservoir sandstone. Shale was not a defined lithofacies in the cored wells, so to include it in the training process, a thick interval of shale was chosen from the Federal 2 well (API# 15-081-21332) and the log variables through that section were added to the training dataset.

Four combinations of well-log variables were used to define four cases of ANNs, to test hypotheses regarding which combination of well-log variables would make the greatest percentage of correct lithofacies predictions. Following the methodology of Dubois et al. (2006), half of the core data was used to train and initially test each ANN, and then each ANN was tested on all of the core data. A table summarizing the well-log variables used in the four cases is included (see Table 3). Case #1 comprises the well-log variables utilized by Dubois et al. (2006). Case #2 uses the same set of variables plus the photoelectric (PE) log, which is commonly used as an aid in interpretation of lithology, to test the hypothesis that adding the PE log will result in a higher percentage of correct lithofacies predictions. Case #3 and case #4 use the variables of Dubois et al. (2006) plus a log of estimated apparent grain density—RHOMAA—generated in Microsoft Excel (see Methods). The difference between case #3 and

case #4 is in the methodology of creating the RHOMAA log; case #3 uses averaged neutron and density porosity, whereas case #4 uses the porosity logs generated using regression analysis of the bulk density log (see Results section on Petrophysics). The PE log was only available on a subset of wells, but the RHOMAA logs were generated for all wells in the study area. Cases #3 and #4 test two hypotheses: 1) adding the RHOMAA log as an additional predictor variable will result in a higher percentage of correct lithofacies predictions, and 2) a case with RHOMAA logs generated with the bulk density regression-analysis porosity logs will provide a percentage of correct predictions higher than a case using RHOMAA logs generated with averaged neutron and density porosity.

A total of sixteen ANNs were created for each of the four cases by adjusting the number of hidden layer nodes and the damping parameter in Kipling.xla to find the values that would result in the highest percentage of accurate lithofacies predictions. For each of the sixteen ANNs created for each of the four cases, statistical success in correctly predicting lithofacies in the cored wells was measured using the methodology of Dubois et al. 2006; results were compared by calculating the total percentage of correct predictions, the percentage of correct predictions in reservoir sandstone lithofacies, and the percentage of lithofacies predicted correctly within one numerical lithofacies class. The ANN from each of the four cases with the highest percentages of correct and within-one-class predictions were identified, and then those four ANNs were compared to each other using the same three categories to see which of the cases provided the most accurate results.

Following the methodology of Dubois et al. (2006), the ANNs identified as most successful for each of the four cases were compared using the same three categories as above in their predictions on the half of the core data not used in training of the ANNs, and in predictions

on all core data. Summarized results of the predictions on the half of the core data not used in

training and results of the predictions on all core data are included (Table 9 and Table 10,

respectively).

Table 9: Statistical success of four cases of artificial neural network prediction of lithofacies on half of core data not used for training. Number of hidden layer nodes (#HLN) and damping parameter (DP) are variables in the structure of artificial neural networks. Accuracy represents statistical success of neural networks in predicting known lithofacies class based on well-log variables such as gamma-ray, photoelectric effect, etc.

Case #	Variables	Optimal Parameters #HLN, DP	Total % Correct	Reservoir sandstone % Correct	% Within 1 Class
1	GR, NPHI DPHI avg., NPHI-DPHI, log ILD, REL POS	10, 0.0001	0.900	0.811	0.963
2	GR, NPHI DPHI avg., NPHI-DPHI, log ILD, REL POS, PE	10, 0.001	0.944	0.962	1.00
3	GR, NPHI DPHI avg., NPHI-DPHI, log ILD, REL POS, RHOmaaND	10, 0.1	0.900	0.867	0.954
4	GR, NPHI DPHI avg., NPHI-DPHI, log ILD, REL POS, RHOmaaPHIX	80, 1	0.945	0.927	0.963

Table 10: Statistical success of four cases of artificial neural network prediction of lithofacies on all core data. Number of hidden layer nodes (#HLN) and damping parameter (DP) are variables in the structure of artificial neural networks. Accuracy represents statistical success of neural networks in predicting known lithofacies class based on well-log variables such as gamma-ray, photoelectric effect, etc.

Case #:	Variables:	Optimal Parameters # HLN, DP	Total % Correct	Reservoir sandstone % Correct	% Within 1 Class
1	GR, NPHI DPHI avg., NPHI-DPHI, log ILD, REL POS	10, 0.0001	1.00	1.00	1.00
2	GR, NPHI DPHI avg., NPHI-DPHI, log ILD, REL POS, PE	10, 0.001	1.00	1.00	1.00
3	GR, NPHI DPHI avg., NPHI-DPHI, log ILD, REL POS, RHOmaaND	10, 0.1	0.942	0.961	0.960
4	GR, NPHI DPHI avg., NPHI-DPHI, log ILD, REL POS, RHOmaaPHIX	80, 1	0.942	0.971	0.968

The results of these analyses show that case #2 and case #4 have the highest, and second highest (or are tied for highest or second highest) percentages in all three categories of comparison of prediction on half and on all of the core data. Case #2, which includes the PE log, in all comparisons has either the highest (or tied for highest) percentage results. In making predictions on the half of the core data not used in ANN training case #2 has higher percentage results than case #1 in all three categories. Thus, the results indicate that adding the PE log as a predictor variable resulted in a higher percentage of correct predictions. Comparing case #2 to case #1 in predictions on all core data, however, shows that the results are the same, indicating that adding the PE log as a predictor variable may not always contribute to a higher percentage of correct predictions. Comparisons of case #3 and case #4 show that case #4 has a higher percentage of correct predictions in all categories save one, where the percentage was the same as case #3. Thus, the results indicate that a case using RHOMAA logs generated with the bulk density regression-analysis porosity logs will provide a percentage of correct predictions higher than a case using RHOMAA logs generated with averaged neutron and density porosity.

Additional comparisons of the results were made using uncored wells. Each of the best ANNs of each of the four cases were used to make lithofacies predictions in wells from the study area where well-site geologist's reports available from the Kansas Geological Survey (KGS) website recorded lithologies in the Shore Airport Formation. Case #1 displayed incorrect predictions in uncored wells (Figure 19, 20), predicting shale in low gamma-ray zones that are known to be sandstone from the well-site geologist's reports; case #4 and case #2 correctly predict sandstone in these intervals. Case #1 and case #3 were not used to generate lithofacies logs for use in 3D modeling because case #1 made incorrect predictions in uncored wells and case #3 had the lowest statistical success in predictions in the cored wells. Log curves of

predicted lithofacies to be used in 3D modeling were generated using case #2 for wells with a PE log, and case #4 for wells without a PE log.
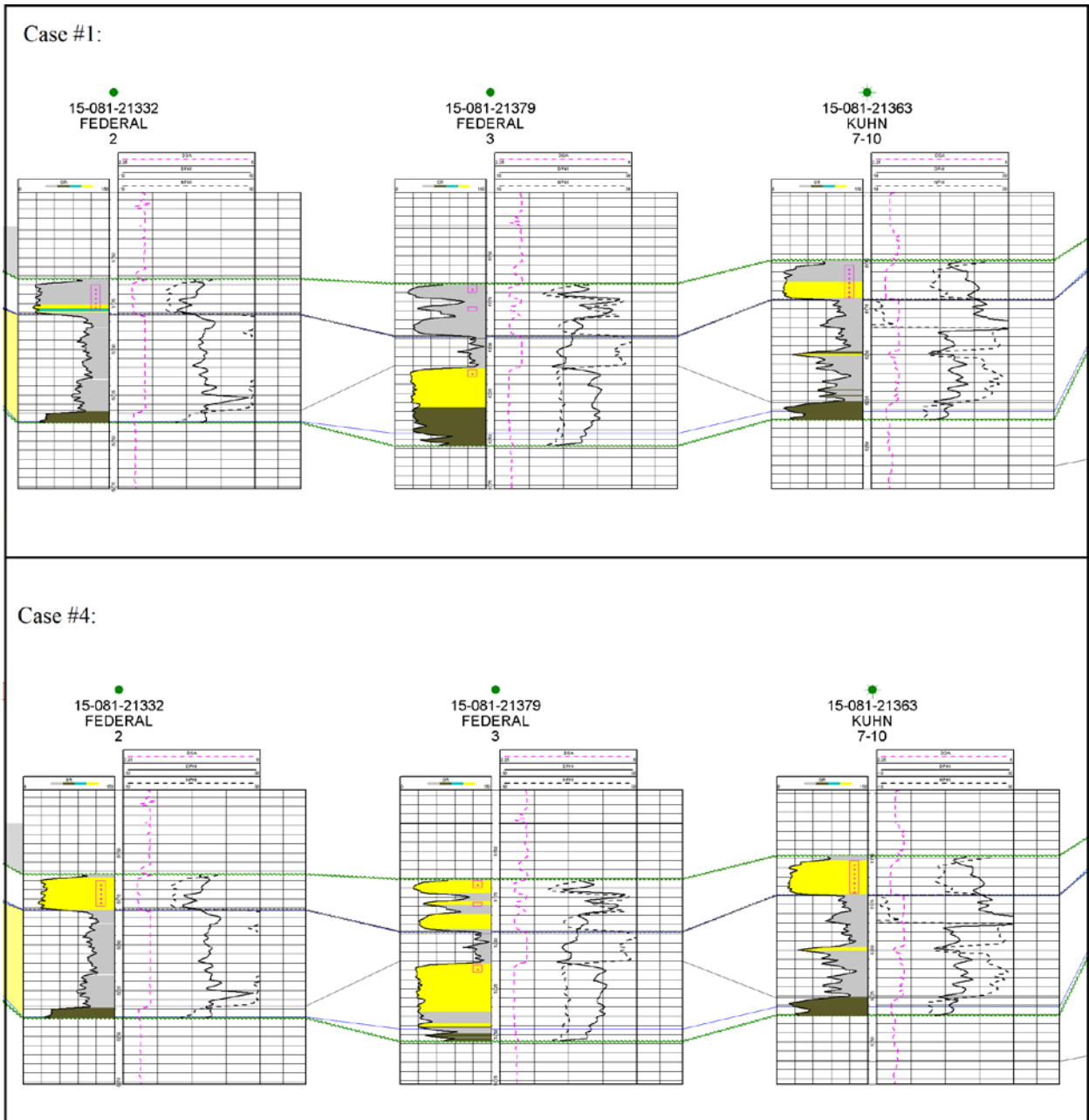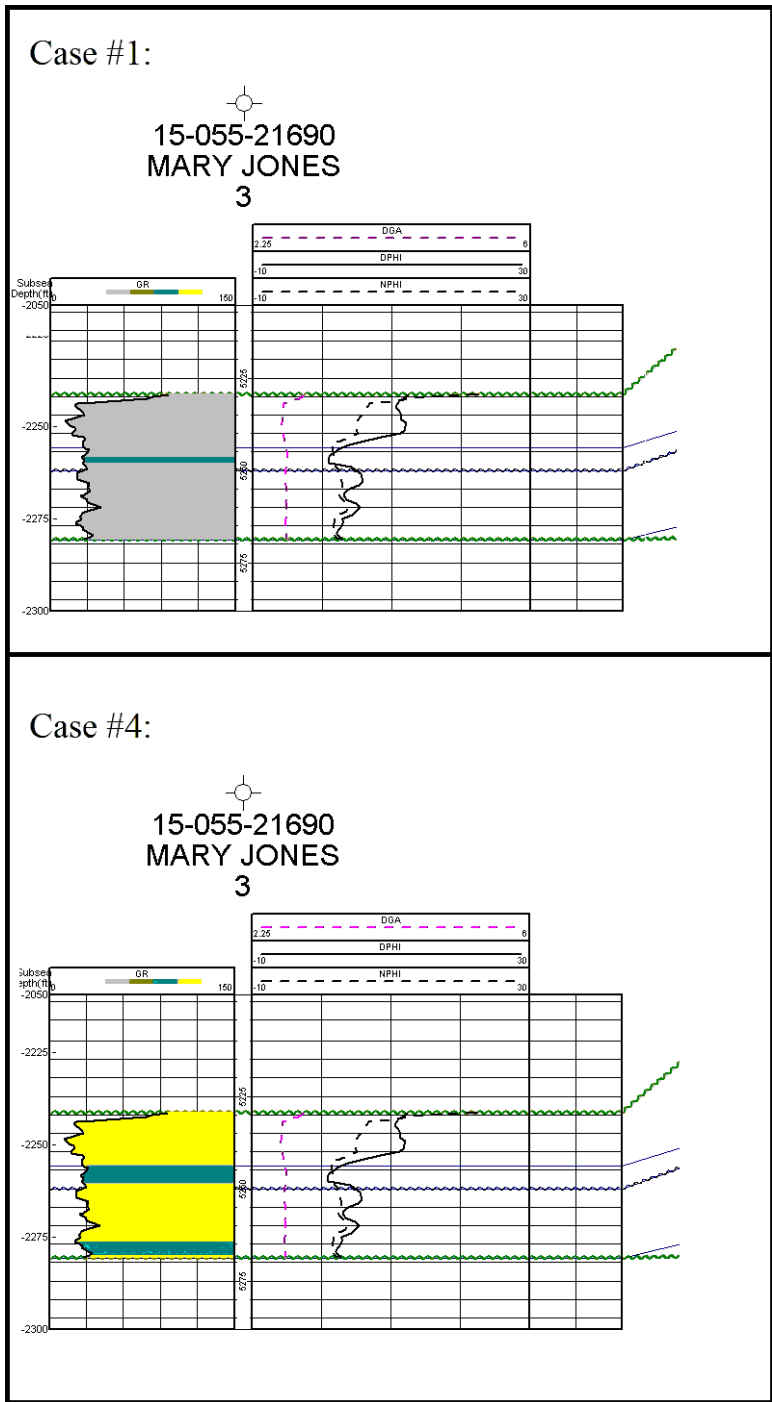
Figure 19: Comparisons of predicted lithofacies in wells for Case #1 and #4. Predicted lithofacies are shown filling the gamma-ray track, and apparent grain density, neutron porosity, and density porosity are in the right track of the logs. Shale is shaded gray, sandstone is yellow, non-basal conglomerate is blue, and basal conglomerate is brown. Case #1 predicts shale in low gamma ray zones that are known from well-site geologist's reports to be sandstone; Case #4 predicts sandstone in these areas. Datum is set at sea level, showing true structural view of correlations, and wells are displayed at even spacing, not reflecting actual well-spacing.

Figure 20: Comparison of predicted lithofacies in Mary Jones #3 well for Case #1 and #4. Predicted lithofacies are shown filling the gamma-ray track, and apparent grain density, neutron porosity, and density porosity are in the right track of the logs. Shale is gray, sandstone is yellow, and conglomerate is blue. Case #1 predicts shale in low gamma ray zones that are known from well-site geologist's report to be sandstone; Case #4 predicts sandstone in these areas. Datum is set at sea level, showing true structural view of correlations.

f. 3D reservoir model

Creation of a 3D cellular model in Petrel was intended to provide a geologically reasonable prediction of the distribution of lithofacies and reservoir properties of porosity, permeability, and fluid saturation. Creation of the model used through several iterations of stochastic modeling processes. Appendix C provides a detailed description of the process of constructing and populating the 3D model with predicted lithofacies, porosity, permeability, and fluid saturation.

Correlation of conglomerates throughout the reservoir on well logs indicated lateral continuity of such layers throughout the length of the reservoir. Therefore, in the modeling process in Petrel variograms, which control the spatial connectivity of lithofacies in the model, reflected the lateral distribution of lithofacies; the elongate shape of the reservoir meant that the major direction of lithofacies variograms was commonly 5–10 times greater than the minor direction (Appendix C, D). In the model the sandstone reservoir lithofacies displayed lateral connectivity between wells and was separated by thin, laterally extensive, non-reservoir conglomerates, giving the reservoir a layered character. A well-to-well cross section of the model showing predicted lithofacies (Figure 21) shows that conglomerate beds are laterally extensive in the north–south direction, but they are not completely continuous across the area. Thus, while the conglomerate beds contribute to reservoir compartmentalization, the model of the reservoir allows the possibility of communication between vertical compartments. The shaly zone in the northern part of the reservoir is illustrated in the model and encloses sand bodies within it, essentially separating the reservoir into three compartments of sandstone: one north of the shaly zone, one in the shaly zone, and the rest of the reservoir to the south of the shaly zone.
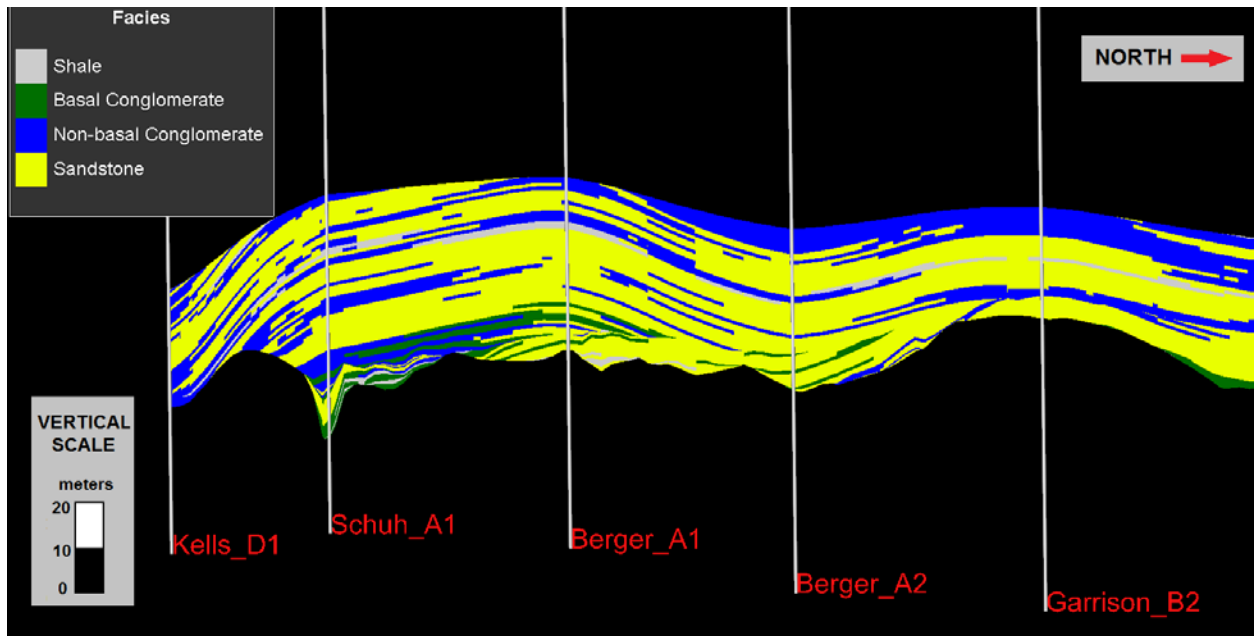
Figure 21: Screenshot of well-to-well cross-section of predicted lithofacies in Petrel model. Wells are vertical lines and are labeled with names at their base; vertical exaggeration is 10x, north is to right. Note lateral discontinuity of some conglomerate beds (e.g., one bed near top of section is present in Schuh A1 and Berger A2 wells, but not in Berger A1). Datum is set at sea level, showing true structural view of correlations, and cross-section shows actual geographic well spacing.

Models of water saturation indicate stock-tank original oil in place (STOOIP) values of 12.1–14.5 million barrels. Current (12/2011) data suggest a cumulative production of over 4.4 million barrels of oil, which calculates to recovery factors of 0.30 to 0.36 of STOOIP relative to model predictions. A recovery factor of around 0.40 of STOOIP can be accomplished by waterflooding some incised-valley-fill sandstone reservoirs (e.g., Montgomery and Morrison, 1999). For this study, the reservoir was divided into drainage polygons corresponding individual producing wells (Figure 22) so that detailed comparison could be made between modeled STOOIP and cumulative production. The comparisons for individual drainage polygons resulted in recovery factors ranging from 0.01 to 1.68 (Table 11; Appendix E), indicating that the models were not as accurate at small scale as at field-wide scale. The drainage polygons may not correspond to actual geological variability in the subsurface, or the populated 3D models may not accurately reflect the actual distribution of lithofacies or petrophysical properties such as porosity or fluid saturations in the reservoir. The patchy and variable nature of cementation noted in sandstone lithofacies in the cores (i.e., cross-bedded sandstone has more cementation than other lithofacies) suggests the possibility that cementation may contribute to reduced reservoir volumes, leading to low recovery factors, such as 0.01, that were estimated in the models. Another possibility is that dead oil zones, such as that noted in the Moody D2 core, exist in the reservoir and contribute to reduced reservoir volumes. In places where the model calculated recovery factors of high proportions, such as 1.68, inaccuracies in the seismic map or well tops on which the model is based may have led to modeled reservoir volumes smaller than what actually exists. Another possibility is that the elongate morphological nature of the reservoir leads to heterogeneities that cause fluids to flow in elongate paths along the incised

valley; in such a situation, the square-shaped drainage polygons used in this study may not be an accurate reflection of the area produced by a single well.
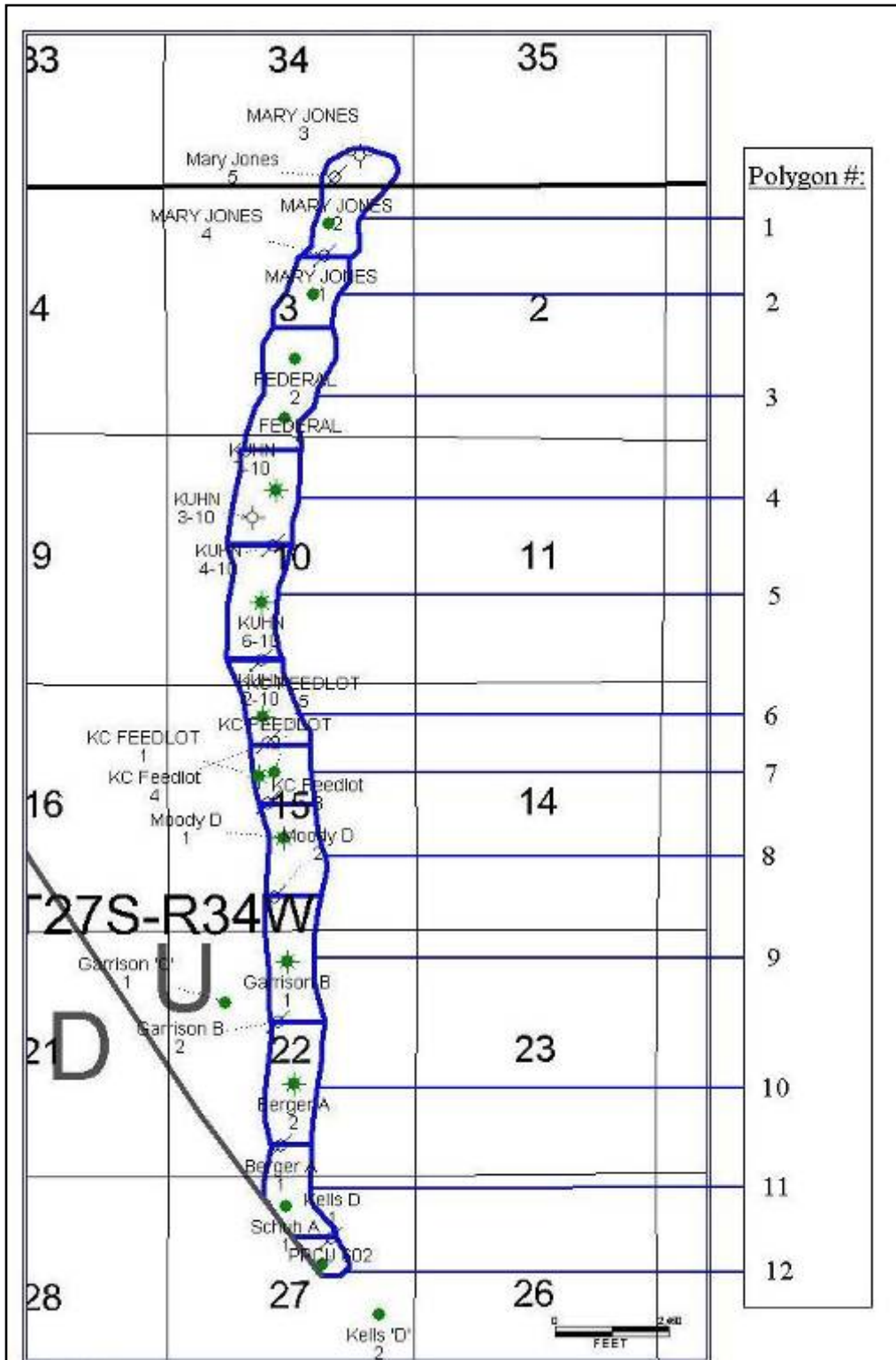
Figure 22: Map of drainage polygons for producing wells, used for comparing STOOIP to cumulative production.

Table 11: Summary of modeled original oil in place (OOIP) in stock-tank barrels (STB), and comparison to cumulative production for Chesterian Shore Airport Formation sandstone reservoir at Pleasant Prairie oilfield. Recovery factor is cumulative production divided by modeled OOIP.

| Polygon # | OOIP 10^3 STB | | Recovery Factor | | |
	Low case	High case	Cum Prod STB	Low Case	High Case
1	1127	1404	208,084	0.15	0.18
2	858	1023	315,436	0.31	0.37
3	796	1000	35,636	0.04	0.04
4	498	587	97,727	0.17	0.20
5	1225	1463	647,476	0.44	0.53
6	736	885	529,194	0.60	0.72
7	437	524	733,671	1.40	1.68
8	1265	1525	679,373	0.45	0.54
9	1479	1765	715,359	0.41	0.48
10	1483	1780	314,764	0.18	0.21
11	1724	2049	119,084	0.06	0.07
12	479	558	4562.5	0.01	0.01
Total	12164	14564	4,400,365	0.30	0.36

Discussion

a. Depositional Environment

Cores from Pleasant Prairie oilfield are interpreted to indicate deposition of the Chesterian Shore Airport Formation in a river-dominated setting. Conglomerate beds interpreted as channel-bottom deposits form the base of stacked fining-upward successions. The successions fine upward from pebble–cobble conglomerates to sublitharenitic to quartzarenitic sandstones, interpreted as the deposits of bar forms in a narrow (0.4 km; 0.25 mile wide) channel. The few fossils found in the cores are associated with conglomerate beds, and may have been derived from older limestone strata, from the walls and floor of the incised valley or from updip exposures. Trace fossils include ripped up, redeposited rhizolith fragments and *Palaeophycus* burrows in the heterolithic lithofacies.

Interpretation of a local depositional environment, such as that present in the incised-valley fill at Pleasant Prairie oilfield, is strongest if considered in the regional geomorphic context. The incised valley at Pleasant Prairie lies at the updip preserved limit of the incised paleovalley trend that extends over 80 km from northern Haskell County, Kansas, south into Oklahoma. This paleovalley trend has been interpreted as a tide-dominated estuarine depositional system (Shonfelt, 1988; Montgomery and Morrison, 1999; Cirilo, 2002). Dalrymple et al. (1992) defined an estuary in the geologic sense as extending from the limit of fluvial depositional influence at the estuary mouth to the limit of tidal depositional influence in the upper reaches of the estuary. The interplay between marine and fluvial depositional processes in estuaries results in a tripartite division of the estuarine system into outer, central, and inner zones in the facies model of Dalrymple et al. (1992); the outer zone is dominated by

marine and tidal processes, the central zone is a relatively low energy zone with mixed marine and fluvial processes, and the inner zone is dominated by fluvial processes.

Sediments strongly influenced by tidal processes record evidence of fluctuations in current intensity or direction on time scales of less than a day. The best single indicator of tidal influence in siliciclastic sediments is cyclicity in sedimentation, such as bundling of sand–mud couplets in cross-bedding structures or in vertically stacked, thinly laminated tidal rhythmites reflecting flood–ebb cycles, and cyclic thick–thin variation in bundle thickness related to diurnal or neap–spring inequalities (Nio and Yang, 1991). Other indicators of tidal influence include reactivation surfaces, flaser, wavy, and lenticular bedding, and herringbone cross-stratification. Studies on the three Chesterian fields south of Pleasant Prairie in the paleovalley have used these types of sedimentary structures to interpret tidal influence (Shonfelt, 1988; Montgomery and Morrison, 1999; Cirilo, 2002).

Near the southernmost part of the paleovalley in Seward County, Kansas, herringbone cross-stratification was identified in the Chesterian sandstone succession (Severy, 1975). Reactivation surfaces, common flaser and lenticular bedding, and possible bidirectional cross-stratification were identified in cores from the Wide Awake oilfield near the southernmost part of the paleovalley (Shonfelt, 1988). Further up the paleovalley, at the Shuck oilfield, reactivation surfaces, common flaser, wavy, and lenticular bedding, and possible bidirectional cross-stratification were identified in cores (Cirilo, 2002). Soft sediment deformation and fluid escape structures at Shuck oilfield were also interpreted to suggest tidal influence (Cirilo, 2002). In cores from South Eubank, the Chesterian sandstone reservoir closest to Pleasant Prairie oilfield, flaser to wavy and convolute bedding, and fluid escape structures were interpreted to suggest a tide-influenced depositional environment (Montgomery and Morrison, 1999). A core from

101

South Eubank was also examined in the course of the present study (MLP Black 4-3, API# 15-081-21068) and found to include possible tidal rhythmites and bidirectional cross-stratification (Figure 23).
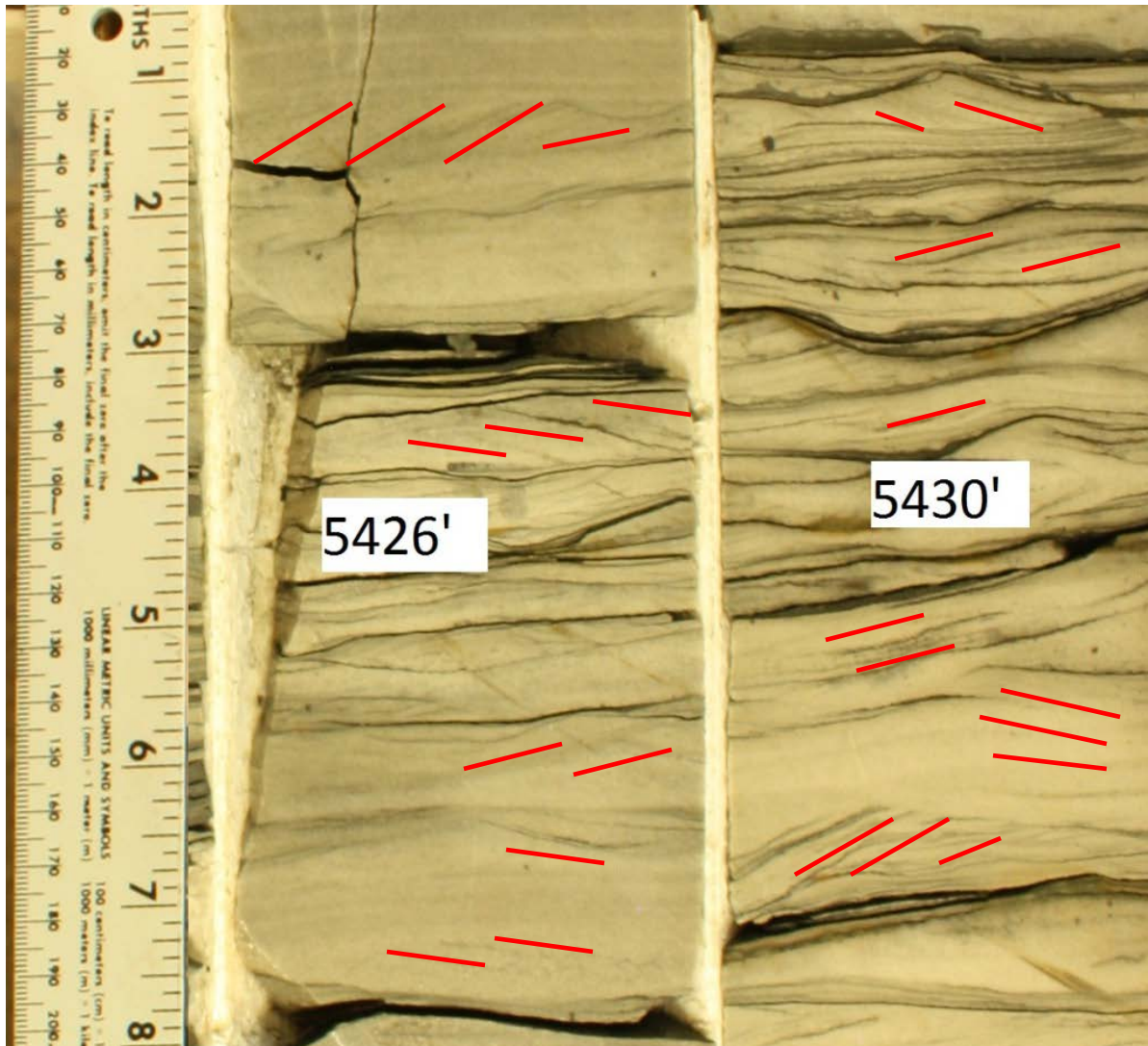
Figure 23: Photograph of MLP Black 4-3 (API# 15-081-21068) core, from the South Eubank oilfield, showing possible bidirectional cross-stratification (red dashes). Ruler for scale at left shows inches (large numbers) and centimeters (small numbers), depths marked on core are feet measured depth.

Carbonate content, including fossils, has also been interpreted as an indicator of tidal or marine influence in the Chesterian sandstones in the paleovalley. For example, at Wide Awake oilfield, near the southern, downdip limit of the paleovalley trend, fossil debris and peloid grains are interpreted to have originated and been deposited contemporaneously with the sand (Shonfelt, 1988). Trace fossils observed in the Shuck oilfield, downvalley from Pleasant Prairie, include *Ophiomorpha, Thalassinoides, Planolites,* and *Terebellina* burrows, which are indicative of marine-influenced environments when found in estuarine settings (e.g., Buatois et al., 2005) and are interpreted as such by Cirilo (2002); in contrast, *Palaeophycus* trace fossils such as those found at Pleasant Prairie may occur in fluvial or estuarine deposits (Buatois et al., 1999).

The sedimentary structures interpreted as indicative of tidal influence in cores from more distal settings in the paleovalley are not present in cores from Pleasant Prairie oilfield. Instead, the mud drapes in the cross-bedded sandstone lithofacies and the flaser to wavy bedding in the heterolithic mudstone–sandstone intervals are the only sedimentary features that might indicate tidal influence. No cyclicity is apparent in the sedimentary structures in the Pleasant Prairie cores. Compared to other downdip oilfields in the paleovalley trend the low abundance of tidal indicators at Pleasant Prairie suggests that tidal influence on sedimentation was minor. Carbonate content in the Pleasant Prairie cores, besides some cement in the sandstones, is limited to clasts of grainstone and calcareous shale in conglomerates and in the pebbly sandstone lithofacies. Minor crinoid debris evident in the uppermost conglomerate beds at Pleasant Prairie could indicate minor tidal influence. In contrast to downdip oilfields where abundant carbonate and fossil content is used to interpret tide-influenced deposition, the lesser amounts of such material at Pleasant Prairie is interpreted to suggest depositional conditions lacking tide influence. Similarly, the trace fossil assemblage observed and interpreted as evidence of a

marine-influenced depositional environment by Cirilo (2002) at the Shuck oilfield is not present

at Pleasant Prairie, where only possible horizontal burrows, consistent with the appearance of

Palaeophycus, were evident in the Moody D2 core (Figure 24). *Palaeophycus* burrows are

documented in depositional environments ranging from fluvial to estuarine to shoreface, and

therefore do not by themselves provide additional insights on depositional environment.

Figure 24: Possible *Palaeophycus* burrows
(arrows) in the Interbedded sandstone and
heterolithic mudstone-sandstone lithofacies,
Moody D2 core.

Taking into account the regional geomorphic context, the differences in sedimentary structures and the contrasting abundance of fossils and carbonate content between Pleasant Prairie oilfield and downdip Chesterian oiflields, the evidence is most consistent with a river-dominated depositional environment at Pleasant Prairie oilfield. The field is situated at the most inland, updip preserved limit of the incised Mississippian paleovalley in southwestern Kansas, which reflecting a river-dominated environment within a larger estuarine system. Other Chesterian cores from more distal portions of the paleovalley (e.g., those described by Shonfelt, 1988; Montgomery and Morrison, 1999; Cirilo, 2002) contain features interpreted as evidence of tidal influence in sedimentary structures, fossils and carbonate content, and trace fossils; such features are lacking in the Pleasant Prairie cores. In sum, the depositional environment at Pleasant Prairie oilfield is interpreted to have been in a range of settings from somewhere in the inner estuary zone (Dalrymple et al. 1992) to a purely fluvial setting beyond the limit of tidal influence (Figure 25).
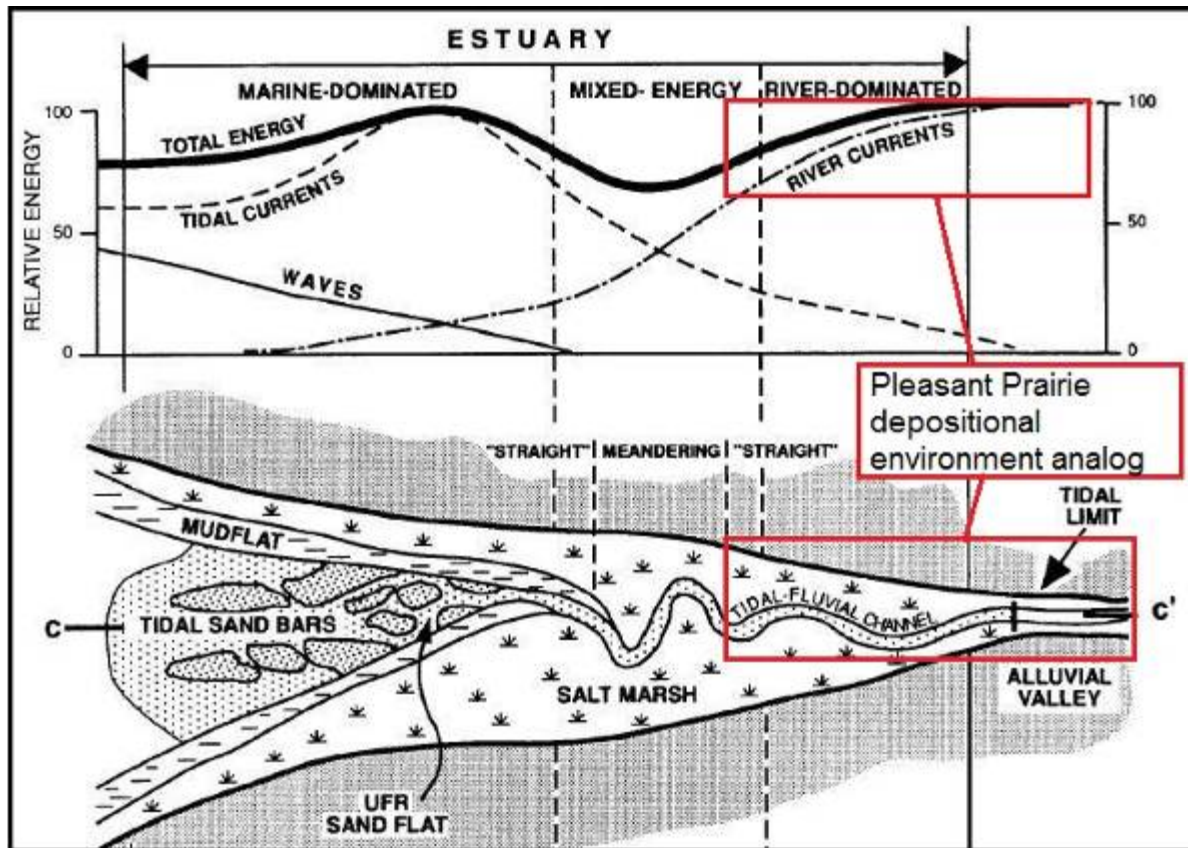
Figure 25: Schematic diagram of a tide-dominated estuary, with suggested location of depositional environment for Pleasant Prairie oilfield indicated by red box. Modified from Dalrymple et al. (1992).

Several depositional processes may explain the shaly zone in the northern part of Pleasant Prairie oilfield, which is not cored. In the context of an estuary, the shaly zone could be a low energy, mid-estuarine zone in a wave-dominated estuary in which muddy sediments accumulated; alternatively, the shaly zone could be interpreted as muddy deposits linked to confluence of smaller tributaries with the channel. Another alternative explanation is that the shaly zone originated as abandoned-channel fill or flood basin deposits more linked to fluvial than to estuarine processes.

The first possibility, a muddy mid-estuary zone, is most likely in a wave-dominated estuary (Dalrymple et al., 1992). If the incised Mississippian paleovalley of southwestern Kansas was a wave-dominated estuary, a muddy zone would be expected. In such an estuary, the facies model of Dalrymple et al. (1992) of a wave-dominated estuary indicates that we should expect to see bayhead deltas and flood tidal deltas (Figure 26), which would occur on opposite sides of a mid-estuary muddy zone. The cores from Pleasant Prairie, however, are from either side of the shaly zone and show the same lithofacies, and conglomerate beds appear to correlate on either side of the zone. Thus, instead of seeing different deposits on either side of the shaly zone that might not be correlated to each other, as would be expected if the shaly zone originated as a low energy mid-estuarine muddy zone, the cores reveal the same deposits on either side.
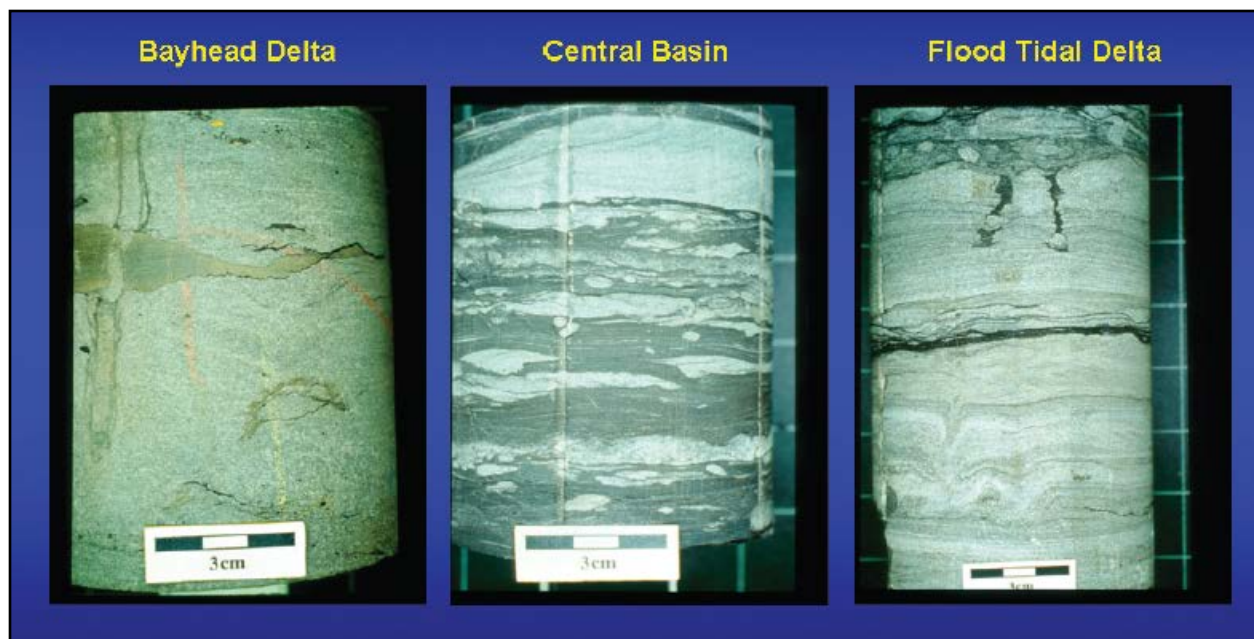
Figure 26: Core photographs illustrating different types of deposits on upstream (bayhead delta) and downstream (flood tidal delta) side of mid-estuarine shaly zone (central basin). From Boyd et al. (2006), after MacEachern and Pemberton (1994).

The proprietary seismic structure contour map of the unconformity between the incised valley deposits and underlying limestones appears to show two tributary streams entering into the main channel cut just upstream of the shaly zone. The tributaries appear as elongate, structurally low features extending off of the main channel cut at nearly perpendicular angles. Confluences of tributaries with main channels are characterized by deep, high energy, mid-channel scour zones with confluence flow-separation bars deposited at channel margins downstream of the scour zone, and by confluence mouth-bars (Figure 27, Bristow et al., 1993). Confluence mouth-bars can build out into the confluence zone, and scour zones are generally areas of higher energy where typical channel bar-forms are not deposited (Bristow et al., 1993). Migration of confluence mouth-bars towards and into scour zones is the likeliest way in which the scour zones are eventually filled with sediment (Bristow et al., 1993). The position of the tributaries on the seismic structure map indicates that a confluence scour zone would be likely to develop where the shaly zone is. Scour zones are high energy environments, and the accumulation of a thick shaly zone in such a setting is unlikely.
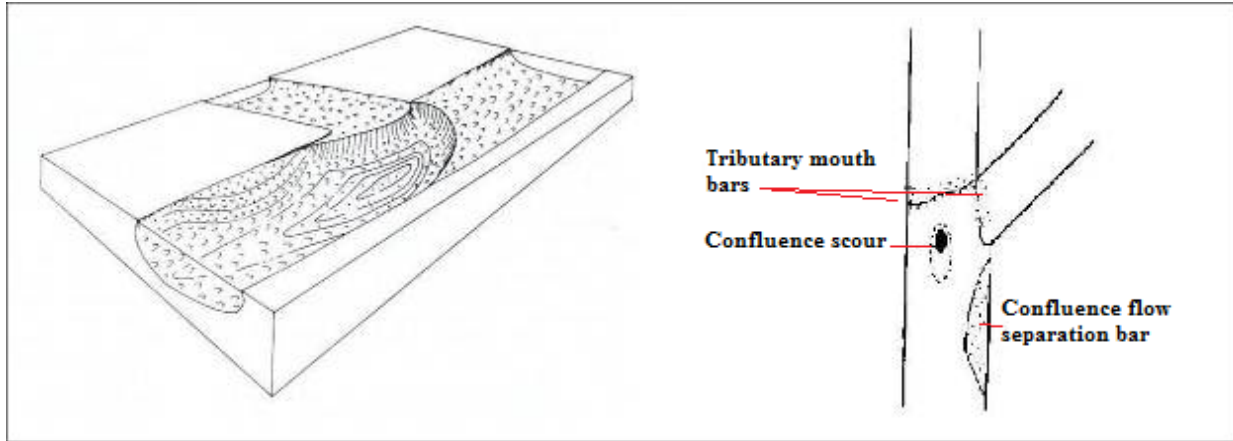
Figure 27: Schematic diagrams of asymmetric confluence zone. Modified from Bristow et al. (1993).

If, however, the shaly zone had been deposited prior to evolution of the confluence zone, a confluence scour zone associated with the tributaries interpreted on the seismic structure map would have cut into the shaly zone. Later migration of confluence mouth-bars may have filled the confluence scour zone and resulted in the observed sharp basal contact of the sandstone overlying the shale (e.g., Figure 16). A scour surface underlying an extensive conglomerate bed and marking the base of a fining-upward succession correlates in well logs to the top of the shaly zone, suggesting that the top of the shaly zone is indeed a scour surface. A confluence scour zone would also explain the notable lack of conglomerate beds overlying the shaly zone; deposition of the typical conglomerate-based fining-upward successions would not occur in a confluence scour zone.

Shaly zones such as the one at Pleasant Prairie oilfield have been documented in other fluvio-estuarine incised valley settings. For example, Blakeney et al. (1990) describe overbank floodplain deposits consisting of siltstone and mudstone with thin interbeds of sandstone in Lower Pennsylvanian Morrowan incised-valley fill deposits of the Stateline Trend in eastern Colorado and western Kansas. A possible explanation of the origin of such fine-grained overbank deposits (Figure 28; Gibling, 2005) illustrates the preservation of floodplain deposits within an incised valley in the modern-day Gangetic Plains of India. Aggradation of fine-grained floodplain sediments may occur outside of a main channel within the incised valley, and after a rise in base level, those sediments may be preserved as the valley continues to fill. Although the drainage system of the Ganges river is much larger than that of the incised Mississippian paleovalley of southwestern Kansas, the example serves as a conceptual illustration of how a body of fine-grained sediment may be preserved within an incised valley. Another example of a shaly zone in the Stateline Trend incised-valley-fill sandstones is noted by

113

Blakeney et al. (1990), who note the presence of an intra-channel shaly zone that contributes to a significant permeability barrier separating two reservoirs. Bowen and Weimer (2003) also note zones of fine-grained, shaly sediment in the dominantly fluvial, updip portions of Morrowan incised-valley-fills. Bowen and Weimer (2003) interpret the shaly zones as abandoned channel-fill and floodplain deposits (Figure 29). The shaly zone at Pleasant Prairie oilfield is not interpreted as a mid-estuarine low energy zone, nor is it interpreted to have formed in association with stream confluences. Instead, in light of the observations and the presence of similar shaly zones in dominantly fluvial incised-valley settings, the shaly zone at Pleasant Prairie oilfield is interpreted as an abandoned channel-fill or floodplain deposit.
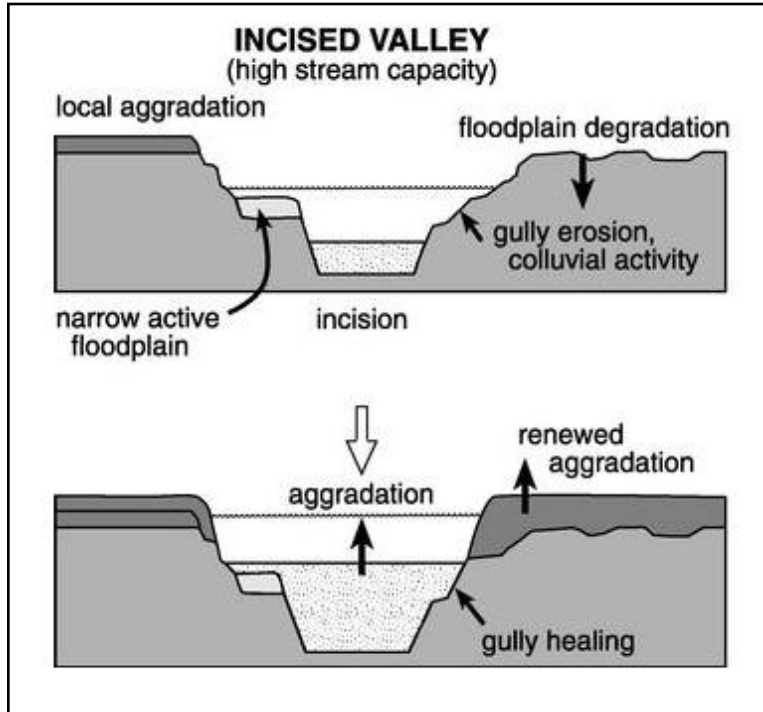
Figure 28: Example of preservation of floodplain deposits within an incised valley from the modern-day Ganges river plain of India. From Gibling, (2005).
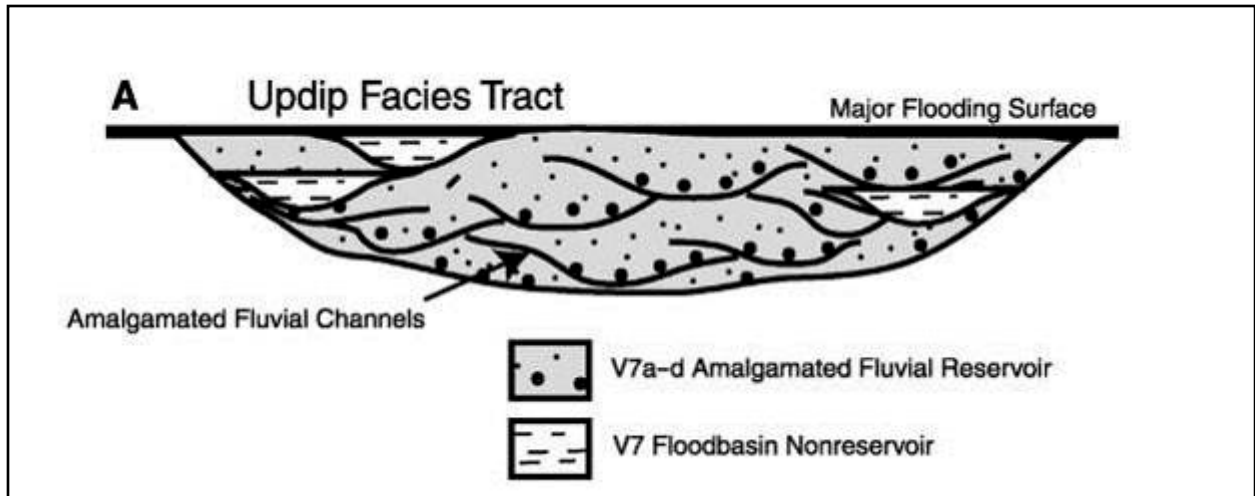
Figure 29: Example of preservation of abandoned channel or floodplain deposits within an incised valley from the Lower Pennsylvanian Morrowan sandstones of Colorado. From Bowen and Weimer, (2003).

b. Reservoir Properties

Core-derived porosity and permeability values for all lithofacies reveal several trends (Table 12). Core analysis data indicates an arithmetic mean porosity of 11.94% for all reservoir sandstone lithofacies, with a range of 0.90–20.10%. Core analysis data indicates geometric mean permeability for the reservoir sandstone lithofacies of 39.82 md, with a median of 109.5 md and a range of 0.01–629 md. Of the individual core-defined sandstone lithofacies, the weakly stratified sandstone has the highest core-derived arithmetic average porosity and median permeability, at 11.42% and 170 md, respectively, whereas the highest geometric mean permeability is 83.37 md in the pebbly sandstone lithofacies.

Average core porosity and permeability are 9.11% and 2.54 md, respectively, for the heterolithic lithofacies and 5.14% and 13.92 md, respectively, for conglomerates. The heterolithic lithofacies has maximum core porosity and permeability of 13.2% and 10 md, respectively, and the conglomerate lithofacies have maximum core porosity and permeability of 10.6% and 72 md.

For all of the non-reservoir lithofacies together (conglomerates and interbedded quartzarenite and heterolithic mudstone–sandstone), core analysis data indicates an arithmetic mean porosity of 5.63 %, with a range of 15–13.2%. Geometric mean permeability for the non-reservoir lithofacies is 0.30 md, with a median of 0.32 md and a range of 0.01–72 md. The non-reservoir lithofacies with the highest core-derived arithmetic average porosity is the interbedded quartzarenite and heterolithic mudstone–sandstone, at 9.11%, whereas the highest geometric mean and median permeabilities are in the basal conglomerate lithofacies at 1.32 and 1.67 md, respectively. The core-derived porosity and permeability data do indicate some potential for reservoir-quality rock in the conglomerates, such as where porosity exceeds 6% (this was used in

Petrel as a cutoff for volumetric modeling) and permeability exceeds 1 md, but any volumetric contribution to the reservoir by conglomerates is small. Only 11 out of 37 core samples meet these criteria.

Table 12: Core-derived porosity and permeability by lithofacies.

Lithofacies	Arithmetic Avg Φ (%)	Geometric Avg k (md)	Median k (md)	Range Φ (%)	Range k (md)
All conglomerate	4.82	0.22	0.15	1.5 - 10.6	0.01 – 72
Basal conglomerate only	7.91	1.32	1.67	7.5 - 10.6	0.06 - 32.5
Non-basal conglomerate only	3.60	0.12	0.06	1.50 - 7.40	0.01 – 72
Pebbly sandstone	10.03	83.37	128	2.2 - 13	0.224 - 418
Weakly stratified sandstone	11.42	38.76	170	1.6 - 20.10	0.03 – 629
Laminated sandstone	13.22	49.62	111.5	0.90 - 17.9	0.01 – 535
Cross-bedded sandstone	10.47	13.08	14.85	1.80 - 15-10	0.04 – 316
Heterolithic mudstone-sandstone	9.11	1.23	0.90	5.5 - 13.2	0.334 - 10.0

Well-log correlation indicates that the conglomerate beds are laterally extensive, generally low-porosity layers that may vertically compartmentalize the reservoir. The 3D Petrel model of the reservoir, however, indicates that the conglomerate beds may not be completely continuous between all wells in the oilfield (e.g., Figure 21). Hence, some communication may exist between vertical compartments of the reservoir.

In contrast, lateral compartmentalization of the reservoir by the thick shaly zone in the northern part of the oilfield is consistent with available production data. Wells to the north and south of the shaly zone respond to water injection differently, producing about one order of magnitude more fluid daily than wells within the shaly zone. The significant difference in volume of daily fluid production indicates that the shaly zone is a closed compartment that effectively separates parts of the reservoir to its north and south.

The dead oil zones are in the weakly stratified sandstone lithofacies in the Moody D2 core and do not appear to contribute to compartmentalization of the reservoir. The superimposed deep and medium resistivity logs indicated the presence of the dead oil zones in the Moody D2 well, but attempts to trace the zones based on resistivity-log response were unsuccessful. The zones are at core depth ranges of approximately 5132–5140 and 5161–5177 feet. The upper dead oil zone is directly above a non-reservoir conglomerate layer and the lower zone is directly above the non-reservoir heterolithic and basal conglomerate. Although minor oil staining occurs directly below the lower dead oil zone, neither of the zones vertically separates reservoir compartments.

c. Comparison to Morrowan Sandstones

Lower Pennsylvanian Morrowan Formation sandstones of eastern Colorado and western Kansas form prolific oil and gas reservoirs and originated in incised valley systems similar to the incised Mississippian paleovalley of southwestern Kansas (e.g., Bowen and Weimer, 2003). The similar nature of the two depositional systems suggests that some Morrowan reservoirs could be analogous to the Chesterian sandstone reservoir at Pleasant Prairie oilfield. Similar depositional environments may have led to similarities in reservoir properties such as vertical and lateral distribution of lithofacies, and compartmentalization. Knowledge and experience of maximizing recovery of reserves from Morrowan reservoirs may be applicable to Pleasant Prairie oilfield and other Chesterian reservoirs in the incised Mississippian paleovalley of southwestern Kansas, and vice versa.

One example of a Morrowan reservoir similar to Pleasant Prairie is the Mount Pearl oilfield in eastern Colorado. Krystinik and Blakeney (1990) interpret the Morrowan sandstone at Mount Pearl oilfield as a series of stacked fluvial point-bar deposits, and the reservoir shows a similar pattern of stacked fining-upward successions as seen at Pleasant Prairie oilfield (Figure 30). Another Morrowan reservoir similar to Pleasant Prairie is the Stockholm SW oilfield, which is one of a series of oilfields near the Colorado–Kansas border collectively termed the Stateline Trend. Brown et al. (1990) describe stacked successions of point-bars and massive sandstone with quartz as the most prevalent cement, and interpret a high energy fluvial depositional environment at the Stockholm SW oilfield; the sandstone lacks bioturbation and displays fining-upward trends from gravelly to medium or coarse sand.

Stateline Trend reservoirs display compartmentalization similar to Pleasant Prairie oilfield. A thick intra-channel shale body separates the reservoir at Stockholm SW from the

downdip Second Wind oilfield. Similarly, at Pleasant Prairie oilfield a thick shale body separates

isolates reservoir compartments to its north and south. Vertical compartmentalization along

scour surfaces occurs in Stateline Trend reservoirs (Blakeney et al., 1990) and, similarly, at

Pleasant Prairie oilfield the same phenomenon occurs where low porosity conglomerate beds
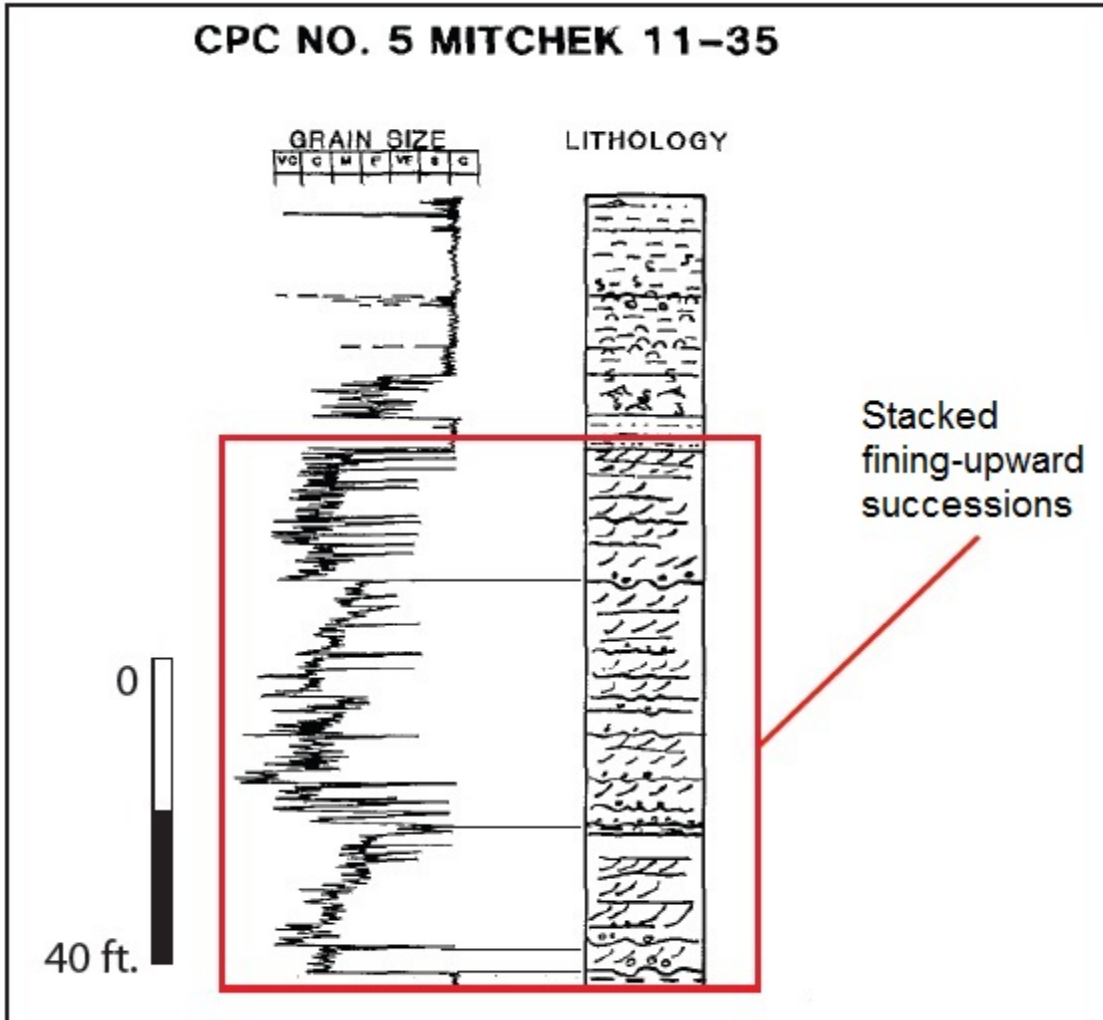
overlie scour surfaces.

Figure 30: Grain size and lithology profile from cored well in Mount Pearl oilfield, a fluvial-dominated Morrowan sandstone reservior in Colorado showing stacked fining-upward successions of fluvial point bar deposits. Modified from Krystinik and Blakeney, (1990).

123

While some similarities exist between Morrowan reservoirs and Pleasant Prairie, differences also exist. Some Morrowan sandstone reservoirs display higher porosity and permeability values than the Chesterian sandstone at Pleasant Prairie (Table 13). Other differences include the generally coarser grain size of Morrowan sandstones and the fact that conglomeratic zones have dissimilar compositions and do not always represent barriers to fluid flow. Rader (1990) notes that conglomeratic zones in Morrowan sandstones can have good porosity and permeability, and cores studied by Bowen and Weimer (2003) show good porosity across such zones. Conglomerates in Morrowan sandstones can also have different types of clasts than those in the Chesterian conglomerates at Pleasant Prairie oilfield. Clasts of limestone and quartz sandstone are most prevalent in the cores from Pleasant Prairie oilfield, with minor amounts of chert. In Morrowan cores, clay-pebble conglomerates with mud matrix (Al-Shaieb et al., 1995), and shale-pebble conglomerates with sandy matrix (Orchard and Kidwell, 1983) have been described; pebble to cobble-size clasts of granitic rock can also occur (J. Youle, personal communication, 2011). Wheeler et al. (1990) classify some Morrowan sandstones as subarkosic due to the presence of feldspar grains, and Rader (1990) notes the presence of volcanic rock fragments in some Morrowan sandstones. No feldspar grains or volcanic rock fragments were observed in the Pleasant Prairie cores.

Such compositional differences may be a reflection of dissimilar substrates of the Morrowan and Mississippian incised paleovalleys, and dissimilar provenances for the Chesterian and Morrowan sandstones. Morrowan valley-fill deposits are commonly incised into underlying marine shale (Krystinik and Blakeney, 1990; Bowen and Weimer, 2003), whereas the Chesterian sandstone at Pleasant Prairie is underlain by limestone. The different substrates of the incised paleovalleys may explain why conglomerates in Morrowan sandstones commonly contain clay

124

and shale pebbles, and the Chesterian sandstones contain abundant limestone clasts. The

Chesterian sandstone is derived primarily from the Central Kansas uplift and Transcontinental

arch to the north, with some input from subjacent arenaceous carbonate (Cirilo, 2002), whereas

igneous rocks of the Ancestral Front Range and Sierra Grande–Apishapa uplift in Colorado

contributed to the Morrowan sandstones (Rader, 1990; Sonnenberg et al., 1990). These different

source areas may help explain why Morrowan sandstones can be more arkosic and contain

granitic clasts.

Table 13: Comparison of core porosity and permeability data from Morrowan sandstones with Chesterian sandstone at Pleasant Prairie oilfield.

	Data Source:	Porosity %	Permeability md
Morrowan Sandstones	Bowen and Weimer, 2003 – Fluvial, Colorado and Kansas	18-28	500-2000
	Bowen and Weimer, 2003 – Estuarine, Colorado and Kansas	8-18	10-500
	Bowen et al., 1990 – Sorrento-Mt. Pearl Field Complex, Colorado	avg. 19	avg 1000
	Brown et al., 1990 – Stockholm SW oifield, Colorado	10-26	200-4600
	Blakeney et al., 1990 – Stateline Trend, Colorado and Kansas	avg. 17	0.5-2000
	Krystinik and Blakeney, 1990 – Fluvial, Colorado and Kansas		up to 20000
	Krystinik and Blakeney, 1990 – Estuarine, Colorado and Kansas		100-200
	Chesterian, Pleasant Prairie oilfield cores	0.90-20.10	0.01-629
	Chesterian, Pleasant Prairie oilfield cores	arith. mean 10	geom. mean 11.48

d. EOR Potential

Volumetric calculations on the 3D reservoir model in Petrel give a range of STOOIP of

12.1–14.6 million barrels, and recovery factor based on cumulative production for the field

ranges from 0.30–0.36 of STOOIP. Such recovery factors seem reasonable for a mature

waterflood in an incised-valley-fill sandstone reservoir (Montgomery and Morrison, 1999), and

the remaining oil in place could present a viable economic target for enhanced oil recovery

operations such as chemical or CO_2 flooding. An incremental recovery of 5–10% of STOOIP

from such an operation could yield an additional 605,000–1.5 million barrels, based on

volumetrics from the Petrel model.

Volumetrics from the 3D reservoir model for drainage polygons of individual producing

wells indicate recovery factors ranging from 0.01 to 1.68 of STOOIP. Some of these recovery

factors are unreasonable (e.g., a recovery factor of 1.68 means a well has produced 1.68 times as

much oil as the model indicates was originally in place), and may reflect actual internal reservoir

heterogeneities not accurately recreated by the Petrel model. Incised-valley-fill reservoirs can be

internally complex and heterogeneous, and such complexity can lead to difficulty in accurate

reservoir modeling. The 3D reservoir model created in Petrel for this study gives reasonable

volumetric calculations at the field-wide scale, but not at the scale of individual wells. Appendix

E contains tables of data on modeled volumetrics and cumulative oil production.

In addition to volumetrics of the 3D reservoir model, a review of production data and

projections for the future of the current waterflood are beneficial to assessing the future

management of the reservoir. Annual oil production peaked in 2000 at 671,567 barrels (KGS

website) and has declined steadily since 2004 (Figure 31). The steady decline in production

since 2004 allows a simplistic decline curve analysis to be performed that gives some idea of the

remaining effective lifespan of the current waterflood. Currently, the reservoir is configured

with 15 producing wells and 8 injectors. Using an arbitrary economic production cutoff of 1

barrel of oil per day (BOPD) yields an annual total of 5475 barrels:

Equation 6:   1 BOPD x 15 wells x 365 days/yr = 5475 bbls, annually

Projecting the current trend of decline shows that this arbitrary economic limit will be reached in

2018 (Figure 32). Projected incremental production from the end of 2011 through 2018 using

the decline curve analysis is 141,809 barrels of oil. The estimated time remaining of economic

production could be impacted by a number of factors, including the addition of new wells to

exploit the reservoir, or changing economic conditions, but the simplistic decline curve analysis

presented here illustrates that the time is approaching for the operators to decide whether or not

to pursue future exploitation of the reservoir through further enhanced oil recovery operations.

The reservoir is well-defined spatially; the 3D seismic survey of the area reveals the

elongate, channel morphology of the incised paleovalley. The well-defined spatial extent of the

reservoir is a positive attribute when considering the Chesterian sandstone at Pleasant Prairie

oilfield as a candidate for enhanced oil recovery operations. If the boundaries were nebulous, the

likelihood of success would be lower due to an increased possibility of injected CO_2 or

chemicals not staying in the reservoir. Wells are present at regular spacing throughout the

reservoir, and this good well control means that the effectiveness of chemical or CO_2 flooding

could be monitored closely. Successful implementation of waterflooding and the fact that the

reservoir is well explored are other indicators of potential success of an enhanced oil recovery

project. If waterflooding had been ineffective in the reservoir, then injection of CO_2 or surfactants may not be likely to significantly enhance oil production either.

The reservoir is currently split into northern and southern leases operated by different companies and is continuous across the lease boundary, therefore CO_2 or chemical flooding in one lease could impact production in both leases. Both operators should be involved in any enhanced oil recovery project. The Chesterian sandstone reservoir at Pleasant Prairie oilfield merits serious consideration as a candidate for an enhanced oil recovery project because it is well defined spatially, has good well control throughout, and has demonstrated good response to waterflooding.
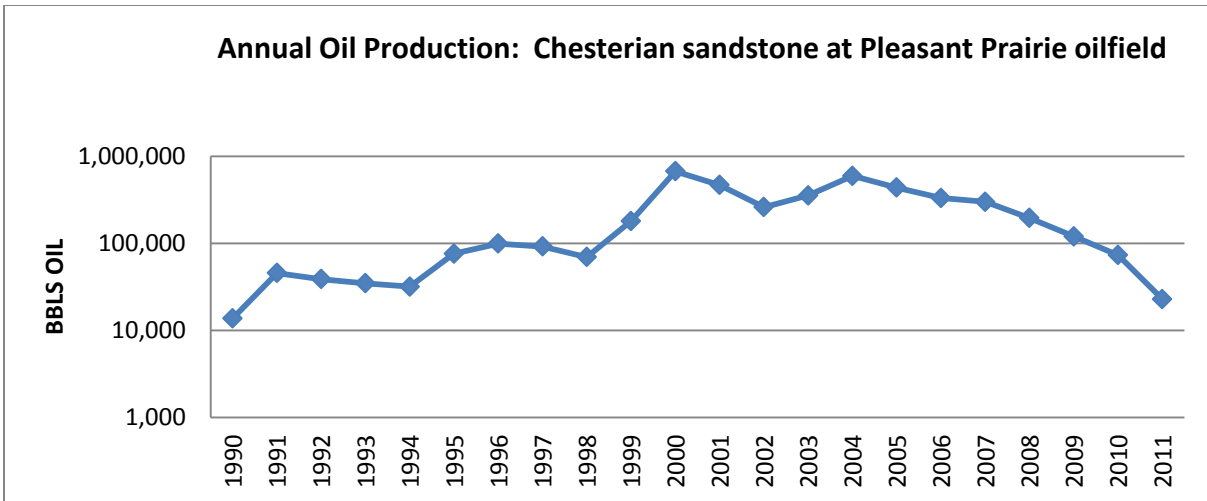
Figure 31: Annual oil production graph for Chesterian sandstone reservoir at Pleasant Prairie oilfield; production data were compiled from KGS website and data provided by field operators.
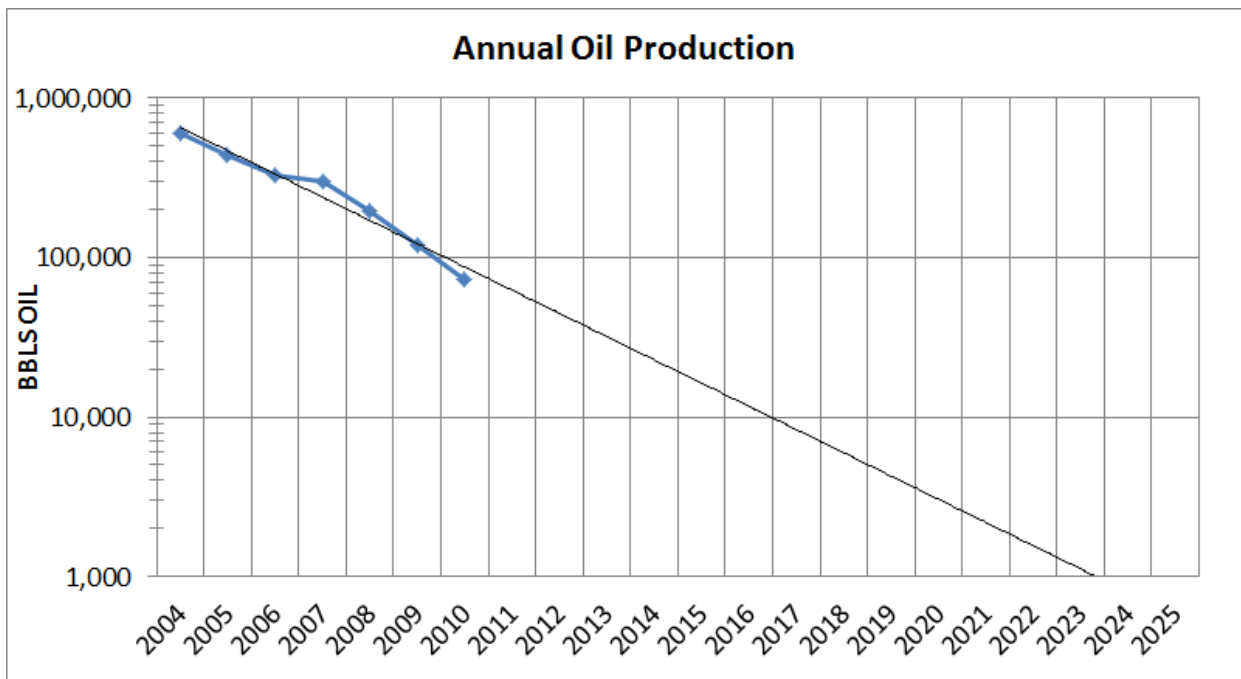
Figure 32: Simple decline curve analysis graph for Chesterian sandstone reservoir at Pleasant Prairie oilfield; production data were compiled from KGS website and data provided by field operators.

Conclusions

The Chesterian Shore Airport Formation at Pleasant Prairie oilfield is a siliciclastic succession that was deposited in a river-dominated environment in the upper reaches of a tide-dominated estuary. The siliciclastic succession was deposited in an incised valley approximately 0.4 km wide by 6 km long as revealed by 3D seismic mapping, and is part of a larger paleovalley trend extending over 80 km south to Oklahoma. The relative position of Pleasant Prairie oilfield, further inland and updip from tide-influenced deposits indicates that reduced tidal influence would be expected compared to those tide-influenced deposits further down the paleovalley. Lithofacies described from two cores in the oilfield are interpreted as bar-form or channel-bottom deposits. Sedimentary structures indicative of tidal sedimentation are notably absent in the Pleasant Prairie cores. Carbonate content, including fossils, in the Chesterian sandstone at Pleasant Prairie is much less than in fields further down the paleovalley, interpreted as indicating reduced marine influence compared to more distal parts of the paleovalley.

The reservoir at Pleasant Prairie oilfield is compartmentalized vertically and laterally. Thin, extensive beds of conglomerate are traceable on well logs throughout the field; they are low porosity, non-reservoir intervals that vertically separate thicker layers of porous reservoir sandstone. The reservoir is separated into three lateral compartments by a thick shaly zone in the northern part of the field. Production data indicates that wells within the shaly zone are not in communication with the rest of the field. The shaly zone likely originated as an abandoned channel or floodplain deposit within the incised valley. Modeling of the reservoir using Petrel suggests that the conglomerate beds may not be completely continuous in inter-well space, meaning that vertically stacked bodies of reservoir sandstone may not be completely isolated.

131

Volumetric calculation of STOOIP in the reservoir model in Petrel indicates 12.1–14.6 million barrels of oil originally in place. Cumulative production through 12/2011 of over 4.4 million barrels gives a recovery factor of 0.30–0.36 of STOOIP, a range of estimates consistent with expected recovery for a mature waterflood in an incised-valley-fill sandstone reservoir. Volumetric calculations of STOOIP in the reservoir model in Petrel at the scale of individual producing wells were not as accurate as at the field-wide scale. Internal reservoir heterogeneities not accurately predicted in the reservoir model, such as widespread cementation or dead oil zones may have led to such inaccuracies. Alternatively, the anomalously low or high recovery factors (e.g., 0.01 or 1.68) may indicate that fluid flow is along preferential pathways that do not correspond to the square drainage polygons used in this study. Simple decline-curve analysis shows that the current waterflood may become uneconomic in as little as 6 years. Projected oil production through the next six years (2012–2018) with the current waterflood is 141,809 barrels. The reservoir is a candidate for further enhanced oil recovery, and should be evaluated thoroughly by the operators; incremental production of 5–10% STOOIP through enhanced oil recovery operations would yield an additional 605,000–1.5 million barrels according to the reservoir model.

Incised-valley-fill reservoirs can be internally complex and are important targets for hydrocarbon exploration and exploitation worldwide. Such reservoirs should be the subjects of further study to gain more insight into internal heterogeneities, so that more accurate models can be made which might assist in more efficient recovery of hydrocarbon resources. Other incised-valley-fill reservoirs, such as some Morrowan reservoirs in Colorado and Kansas, originated in settings similar to the Pleasant Prairie oilfield and display similar reservoir properties to those observed in this study and may also be candidates for future enhanced oil recovery operations.

References:

Abegg, F. E., 1994A, Lithostratigraphy of the Shore Airport Formation (Chesterian), in southwestern Kansas: *in*, Baars, D. L., (compiler); Revision of stratigraphic nomenclature in Kansas: Kansas Geological Survey, Bulletin, no. 230, p. 21-38.

Abegg, F. E., 1994B, Lithostratigraphy of the Hugoton and Stevens members of the St. Louis Limestone and the Ste. Genevieve Limestone (Upper Mississippian), southwestern Kansas: *in*, Baars, D. L., (compiler); Revision of stratigraphic nomenclature in Kansas: Kansas Geological Survey, Bulletin, no. 230, p. 39-66.

Allen, J. R. L., 1980, Sand waves: A model of origin and internal structure: Sedimentary Geology, v. 26, p. 281-328.

Al-Shaieb, Z., Puckette. J., and Abdalla, A., 1995, Influence of sea-level fluctuation on reservoir quality of the Upper Morrowan sandstones, northwestern shelf of the Anadarko Basin: *in* Sequence Stratigraphy of the Mid-continent, Tulsa Geological Society, p. 249-268.

Archie, G. E., 1942, The electrical resistivity log as an aid in determining some reservoir characteristics: Petroleum Transactions of the American Institute of Mining, Metallurgical and Petroluem Engineers (AIME), v. 146, p. 54–62.

Bhattacharya, A., 1997, On the origin of non-tidal flaser bedding in point bar deposits of the river Ajay, Bihar and West Bengal, NE India: Sedimentology, v. 44, p. 973-975.

Blakeney, B. A.,Krystinik, L. F., and Downey, A. A., 1990,Reservoir heterogeneity in Morrow
valley fills, Stateline Trend – Implications for reservoir management and field expansion:
in, Sonnenberg, S. A., Shannon, L. T., Rader, K., von Drehle, W. F., and Martin, G. W.,
(editors) Morrow sandstones of southeast Colorado and adjacent areas: Rocky Mountain
Association of Geologists, p. 131-142.

Bohling G. C., and Doveton, J. H., 2000, Kipling.xla: An Excel add-in for nonparametric
regression and classification, Kansas Geological Survey: http://www.kgs.ku.edu/softwar
e/Kipling/Kipling1.html (accessed January 3, 2012).

Bowen, D. W., and Weimer, P., 2003, Regional sequence stratigraphic setting and reservoir
geology of Morrow incised-valley sandstones (lower Pennsylvanian), eastern Colorado
and western Kansas: AAPG Bulletin, vol. 87, p. 781-815.

Boyd, R., Dalrymple, R. W., and Zaitlin, B. A., 2006, Estuarine and incised-valley facies
models: *in* Posamentier, H. W., and Walker, R. W., (editors), Facies Models Revisited:
SEPM Special Publication 84, p. 171-236.

Bristow, C. S., Best, J. L., and Roy, A. G., 1993, Morphology and facies models of channel
confluences: *in* Marzo, M., and Puigdefabregas, C., (editors), Alluvial Sedimentation:
Special Publication Number 17 of the International Association of Sedimentologists, p.
91-100.

Brown, L. G., Miller, W. A., Hudley-Goff, E. M., and Veal, S. L., 1990, Stockholm southwest
field: *in,* Sonnenberg, S. A., Shannon, L. T., Rader, K., von Drehle, W. F., and Martin,
G. W., (editors) Morrow sandstones of southeast Colorado and adjacent areas: Rocky
Mountain Association of Geologists, p. 117-130.

Buatois, L. A., Mangano, M. G. and Carr, T. R. 1999. Sedimentology and ichnology of
Paleozoic estuarine and shoreface reservoirs, Morrow Sandstone, Lower Pennsylvanian of
Southwest Kansas, USA: Current Research in Earth Sciences, Kansas Geological Survey
Bulletin, no. 243, 35 p.

Buatois, L. A., Gingras, M. K., MacEachern, J., Mangano, M. G., Zonneveld, J., Pemberton, S.
G., Netto, R. G., and Martin, A., 2005, Colonization of brackish-water systems through
time: Evidence from the trace-fossil record: Palaios, v. 20, p. 321-347.

Cirilo, L. L., 2002, Transgressive estuarine fill of an incised paleovalley, Upper Mississippian
Chesterian Series, Shuck field area, Seward County, Kansas: Unpublished .M.S. thesis,
University of Houston, Houston, TX, 194 p.

Dalrymple, R. W., Zaitlin, B. A., and Boyd, R., 1992, Estuarine facies models: Conceptual basis
and stratigraphic implications: Journal of Sedimentary Petrology, v. 62, p. 1130-1146.

Davis, D. H., 1954, Estimating porosity of sedimentary rocks from bulk density: The Journal of
Geology, v. 62, p. 102-107.

Doveton, J., 1999, Integrated petrophysical methods for the analysis of reservoir
microarchitecture—a Kansas Chester sandstone case study: *in* Merriam, D. F., (editor)
Transactions of the 1999 AAPG Midcontinent Section Meeting (Geoscience for the 21st
Century), p. 91-101.

Dubois, M. K., Byrnes, A. P., Bohling, G. C., and Doveton, J. H., 2006, Multiscale geologic and petrophysical modeling of the giant Hugoton gas field (Permian), Kansas and Oklahoma, U.S.A., *in* Harris, P. M. and Weber, L. J., (editors), Giant hydrocarbon reservoirs of the world: From rocks to reservoir characterization and modeling: AAPG Memoir 88/SEPM Special Publication, p. 307– 353.

Everitt, B. S., Landau, S., and Leese, M., 2001, Cluster Analysis, 4th Edition: New York, Oxford University Press, 237 p.

Fugitt, L. B., and Wilkinson, R. D., 1959, Eubank Field: *in* Kansas Oil and Gas Fields, Vol. 2, Kansas Geological Society, p. 13-20.

Gibling, M. R., Tandon, S. K., Sinha, R., and Jain, M., 2005, Discontinuity-bounded alluvial sequences of the southern Gangetic Plains, India: Aggradation and degradation in response to monsoonal strength: Journal of Sedimentary Research, v. 75, p. 369-385.

Goebel, E. D., 1968, Mississippian rocks of western Kansas: AAPG Bulletin, vol. 52, p. 1732-1778.

Hartman, D. J., and Coalson, E. B., 1990, Evaluation of the Morrow sandstone in Sorrento Field, Cheyenne County, Colorado: *in,* Sonnenberg, S. A., Shannon, L. T., Rader, K., von Drehle, W. F., and Martin, G. W., (editors) Morrow sandstones of southeast Colorado and adjacent areas: Rocky Mountain Association of Geologists, p. 91-100.

Goebel, E. D., and Stewart, G. F., 1979, Kansas: *in,* Craig, C. L. and Connor, C. W., (coordinators) Paleotectonic investigations of the Mississippian System in the United States: U.S. Geological Survey, Professional Paper 1010, p. 115-123.

Johnson, K. S., 1989, Geologic evolution of the Anadarko Basin: *in*, Johnson, K. S., (editor);

      Anadarko Basin Symposium: Oklahoma Geological Survey, Circular 90, p. 3-12.

Jorgensen, D. G., 1989, Paleohydrology of the Anadarko Basin, Central United States: *in*,

      Johnson, K. S., (editor); Anadarko Basin Symposium: Oklahoma Geological Survey,

      Circular 90, p. 176-193.

Kansas Geological Survey (KGS) website: http://www.kgs.ku.edu

Krystinik, L. F., and Blakeney, B. A., 1990, Sedimentology of the upper Morrow formation in

      eastern Colorado and western Colorado: *in,* Sonnenberg, S. A., Shannon, L. T., Rader,

      K., von Drehle, W. F., and Martin, G. W., (editors) Morrow sandstones of southeast

      Colorado and adjacent areas: Rocky Mountain Association of Geologists, p. 37-50.

Kvale, E. P., and Vondra, C. F., 1993, Effects of relative sea-level changes and local tectonics on

      a Lower Cretaceous fluvial to transitional marine sequence, Bighorn Basin, Wyoming,

      USA: *in* Marzo, M., and Puigdefabregas, C., (editors), Alluvial Sedimentation: Special

      Publication Number 17 of the International Association of Sedimentologists, p. 383-400.

Leverett, M. C., 1941, Capillary behavior in porous solids: Transactions of the American

      Institute of Mining, Metallurgical and Petroluem Engineers (AIME), v. 142, p. 152-169.

MacEachern, J. A., and Pemberton, S. G., 1994, Ichnological aspects of incised valley fill

      systems from the Viking Formation of the Western Canada Sedimentary Basin, Alberta,

      Canada: *in* Dalrymple, R. W., Boyd, R., Zaitlin, B. A., and Scholle, P. A., (editors),

      Incised-valley Systems: Origin and Sedimentary Sequences, SEPM Special Publication

      51, p. 129-158.

Maples, C. G., 1994, Revision of Mississippian stratigraphic nomenclature in Kansas, *in* Baars, D.L., (compiler), Revision of stratigraphic nomenclature in Kansas: Kansas Geological Survey, Bulletin 230, p. 67-74.

Martin, A. J., 2000, Flaser and wavy bedding in ephemeral streams: a modern and an ancient example: Sedimentary Geology, v. 136, p. 1-5.

Merriam, D. F., 1963, The Geologic History of Kansas: Kansas Geological Survey, Bulletin 162, 307 p.

Montgomery, S. L., and Morrison, E., 1999, South Eubank Field, Haskell County, Kansas: A case of field redevelopment using subsurface mapping and 3-D seismic data: AAPG Bulletin, v. 83, p. 393-409.

Nio, S. D., and Yang, C. S., 1991, Diagnostic attributes of clastic tidal deposits: a review *in* Smith, D. G., Reinson, G. E., Zaitlin, B. A., and Rahmani, R. A., (editors), Clastic Tidal Sedimentology: Canadian Society of Petroleum Geologists, Memoir 16, p. 3-27.

Orchard, D. M., and Kidwell, M. R., 1983, Morrowan stratigraphy, depositional systems, and hydrocarbon accumulation, Sorrento field, Cheyenne County, Colorado, ABSTRACT: AAPG Bulletin, v. 67, p. 1326.

Perry, W. J., Jr., 1989, Tectonic evolution of the Anadarko Basin region, Oklahoma: U.S. Geological Survey, Bulletin 1866-a, 19p. 1989**.**

Qi, L., Carr, T. R., and Goldstein, R. H., 2007, Geostatistical three-dimensional modeling of oolite shoals, St. Louis Limestone, southwest Kansas: AAPG Bulletin, v. 91, p. 69-96.

Rader, K., 1990, Petrography of Morrow sandstones in southeast Colorado, southwest Kansas, and northwest Oklahoma: *in,* Sonnenberg, S. A., Shannon, L. T., Rader, K., von Drehle, W. F., and Martin, G. W., (editors) Morrow sandstones of southeast Colorado and adjacent areas: Rocky Mountain Association of Geologists, p. 51-58.

Rascoe, B., Jr., and Adler, F. J., 1983, Permo-Carboniferous hydrocarbon accumulations, Mid-Continent, U.S.A.: AAPG Bulletin, v. 67, p. 979-1001.

Rollins, J. B., Holdtich, S. A., and Lee, W. J., 1992, Characterizing average permeability in oil and gas formations: SPE Formation Evaluation, p. 99-105.

Ross, C. A., and Ross, J. R. P., 1985, Late Paleozoic depositional sequences are synchronous and worldwide: Geology v. 13, p. 194-197.

Rygel, M. C., Fielding, C. R., Frank, T. D., and Birgenheier, L. P., 2008, The magnitude of late Paleozoic glacioeustatic fluctuations: A synthesis: Journal of Sedimentary Research, v. 78, p. 500-511.

Sawin, R. S., Franseen, E. K., Watney, W. L., West, R. R., and Ludvigson, G. A., 2009, New stratigraphic rank for the Carboniferous, Mississippian, and Pennsylvanian in Kansas: Kansas Geological Survey, Current Research in Earth Sciences, Bulletin 256, pt. 1, p. 1-4.

Severy, C. L., 1975, Subsurface Stratigraphy of the Chesterian Series, Southwest Kansas**:** Unpublished M.S. thesis, University of Colorado, Boulder, CO, 61 p.

Shonfelt, J. P., 1988, Geologic heterogeneities of a Chesterian sandstone reservoir, Kinney-
Lower Chester field, Stevens and Seward counties, Kansas, and their affect on
hydrocarbon production: Unpublished M.S. thesis, Wichita State University, Wichita,
KS, 206 p.

Smith L. B., and Read, J. F., 2000, rapid onset of late Paleozoic glaciation on Gondwana:
Evidence from Upper Mississippian strata of the Midcontinent, U.S.A.: Geology, v. 28,
p. 279-282.

Sonnenberg, S. A., Shannon, L. T., Rader, K., and von Drehle, W. F., 1990, Regional structure
and stratigraphy of the Morrowan Series, Southeast Colorado and adjacent areas: *in,*
Sonnenberg, S. A., Shannon, L. T., Rader, K., von Drehle, W. F., and Martin, G. W.,
(editors) Morrow sandstones of southeast Colorado and adjacent areas: Rocky Mountain
Association of Geologists, p. 1-8.

Sorenson, R. P., Kelly, S. P., and Cantwell, D., 1999, Tar mat formation within the Hitch oil
field, Seward County, Kansas: *in* Merriam, D. F., (editor) Transactions of the 1999
AAPG Midcontinent Section Meeting (Geoscience for the 21st Century), p. 156-165.

Van Wagoner, J. C., Mitchum, R. M., Campion, K. M., and Rahmanian, V. D., 1990, Siliciclastic
sequence stratigraphy in well logs, cores, and outcrops: concepts for high-resolution
correlation of time and facies: AAPG Methods in Exploration Series 7, 55 p.

Warren, J. E., Skiba, F. F., and Price, H. S., 1961, An evaluation of the significance of
permeability measurements: Journal of Petroleum Technology, v.12, p. 739-744.

Wheeler, D. M., Scott, A. J., Coringrato, V. J., and Devine, P. E., 1990, Stratigraphy and
depositional history of the Morrow Formation, Southeast Colorado and Southwest
Kansas: *in,* Sonnenberg, S. A., Shannon, L. T., Rader, K., von Drehle, W. F., and Martin,
G. W., (editors) Morrow sandstones of southeast Colorado and adjacent areas: Rocky
Mountain Association of Geologists, p. 9-36.

Zaitlin, B. A., Dalrymple, R. W., and Boyd, R., 1994, The stratigraphic organization of incised-
valley systems associated with relative sea-level change: *in* Dalrymple, R. W., Boyd, R.,
Zaitlin, B. A., and Scholle, P. A., (editors), Incised-valley Systems: Origin and
Sedimentary Sequences, SEPM Special Publication 51, p. 45-60.

APPENDIX A: CORE DESCRIPTIONS

LEGEND

LITHOLOGY

SANDSTONE

CONGLOMERATE

LIMESTONE

SEDIMENTARY STRUCTURES & LITHOLOGIC FEATURES

LAMINATION

CROSS-BEDDING

FLASER TO WAVY BEDDING

BLACK CARBONACEOUS DEBRIS

MUD STREAK

STYLOLITE

CHERT NODULE

CONTACTS

UNCONFORMITY

GRADATIONAL CONTACT

ABRUPT CONTACT

SCOURED CONTACT

FOSSILS

BONE FRAGMENT

BRACHIOPOD

BURROW

HORN CORAL

ECHINOID FRAGMENT
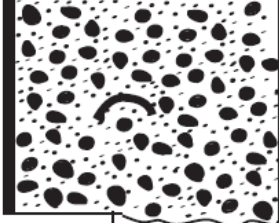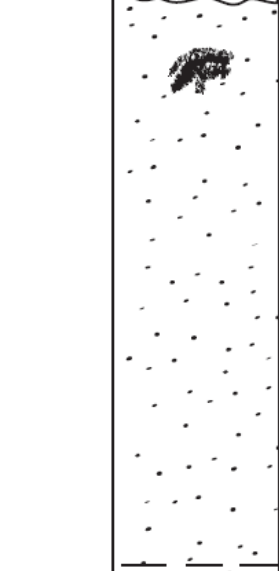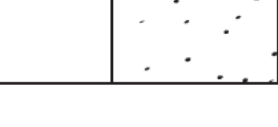
WISPY PLANT FRAGMENTS

ROOT TRACE

WOOD FRAGMENT

NAME: MARY JONES #2	INTERVAL: 5157-5181 ft.	PAGE: 1 of 4
LOCATION: NW SE NW NE Sec. , T27S R34W		BOXES: 1-10 of 34
COMPANY: CIMAREX ENERGY CO.	DESCRIBED BY: PETER SENIOR	DATE: Jan. 2011

Column headers: DEPTH (FT. / M) | TEXTURE & SORTING: (GN, PK, WK, MUDST; GRAVEL, COARSE, MEDIUM, FINE, SILT, CLAY; V WELL, WELL, MOD, POOR) | LITHOLOGY | SEDIMENTARY STRUCTURES | FOSSILS | BOX # | DESCRIPTION (Lithology, Color, Roundness) | INTERPRETATION

Box 1-2 (5157-5161.6')

5157-5161.6' Conglomerate
Yellowish gray Qtz. sand matrix., rounded to well rounded. Subangular to well rounded, coarse sand to cobble sized grainstone & mudstone intraclasts. Calcite cemented. Scoured basal contact.

Interpretation:
Conglomerate
Lag deposit in the deeper part of channels, possibly in the thalweg.

Box 3-7 (5161.6-5173.8')

5161.6-5173.8' Weakly stratified sandstone
Pale yellowish brown to dark yellowish brown, subrounded to well rounded. Patchy non-oil stained areas white to light gray colored and tightly calcite-cemented. Laminated at top but otherwise structureless. Wispy fragments of plant material are visible in places, especially calcite cemented areas, with some long axes aligned by deposition giving a crude stratified appearance. Gradational basal contact.

Interpretation:
Weakly stratified sandstone
Possibly ripples or dunes; lower flow regime. Mid-upper bar deposits.

Box 8-10 (5173.8-5186')

5173.8-5186' Laminated sandstone
Pale yellowish brown to dark yellowish brown, subrounded to well rounded. Patchy non-oil stained areas white to light gray colored tightly calcite or silica cemented. Abrupt basal contact.

Interpretation:
Laminated sandstone
Ripples; lower flow regime. Upper bar deposits.

			NAME: MARY JONES #2			INTERVAL: 5181-5205 ft.		PAGE: 2 of 4

NAME: MARY JONES #2	INTERVAL: 5181-5205 ft.	PAGE: 2 of 4
LOCATION: NW SE NW NE Sec. , T27S R34W		BOXES: 11-20 of 34
COMPANY: CIMAREX ENERGY CO.	DESCRIBED BY: PETER SENIOR	DATE: Jan. 2011

DEPTH — 1573

TEXTURE & SORTING:
GN | PK | WK | MUDST
GRAVEL | COARSE | MEDIUM | FINE | SILT | CLAY
V WELL | WELL | MOD | POOR

FT. | M

LITHOLOGY — SEDIMENTARY STRUCTURES — FOSSILS — BOX #

DESCRIPTION
Lithology
Color
Roundness

INTERPRETATION

Box 11

5173.8-5186' Laminated sandstone
Pale yellowish brown to dark yellowish brown, subrounded to well rounded. Patchy non-oil stained areas white to light gray colored tightly calcite or silica cemented. Abrupt basal contact.

Laminated sandstone
Ripples; lower flow regime. Upper bar deposits.

Box 12, 13, 14, 15

5186-5192' Conglomerate
Qtz. sand matrix, pale yellowish brown to moderate yellowish brown in basal 1.5' due to oil stain, white to v. light gray above, rounded to well rounded. Coarse sand to cobble size, subangular to rounded grainstone and mudstone intraclasts. Cross-bedding developed in sand rich zone at 5189 with intraclasts oriented along bedding. Calcite cemented. Abrupt basal contact.

Conglomerate
Lag deposit in the deeper part of channels, possibly in the thalweg.

Box 16, 17, 18, 19, 20

5192-5210.5' Laminated sandstone
Dk yellowish orange and grayish orange, dusky brown. Heavy oil staining obscures sedimentary structures in places. Patchy non-oil stained areas white to light gray colored tightly silica cemented. Very fine to fine grained, subangular to well rounded. Gradational basal contact.

Laminated sandstone
Ripples; lower flow regime. Upper bar deposits.

Depth markers (ft): 5185, 5190, 5195, 5200
Depth markers (M): 1580, 1581, 1582, 1583, 1584, 1585, 1586

145

NAME: MARY JONES #2

INTERVAL: 5205-5229 ft.

LOCATION: NW SE NW NE Sec. , T27S R34W

COMPANY: CIMAREX ENERGY CO.

DESCRIBED BY: PETER SENIOR

DEPTH	TEXTURE & SORTING:	LITHOLOGY	SEDIMENTARY STRUCTURES	FOSSILS	BOX #	DESCRIPTION Lithology Color Roundness	INTERPRETATION

Box 20-21:

5192-5210.5' Laminated sandstone
Dk yellowish orange and grayish orange, dusky brown. Heavy oil staining obscures sedimentary structures in places. Patchy non-oil stained areas white to light gray colored tightly silica cemented. Very fine to fine grained, subangular to well rounded. Gradational basal contact.

Laminated sandstone
Ripples; lower flow regime. Upper bar deposits.

Box 22-24:

5210.5-5212.5 Conglomerate
Very light gray Qtz. sand matrix, subrounded to well rounded. Subangular to rounded coarse sand to cobble size clasts of grainstone and crystalline carbonate. Sand-filled root fragment traces, abraded marine fossil fragments. Calcite cemented. Gradational basal contact.

Conglomerate
Lag deposit in the deeper part of channels, possibly in the thalweg.

Box 25-29:

5212.5-5231.5' Cross-bedded sandstone
Dk yellowish orange and grayish orange, dusky brown, subangular to well rounded. Heavy oil staining obscures sedimentary structures in places. Patchy non-oil stained areas white to light gray colored tightly calcite or silica cemented. Localized well-developed cross-bedding at 5215' and 5223.5'. Streaks of mud and black carbonaceous debris abundant from 5212.5-15' and again from 5224.5-30.5'. Gradational basal contact.

Cross-bedded sandstone
Dunes; lower flow regime. Mid-lower bar deposits. Trough cross-beds and plant material suggestive of proximal, fluvial type of setting. Mud streaks could indicate minor tidal influence.

NAME: MARY JONES #2	INTERVAL: 5229-5243 ft.	PAGE: 4 of 4
LOCATION: NW SE NW NE Sec. , T27S R34W		BOXES: 30-34 of 34
COMPANY: CIMAREX ENERGY CO.	DESCRIBED BY: PETER SENIOR	DATE: Jan. 2011

DESCRIPTION
Lithology
Color
Roundness

INTERPRETATION

5212.5-5231.5' Cross-bedded sandstone
Dk yellowish orange and grayish orange, dusky brown, subangular to well rounded. Heavy oil staining obscures sedimentary structures in places. Patchy non-oil stained areas white to light gray colored tightly calcite or silica cemented. Localized well-developed cross-bedding at 5215' and 5223.5'. Streaks of mud and black carbonaceous debris abundant from 5212.5-15' and again from 5224.5-30.5'. Gradational basal contact.

Cross-bedded sandstone
Dunes; lower flow regime. Mid-lower bar deposits. Trough cross-beds and plant material suggestive of proximal, fluvial type of setting. Mud streaks could indicate minor tidal influence.

5231.5-5239.5 Conglomerate
Light gray to medium light gray, well rounded Qtz. sand matrix. Subangular to well rounded coarse sand to cobble size intraclasts of mudstone, chert, and grainstone. Few streaks of black carbonaceous debris. Calcite cemented. Scoured basal contact.

Conglomerate
Lag deposit in the deeper part of channels, possibly in the thalweg.

5239.5-5243 Limestone
Very light gray to light gray, stylolitic throughout. Coated grain & skeletal fragment grainstone grading downward after ~1 ft. to peloidal packstone-wackestone.

Limestone
Carbonate deposition in shallow marine environment.

147

NAME: MOODY 'D' #2	INTERVAL: 5112-5136 ft.	PAGE: 1 of 3
LOCATION: NE SE SW Sec. 15, T27S R34W		BOXES: 1-3 of 8
COMPANY: OXY USA INC.	DESCRIBED BY: PETER SENIOR	DATE: Jan. 2011

Column headers: DEPTH (FT. / M), TEXTURE & SORTING (GN, PK, WK, MUDST; GRAVEL, COARSE, MEDIUM, FINE, SILT, CLAY; V WELL, WELL, MOD, POOR), LITHOLOGY, SEDIMENTARY STRUCTURES, FOSSILS, BOX #, DESCRIPTION (Lithology, Color, Roundness), INTERPRETATION

DESCRIPTION

5112-5112.5' Conglomerate
Yellowish gray Qtz. sand matrix, rounded to well rounded. Subangular to well rounded, very coarse sand to cobble size grainstone & mudstone clasts. Calcite cemented. Scoured basal contact.

5112.5-5116.9' Pebbly Sandstone
Moderate to dk. yellowish brown, rounded to well rounded. Streaks of coarse sand to pebble size, subangular to well rounded calcareous mudstone intraclasts oriented along bedding. Abrupt basal contact.

5116.9-5117.9' Conglomerate
Yellowish gray Qtz. sand matrix, rounded to well rounded. Coarse sand to pebble size, subangular to well rounded mudstone intraclasts. Calcite cemented. Scoured basal contact.

5117.9-5124' Pebbly Sandstone
Pale yellowish brown base (0.5 ft.) then mod. to dk. yellowish brown, to dusky yellow, rounded to well rounded. Coarse sand to pebble size, subangular to well rounded calcareous mudstone intraclasts. Clasts are not as commonly aligned to bedding as above. Few streaks of mud and black carbonaceous debris throughout. Abrupt basal contact.

5124-5140' Weakly stratified Sandstone
Moderate yellowish to dk. yellowish brown to dusky yellowish brown upper ~8 ft.; med. dk. gray to dk gray to grayish black, pale yellowish brown lower ~8 ft. Subangular to well rounded. Few coarse sand to granule size calcareous mudstone intraclasts in lower ~6ft. Has some well developed cross-lamination in places, other faintly developed cross-stratification. Dead oil zone in lower ~8ft. Abrupt basal contact.

INTERPRETATION

Conglomerate
Lag deposit in the deeper part of channels, possibly in the thalweg.

Pebbly sandstone
Dunes, clasts indicate moderate to high flow velocity; lower flow regime. Mid-lower bar deposits.

Conglomerate
Lag deposit in the deeper part of channels, possibly in the thalweg.

Pebbly sandstone
Dunes, clasts indicate moderate to high flow velocity; lower flow regime. Mid-lower bar deposits.

Weakly stratified sandstone
Possibly ripples or dunes; lower flow regime. Mid-upper bar deposits.

148

DESCRIPTION
Lithology
Color
Roundness

Box 3

5124-5140' Weakly stratified Sandstone
Moderate yellowish to dk. yellowish brown to dusky yellowish brown upper ~8 ft.; med. dk. gray to dk gray to grayish black, pale yellowish brown lower ~8 ft. Subangular to well rounded. Few coarse sand to granule size calcareous mudstone intraclasts in lower ~6ft. Has some well developed cross-lamination in places, other faintly developed cross-stratification. Dead oil zone in lower ~8ft. Abrupt basal contact.

5140-5145' Conglomerate
Qtz. sand matrix, white to very light gray in lower 3 feet, and yellowish gray from oil staining in upper 2 feet, rounded to well rounded throughout. Coarse sand to cobble size, subangular to well rounded grainstone and mudstone clasts. Calcite cemented. Scoured basal contact.

5145-5163' Laminated Sandstone
Moderate to dark yellowish brown, rounded to well rounded. Well developed low angle cross-lamination abundant throughout. Dead oil zone in lower ~2 ft. Basal contact unknown (missing core).

INTERPRETATION

Weakly stratified sandstone
Possibly ripples or dunes; lower flow regime. Mid-upper bar deposits.

Conglomerate
Lag deposit in the deeper part of channels, possibly in the thalweg.

Laminated sandstone
Ripples; lower flow regime. Upper bar deposits.

NAME: MOODY 'D' #2	INTERVAL: 5160-5196 ft.	PAGE: 3 of 3
LOCATION: NE SE SW Sec. 15, T27S R34W		BOXES: 5-8 of 8
COMPANY: OXY USA INC.	DESCRIBED BY: PETER SENIOR	DATE: Jan. 2011

DEPTH		TEXTURE & SORTING:									LITHOLOGY	SEDIMENTARY STRUCTURES	FOSSILS	BOX #	DESCRIPTION Lithology Color Roundness	INTERPRETATION

TEXTURE & SORTING header: GN, PK, WK, MUDST; GRAVEL, COARSE, MEDIUM, FINE, SILT, CLAY; V WELL, WELL, MOD, POOR. DEPTH in FT. and M.

5145-5163' Laminated Sandstone
Moderate to dark yellowish brown, rounded to well rounded. Dead oil zone in lower ~2 ft. Basal contact unknown (missing core).

Laminated sandstone
Ripples; lower flow regime. Upper bar deposits.

Box # 5. Depth 5161 / 1573.

5163-5172' Missing Core

5172-5177' Weakly stratified Sandstone
Light olive gray to dusky yellowish brown, rounded to well rounded. Subparallel streaks of black carbonaceous debris throughout. Dead oil zone. Calcareous mudstone intraclasts, streaks of mud and black carbonaceous debris in base. Abrupt basal contact.

Weakly stratified sandstone
Possibly ripples or dunes; lower flow regime. Mid-upper bar deposits.

Box # 6. Depth 5175 / 1577, 1578.

5177-5183' Interbedded Sandstone & Heterolithic Sandstone-mudstone
Heterolithic sandstone-mudstone consists of white to lt. gray fine sand, subangular to well rounded, interbedded with streaks of med. dk. gray mud. Heterolithic intervals flaser to wavy bedded, with abundant microfaulting in upper 1 foot, and contain few horizontal unwalled burrows. Fine sandstone oil-stained to dusky yellowish brown color at 5180.1-5180.75. Abrupt basal contact.

Interbedded Sandstone & Heterolithic Sandstone-mudstone
Ripples, silt-mud content indicates low flow velocities. Waning flow of flood on top of bar.

Box # 7. Depth 5180 / 1579, 1580.

5183-5186.8' Conglomerate
White to very light gray, to dusky yellowish brown. Qtz. sand matrix subrounded to well rounded. Coarse sand to cobble size, subangular to well rounded Chert, mudstone, and Qtz. sandstone intraclasts. Calcite and silica cemented. Scoured basal contact.

Conglomerate
Lag deposit in the deeper part of channels, possibly in the thalweg.

Depth 5185 / 1581.

5186.8-5196' Limestone
very light gray, skeletal fragment wackestone-packstone, stylolitic throughout, chert nodules up to 4 cm diameter common below 5190'.

Limestone
Carbonate deposition in shallow marine environment.

Box # 8. Depth 5190 / 1582, 1583. 5195.
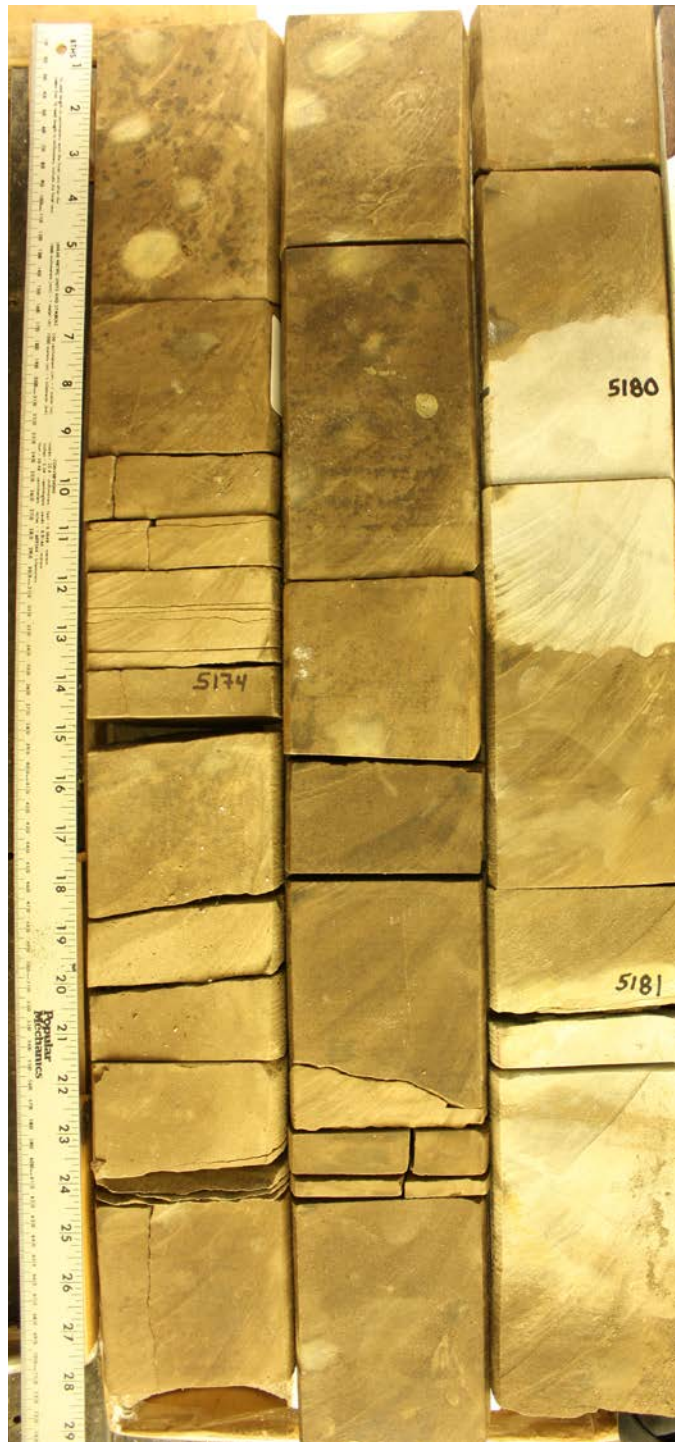
APPENDIX B: CORE IMAGES

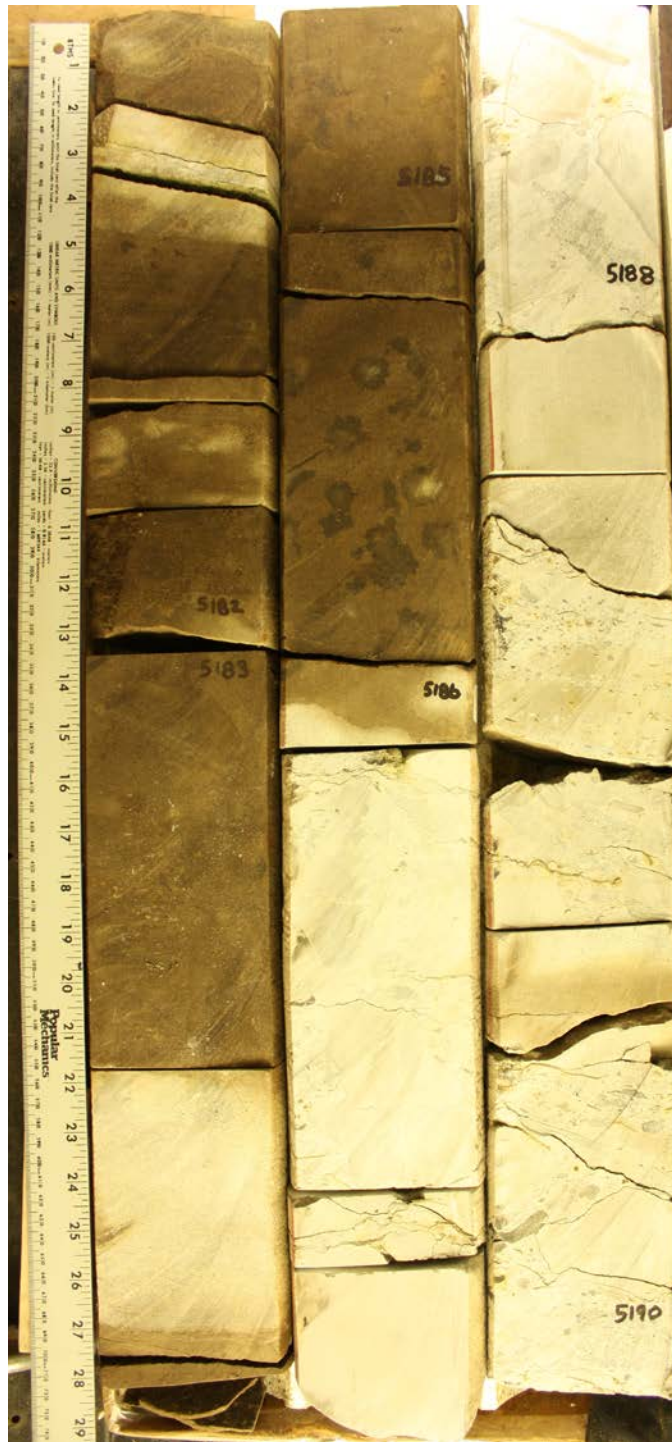Cores are marked in measured depth in feet. Ruler on left side of photos is scaled in inches and centimeters.
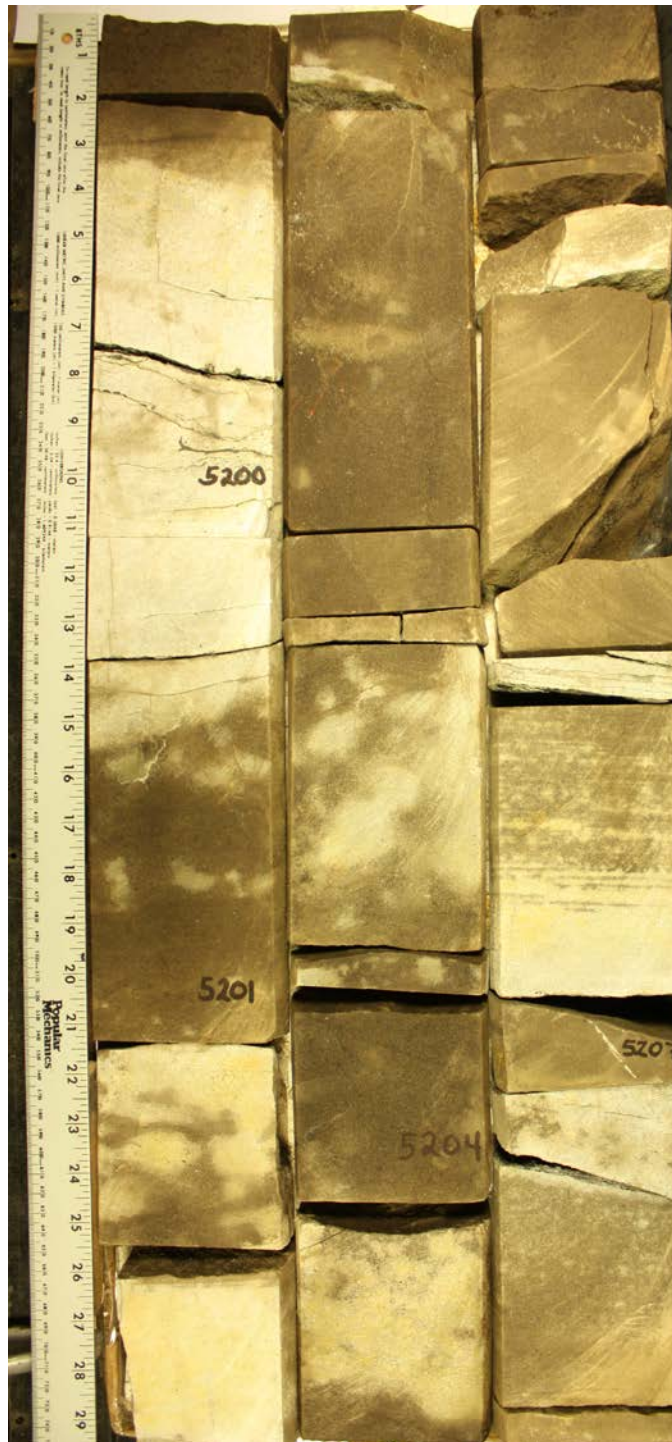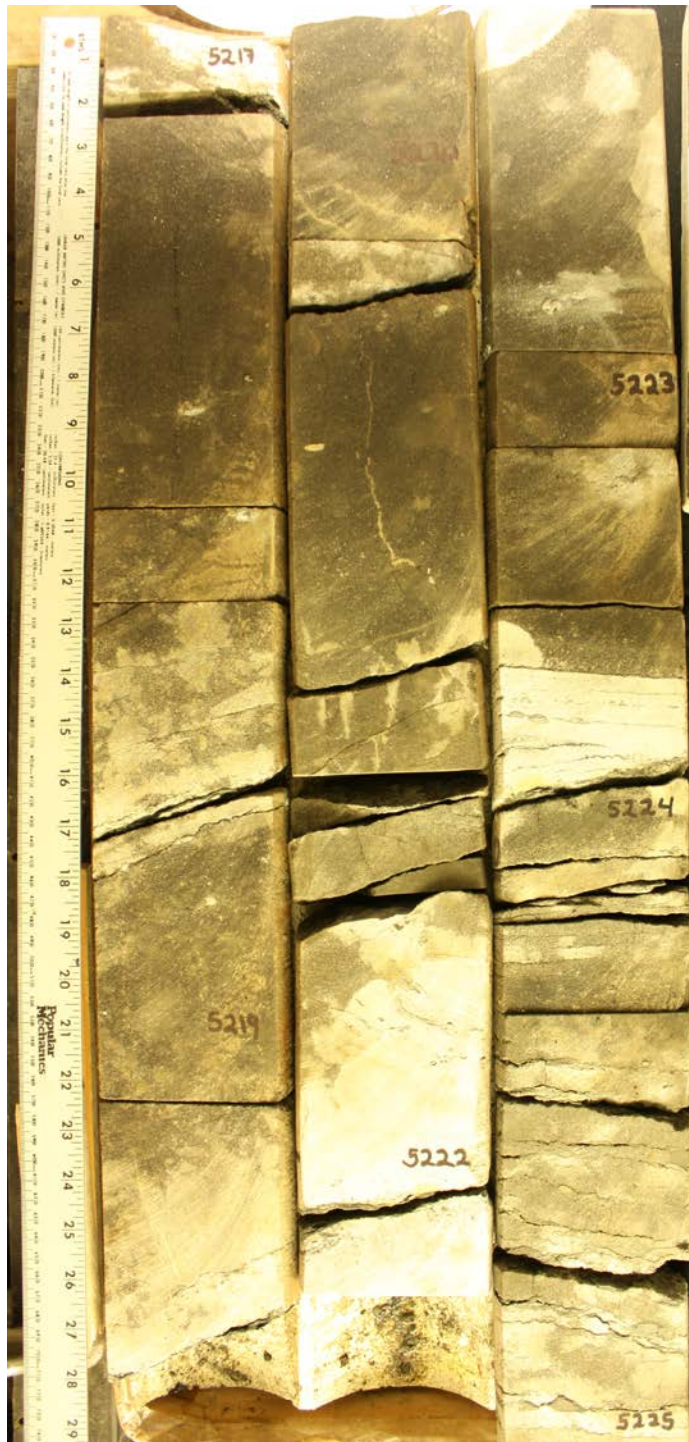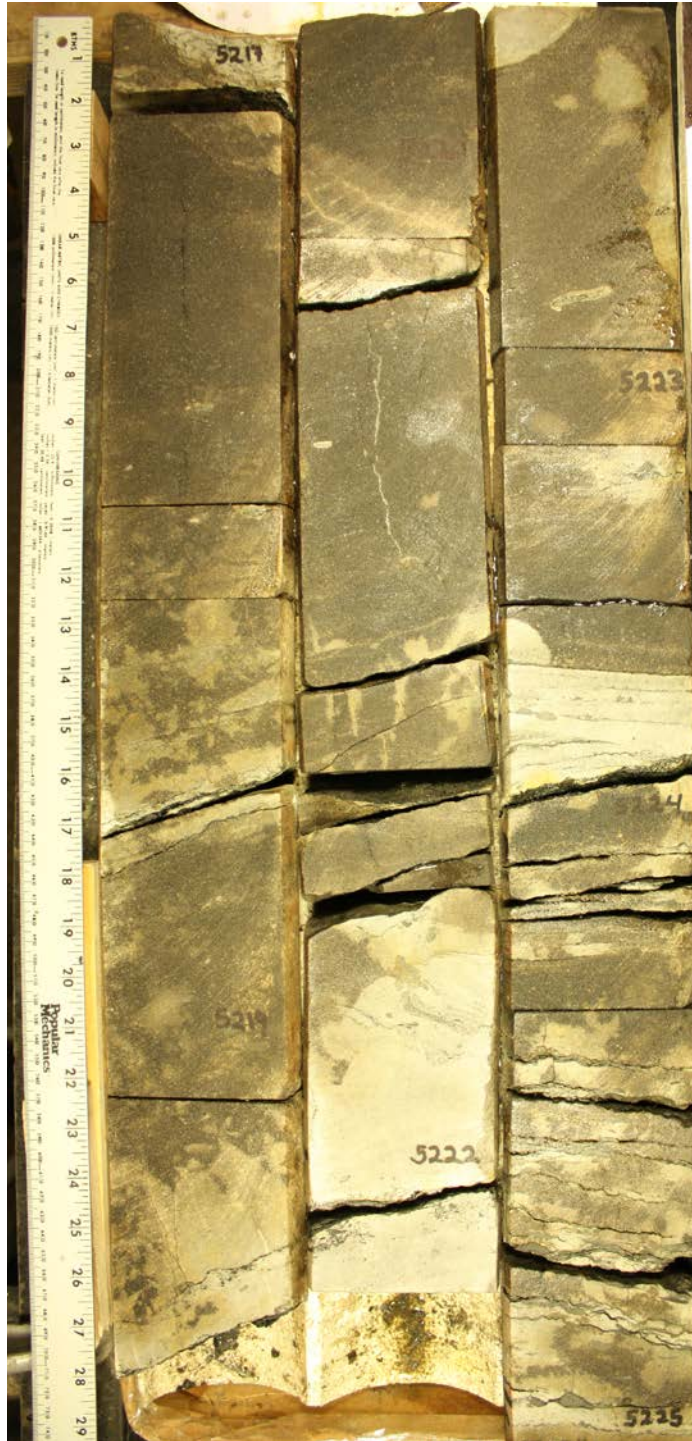
Mary Jones #2 (API# 15-081-21334)
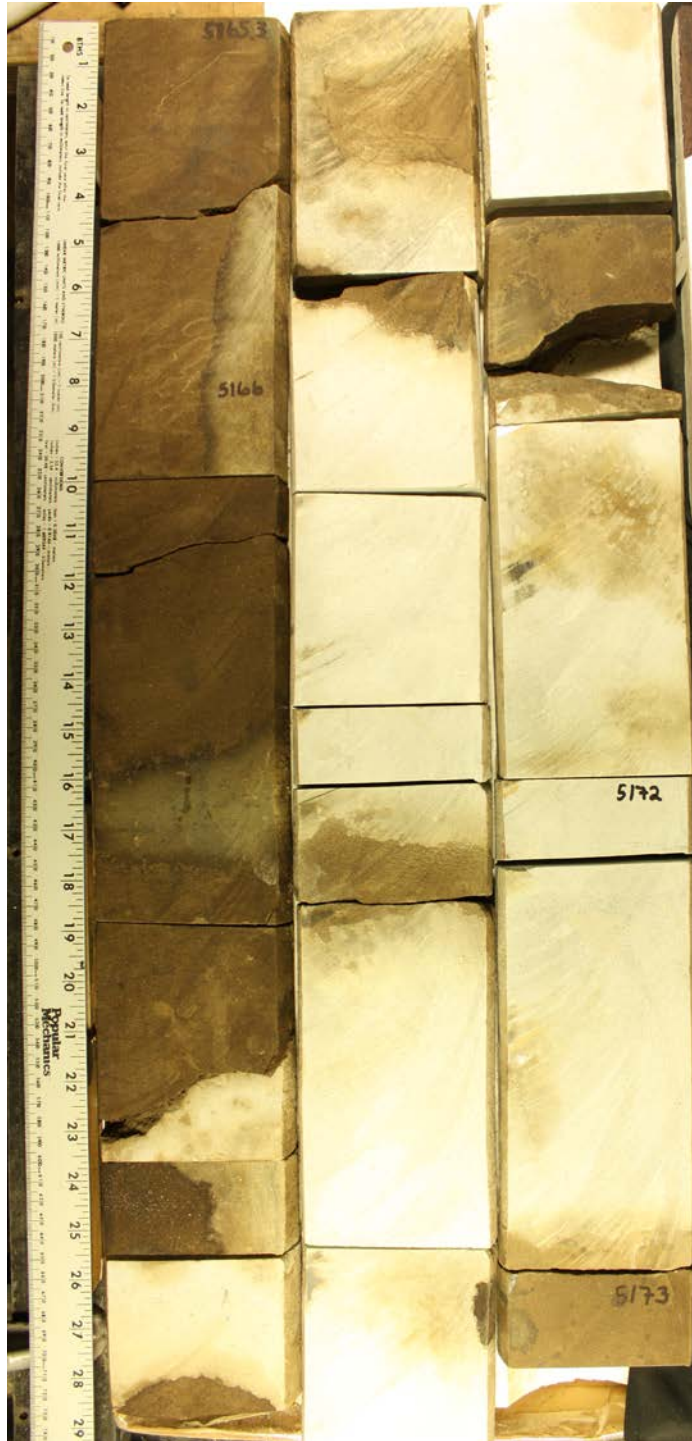
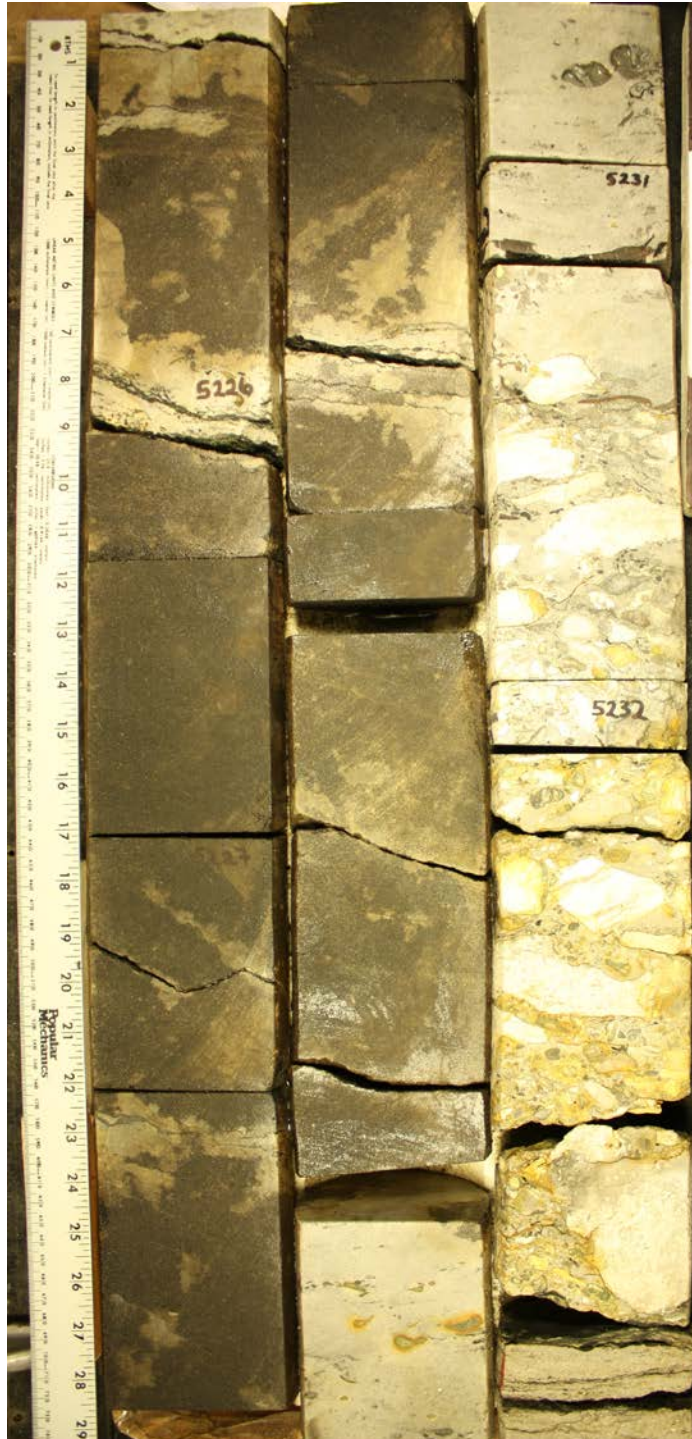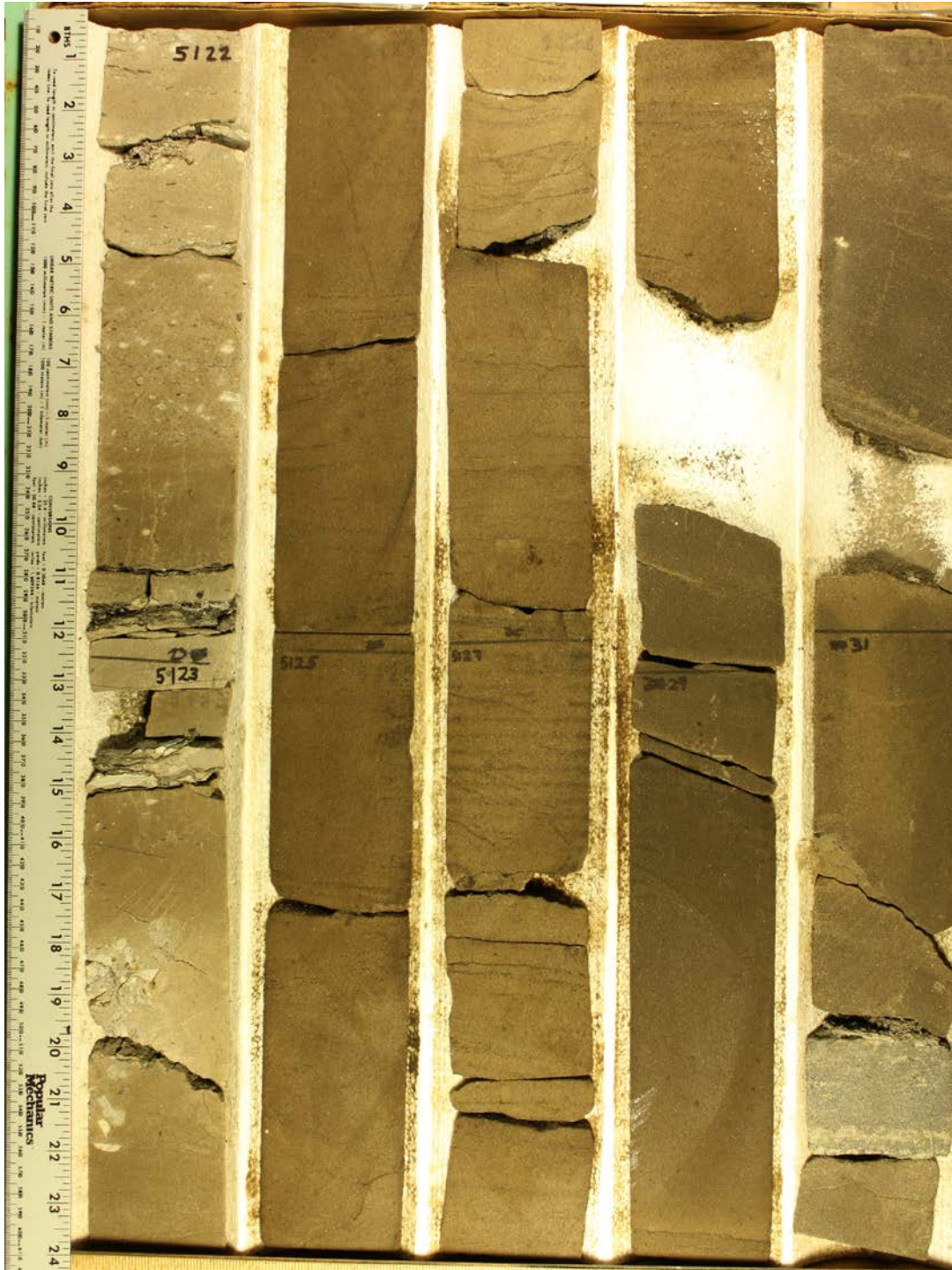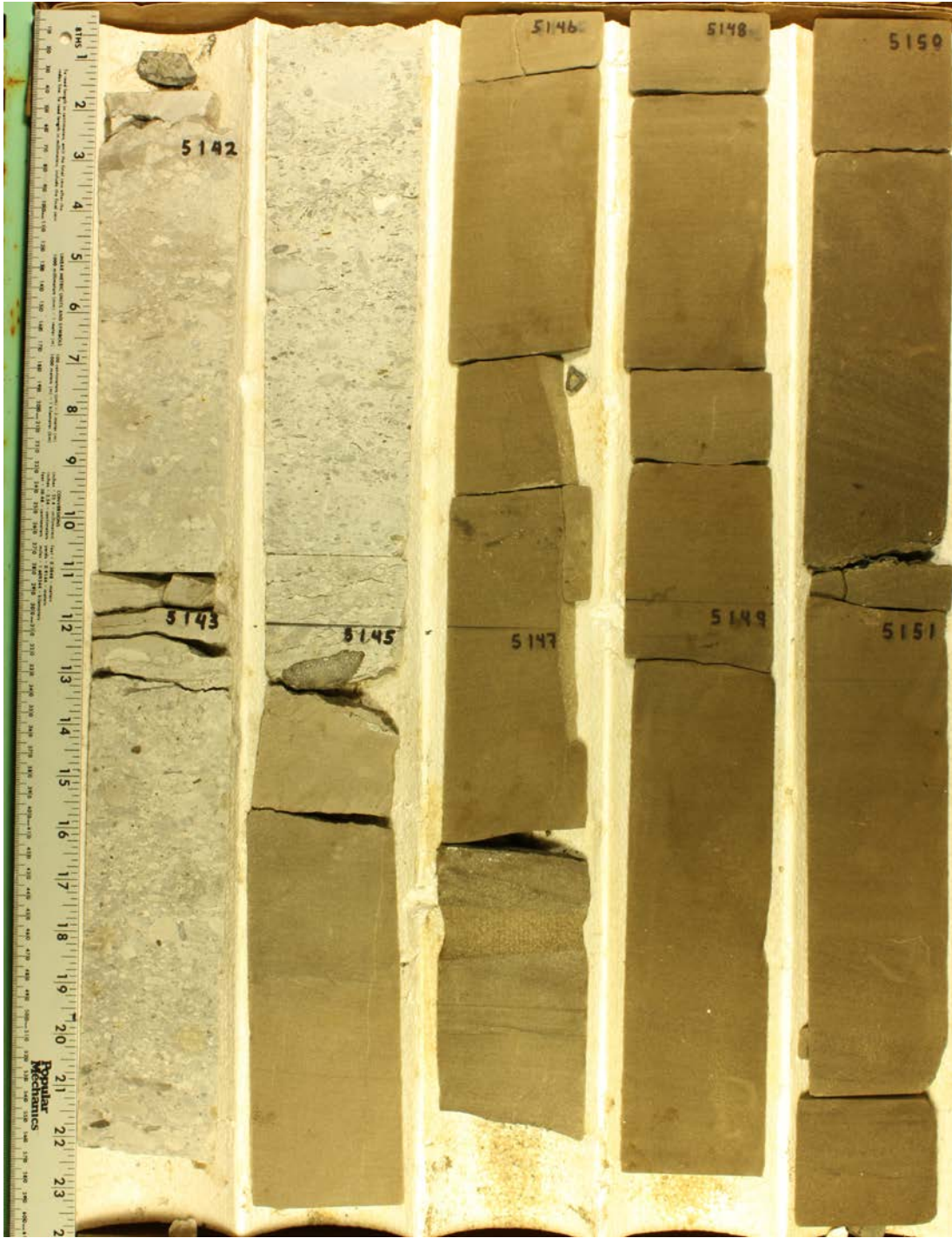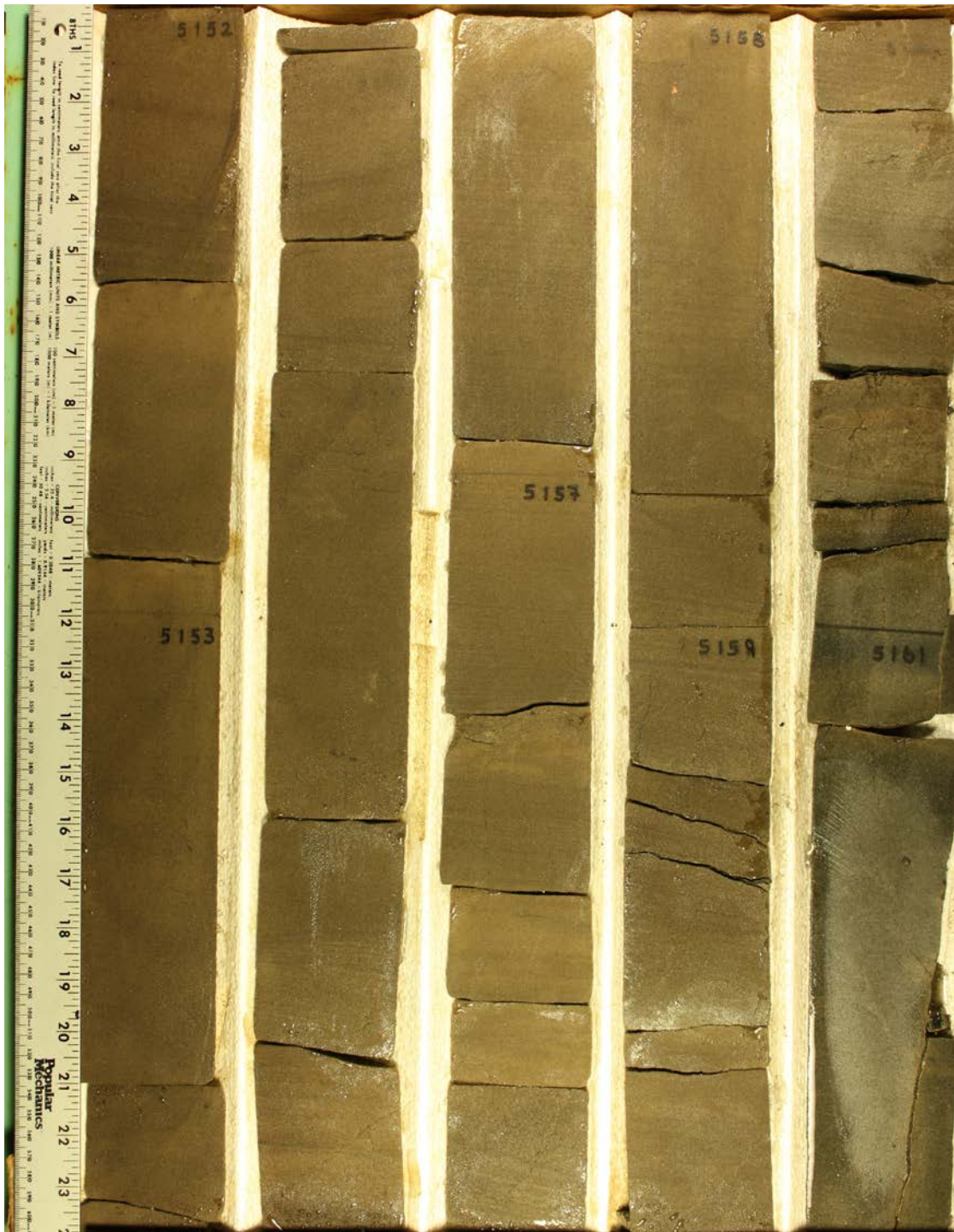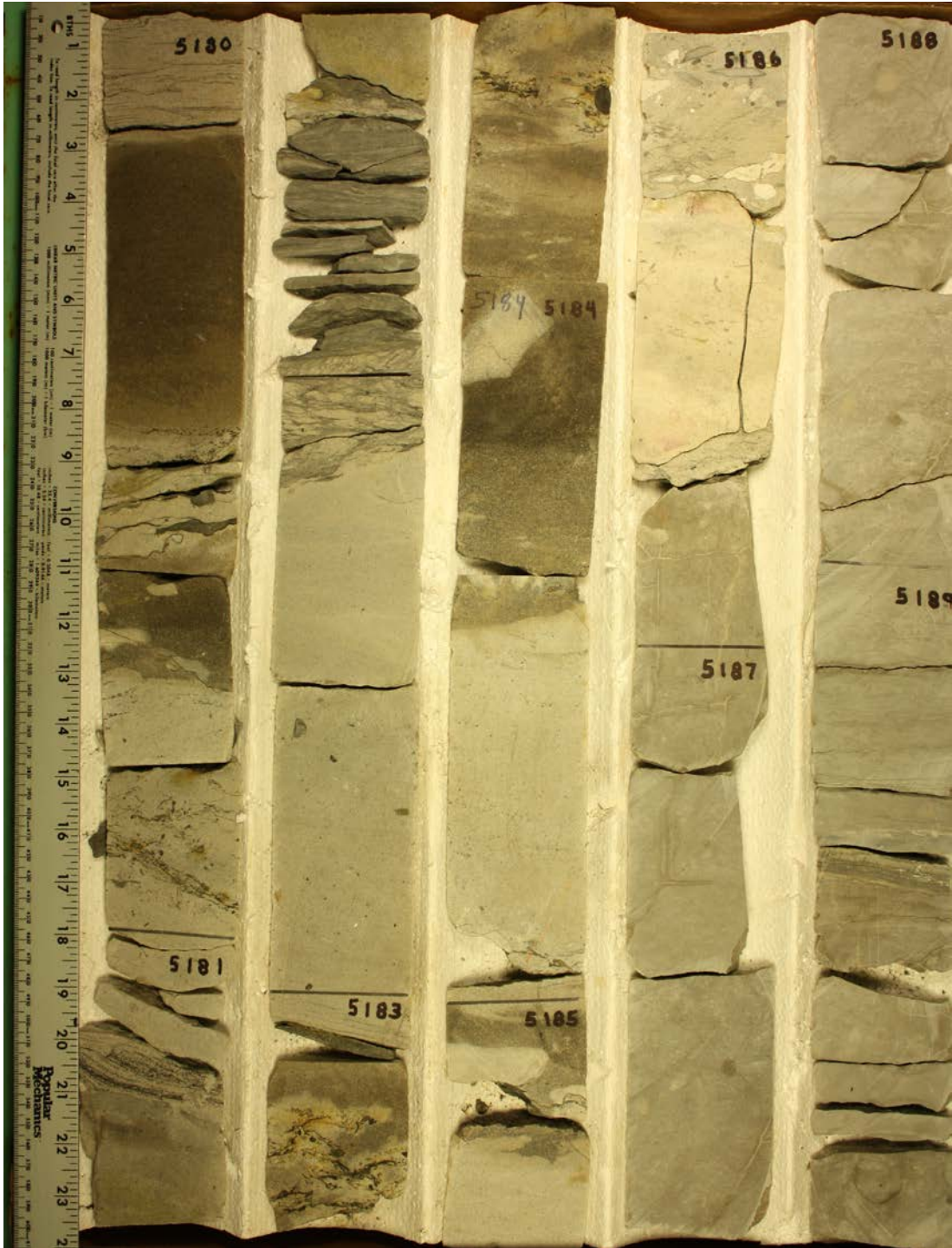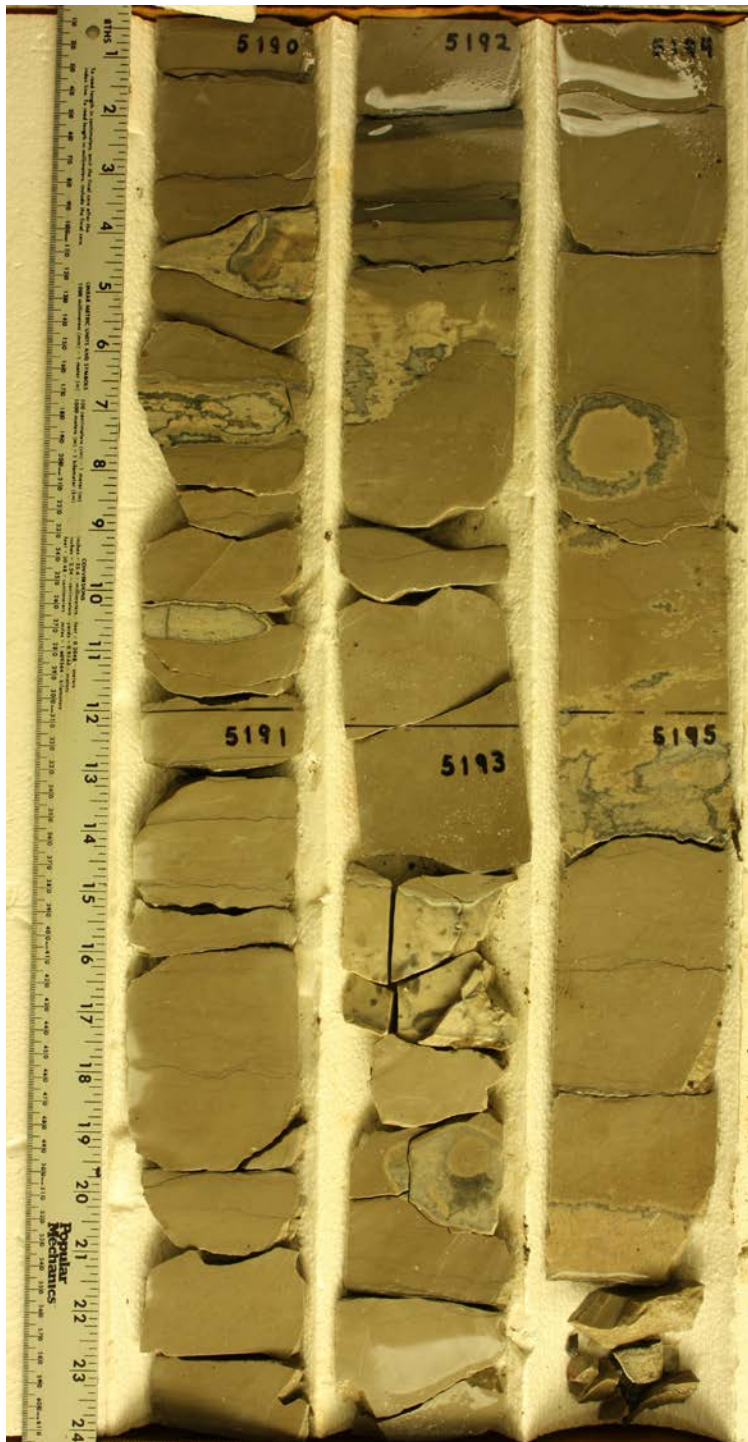**APPENDIX C: PETREL MODELING**

The initial step in creating the 3D reservoir model was setting up a database of wells. Data imported included well names and types, locations, dates, elevations, total depths, and all available formation tops. After the well database was created all available logs were imported, including original logs such as gamma ray and neutron and density porosity, and logs generated during the course of this study such as predicted lithofacies and estimated 'true' porosity. A total of 335 wells comprise the database, with a subset of 25 wells in the channel-filling sandstone reservoir.

With a complete well base assembled, the next step towards creating the 3D reservoir model was establishing a structural framework. A proprietary 3D seismic structure map of the unconformity surface between the Chesterian Shore Airport Formation and underlying Ste. Genevieve Limestone was provided, in which the incised channel containing the reservoir was very clearly and sharply defined. The 3D seismic structure map defined the spatial character of the channel much more clearly than any structure map using only formation top data could have. Formation top data were integrated into the seismic structure map to create a new structure map of the unconformity surface. The resulting structure map provides the basal and lateral constraints for the 3D model of the channel-filling sandstone reservoir (Figure 1). The structure map of the unconformity surface covers an area extending beyond the incised channel, but the final 3D model of the reservoir includes only the channel.
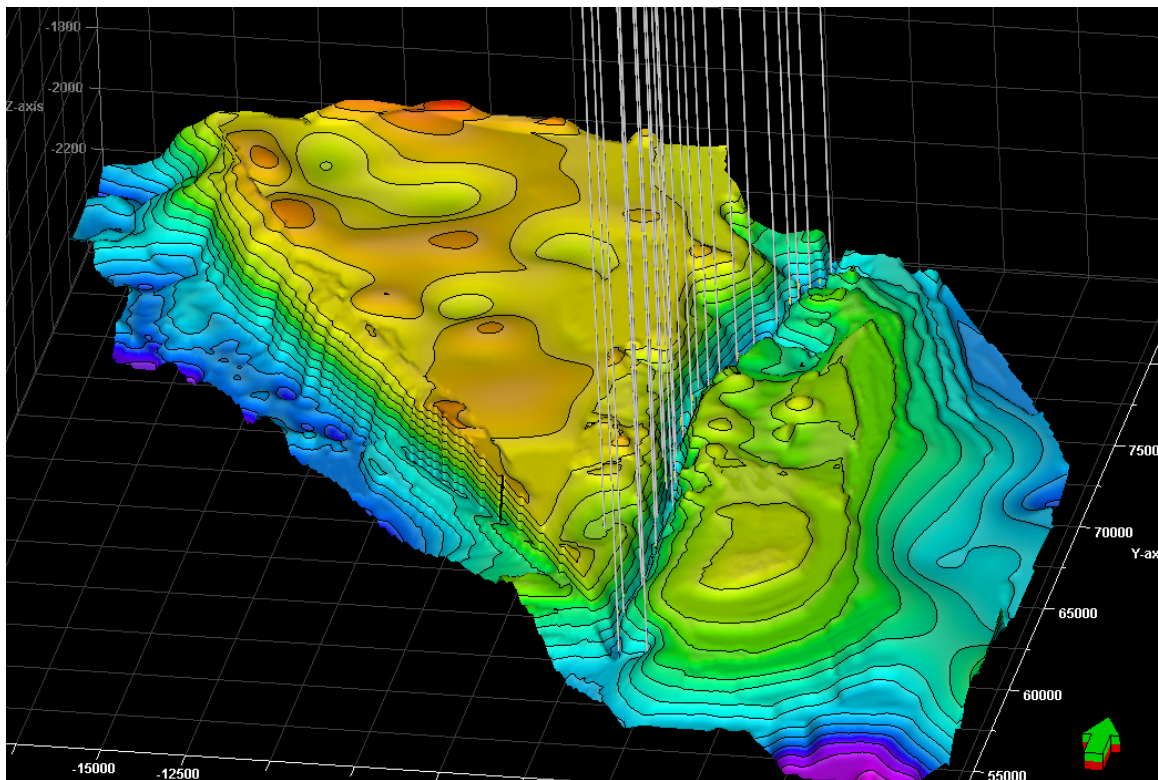

Fig. 1: Structure map of the unconformity surface between the Chesterian Shore Airport Formation and underlying Ste. Genevieve Limestone, constructed by merging a proprietary 3D seismic structure map with formation top data from wells. Vertical exaggeration 10x, north indicated by arrow in lower right corner.

173

Formation top data of the top of the Chesterian and a basal scour surface of a conglomerate bed traceable throughout the field (see Results) within the reservoir were used to complete the structural framework of the reservoir model. Structure maps of the top of the Chesterian and the scour surface were created using the formation top data of the 25 wells in the channel-filling sandstone reservoir; these structure maps were essentially planar, intersecting the walls of the incised valley at sharp angles. The top of the Chesterian is the top of the model, and the scour surface divides the reservoir model into upper and lower zones. Figures 2 and 3 show how the two surfaces intersect the structure map of the Shore Airport–Ste. Genevieve unconformity surface.

Figure 2: Structure map of the scour surface (brown) intersecting the unconformity surface between the Chesterian Shore Airport Formation and underlying Ste. Genevieve Limestone. Vertical exaggeration 10x, north indicated by arrow in lower right corner.
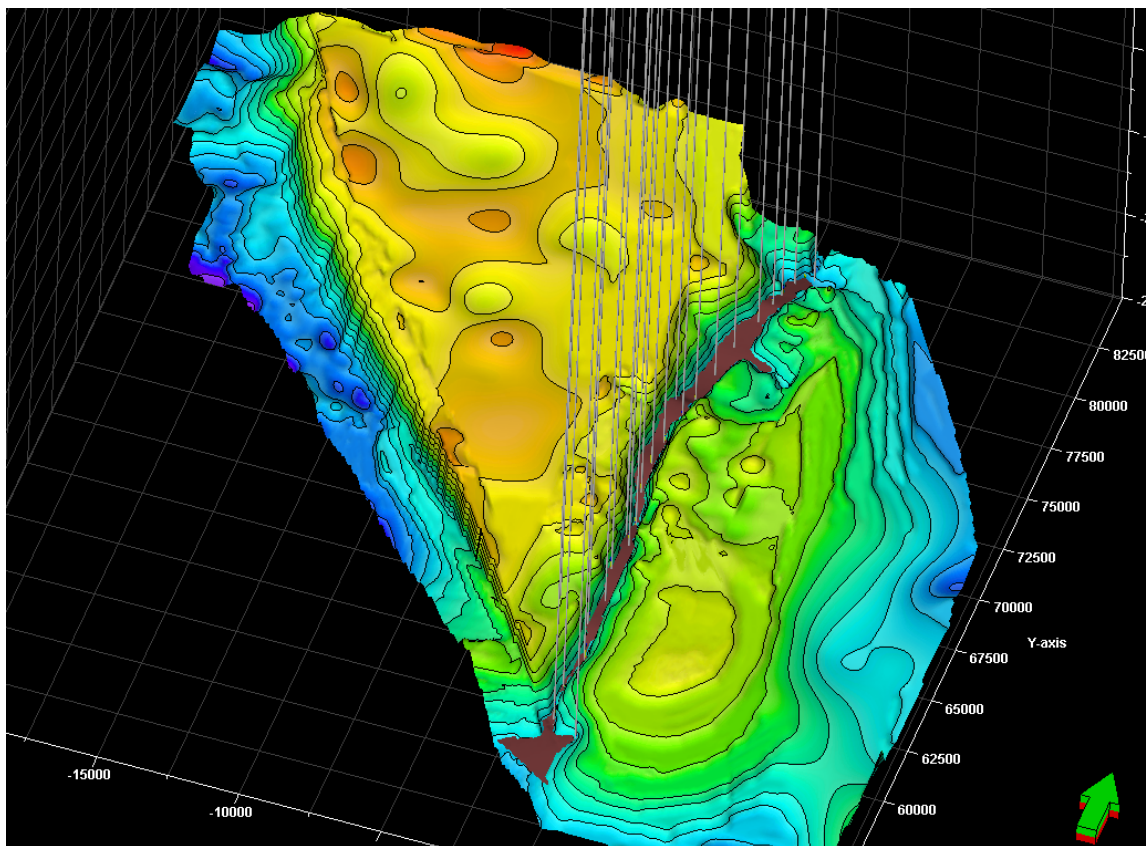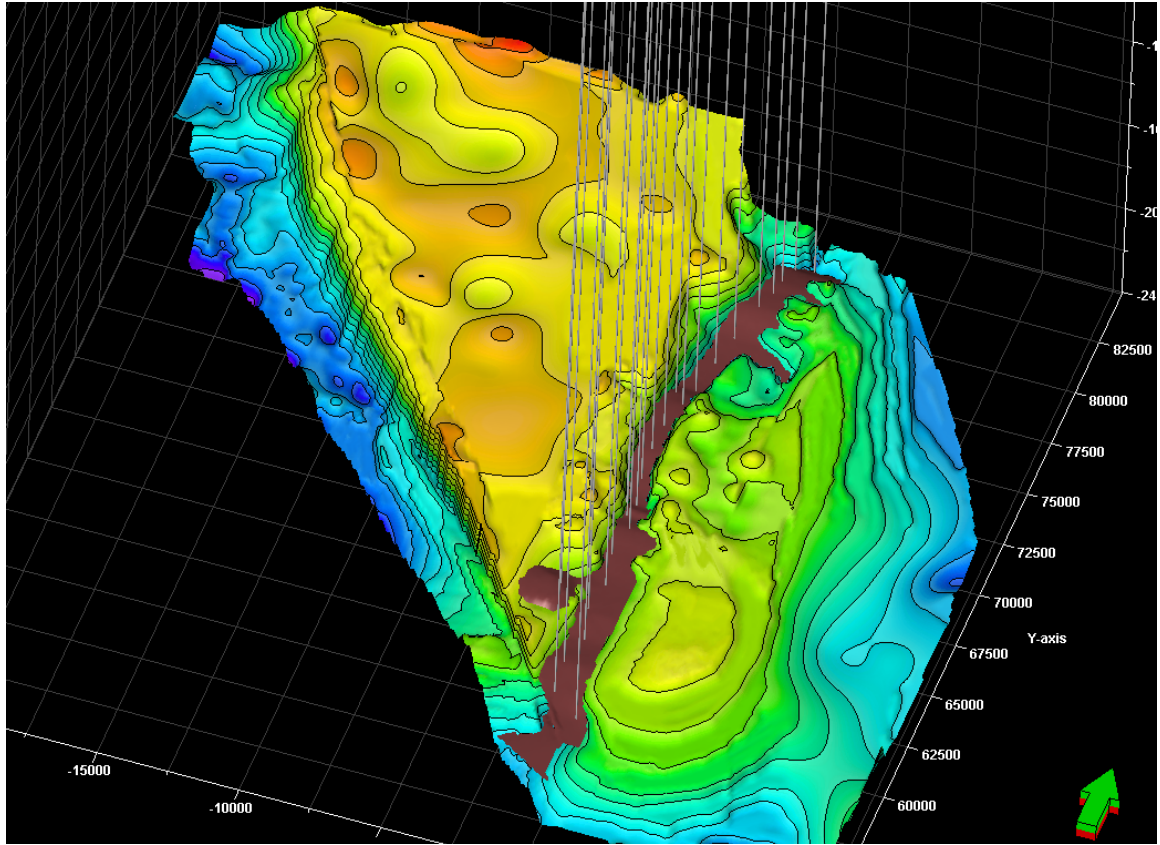
Figure 3: Structure map of the top of the Chesterian (brown) intersecting the unconformity surface between the Chesterian Shore Airport Formation and underlying Ste. Genevieve Limestone. Vertical exaggeration 10x, north indicated by arrow in lower right corner.

The 'Pillar Gridding' process in Petrel was used to generate an initial wire frame for modeling, and to set the horizontal dimensions of the grid cells (Figure 4). Next, two isochores, maps of true vertical thickness, were created. An upper isochore defines the interval between the top of the Chesterian and the scour surface, and a lower isochore defines the interval between the scour surface and the Shore Airport–Ste. Genevieve unconformity surface. The isochore maps and the formation tops for the scour surface are inputs in the 'Make Zones' process in Petrel (Figure 5). For this study, the model was built from the top down. The upper zone is built to the thickness of the upper isochore, not to extend past the scour surface formation tops; the lower zone is built from the base of the built upper zone downwards using the lower isochore. After completing the 'Make Zones' process the zones can be made into a 'property' using the 'Geometrical modeling' process so that they are visible in Petrel and can be examined in cross-sectional view (Figure 6, 7)
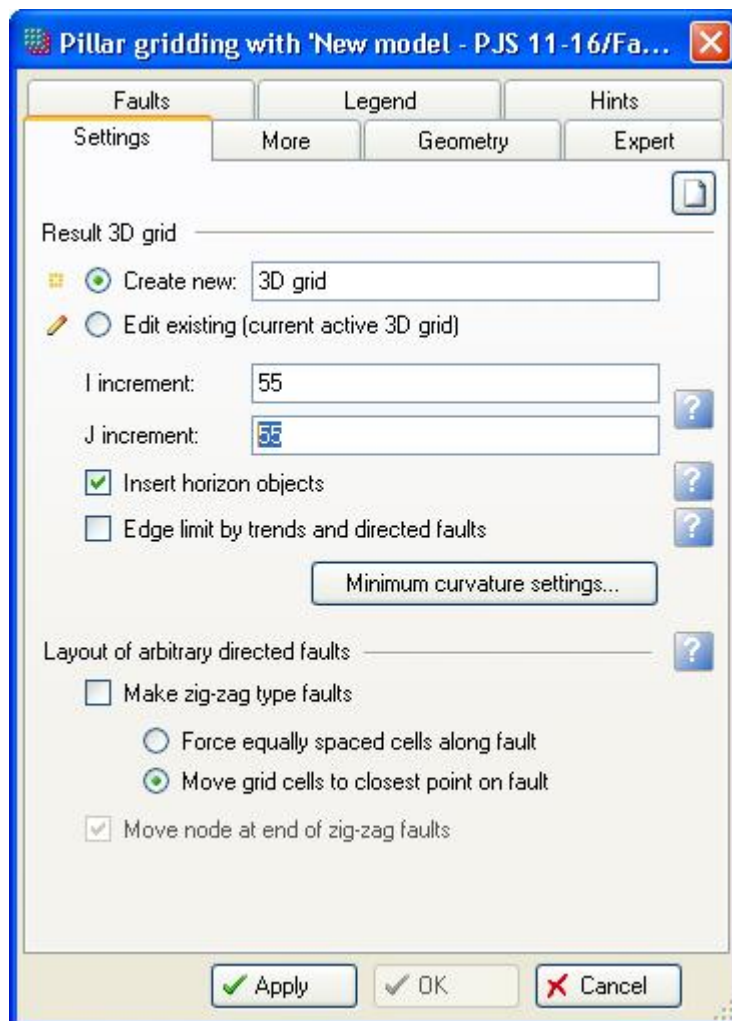
Figure 4: Screenshot of the 'Pillar Gridding' process window in Petrel, showing specification of horizontal dimensions of grid cells as 'I increment' and 'J increment'.
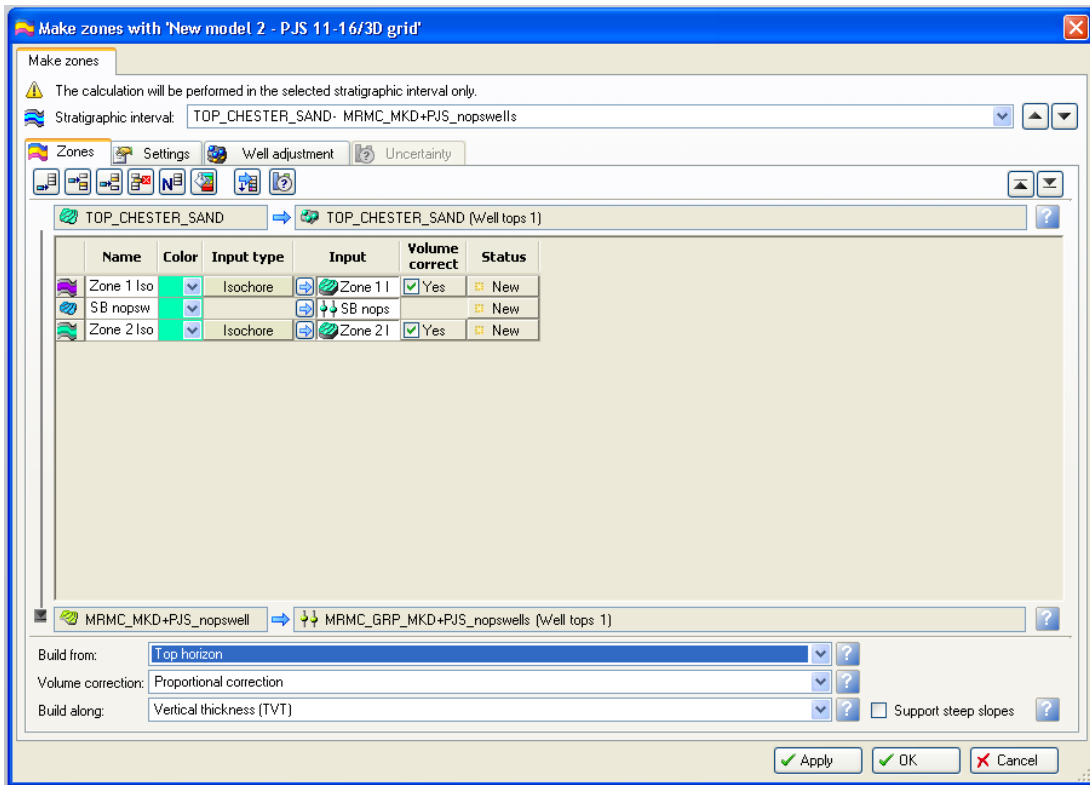
Figure 5: Screenshot of the 'Make Zones' process window in Petrel, showing input of structure maps and specification to build the zones from the top horizon.
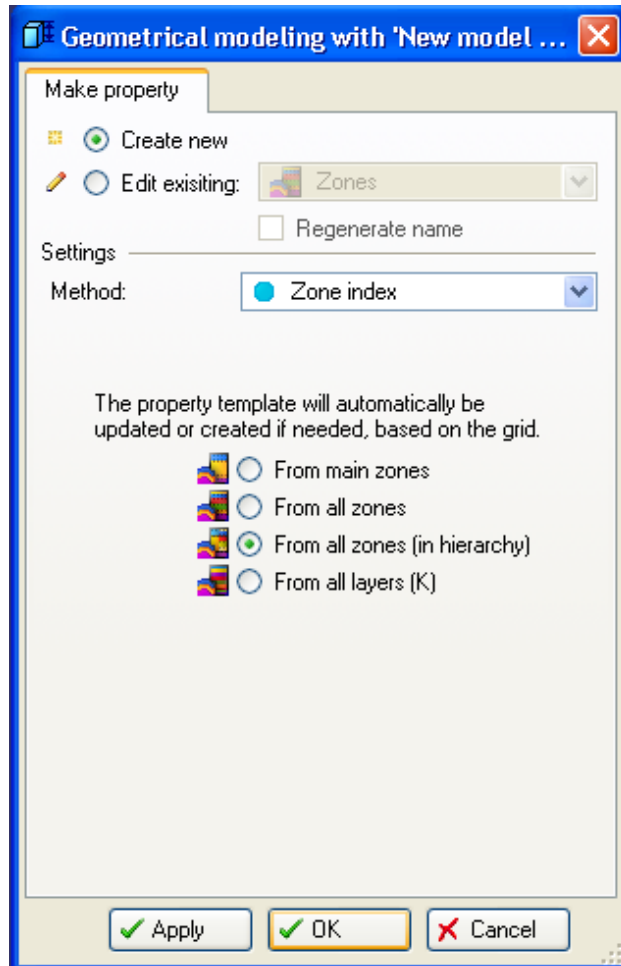
Figure 6: Screenshot of the 'Geometrical Modeling' process window in Petrel, where zones can be made into a visible property.

Figure 7: Screenshot of the Shore Airport–Ste. Genevieve unconformity surface with upper and lower zones shown in cross-section. Arrow indicates north direction.

Next, the 'Make Layers' process in Petrel was used to specify the vertical thickness of the layers of the model. The 'Make Layers' process separately layers each zone; different methods of layering and specifications for vertical thickness of the layers are possible for different zones. For this study, the vertical thickness of the layers set to 2 feet for both zones (Figure 8). The two zones were built from the top down in the 'Make Zones' process, and they were also layered from the top down. The layering method was set to 'follow surface' for both zones, and for the upper zone the surface to be followed was the structure map of the top of the Chesterian; the lower zone was set to follow the scour surface structure map. To summarize, the model is defined by a framework of structure maps, the area to be modeled is divided into 55x55 foot cells, isochore maps of the thicknesses between the structural maps are used to build zones, and the zones layered in 2 foot intervals. The end result is a 3D cellular model of the channel-filling sandstone reservoir, composed of 55x55x2 foot cells (Figure 9).

Figure 8: Screenshot of the 'Make Layers' process window in Petrel, showing specification of a 2-foot thickness for the layers (cell thickness), structure maps as reference surfaces, and 'follow surface' as the method of layering.
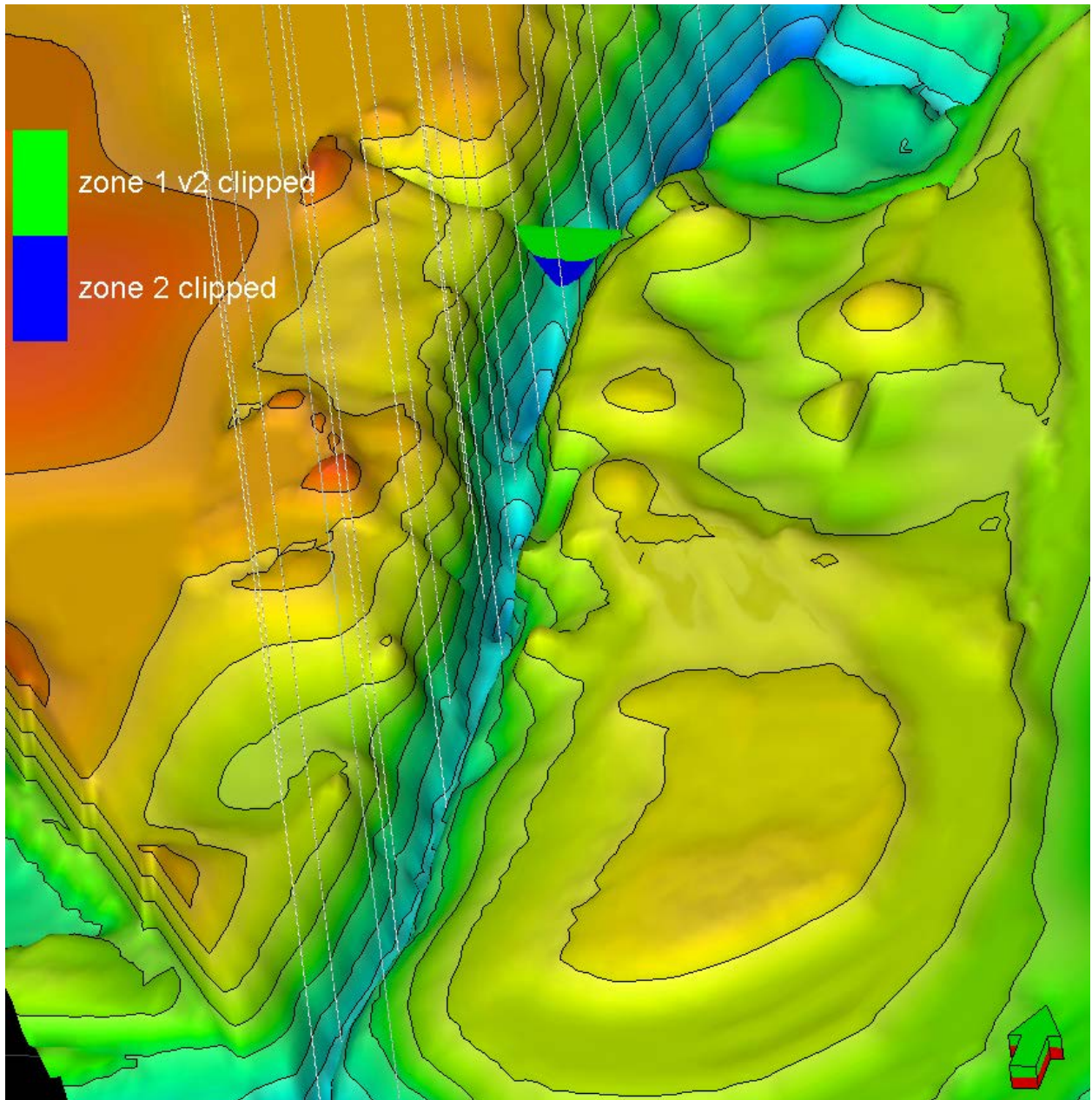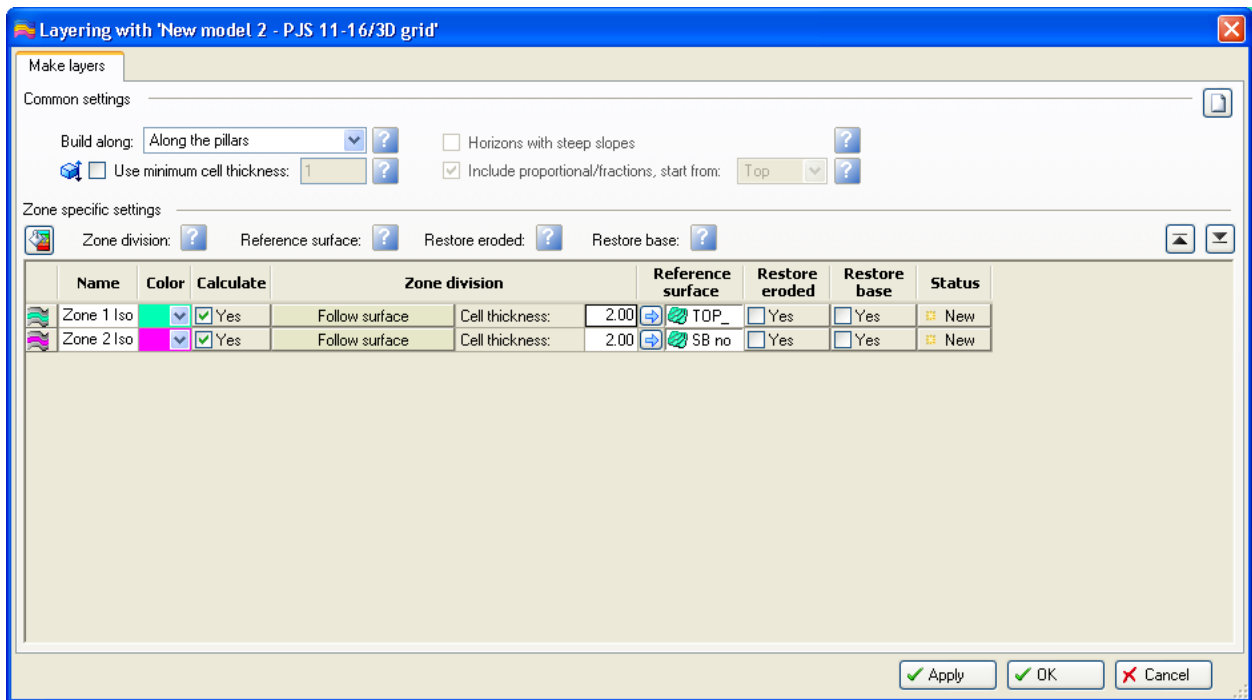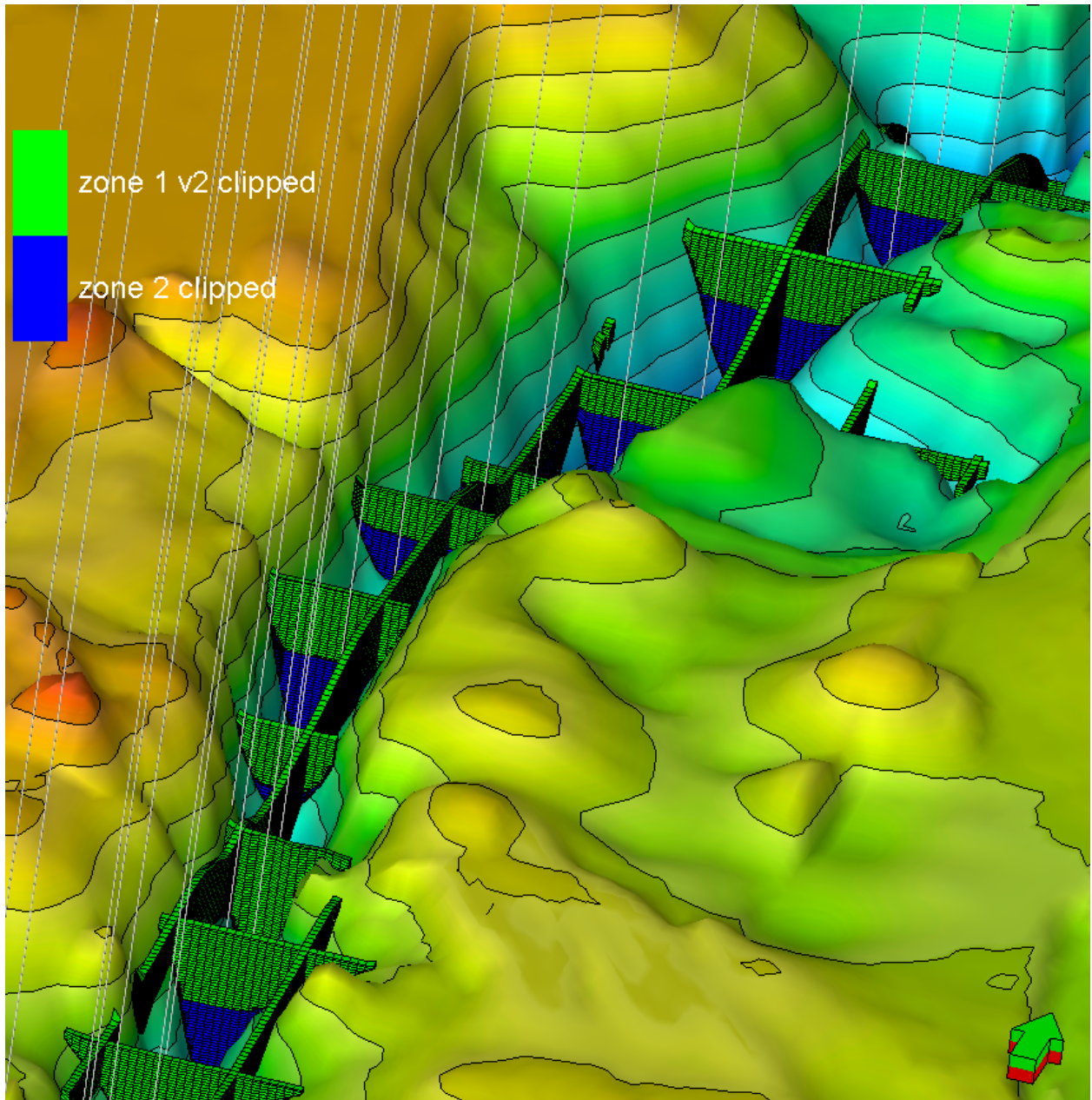
Figure 9: Screenshot of the Shore Airport–Ste. Genevieve unconformity surface with layered upper and lower zones shown in cross-section. Arrow indicates north.

With the 3D cellular model built, the next step was to populate the cells with values for predicted lithofacies and porosity. The model was populated using stochastic processes based on the well log data imported in the beginning of the project. Before stochastic processes could be used however, two steps had to be taken. The 0.5-foot vertical resolution scaled well logs of predicted lithofacies and porosity had to be upscaled to the 2-foot vertical resolution scale of the model, and then the upscaled data had to be smoothed and analyzed for trends.

The 'Scale up well logs' process in Petrel allows the user to select any well log and upscale it to model-scale resolution. Upscaling from a finer to a coarser vertical resolution may be done a number of ways. For the predicted lithofacies logs, the method selected is 'most of' (Figure 10); meaning that of the multiple 0.5-foot interval predicted lithofacies values that occur in a 2 foot-thick model cell, the most common value is assigned to that cell. For the porosity logs, however, the method is simply to take an arithmetic average of the 0.5-foot resolution data within each 2 foot-thick cell. The reason for the different methods is that the two sets of data, predicted lithofacies and porosity, are different. The predicted lithofacies values are discrete and can only be certain values, so the 'most of' method is appropriate, because arithmetically averaging the data could lead to a numbers that would not fit into any discrete class. Porosity data are continuous, they can be any number along a continuum and still be valid, and so arithmetically averaging is an acceptable way to upscale from a finer to a coarser resolution. Any process that upscales data from a finer to a coarser resolution will inevitably lose some of the original data, and Figure 11 is an example where very thin beds of conglomerate are lost in the upscaled predicted lithofacies.
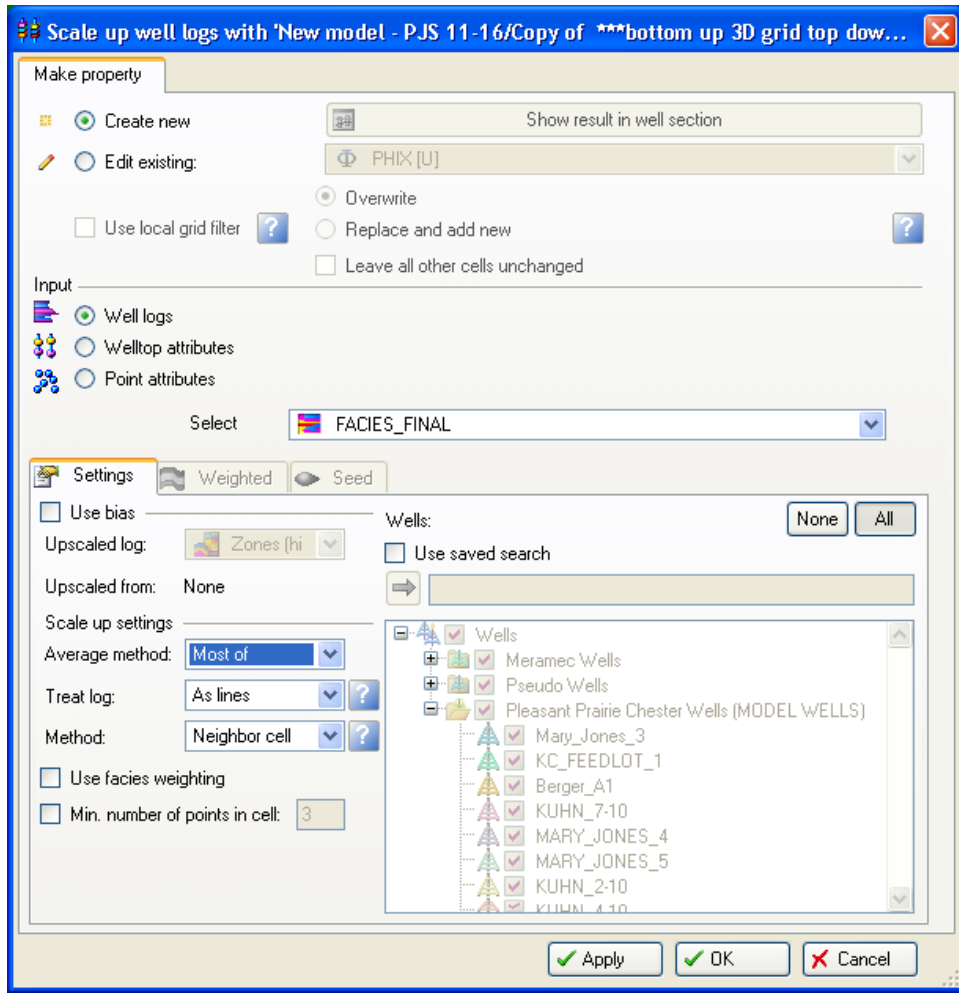
Figure 10: Screenshot of the 'Scale up well logs' process window in Petrel, showing the 'most of' method selected for upscaling logs of predicted lithofacies.
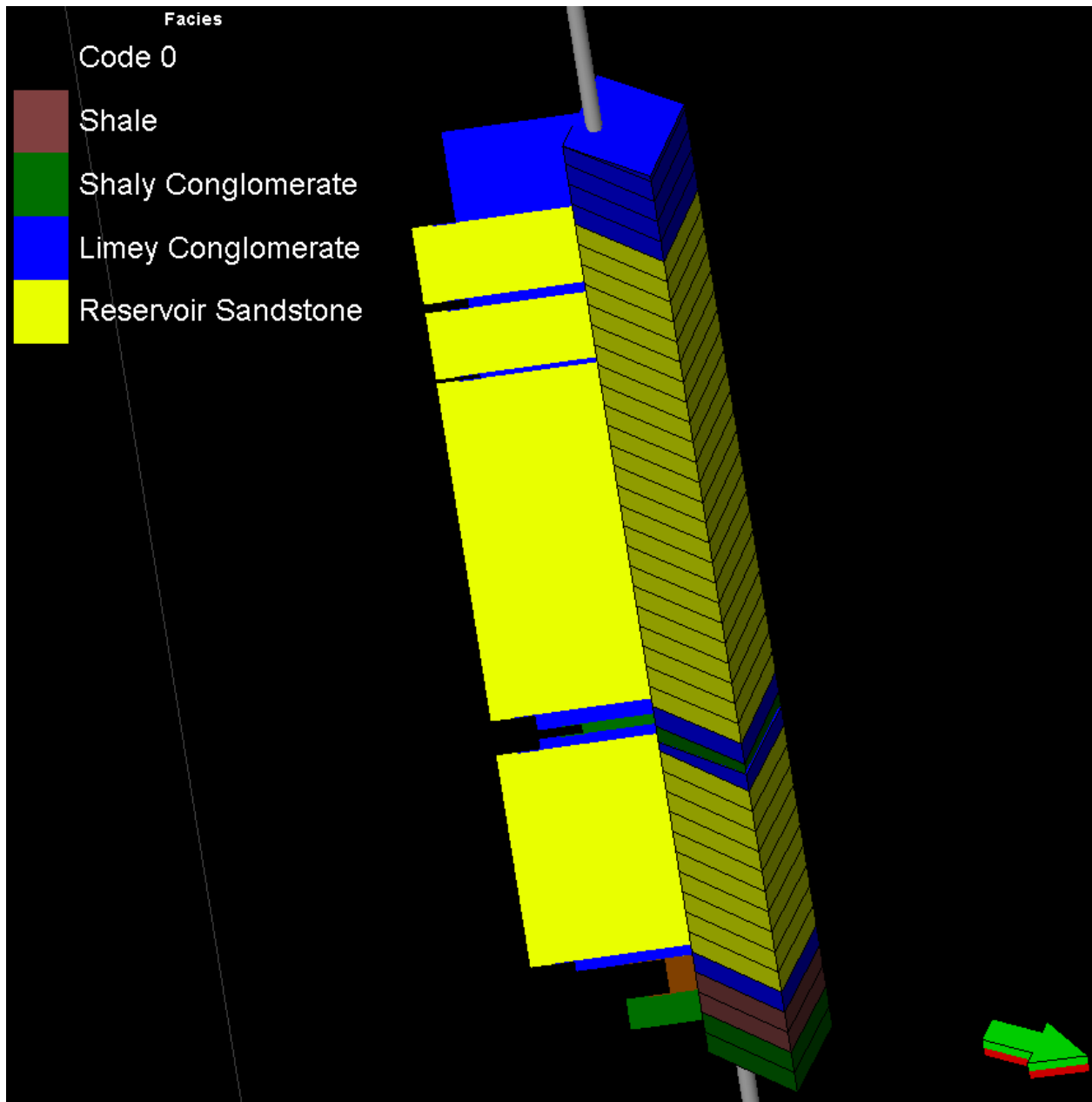
Figure 11: Screenshot comparing log (left) and upscaled (right) predicted lithofacies of a well (Moody D1, API# 15-081-21254), showing loss of two very thin conglomerate beds in the upscaled cells.

The 'Data Analysis' process in Petrel was used to transform the porosity data distribution, and then to do variogram analysis on the upscaled porosity property. The transforming of the porosity data consisted of three steps: input and output truncation, fitting a distribution curve to the data, and smoothing the curve. The input and output truncation steps allow the user to specify minimum and maximum values, if necessary, that can be input into the distribution curve or outputs from it. The porosity logs had already been 'clipped' to remove values below zero, so there was no need to truncate the minimum value for porosity. However, due to the unreliability of the porosity log readings in the shale lithofacies, a porosity of 6% was manually set in the logs. The arithmetic averaging method in the upscaling of the logs resulted in some shale lithofacies having a porosity greater than 6%, so the input and output truncation was used to re-set this specification so that in the final 3D cellular model, shale would have 6% porosity. Fitting a distribution curve to the data and smoothing the curve is illustrated in Figures 12 and 13. The smoothed distribution curves for each lithofacies in each zone serve as a guide in the population of the 3D cellular model.
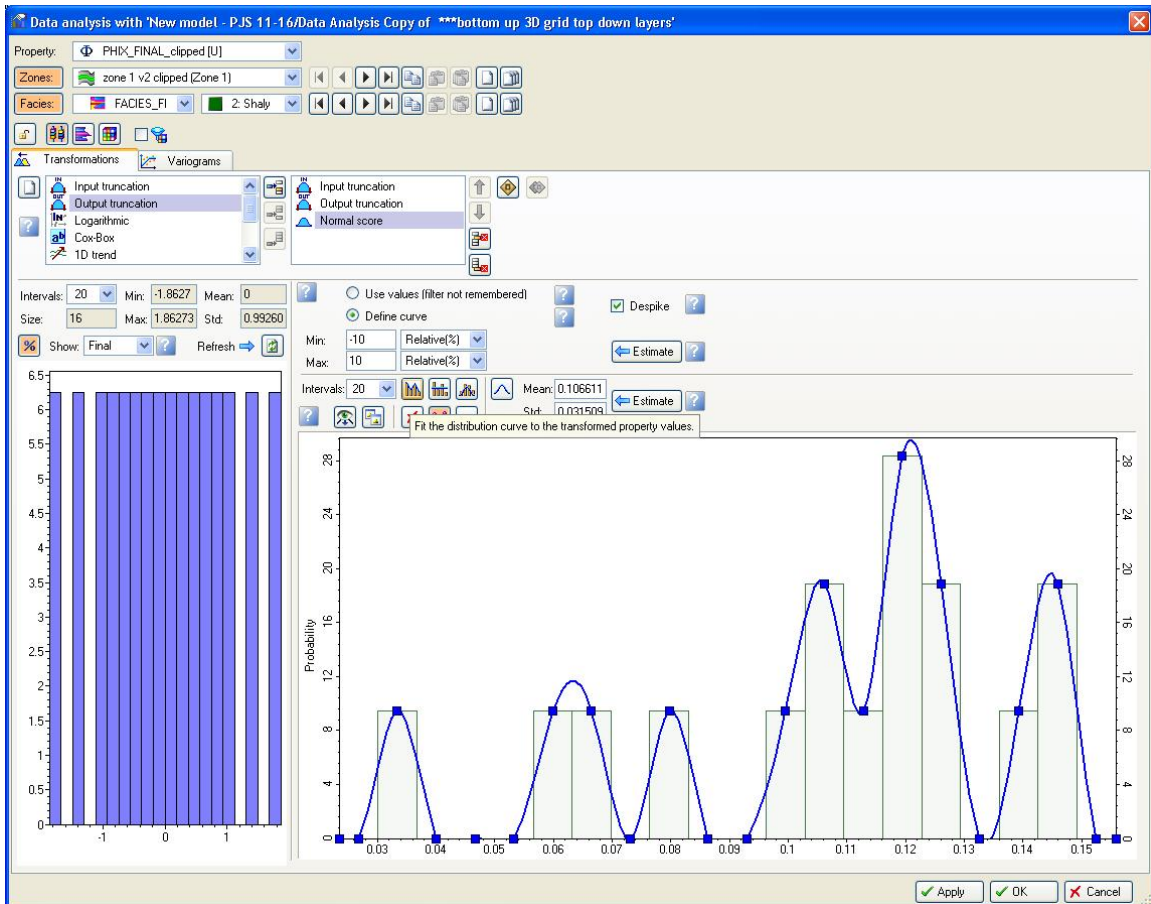
Figure 12: Screenshot of 'Data Analysis' process in Petrel, showing distribution curve fit to data for the shaly conglomerate lithofacies in zone 1.
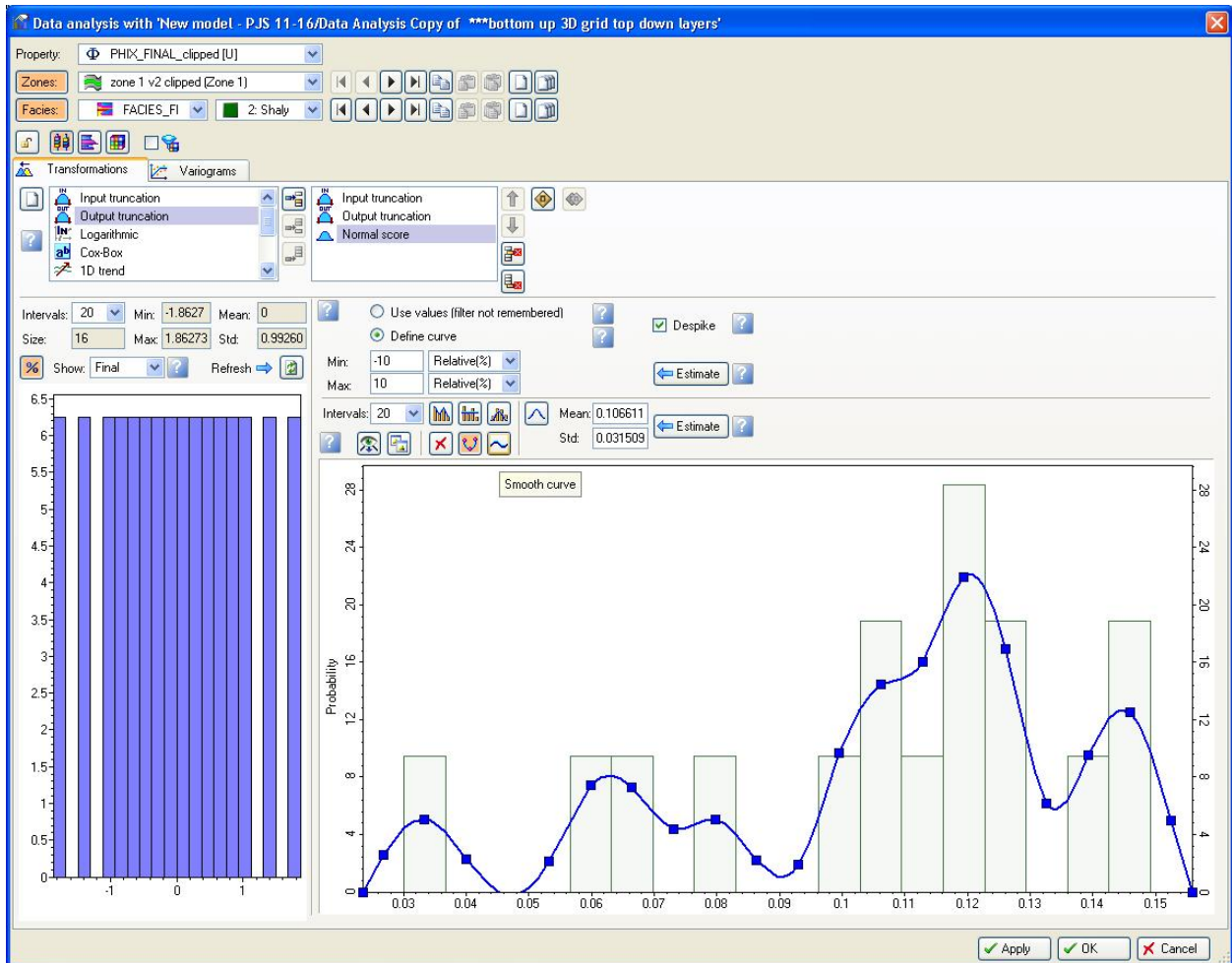
Figure 13: Screenshot of 'Data Analysis' process in Petrel, showing distribution curve smoothed for the shaly conglomerate lithofacies in zone 1.

Variograms represent measurements of the spatial correlation of data. Variograms in Petrel are omnidirectional; they are created for major, minor, and vertical directions, the minor direction being 90° counterclockwise from the major. An example of the variogram window in Petrel is shown in Figure 14. Variograms were created in the 'Data Analysis' process for each of the four lithofacies in both of the zones for the upscaled porosity property. Variogram parameters for the upscaled lithofacies property were input directly into the 'Facies Modeling' process window. Several combinations of major, minor, and vertical ranges were used before a reasonable model was obtained. The first several models of lithofacies showed an unrealistically random appearing distribution of lithofacies (Figure 15). Well log correlations of conglomerate beds and production data showing compartmentalization of the reservoir in the northern area (see Results, Discussion) were used as guides in attempting to create a reasonable lithofacies model. The final lithofacies model showed good connectivity of some conglomerate beds and potential compartmentalization of the reservoir in the northern area (Figure 16). Appendix D contains tables of Variogram parameters for the lithofacies and porosity properties.

The best variograms for both porosity and lithofacies always had one thing in common. The major range was always significantly greater than the minor range, and was always best left at due north. The characteristic directionality and geometry of spatial correlation revealed by the variograms is a reflection of the narrow, elongate shape of the reservoir and the corresponding, inherently downdip direction of sedimentation. In channel-filling reservoirs such as the Chesterian sandstone at Pleasant Prairie oilfield, where deposition of sediment is within a narrow, generally straight incised channel, bodies of reservoir-quality sandstone often accumulate as elongate bar forms parallel to the incised channel. Thus, the major direction of similarity in properties such as lithofacies and porosity develops in the same elongate, channel-parallel manner.
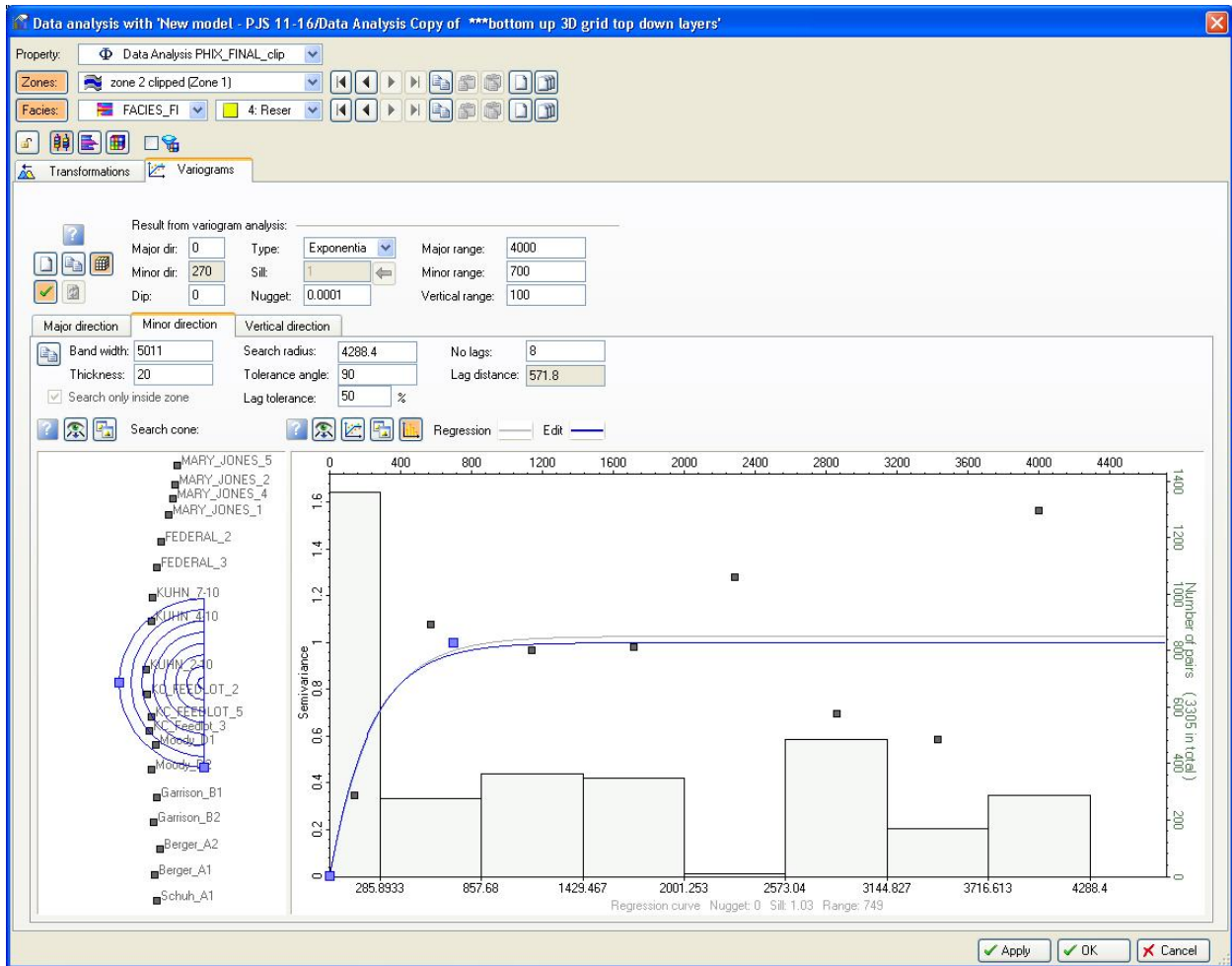
Figure 14: Screenshot of a variogram for porosity in the 'Data Analysis' process window in Petrel, showing variogram type and variables.

The 3D cellular model was populated with lithofacies by using Sequential indicator simulation (SIS) in the 'Facies Modeling' process in Petrel. SIS is a stochastic modeling method commonly applied to discrete data such as lithofacies; it is the default method in Petrel for the 'Facies Modeling' process. Figure 16 and 17 show the 'Facies modeling' process window; for each lithofacies in each zone the major, minor, and vertical ranges of variograms are input, and for each zone under the 'fraction' tab the option 'upscaled cells' is marked. The setting in the 'fraction' tab is forcing the final population of each lithofacies in the entire 3D model to be as close as possible to the relative proportions of each lithofacies in the upscaled cells. This setting was activated because the default had equal proportions for each lithofacies, a situation which would result in an unrealistic model. The resulting final lithofacies model provided a reasonable and useful visualization of the reservoir and helped in understanding how the distribution of lithofacies affected reservoir performance (see Results, Discussion).
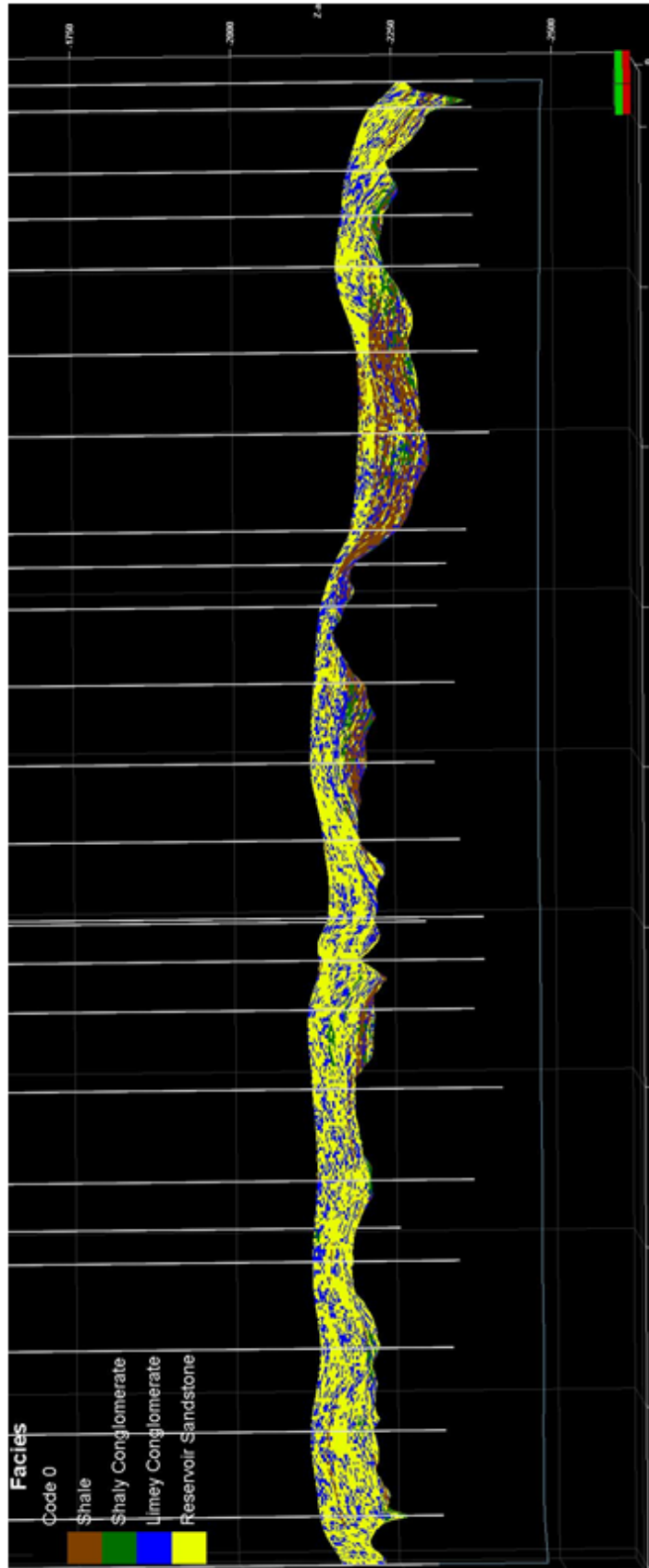
Figure 15: Screenshot of a well-to-well cross-section of an early predicted lithofacies model, note poor connectivity and seemingly random placement of predicted lithofacies.

190
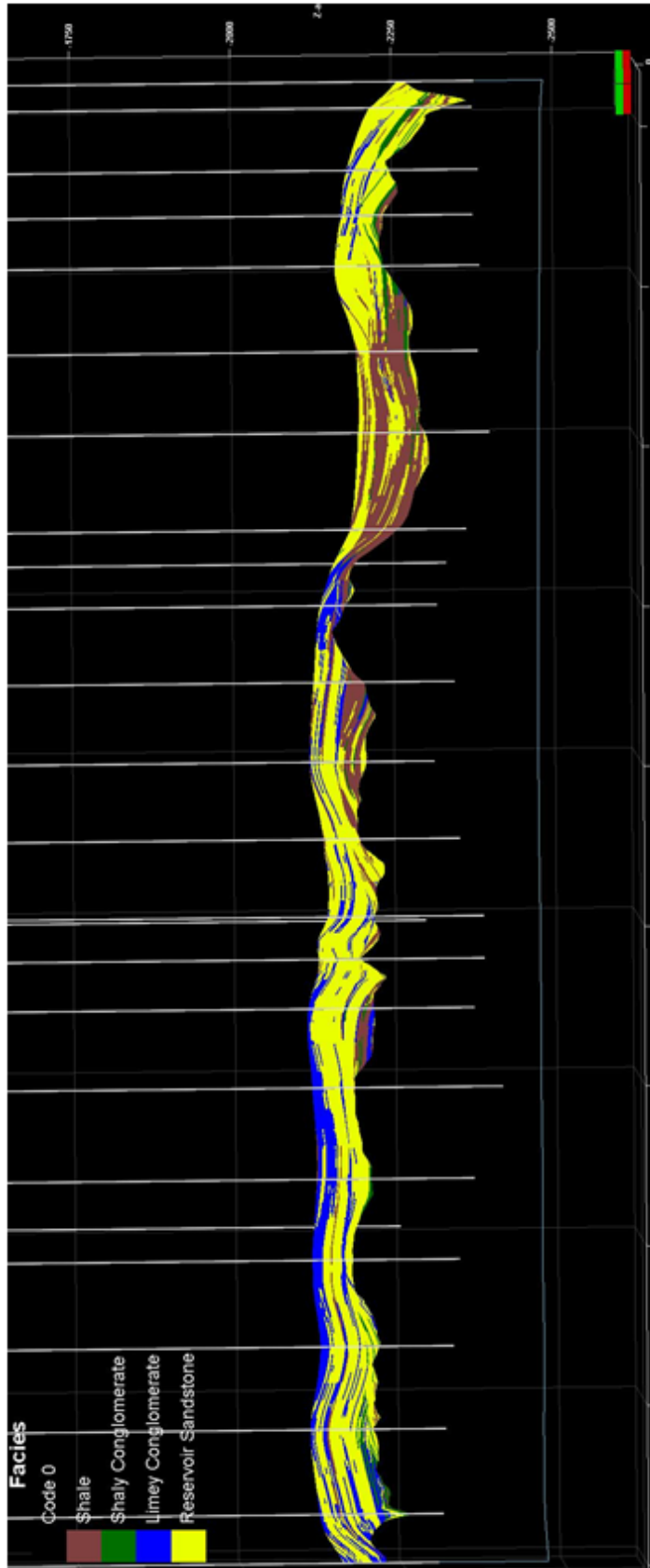
Figure 16: Screenshot of a well-to-well cross-section of the final predicted lithofacies model, note good connectivity of lithofacies.
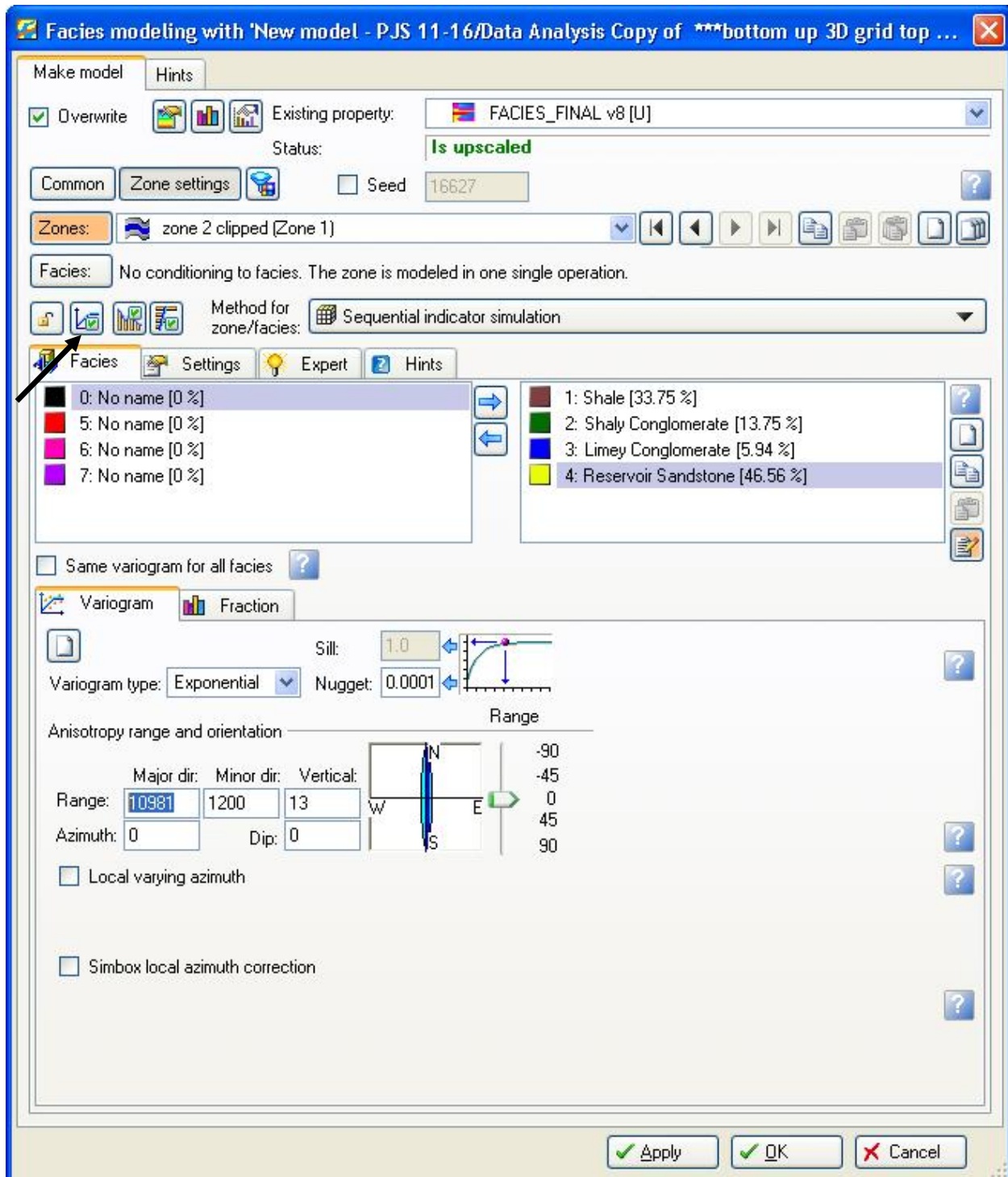
Figure 16: Screenshot of the 'Facies Modeling' process window in Petrel showing the 'use the variograms made in the data analysis' button (arrow) pushed.
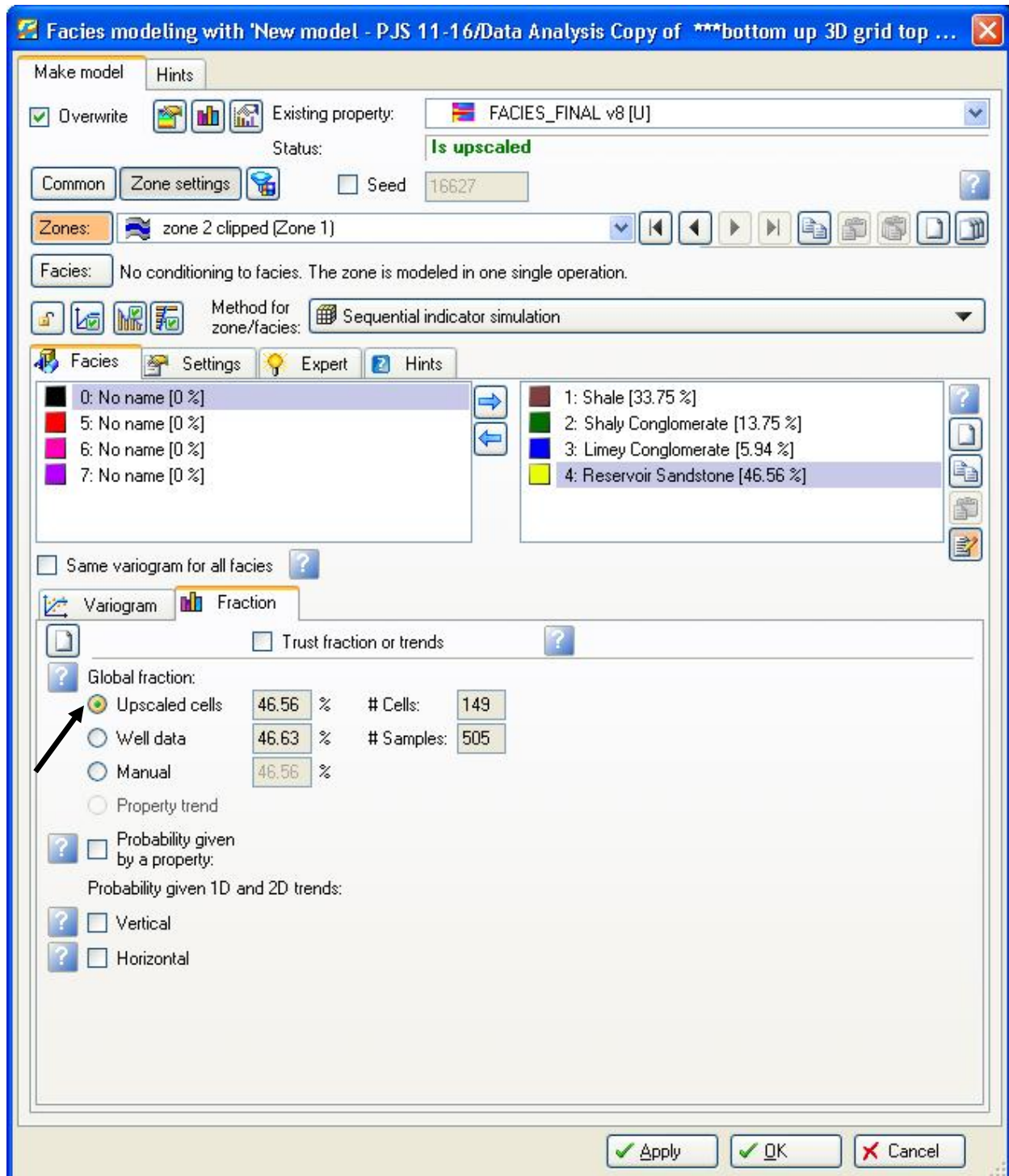
Figure 17: Screenshot of the 'Facies Modeling' process window in Petrel, showing the 'upscaled cells' option (arrow) marked in the Fraction tab.

The 'Petrophysical Modeling' process in Petrel was used to populate the 3D cellular model with porosity using Sequential Gaussian Simulation (SGS). SGS is a stochastic modeling process commonly applied to continuous data such as porosity. In the 'Petrophysical Modeling' window two buttons are pushed, one to apply the data transforms and the other to apply the variograms (Figure 18). The buttons are pushed for each lithofacies in each zone, and the method for each lithofacies is set to SGS.
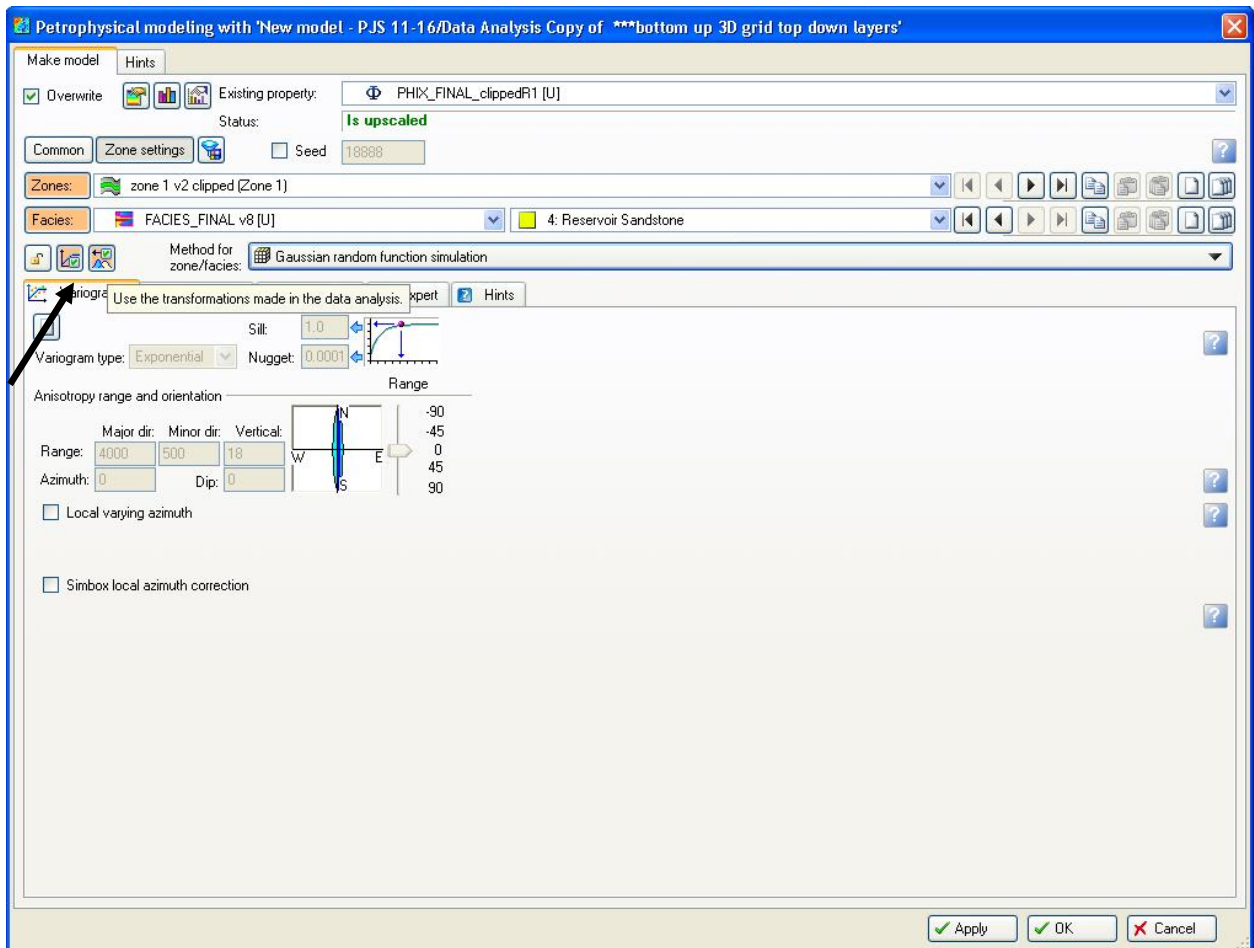
Figure 18: Screenshot of the 'Petrophysical Modeling' process window in Petrel, showing buttons (arrow) pushed to apply variograms and transformations done in 'Data Analysis' process to the porosity property of the reservoir sandstone lithofacies in zone 1.

Because SGS is a stochastic modeling process, each population of the 3D cellular model with porosity is an equally probable realization. In order to select the 'best' realization for further use in reservoir modeling, a total of nine realizations were made and their pore volumes compared in detail. Each realization had different total pore volumes, zone pore volumes, and lithofacies pore volumes within each zone. Seeing the range of possible outcomes allowed selection of the 'best' realization for further use, based on which of the realizations had the most 'average' pore volumes; the most 'average' realization is more reflective of the overall outcome of the modeling process than realizations at either the high or low extremes of pore volumes. Figures 19-22 show the percent deviation from average pore volumes for each of the realizations. Realization 8 was clearly the most 'average' and was selected to use in further reservoir modeling.
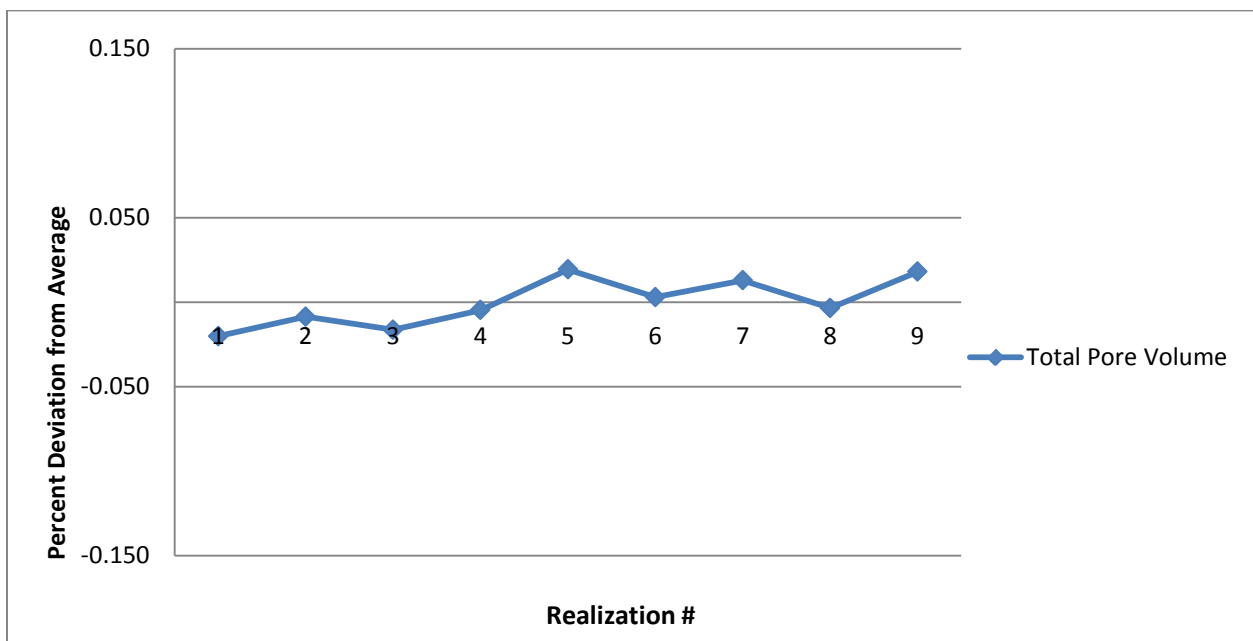
Figure 19: Graph showing percent deviation from average of total pore volume for nine realizations of porosity model made in Petrel.
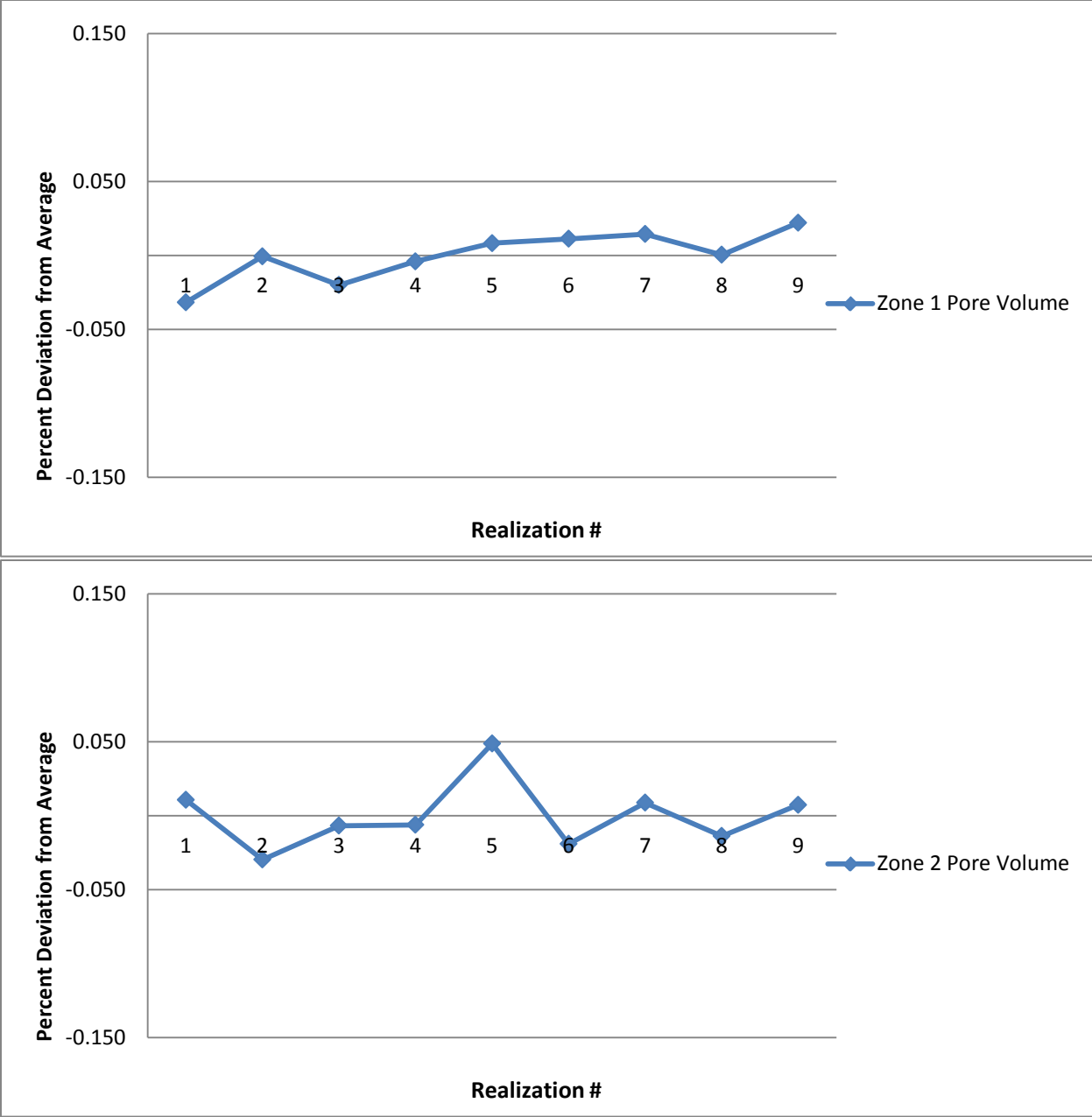
Figure 20: Graph showing percent deviation from average of pore volume of each zone (Zone 1 is upper zone in Petrel model, Zone 2 is lower) for nine realizations of porosity model made in Petrel.
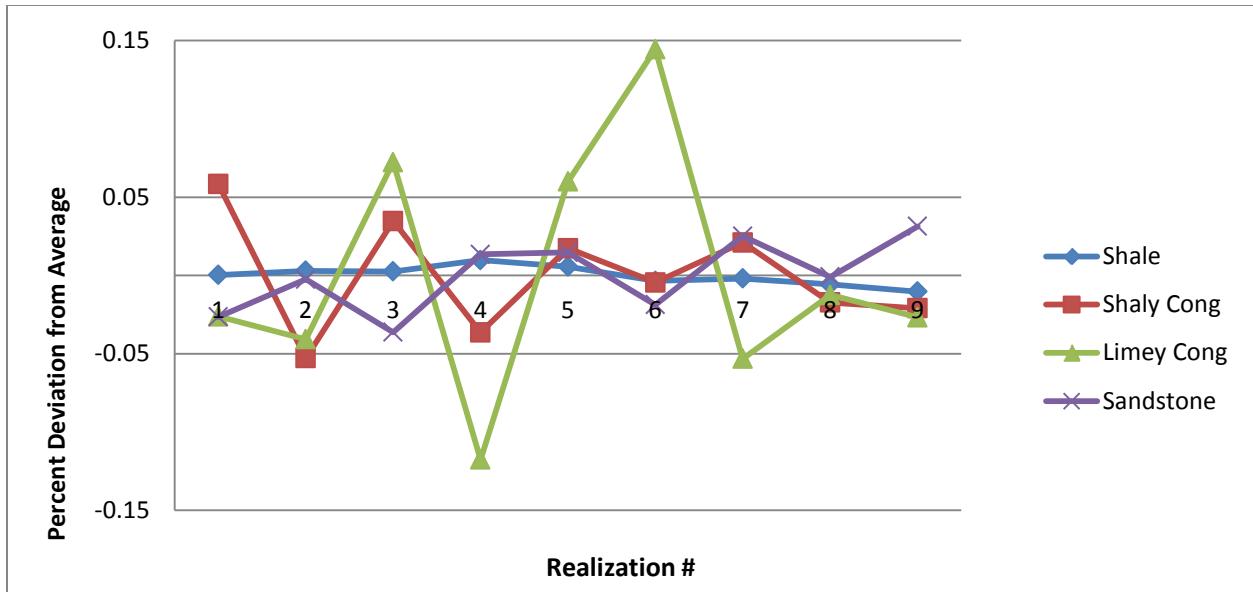
Figure 21: Graph showing percent deviation from average of total pore volume of each lithofacies for nine realizations of porosity model made in Petrel.
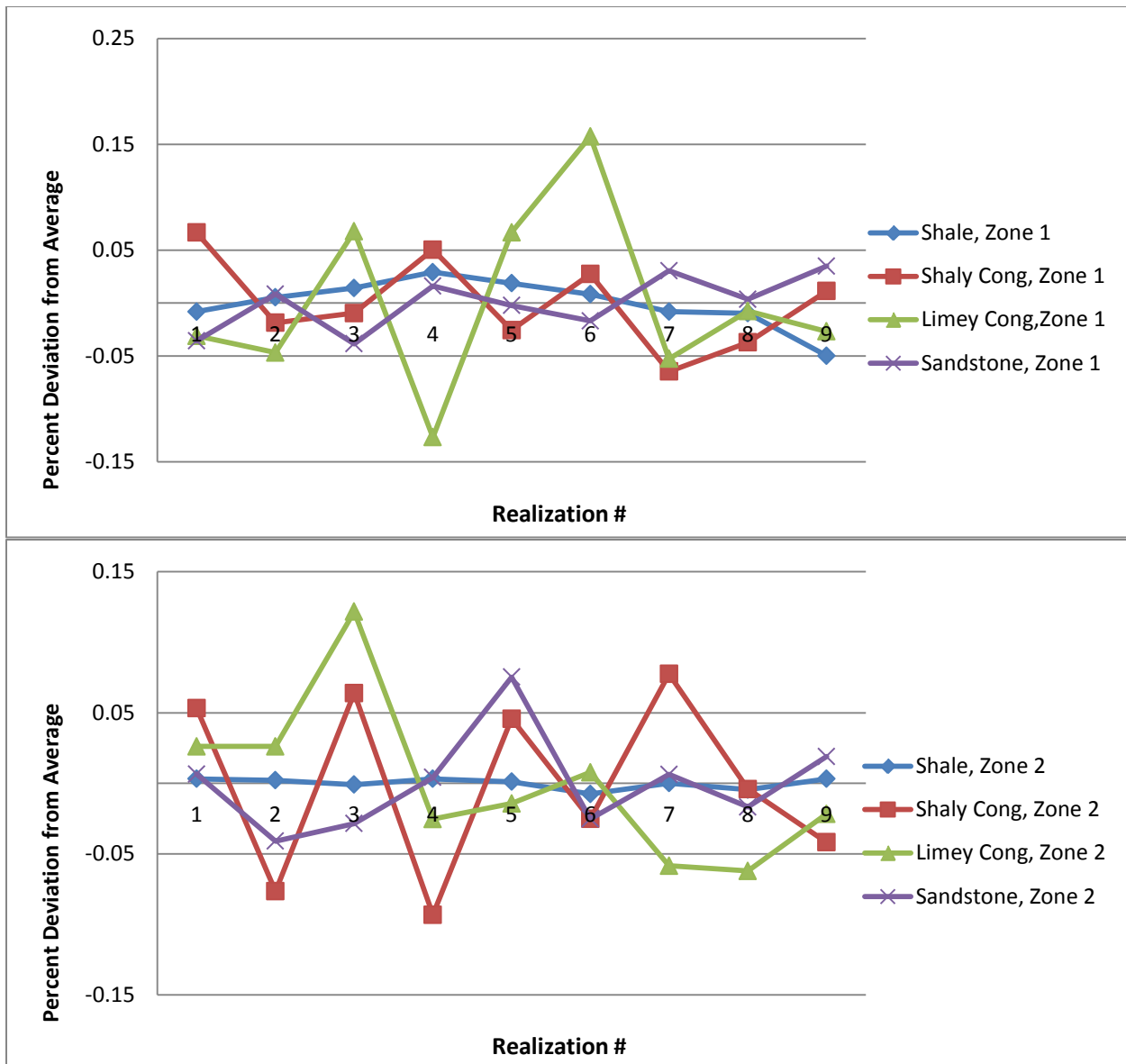
Figure 22: Graph showing percent deviation from average of pore volume of each lithofacies in each zone (Zone 1 is upper zone in Petrel model, Zone 2 is lower) for nine realizations of porosity model made in Petrel.

Populating the 3D cellular model with permeability was much faster and more straightforward than the processes for lithofacies and porosity. Permeability is a mathematical function of porosity and lithofacies. Lithofacies-specific mathematical transforms of porosity (see Results section on petrophysics) to permeability were used to populate each cell in the 3D model with permeabilityby use of the 'Property Calculator' in Petrel (Figure 23).
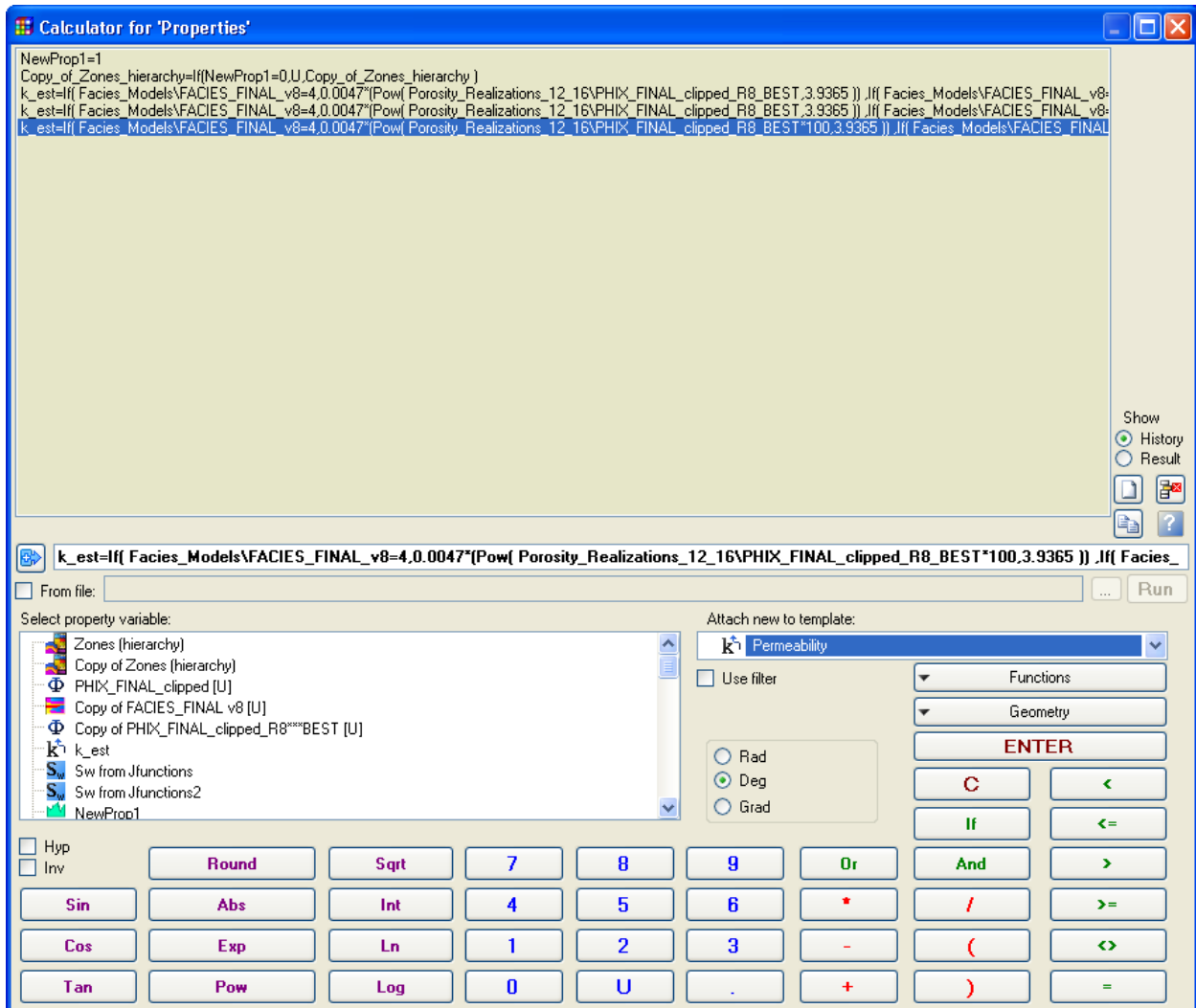
Figure 23: Screenshot of the 'Property Calculator' in Petrel, showing input of a facies-specific equation for permeability.

For fluid saturations the model was populated with water saturation only; since oil saturation is 1-Sw, a water saturation model is sufficient to provide effective visualization of both oil and water distribution in the reservoir. Populating the model with water saturation also enables

volumetric calculations of original oil in place (OOIP) in Petrel. Two methods of populating the model with water saturation were used: XYZ Kriging, and the J-Function equation. XYZ Kriging is done in petrophysical modeling process, but the J-Function equation was done in a commercially-available add-in module not normally included in the Petrel software package called Blueback Reservoir. Water saturation models using several combinations of variables were made using both methods. The variables were irreducible water saturation (Swirr), Formation Volume Factor (FVF), and Free Water Level (FWL). Models were made using Swirr of 0.10, 0.15, and 0.20, FVF of 1.15, 1.2, and 1.25, and FWL of -2250 and -2260 feet subsea. The combination of different variables resulted in a total of 36 models, 18 for each of the two methods.

Kriging is essentially an interpolation algorithm, assigning values of a variable to grid cells based on some weighting of known values in other cells. XYZ Kriging forces the kriging process to follow sea level rather than the curvature of the layers in the model, so that the end result is a more realistic picture of fluid distributions within the reservoir. In contrast to Kriging, the J-Function equation is a simpler variable-driven equation in which a series of inputs for each cell is transformed into a value for water saturation. The standard J-Function equation is given by:

$$\textbf{J= Pc/(interfacial tension)(cos(contact angle)) * (k/phi)}^{1/2}$$

In the standard form, this equation requires capillary pressure data (Pc, interfacial tension, contact angle). However, in the absence of such data, a revised J-Function equation can be used. In the Blueback Reservoir module in Petrel, which has a Water saturation modeling Process, the J-Function equation is given as:

$$\textbf{J= (z-HAFWL) * (k/phi)}^{1/2}$$

Where z is the subsea depth of each grid cell, and HAFWL is height above free water level for each grid cell. Water saturation as a function of J is given by:

$$\textbf{J(Swn)=a*Swn}^{b}$$

The constants **a** and **b** are calculated by the Blueback Reservoir module using logarithmic linear regression of points in a cross-plot of J vs. Sw (Figure 24).   Swn is normalized water saturation, and is defined as:

$$\textbf{Swn= (Sw – Swirr)/(Swmax – Swirr)}$$

Where **Swirr** is irreducible water saturation and **Swmax** is maximum water saturation. The Blueback Reservoir module calculates water saturation by combining two J-Function equations and solving for Swn:

$$\textbf{J= (z-HAFWL) * (k/phi)}^{1/2} = \textbf{a*Swn}^{b}$$

Rearranging to solve for Swn yields:

$$\textbf{Swn = (J/a)}^{1/b}$$

The Blueback Reservoir module calculates J and Sw using the grid cells corresponding to each well, using a cross-plot of J vs. Sw for those cells to calculate constants **a** and **b**, and then populates the entire model with Sw values.
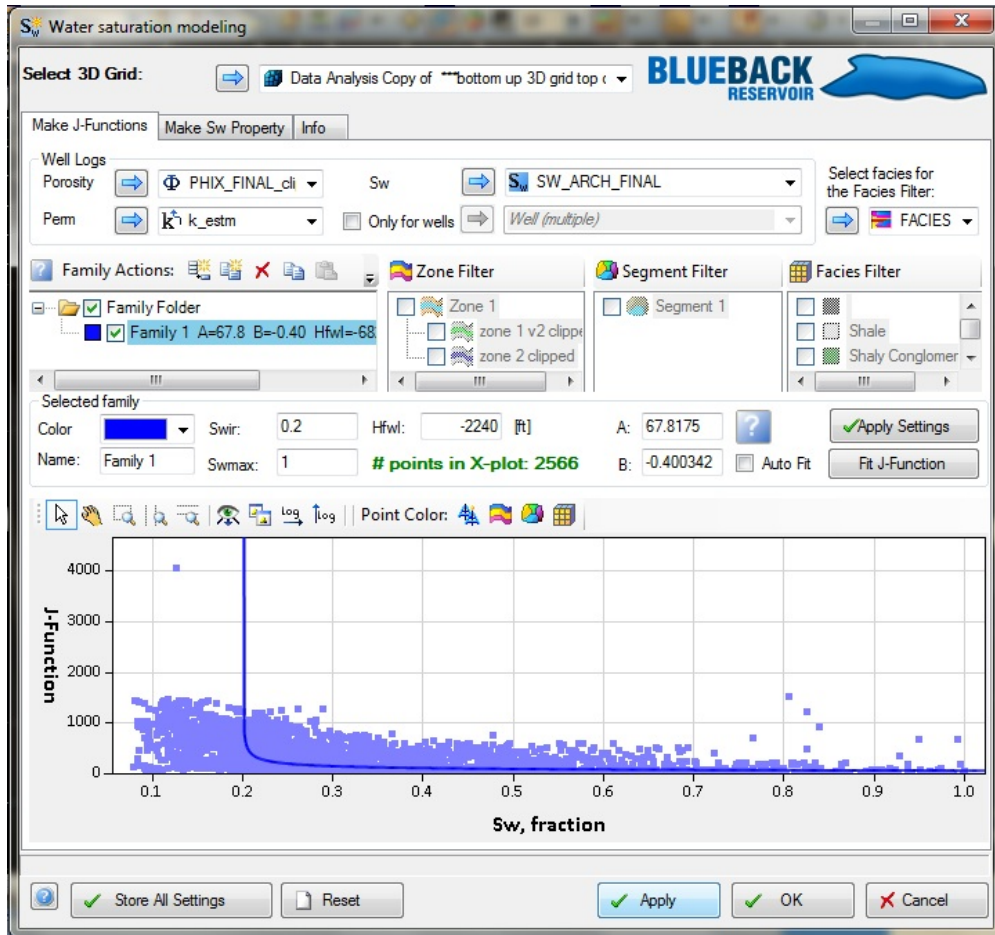
Figure 24: Screenshot of the Blueback Reservoir module in Petrel, showing input of parameters for calculation of J-Function equation and parameters **a** and **b**.

For the J-Function equation method of water saturation modeling, the Blueback Reservoir module allows input of Swirr and FWL. However, the 'Petrophysical Modeling' process window, where the XYZ Kriging method of water saturation modeling is done, does not allow specification of these variables. Instead, Swirr for the XYZ Kriging models were activated using the 'Property Filter' (Figure 25) and FWL was set in the 'Volume Calculation' process (Figure 26) in Petrel when it was run on those models. The same FWL used for the J-Function equation models was set in the 'Volume Calculation' process when used on those models. For both the J-Function and XYZ Kriging water saturation models, FVF is set in the 'Volume Calculation' process in Petrel (Figure 27).

The 'Volume Calculation' process in Petrel was used to calculate stock tank barrels of original oil in place (STOOIP) for each of the 36 water saturation models. The process calculated total STOOIP for each model, and provided a summary of the STOOIP in each drainage polygon (see Results) and for each lithofacies in each drainage polygon. Appendix E contains tables of volumetric calculation results for all 36 water saturation models, including the method used and the values for Swirr, FWL, and FVF for each model.
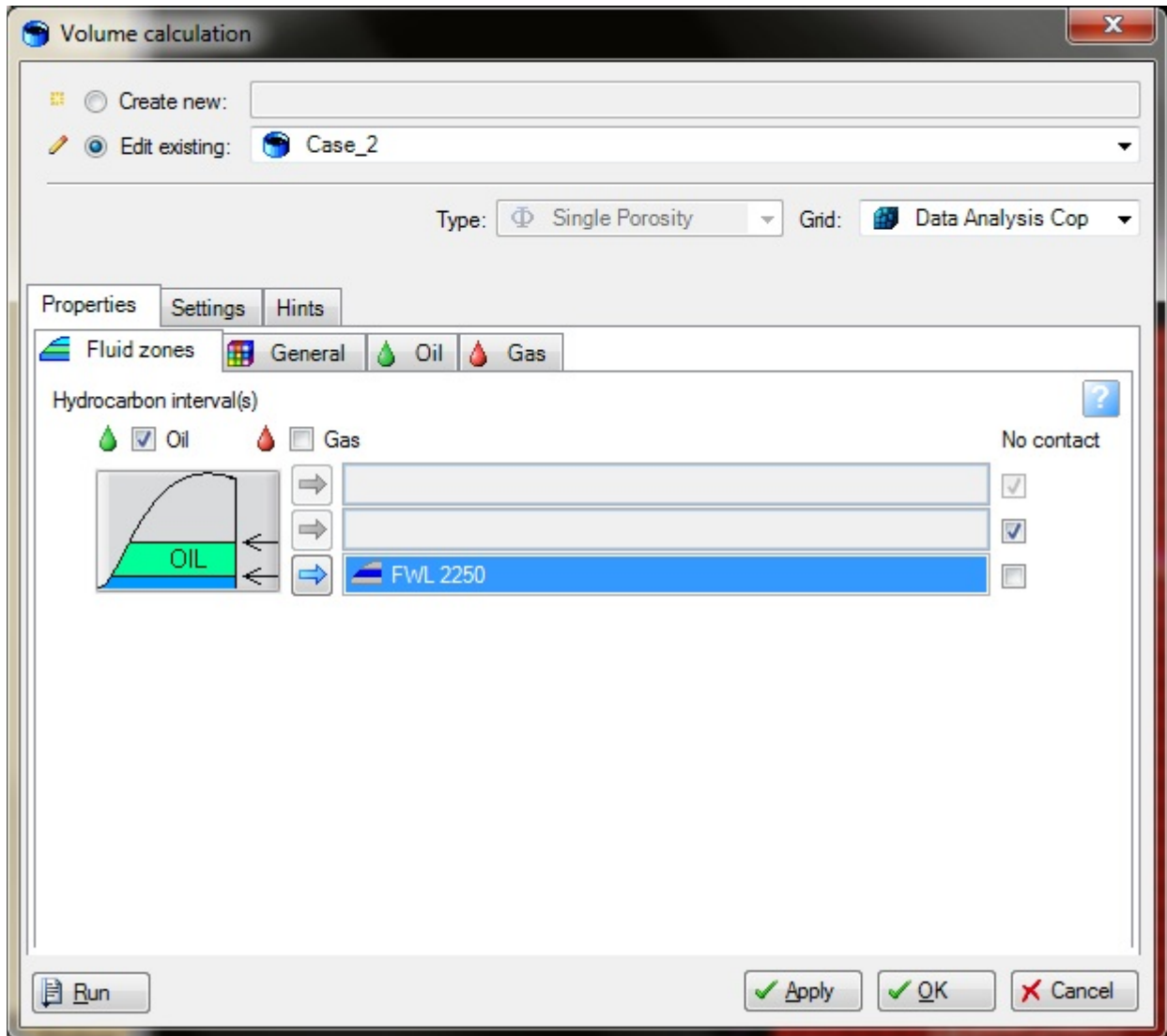
Figure 26: Screenshot of 'Volume Calculation' process in Petrel, showing input of FWL for calculation of STOOIP.
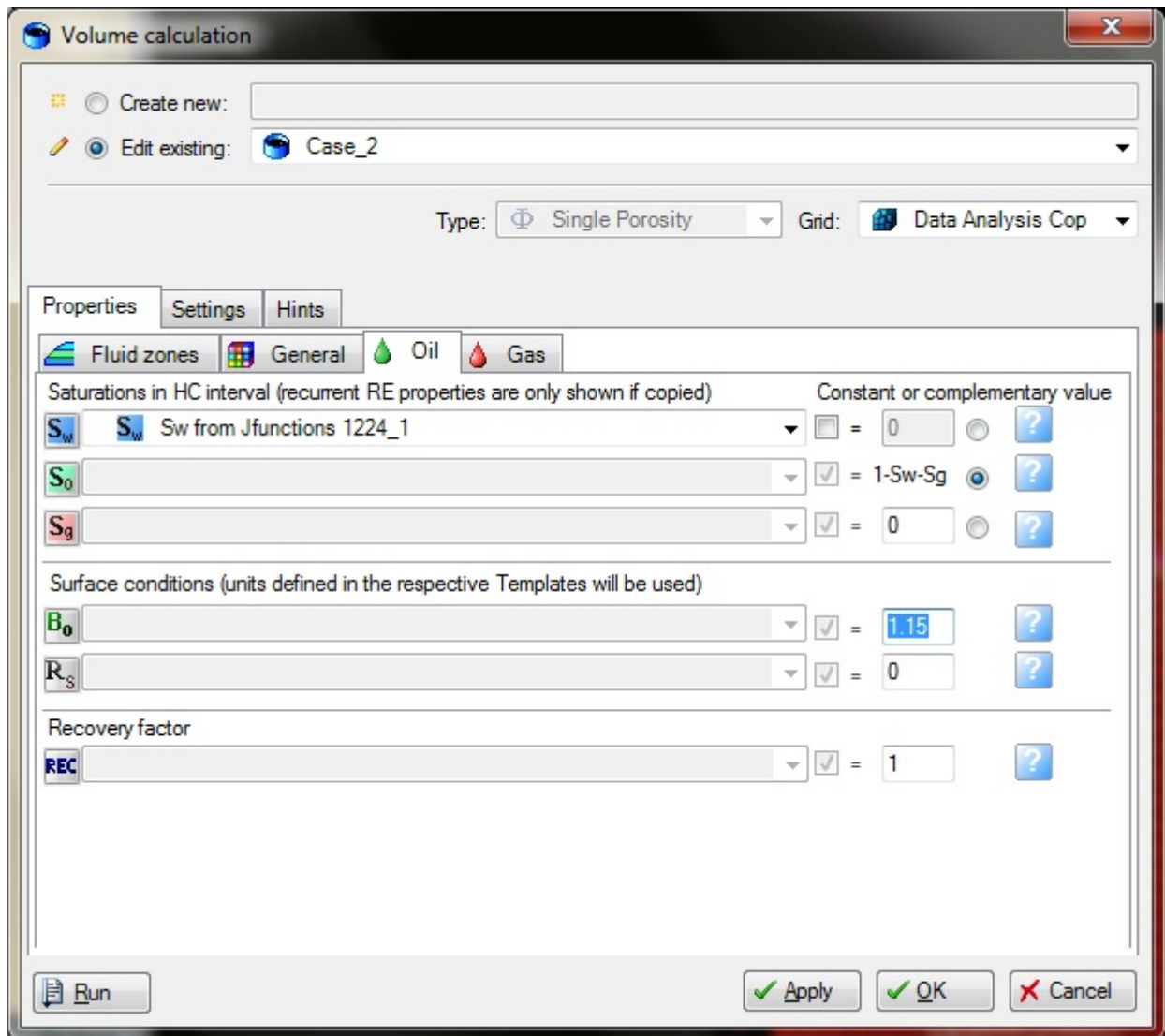
Figure 27: Screenshot of 'Volume Calculation' process in Petrel, showing specification of FVF, written as Bo in the window, for calculation of STOOIP.

APPENDIX D: VARIOGRAMS

Table 1: Lithofacies variogram parameters for each lithofacies in each zone.

		Major Range	Minor Range	Vertical Range	Major Azimuth	Minor Azimuth	Variogram Type	Nugget	Sill
Zone 1	Shale	4500	1200	6	0	270	Exponential	0.0001	1.00
	Shaly cong	10000	2000	10	0	270	Exponential	0.0001	1.00
	Limey cong	13000	2000	10	0	270	Exponential	0.0001	1.00
	SS	14000	1800	15	0	270	Exponential	0.0001	1.00
Zone 2	Shale	5000	1600	16	0	270	Exponential	0.0001	1.00
	Shaly cong	14635.1	1600	10	0	270	Exponential	0.0001	1.00
	Limey cong	9000	900	10	0	270	Exponential	0.0001	1.00
	SS	10981.6	1200	13	0	270	Exponential	0.0001	1.00

Table 2: Porosity variogram parameters for each lithofacies in each zone.

Major Direction

		Band width	Thickness	Search Radius	Tolerance Angle	Lag Tolerance %	# Lags	Lag Distance	Major Range	Major Azimuth	Variogram Type	Nugget	Sill
Zone 1	Shale	2090.9	20	19213.5	44.3	50	8	2561.8	5000	0	Exponential	0.0001	1.00
	Shaly cong	1439.4	20	12004.8	69.2	50	8	1600.6	5800	0	Exponential	0.0001	1.00
	Limey cong	1693.8	20	17189.9	90	50	8	1960.2	7500	0	Exponential	0.0001	1.00
	SS	1925.8	20	23236.2	61.5	50	8	3098.2	4000	0	Exponential	0.0001	1.00
Zone 2	Shale	1292.3	20	9673.1	90	50	8	1289.7	5500	0	Exponential	0.0001	1.00
	Shaly cong	2624.8	20	9924.2	57.7	50	8	1323.2	5000	0	Exponential	0.0001	1.00
	Limey cong	1492.3	20	16190.5	60.3	50	8	2158.7	3800	0	Exponential	0.0001	1.00
	SS	1117.6	20	17320.8	50.8	50	8	2309.4	4000	0	Exponential	0.0001	1.00

Table 3: Porosity variogram parameters for each lithofacies in each zone.

Minor Direction

		Band width	Thickness	Search Radius	Tolerance Angle	Lag Tolerance %	# Lags	Lag Distance	Minor Range	Minor Azimuth	Variogram Type	Nugget	Sill
Zone 1	Shale	3610.9	20	6146.6	90	50	8	478.5	500	270	Exponential	0.0001	1.00
	Shaly cong	6342.6	20	4600.7	90	50	8	613.4	2500	270	Exponential	0.0001	1.00
	Limey cong	5526.4	20	4116	90	50	8	548.8	500	270	Exponential	0.0001	1.00
	SS	4860.1	20	4270.9	90	50	8	569.5	500	270	Exponential	0.0001	1.00
Zone 2	Shale	6863	20	5157.3	90	50	8	337.2	500	270	Exponential	0.0001	1.00
	Shaly cong	8038.6	20	7470.6	90	50	8	996.1	1200	270	Exponential	0.0001	1.00
	Limey cong	3788.2	20	3771.3	90	50	8	502.8	500	270	Exponential	0.0001	1.00
	SS	5011	20	6589.6	90	50	8	878.6	1500	270	Exponential	0.0001	1.00

Table 4: Porosity variogram parameters for each lithofacies in each zone.

Vertical Direction

		Band width	Search Radius	Tolerance Angle	Lag Tolerance %	# Lags	Lag Distance	Vertical Range	Variogram Type	Nugget	Sill
Zone 1	Shale	50	200	70	50	8	26.7	20	Exponential	0.0001	1.00
	Shaly cong	50	200	70	50	8	26.7	20	Exponential	0.0001	1.00
	Limey cong	50	200	70	50	8	26.7	90	Exponential	0.0001	1.00
	SS	50	200	70	50	8	26.7	18	Exponential	0.0001	1.00
Zone 2	Shale	50	200	70	50	8	26.7	45	Exponential	0.0001	1.00
	Shaly cong	50	200	70	50	8	26.7	30	Exponential	0.0001	1.00
	Limey cong	50	200	70	50	8	26.7	20	Exponential	0.0001	1.00
	SS	50	200	70	50	8	26.7	20	Exponential	0.0001	1.00

APPENDIX E: VOLUMETRICS
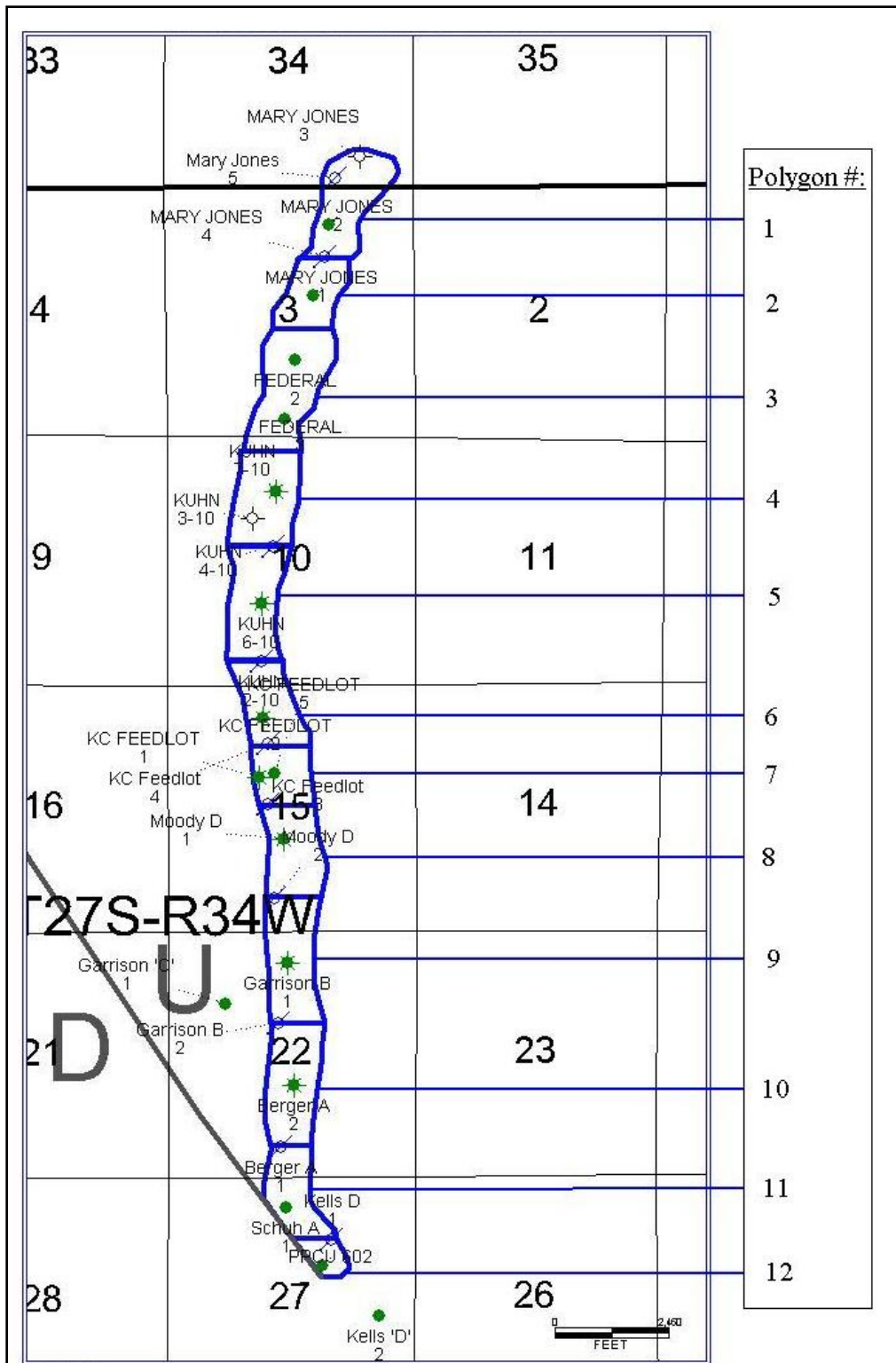
Figure 1: Map of drainage polygons.

210

Table 1: Summary of stock-tank original-oil-in-place (STOOIP) for 36 water saturation models.

Case #	Method	Swirr	FVF	FWL	STOOIP 10^3 STB Total	Drainage Polygons 1	2	3	4	5	6	7	8	6, 7, 8	9
1	J-Func.	0.1	1.15	-2250	14569	113	1127	969	703	363	556	1392	863	2811	485
2	J-Func.	0.1	1.15	-2260	15063	155	1218	1011	750	434	569	1414	878	2861	496
3	J-Func.	0.15	1.15	-2250	14178	98	1106	957	694	349	537	1348	836	2721	468
4	J-Func.	0.15	1.15	-2260	14226	147	1150	955	708	410	538	1335	829	2702	469
5	J-Func.	0.2	1.15	-2250	13858	109	1096	931	688	354	531	1309	807	2647	456
6	J-Func.	0.2	1.15	-2260	14226	147	1150	955	708	410	538	1335	829	2702	469
7	J-Func.	0.1	1.2	-2250	14048	109	1080	929	674	347	533	1334	827	2694	465
8	J-Func.	0.1	1.2	-2260	14435	149	1167	969	718	416	546	1355	841	2742	476
9	J-Func.	0.15	1.2	-2250	13887	157	1133	929	698	414	531	1295	799	2625	454
10	J-Func.	0.15	1.2	-2260	13633	141	1102	915	679	393	515	1280	795	2590	449
11	J-Func.	0.2	1.2	-2250	13281	104	1050	893	659	339	509	1255	774	2538	437
12	J-Func.	0.2	1.2	-2260	13308	151	1086	890	669	396	509	1241	766	2516	435
13	J-Func.	0.1	1.25	-2250	13486	104	1037	891	647	334	511	1280	794	2585	446
14	J-Func.	0.1	1.25	-2260	13858	143	1120	930	690	399	524	1301	808	2633	457
15	J-Func.	0.15	1.25	-2250	13044	90	1018	880	639	321	494	1240	769	2503	431
16	J-Func.	0.15	1.25	-2260	13088	135	1058	879	651	377	495	1228	763	2486	431
17	J-Func.	0.2	1.25	-2250	12749	100	1008	857	633	326	489	1204	743	2436	419
18	J-Func.	0.2	1.25	-2260	12776	145	1043	854	642	381	488	1192	735	2415	418
19	XYZ Krig.	0.1	1.15	-2250	13586	151	1048	1014	691	291	503	1208	745	2456	459
20	XYZ Krig.	0.1	1.2	-2250	13000	144	1004	971	662	279	482	1158	714	2354	440
21	XYZ Krig.	0.1	1.25	-2250	12480	139	964	932	636	268	463	1112	685	2260	422
22	XYZ Krig.	0.15	1.15	-2250	12885	151	1040	908	689	291	498	1206	729	2433	458

Table 1 (continued): Summary of stock-tank original-oil-in-place (STOOIP) for 36 water saturation models.

Case #	Method	Swirr	FVF	FWL	Total	Drainage Polygons								
						10	11	10, 11	12	13	14	15	16	17
1	J-Func.	0.1	1.15	-2250	14569	1465	1349	2814	660	837	735	1081	1003	958
2	J-Func.	0.1	1.15	-2260	15063	1478	1350	2828	673	839	740	1090	1013	954
3	J-Func.	0.15	1.15	-2250	14178	1409	1300	2709	647	808	708	1044	960	907
4	J-Func.	0.15	1.15	-2260	14226	1396	1275	2671	636	792	699	1029	957	901
5	J-Func.	0.2	1.15	-2250	13858	1359	1267	2626	625	787	687	1011	936	905
6	J-Func.	0.2	1.15	-2260	14226	1396	1275	2671	636	792	699	1029	957	901
7	J-Func.	0.1	1.2	-2250	14048	1404	1293	2697	632	802	705	1036	961	918
8	J-Func.	0.1	1.2	-2260	14435	1417	1294	2711	645	804	709	1044	971	915
9	J-Func.	0.15	1.2	-2250	13887	1344	1242	2586	616	772	676	996	933	896
10	J-Func.	0.15	1.2	-2260	13633	1338	1222	2560	610	759	670	986	917	864
11	J-Func.	0.2	1.2	-2250	13281	1303	1214	2517	599	754	658	969	897	868
12	J-Func.	0.2	1.2	-2260	13308	1288	1191	2479	591	740	648	955	894	858
13	J-Func.	0.1	1.25	-2250	13486	1348	1242	2590	607	770	677	995	922	881
14	J-Func.	0.1	1.25	-2260	13858	1360	1242	2602	620	772	681	1002	932	878
15	J-Func.	0.15	1.25	-2250	13044	1297	1196	2493	596	743	652	961	883	834
16	J-Func.	0.15	1.25	-2260	13088	1284	1173	2457	585	729	643	947	880	829
17	J-Func.	0.2	1.25	-2250	12749	1251	1166	2417	575	724	632	931	861	833
18	J-Func.	0.2	1.25	-2260	12776	1237	1143	2380	567	710	622	917	858	824
19	XYZ Krig.	0.1	1.15	-2250	13586	1389	1345	2734	433	709	645	1010	1006	940
20	XYZ Krig.	0.1	1.2	-2250	13000	1325	1276	2601	415	680	618	968	964	901
21	XYZ Krig.	0.1	1.25	-2250	12480	1272	1225	2497	398	652	593	929	925	865
22	XYZ Krig.	0.15	1.15	-2250	12885	1246	1038	2284	433	707	644	978	934	936

STOOIP 10^3 STB

Table 1 (continued): Summary of stock-tank original-oil-in-place (STOOIP) for 36 water saturation models.

Case #	Method	Swirr	FVF	FWL	Total	Drainage Polygons								6, 7, 8	9
						1	2	3	4	5	6	7	8		
23	XYZ Krig.	0.15	1.2	-2250	12348	144	996	870	661	279	477	1156	698	2331	439
24	XYZ Krig.	0.15	1.25	-2250	11854	139	956	835	634	268	458	1110	670	2238	422
25	XYZ Krig.	0.2	1.15	-2250	10354	151	959	537	630	291	482	1142	593	2217	425
26	XYZ Krig.	0.2	1.2	-2250	9923	144	919	515	604	279	461	1095	569	2125	407
27	XYZ Krig.	0.2	1.25	-2250	9526	139	882	494	580	268	443	1051	546	2040	391
28	XYZ Krig.	0.1	1.15	-2260	13665	175	1065	1016	696	315	508	1208	745	2461	460
29	XYZ Krig.	0.1	1.2	-2260	13086	168	1020	974	667	301	486	1158	714	2358	440
30	XYZ Krig.	0.1	1.25	-2260	12562	161	980	935	641	289	467	1112	685	2264	423
31	XYZ Krig.	0.15	1.15	-2260	12974	175	1057	910	695	315	503	1206	729	2438	459
32	XYZ Krig.	0.15	1.2	-2260	12434	168	1013	872	666	301	482	1156	698	2336	440
33	XYZ Krig.	0.15	1.25	-2260	11936	161	972	837	640	289	463	1110	670	2243	422
34	XYZ Krig.	0.2	1.15	-2260	10444	175	976	539	636	315	486	1142	593	2221	426
35	XYZ Krig.	0.2	1.2	-2260	10009	168	935	517	609	301	466	1095	569	2130	408
36	XYZ Krig	0.2	1.25	-2260	9608	161	898	496	585	289	447	1051	546	2044	391
MIN					9526	90	882	494	580	268	443	1051	546	2040	391
MAX					15063	175	1218	1016	750	434	569	1414	878	2861	496

Table 1 (continued): Summary of stock-tank original-oil-in-place (STOOIP) for 36 water saturation models.

Case #	Method	Swirr	FVF	FWL	STOOIP 10^3 STB Total	Drainage Polygons 10	11	10, 11	12	13	14	15	16	17
23	XYZ Krig.	0.15	1.2	-2250	12348	1194	994	2188	415	677	617	937	895	897
24	XYZ Krig.	0.15	1.25	-2250	11854	1146	955	2101	398	650	593	900	859	861
25	XYZ Krig.	0.2	1.15	-2250	10354	652	385	1037	428	631	583	793	766	906
26	XYZ Krig.	0.2	1.2	-2250	9923	625	369	994	410	605	559	760	734	868
27	XYZ Krig.	0.2	1.25	-2250	9526	600	354	954	394	581	537	730	704	834
28	XYZ Krig.	0.1	1.15	-2260	13665	1383	1332	2715	433	709	645	1010	1012	944
29	XYZ Krig.	0.1	1.2	-2260	13086	1325	1276	2601	415	680	618	968	969	904
30	XYZ Krig.	0.1	1.25	-2260	12562	1272	1225	2497	398	652	593	929	931	868
31	XYZ Krig.	0.15	1.15	-2260	12974	1246	1038	2284	433	707	644	978	940	940
32	XYZ Krig.	0.15	1.2	-2260	12434	1195	994	2189	415	677	617	937	901	901
33	XYZ Krig.	0.15	1.25	-2260	11936	1147	955	2102	398	650	593	900	865	865
34	XYZ Krig.	0.2	1.15	-2260	10444	653	385	1038	428	631	583	793	772	910
35	XYZ Krig.	0.2	1.2	-2260	10009	625	369	994	410	605	559	760	740	872
36	XYZ Krig	0.2	1.25	-2260	9608	600	354	954	394	581	537	730	710	837
MIN					9526	600	354	954	394	581	537	730	704	824
MAX					15063	1478	1350	2828	673	839	740	1090	1013	958